Numerical simulation and experimental investigation of quantum dash lasers at elevated temperatures

Design and operation of monolithic InAs/InP quantum dash ridge laser diodes operating in the C-band

Sebastian Schaefer

Thesis submitted to the University of Ottawa
in partial Fulfillment of the requirements for the
Doctor of Philosophy in Physics

Department of Physics
Faculty of Science

© Sebastian Schaefer, Ottawa, Canada, 2024

Contents

List of Figures vii

List of Tables x

Abstract xi

Statement of Originality xii

Acknowledgments xiv

Abbreviations xv

1 Introduction 1

2 Semiconductor physics 9

2.1 Crystalline materials . . . 9
2.1.1 Crystal lattices . . . 9
2.1.2 Common crystal structures . . . 11
2.1.3 Reciprocal lattices . . . 12
2.2 Electronic band theory . . . 13
2.2.1 Valence electrons . . . 13
2.2.2 The Born-Oppenheimer approximation . . . 14
2.2.3 The mean-field approximation . . . 14
2.2.4 Electronic motion in periodic potentials . . . 15
2.2.5 Bands of allowed energy . . . 17
2.2.6 Quasi-particles . . . 17
2.2.7 Band structure for material classification . . . 19
2.2.8 Electronic dispersion . . . 19
2.2.9 Density of states . . . 25
2.2.10 Occupation functions . . . 28
2.2.11 Effective mass . . . 29
2.2.12 Doping . . . 31

2.2.13 Defect states 32
2.2.14 Strain 34
2.3 Semiconductor optoelectronics 36
2.3.1 Fermi's golden rule 36
2.3.2 Optical transitions 39
2.3.3 Refractive index 41
2.4 The role of dimensionality 47
2.4.1 Heterostructures 48
2.4.2 Envelope function selection rules 55
2.5 Semiconductor growth 57
2.5.1 Wafer growth 57
2.5.2 Heterostructure growth 58
2.5.3 Quantum dot and dash formation 62
2.5.4 Size fluctuations 63
2.5.5 Barrier composition 64

3 Laser fundamentals 66
3.1 Characteristics of a laser 67
3.2 Optical resonators 68
3.2.1 Cavity modes 69
3.2.2 Quality factor 71
3.2.3 Mode shape 71
3.3 Gain media 79
3.3.1 Materials for gain media 80
3.3.2 Einstein coefficients 82
3.3.3 The lasing condition 84
3.3.4 Optical dispersion 85
3.3.5 Transition linewidths 86
3.3.6 Gain saturation 87
3.4 Semiconductor diode lasers 88
3.4.1 Waveguide design 89
3.4.2 Voltage, power, and current characteristics 91
3.4.3 Continuous wave and pulsed lasers 95
3.4.4 Mode-locking in quantum dash lasers 101
3.4.5 Temperature dependence of laser performance 103
3.5 Mode-locked quantum dash lasers 106

4 Numerical and experimental methodology 108
4.1 Device growth 108

4.2 Experimental methods . . . 109
- 4.2.1 Note on origin of data . . . 109
- 4.2.2 Photoluminescence . . . 109
- 4.2.3 LI and IV characteristics . . . 110
- 4.2.4 Spectral measurements . . . 111
- 4.2.5 Dispersion . . . 111

4.3 Numerical methods . . . 113

4.4 Simulation flow . . . 114
- 4.4.1 Simulation setup . . . 115
- 4.4.2 Material macros . . . 117

4.5 Drift diffusion simulation . . . 118
- 4.5.1 Hydrodynamic model . . . 120
- 4.5.2 Active and passive device regions . . . 122
- 4.5.3 Band structure . . . 122
- 4.5.4 Carrier mobility . . . 123
- 4.5.5 Carrier distributions . . . 125
- 4.5.6 Recombination . . . 128

4.6 Treatment of quantum dots and dashes . . . 131
- 4.6.1 Calculating confined states . . . 131
- 4.6.2 Integration with the full device simulation . . . 133
- 4.6.3 Carrier capture and escape . . . 136

4.7 Optical calculations . . . 139
- 4.7.1 Maxwell's equations . . . 139
- 4.7.2 The scalar wave equation . . . 141
- 4.7.3 Green's function . . . 144
- 4.7.4 The Wronskian . . . 144
- 4.7.5 Langevin forces and spectral diffusion coefficients . . . 148
- 4.7.6 Numerical approach . . . 150
- 4.7.7 Gain calculations . . . 151

4.8 Adding thermal effects . . . 156

4.9 Version control . . . 158

5 Model development and calibration 160

5.1 Baseline laser design . . . 160
- 5.1.1 Substrate . . . 161
- 5.1.2 Active region . . . 162
- 5.1.3 Separate confinement heterostructure . . . 162
- 5.1.4 Spacer . . . 163
- 5.1.5 Etch stop . . . 163

5.1.6 Ridge . . . 164
5.2 Model assumptions . . . 164
5.2.1 Time independent simulation of a pulsed device . . . 164
5.2.2 Lateral optical modes . . . 166
5.2.3 Boundary conditions . . . 167
5.2.4 Ohmic contacts . . . 167
5.2.5 Fixed refractive indices in passive regions . . . 168
5.2.6 Interface grading . . . 168
5.2.7 Static quantum-mechanical states . . . 169
5.2.8 Absence of self-heating . . . 169
5.3 Comparing numerical results with experimental data . . . 170
5.4 Wetting layer inclusion . . . 170
5.4.1 Calculated quantum dash states . . . 172
5.4.2 Inclusion of advanced gain model . . . 176
5.4.3 Voltage-current and current-power characteristics . . . 178
5.4.4 Characteristic temperatures . . . 181
5.4.5 Internal efficiency and loss . . . 182
5.4.6 Spectral properties . . . 184
5.5 Understanding carrier distributions . . . 187
5.5.1 Hole-electron ratio . . . 188
5.5.2 Comparison with a baseline device . . . 191

6 Impact of structural design variations on device performance 194

6.1 Defining a design goal . . . 194
6.2 Design variations . . . 196
6.2.1 Tunneling injection . . . 197
6.2.2 Tunnel diode contacts . . . 198
6.2.3 Heat spreaders . . . 199
6.2.4 Buried heterojunction . . . 200
6.2.5 Number of quantum dash layers . . . 200
6.2.6 Quantum dash layer spacing . . . 203
6.2.7 Separate confinement heterostructure-ridge separation . . . 205
6.2.8 Unipolar barrier layers . . . 207
6.3 Comparison of experimental results for second growth cycle . . . 210
6.3.1 Experimental LIV curves . . . 213
6.3.2 Lateral multi-mode lasing . . . 213
6.3.3 Comparison of LIV parameters . . . 221
6.3.4 Characteristic temperatures . . . 225
6.3.5 Comparison with original design . . . 226

7 Conclusion and outlook **230**

8 Appendix **233**

8.1 Simulation variables 233
8.2 Distribution of LIV parameters for baseline design 252
8.3 Second growth cycle 254
8.3.1 Internal efficiency and modal loss 254
8.3.2 All LIV parameters 254
8.3.3 LI curves: first derivative 255
8.3.4 Characteristic temperature fitting 257
8.4 Code snippets 261
8.4.1 Data analysis functions 261
8.4.2 Creating PICS3D files 266

Bibliography **268**

List of Figures

1 Contributors to work presented within the thesis . . . xiii

1.1 OTDM and WDM setups . . . 3

2.1 Bravais lattices in three dimensions . . . 10
2.2 Zincblende and wurtzite crystal structures . . . 11
2.3 Relative band position for metals, semiconductors, and insulators . . . 18
2.4 Dispersion diagrams for InAs and Silicon . . . 21
2.5 Density of states as a function of system dimensionality . . . 28
2.6 InAs band edge near Γ, Brilluoin zone, and available optical transitions . . 39
2.7 Anderson's rule and band alignment in heterojunctions . . . 50
2.8 Comparison between MBE and MOCVD . . . 59
2.9 CBE system . . . 60
2.10 Optical fiber attenuation and dispersion compared to the band gap of InGaAsP lattice matched to InP . . . 61
2.11 Stranski-Krastanov growth of quantum dots and dashes . . . 63
2.12 AFM image of growth condition impact on QDash formation . . . 63

3.1 Spectral components of a laser . . . 67
3.2 Cavity modes . . . 68
3.3 Spectral mode shape in Fabry-Perot resonator . . . 74
3.4 Sample spatial mode shape in ridge waveguide laser . . . 77
3.5 Absorption and recombination processes in a two-level system . . . 82
3.6 Basic ridge waveguide diode laser . . . 89
3.7 Schematic IV and LI curve for a diode laser . . . 92
3.8 Gain and photon statistics . . . 94
3.9 Sideband generation . . . 97
3.10 Spectral and spatial hole burning . . . 102
3.11 Band gap and density of states as a function of temperature . . . 104

4.1 Photoluminescence measurement setup . . . 109
4.2 LI characteristic for manual and semi-automatic characterization setups . . 110

4.3 Dispersion compensation measurement setup . . . 112
4.4 PICS3D simulation flow . . . 114
4.5 Mesh . . . 114
4.6 Carrier density and DOS in PICS3D as a function of chemical potential . . 127
4.7 Recombination and thermalization processes in semiconductors . . . 128
4.8 Level alignment between QD and full device simulation in PICS3D . . . 134
4.9 Carrier capture and escape via thermionic emission . . . 137
4.10 Comparison of the prediction of various model versions . . . 159

5.1 Band edge, refractive index and cross-section for baseline design . . . 160
5.2 Lateral modes for baseline design . . . 167
5.3 Photoluminescence power spectra for reference sample . . . 171
5.4 Details of the quantum dash structure . . . 172
5.5 Isosurfaces for calculated dash states . . . 173
5.6 Quantum dot and dash states and resulting density of states . . . 174
5.7 Recreation of the Gioannini gain model . . . 176
5.8 IV- and LI-characteristic for 1500 µm baseline device at 293 K . . . 178
5.9 LIV parameter comparison between baseline design and experimental reference at 293 K . . . 180
5.10 Temperature dependence of I_{th} and η_d for baseline design and experimental reference . . . 182
5.11 Internal efficiency and modal loss at 293 K . . . 183
5.12 Comparison between experimental and simulated lasing spectra and gain curves for 750 µm baseline device at 293 K . . . 184
5.13 Simulated group refractive index as a function of injection current . . . 185
5.14 Comparison between experimental and simulated group delay and group refractive index . . . 186
5.15 Carrier concentration for 750 µm and 1500 µm devices at 293 and 343 K . . 188
5.16 Carrier concentration for short and long devices at room temperature . . . 189
5.17 Normalized carrier concentrations for 750 µm and 1500 µm devices at 293 and 343 K . . . 192

6.1 Design changes investigated . . . 196
6.2 LI curve and LIV parameters for devices with varying numbers of quantum dash layers . . . 201
6.3 Characteristic temperatures and internal efficiency for devices with varying numbers of quantum dash layers . . . 203
6.4 LIV parameters and characteristic temperatures as a function of quantum dash layer spacing . . . 204

6.5 Optical power distribution for different sub-ridge spacer thicknesses 205
6.6 Band offsets for undoped InAlAs, InP, and 1.15Q 208
6.7 LIV parameters and characteristic temperatures as a function of unipolar barrier thickness 209
6.8 Experimental laser power as a function of current density for different cavity lengths and temperatures in batch 2 212
6.9 Reproducibility of power discontinuity for baseline design 214
6.10 Second derivative of LI curve for batch 2 devices measured with the bar testing setup at 20°C 218
6.11 Normalized second derivative of experimental laser power as a function of current density for different cavity lengths and temperatures in batch 2 . . 219
6.12 Spectral evolution and mode-locking purity as a function of bias in batch 2 220
6.13 Overview of all experimental diode voltages for batch 2 221
6.14 Overview of all experimental series resistance for batch 2 222
6.15 Overview of all experimental threshold currents for batch 2 223
6.16 Overview of all experimental slope efficiencies for batch 2 224
6.17 Characteristic temperatures T_0 and T_1 for all designs in batch 2 225
6.18 Comparison with B0 design as a function of cavity length 226
6.19 Comparison with B0 design as a function of temperature 227
6.20 Comparison with B0 design in terms of wall plug efficiency as a function of temperature 228
6.21 Experimental lasing spectra for different device designs 229

8.1 Distribution of extracted parameters at room temperature for batch 1 devices with 5 QDLs 253
8.2 Internal efficiency and modal loss for all designs in batch 2 254
8.3 All LIV parameters measured for devices from the second growth cycle . . . 255
8.4 First derivative of LI curve for batch 2 devices 256
8.5 Characteristic temperature T_1 fitting for 750 µm cavities 257
8.6 Characteristic temperature T_1 fitting for 2000 µm cavities 257
8.7 Characteristic temperature T_1 fitting for 1500 µm cavities 258
8.8 Characteristic temperature T_1 fitting for 2000 µm cavities 258
8.9 Characteristic temperature T_1 fitting for 750 µm cavities 259
8.10 Characteristic temperature T_1 fitting for 2000 µm cavities 259
8.11 Characteristic temperature T_1 fitting for 1500 µm cavities 260
8.12 Characteristic temperature T_1 fitting for 2000 µm cavities 260

List of Tables

2.1 Points of high symmetry in reciprocal space for diamond and zincblende semiconductors 22

3.1 Potential gain media 81

4.1 Material parameters for semiconductors used in the simulation 118

5.1 Baseline design parameters 161
5.2 Quantum dash dimensions 173

6.1 Design changes investigated in the literature review 196
6.2 Fabricated batch 2 designs 210

Abstract

The ever increasing data streams transmitted via optical networks, combined with a growing interest in reducing the energy consumption of these same networks, have made it clear that a new generation of light sources is needed for the networks of the future. In this work, we examine one candidate device, a mode-locked ridge waveguide quantum dash laser. Quantum dash and dot gain media both exhibit spontaneous mode-locking, reduced sensitivity of their performance to temperature, and lower threshold current densities. Dashes additionally offer higher peak gain and broader gain bandwidths, but show higher phase noise than dots.

We develop a quantum dash laser model in a commercial laser simulation package, Crosslight PICS3D, that predicts several device performance characteristics, including threshold current density and slope efficiency. The model is calibrated to experimental results at temperatures of up to 70°C. Using the numerical model, we identify the crucial role the wetting layer plays in the overall device behaviour. Its ability to capture and trap carriers accounts for a significant portion of the non-radiative recombination occurring in these devices and is a major driver in the roll-off observed for higher current densities and temperatures.

The model is then used to test a variety of design considerations that would offer potential pathways towards a higher performing device, creating a short list of considerations that are to be examined experimentally. Three proposed designs were grown and fabricated. The designs studied varied the number of quantum dash layers, increased the quantum dash layer spacing within the separate confinement heterostructure, and added an unipolar barrier to prevent electron escape into the p-cladding. We find that the addition of a 100 nm InAlAs barrier at the interface between the separate confinement heterostructure and the p-cladding increases the wall plug efficiency by up to 20% at elevated temperatures without altering the lasing spectrum bandwidth.

Statement of Originality

I, Sebastian Schaefer, hereby declare that the work presented in this Ph.D. thesis, titled "Numerical simulation and experimental investigation of quantum dash lasers at elevated temperatures", is entirely my own and has not been submitted in part or in full for any other degree at any other institution. The research conducted, the experimental data collected, the simulations performed, and the analyses carried out are the result of my independent research efforts, except where otherwise acknowledged. All sources of information, including but not limited to publications, patents, websites, personal communications, and other documents, have been properly cited in accordance with academic conventions and ethical guidelines. All figures in this work not explicitly labelled as reproductions or adaptations were created by me and are original work.

I affirm that the intellectual contributions made by others to this work have been appropriately acknowledged, and all collaborative research undertaken during the course of this Ph.D. project is duly recognized in the relevant sections of this thesis. The quantum dash growth was conducted by Philip J. Poole, while the overgrowth and fabrication was done by staff at the Canadian Photonics Fabrication Centre. Some experimental results presented in this thesis were not collected by me. If experimental data was not collected by me directly, a statement attributing the figure or table caption containing said data will denote other researchers' contributions. The most significant contributions were by Ping Zhao and Ras-Jeevan K. Obhi. The latter also contributed through her work on quantum dashes, which are an essential part of the full laser simulation presented here.

I understand that plagiarism and any form of academic misconduct are serious violations of ethical and academic standards. I have adhered to the principles of intellectual integrity and have made every effort to ensure that the work contained in this thesis represents an original and significant contribution to the field of physics.

Sebastian Schaefer

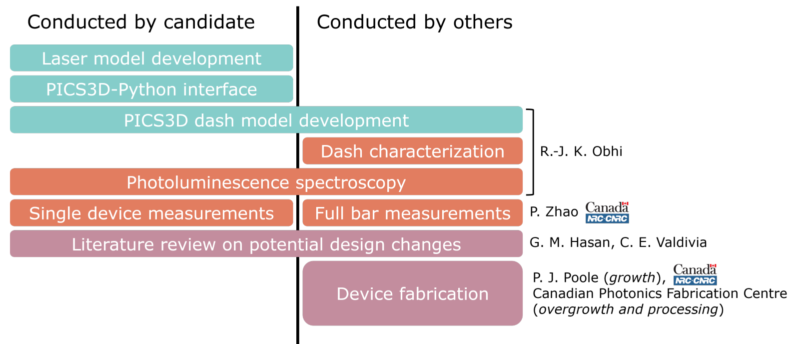

Figure 1: Contributors to work presented within the thesis

Acknowledgments

There are many people without whom this work would not have been possible. First and foremost, I would like to thank my supervisor, Prof. Karin Hinzer, without whom this thesis would never have come to fruition. Her continued support, guidance and encouragement are the reason this document ever saw the light of day. Despite the premature end of our collaboration I would also like to thank Prof. Antonio Badolato who started me on this Ph.D journey and oversaw the first years of my degree. I appreciated his feedback and insights regarding all things solid state.

I would also like to thank the many people that made this work possible and the hours more bearable, both at the SUNLAB and the National Research Council of Canada. At the SUNLAB, I would like extend my gratitude to those that were part of the TERAQD project, that being Trevor Hall, John Cook, Christopher Valdivia, Paige Wilson, Gazi Hasan, Matt Wilkins, Jaskiran Kaur, and especially, Ras-Jeevan K. Obhi, who helped me think through many a problem throughout this project and was there in many a moment of despair. At the National Research Council, I would like to extend my gratitude to our always knowledgeable and helpful collaborators, Philip J. Poole, Pedro Barrios, Silas Chen, Zhenguo Lu, Jiaren Liu, Mohamed Rahim, Ping Zhao, Linda Mao, and Eric Liu. Without their support in fabricating devices, conducting experiments, and providing feedback and insight, none of this work would have been possible.

I would also like to thank Prof. Adina Luican-Mayer, whose valuable advice and guidance at crucial parts of this journey helped me get to this point. Furthermore, I would like to extend my deepest gratitude to my friends and family, who have helped me along the way in both word and deed. Honorable mention goes to Meghan Beattie and Mandy Lewis, who took the time to read through parts of this thesis to make sure I am not embarrassing myself too much. I would also like to extend an extra special thank you to my mum, who was there as an unfailing support and reeled me back in whenever I got too far off track. Lastly, I would like to thank my partner Helen for her continued support in the face of unending deadline extensions.

This work was conducted on un-ceded Anishinabe Algonquin territory.

Abbreviations

Non-exhaustive list of abbreviations (and jargon) used in the text and their meaning, and, where appropriate, SI unit.

Abbr.	SI Unit	Meaning	Explanation
AFM		Atomic Force Microscope	Raster imaging method based on vertical displacement of a nanoscale tip
Laser		Light Amplification via Stimulated Emission of Radiation	A device that transforms an input of energy into a spatially and temporally coherent beam of photons with low angular divergence
QD		Quantum Dot	Nanostructure confining carrier movement in three dimensions
QDash		Quantum Dash	Nanostructure confining carrier movement in two dimensions
QW		Quantum Well	Nanostructure confining carrier movement in one dimension
QDL		Quantum Dash Layer	Layer containing capped quantum dashes
V_d	V	Diode voltage	Forward bias voltage at which a diode starts conducting current
R	Ω	Resistance	Series resistance of a diode
I_{th}	mA	Threshold current	Current at which laser diode starts lasing
n_d	mW/mA	Efficiency	Efficiency at which bias current is converted into laser light
η_d		External quantum efficiency	Efficiency at which input carriers are converted into output photons in a lasing mode
T_0	K	Characteristic temperature for the threshold current	

Abbr.	**SI Unit**	**Meaning**	**Explanation**
T_1	K	Characteristic temperature for the slope efficiency	
SCH		Separate Confinement Heterostructure	
1.15Q		$In_{0.815}Ga_{0.185}As_{0.405}P_{0.595}$	Quarternary alloy that constitutes the SCH and barrier between adjacent QDLs, with a fundamental bulk transition wavelength of 1.15 µm
FWHM		Full-Width Half-Maximum	Width of a peak in a signal using its width at half the peak value on either side of the maximum
SRH rec.		Shockley-Read-Hall recombination	Defect-mediated non-radiative recombination of carriers in a semiconducting material
MOCVD		Metalorganic chemical vapour deposition	Semiconductor growth method often used for epitaxy
MOVPE		Metalorganic vapour phase epitaxy	Semiconductor growth method often used for epitaxy
VCSEL		Vertical Cavity Surface Emitting Laser	Laser geometry where laser emission is perpendicular to the plane of the growth region
MLL		Mode-locked laser	Laser which emits light on multiple modes with a defined phase relationship between them
WPE		Wall plug efficiency	Efficiency with which a laser converts electrical into optical power, assuming negligible losses in electrical support systems

1

Introduction

We live in a society that is producing and transferring an incredible volume of data every day. In 2022, every minute of every day, the 5 billion people that had access to the internet were sending 16 million texts and 231 million emails, uploaded 500 hours of video footage to YouTube, and conducted over 6 million web searches. All in all, over 97 zettabytes of data were transferred in 2022 [1]. If we use solid state hard drives similar to the one this thesis is written on to store all that data and move it between locations, we would need approximately 200 million hard drives, each weighing in at just over 40 g. Assuming the best case scenario of perfectly densely packed data, with each hard drive filled to the brim, moving all the data using physical hard drives would then result in shipping roughly 8 million tons of weight around, not far off from the 11 million tons of crude oil that were transported via ship in 2021 [2, 3]. This illustrates the sheer scale of information transported, which generally happens seamlessly and out-of-sight. And the data transported is only projected to increase, as estimates predict an almost doubling of all data traffic to 181 zettabyte by 2025 [1, 4]. It is therefore important to increase the capacity of the networks that enable this flow of data to be ready for this deluge on the horizon.
Moving vast quantities of data about however comes at a price: energy. Transferring information takes vast amounts of energy, and the communication technologies that enable this transfer were estimated to consume somewhere between 1 to 1.5 % of global electricity production in 2018 [5]. An impressive increase in the energy efficiency of communication devices, especially on the network side, has caused the relative share of electricity demand to remain stable while transferring ever greater data volumes, but there is evidence that there are severe limitations for further efficiency increases using traditional network hardware. As processors hit physical limits and Moore's law grinds to a halt, future data demand is likely to be matched by a proportional increase in energy demand [6]. In 2020, communication technologies were estimated to already produce somewhere between

600 to 700 $MtCO_2e$[1], or 1.8 to 2.8 % of annual greenhouse gas emissions [6, 7]. And while some of this shared information may cause a reduction in green house gas emissions elsewhere through higher process efficiencies or reduced travel, the magnitude of the emissions savings are hard to quantify, and difficult to compare, and should therefore not factor meaningfully into sustainability considerations [6, 8, 9]. Somewhere between 42 to 68 % of these greenhouse gas emissions are created by the network infrastructure, that is the network of hubs and data centres that route, store, and manipulate data [7, 10]. A lot of this energy is not spent on computations however. Since most of the potential electrical energy that enters a data centre eventually turns into heat, they grow hot quickly. Since a lot of networking hardware is designed to operate in a relatively narrow temperature window, an extensive amount of cooling is required to avoid equipment failure and extend component lifetimes. For an average data centre, roughly one third of the energy input goes towards cooling equipment operation [11]. Depending on the equipment and cooling setup, running these facilities at higher temperatures can result in significant energy savings [12]. Having photonic components that are capable of operating at elevated temperatures could therefore translate directly into energy savings, thereby reducing the ecological footprint of communication technologies. It also lowers the threshold for the deployment of fibre optical systems, as smaller network hubs built to serve lower density communities in rural settings require less capital overhead if cooling can be sized differently or even be mostly foregone.

This work is focused on mode-locked semiconductor laser diodes, which could increase the data rates of existing network infrastructure while simultaneously offering a reduction in complexity and energy consumption. Laser diodes already play a crucial role in fiber-optical networks, which make up a large portion of the physical transport layer for high throughput interconnects and long haul telecommunications. The data rates, fidelity, and reach of fiber bundles are unparalleled over long distances, which is why 99 % of intercontinental data transfers are estimated to occur via fiber [15]. The role of the laser diode in these networks is to act as a light source which is then modulated in order to encode information. This information will be processed digitally, using electronic components with maximum operating frequencies in the 10s of GHz, thereby limiting the maximum modulation frequency [16]. The modulation frequency in turn limits the maximum achievable bit rate per channel, which is the rate at which information can be written to or read from a single channel. In order to achieve higher data rates from a single data stream, multiple channels are combined into one data stream. The channels remain distinguishable by division of the signal into multiple time, polarization, wavelength (frequency), or

[1] $MtCO_2e$ is the mass of emitted gasses, scaled by a factor that varies depending on their effect on the global greenhouse effect compared to CO_2. A gas that results in greater atmospheric heating than CO_2 will have its weight scaled by its global warming potential to reflect an increased impact on global climate.

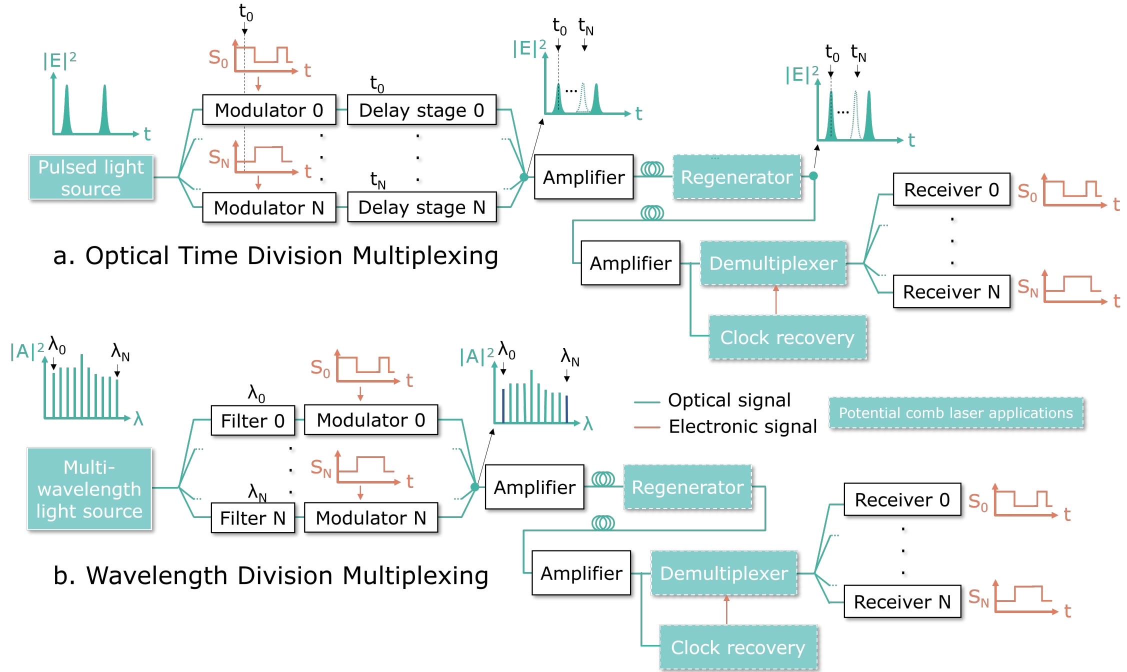

Figure 1.1: Sample optical time division and wavelength division multiplexing setups. Potential applications for a comb laser are indicated by the devices with a light teal background. Inspired by [13] and [14].

quadrature channels. This act of signal division is known as multiplexing, and multiple methods of multiplexing can be combined to push bit rates even further [17]. Wavelength division multiplexing (WDM), also known as frequency division multiplexing (FDM), and optical time division multiplexing (OTDM) are the most mature schemes in fiber optical systems [17–19]. A sample setup for each system is shown in Fig. 1.1. A light source produces a base signal, that is then modulated by an array of modulators. There are a variety of modulation schemes, ranging in complexity from simple return-to-zero one-off keying (RZ-OOK) common in OTDM to more complex protocols such as phase or amplitude shift keying (PSK or ASK) for WDM [20]. The choice of protocol defines the maximum possible bit rate per channel, but is dependent on the speed and stability of the available equipment [21].

In the case of OTDM, the light source has to produce a continuous stream of narrow pulses, with as little pulse jitter and background noise as possible to avoid cross-talk between adjacent time bins. For a pulsed source emitting pulses at the repetition rate f_{rep} split into N channels with each channel modulated at f_{mod}, as illustrated in Fig. 1.1a, the highest achievable transmission speed is then $N \cdot f_{mod}$, given that the pulse width is smaller than the width of the modulated time window f_{mod}^{-1}. For 40 GHz modulation, the upper pulse width limit is then approximately 250 ns.

For WDM, there are two traditional approaches to creating multi-wavelength light sources: arrays of thermally stabilized vertical cavity surface emitting lasers (VCSELs) or distributed feedback (DFB) lasers, or current-tunable multi-section distributed Bragg reflector (DBR) lasers [22, 23]. To avoid cross-talk and to account for drift in the carrier wavelength, channel spacing was kept around 100 GHz, or 0.8 nm in the C-band around 1550 nm (see Fig. 2.10a.) [23]. This spacing was decreased using coherent WDM, which introduces a fixed phase relationship between neighbouring channels, thereby eliminating the phase noise. This allows a higher number of channels in a given wavelength range than conventional WDM, with channel spacing decreasing below 25 GHz, raising the data rates fourfold [24]. One method of obtaining these phase-stable multi-wavelength sources are mode-locked quantum dash lasers. They have shown stable mode-locking with narrow channel spacing for over 48 channels, resulting in single fiber data rates of 10.8 Tbit/s [25]. Additionally, they are ideal platforms for future hybrid WDM/OTDM schemes due their narrow pulse widths and negligible timing jitter [17, 26].

The goal of this work was to analyze a mode-locked monolithic ridge waveguide InAs/InP quantum dash laser, understand its internal dynamics, identify performance limiting mechanisms, and then propose different design changes to alleviate these shortcomings. The design is developed and fabricated by researchers at the National Research Council of Canada (NRC). The optimization of the design was done primarily with respect to a reduction of performance degradation with temperature, focusing on output power and efficiency at higher temperatures. Higher temperatures in the context of this work refer to the 70 to 85°C range, the upper limit for the auxiliary systems in most networking equipment.

This work is split into five chapters, not counting the introduction and conclusion. **Chapters 2**, **3**, and **4** explain semiconductor fundamentals relevant to this work, mode-locked lasers, and numerical simulation methodology as it applies to the work at hand. **Chapters 5** and **6** present the results of this work. **Chapter 5** outlines the calibration of the model, and illustrates the differences between the physical system and the model at hand. The last chapter, **Chapter 6**, looks at potential design variations from literature on devices in other material systems, focusing on improving the temperature stability. Multiple designs are examined using numerical simulation, and the most promising design changes are fabricated and tested.

The first theory chapter, **Chapter 2**, introduces the fundamentals of semiconductors with a focus on properties relevant to semiconductor lasers. We use the Bloch theorem to illustrate the origin of the band states in zincblende semiconductors, since this work focuses on devices in the InGaAsP material system. These states are used to discuss the behaviour of the system under strain and temperature, and the consequences for intra- and interband optical transitions as a result. Doping and defects are discussed, both as a means for

device structuring and potential sources of loss. The role of dimensionality is discussed, and a framework for calculating confined states using the effective mass approximation is developed. Lastly, a brief survey of growth methods used for these devices is provided, to serve as a foundation for the discussion of the available design space for material and geometry related parameters in later chapters.

Chapter 3 explains laser essentials required to understand monolithic mode-locked semiconductor diode lasers. The concept of cavity modes is introduced and expressions for the spectral and spatial mode shapes of a plane mirror Fabry-Perot cavity are derived, identical to the one in the laser design examined in this work. The requirements for laser gain media are examined, and requirements for coherent light emission from semiconductor gain media are explained. The current theory of mode-locking in semiconductor diode lasers is then discussed and how it pertains to the device at hand. The final part of the chapter is a discussion of temperature-related semiconductor laser performance degradation, where common degradation mechanisms are examined, such as the alteration of the band structure leading to a reduction in carrier confinement and changes in the occupation broadening diminishing the peak gain.

The last chapter providing background, **chapter 4**, is concerned with the numerical simulation of semiconductor optoelectronics. The basics of finite element drift-diffusion calculation are examined in the context of device simulation in Crosslight PICS3D, the modelling environment we predominantly used in this work. Since a few simulation runs involve thermal modelling, a discussion of the heat generation and transport models available in PICS3D is included. The environment's optical solver is examined in great detail, as well as its connection to the drift-diffusion model to achieve a degree of self-consistency between optical and electrical model predictions. Since the optical mode solver shares several similarities with the solver used in the calculation of confined states the calculation of states is discussed as well. A few important material parameters and their models are explored, and a brief discussion of the interpolation approach of properties for the quarternary semiconductor alloys is included.

Chapter 5 introduces the basic structure of the device and specific, design-related assumptions made in the model approximation. Uncertainties about material and structural properties are highlighted where they seem pertinent, and the underlying reasoning for the approximations or estimates used in the model is explained. The calibration of the model for the baseline design as a function of temperature and cavity length is then shown. The baseline design is a device featuring five layers of quantum dashes that acted as the initial reference point for the model. Lastly, we examine the distribution of carriers and photons in the device and correlate it to expected parameter impacts.

Chapter 6 is the final chapter and culminates the previous sections' work into suggestions for potential performance improvements. It starts with a review of previous attempts at

performance improvement, gathering approaches tried in other material systems or for different device designs, such as buried heterostructure lasers or devices featuring tunneling injection quantum wells. This list of potential improvements is then examined for feasibility and ease of integration into the existing device. The options showing the greatest promise in terms of performance improvement combined with a manageable increase in fabrication complexity were evaluated numerically, and the simulation results were used to generate a reduced list of devices to examine experimentally. The list consists of two avenues of design optimization, in addition to including a general reduction of the total number of quantum dash layers to four. Guided by simulation results, the effect of increasing the spacing between adjacent quantum dash layers was examined, as well as the addition of an InAlAs electron blocking layer at the top of the separate confinement heterostructure. These designs were then fabricated at the NRC and tested to validate model predictions. An improvement in the performance of devices is found for either design approach, more pronounced for shorter cavity lengths. Interestingly, the combining both design changes is not cumulative.

The **appendix** has two sections of additional information the interested reader might find useful when trying to examine the results presented in this work more thoroughly or if the reader is interested in using the suite of scripts designed to support Crosslight PICS3D. The first part of the appendix presents additional experimental data that was used to derive some of the higher level performance parameters that were presented throughout the different chapters, predominantly chapter 6. They were moved to the appendix to keep the flow of the specific sections more succinct. The second part features an introduction describing the operation of selected scripts that were used to create and run simulations in PICS3D with less user oversight, and provide useful interfaces to manage the large volume of data created by each simulation run.

List of publications and conference presentations

The work described in this thesis also led to two publications and several conference presentations, listed below:

- R.-J. K. Obhi, S. Schaefer, C. E. Valdivia, P. J. Poole, J. R. Liu, Z. G. Lu, K. Hinzer. "Height distributions of uncapped InAs/InGaAsP/InP quantum dashes and their effect on emission wavelengths" Proc. SPIE 12010, Photonic and Photonic Properties of Engineered Nanostructures XII. 20100C 2022.

- R.-J. K. Obhi, S. Schaefer, C. E. Valdivia, J. R. Liu, Z. G. Lu, P. J. Poole, K. Hinzer. "Indium arsenide single quantum dash morphology and composition for wavelength tuning in quantum dash lasers" Applied Physics Letters 122(5), 2023.

- S. Schaefer, R.-J. K. Obhi, C. E. Valdivia, P. J. Poole, P. Barrios, J. R. Liu, Z. G. Lu, K. Hinzer. "Quantifying Loss Mechanisms in InGaAsP/InP Quantum Dash and Quantum Well Lasers", Photonics North, May 2021.

- S. Schaefer, C. E. Valdivia, R.-J. K. Obhi, K. Hinzer. "Effect of Wetting Layers on Quantum Dash Laser Operation in Crosslight PICS3D", International Conference on Numerical Simulation of Optoelectronic Devices, September 2021.

- S. Schaefer, R.-J. K. Obhi, C. E. Valdivia, P. J. Poole, P. Barrios, J. R. Liu, Z. G. Lu, K. Hinzer. "Effect of temperature on internal efficiency in InGaAsP/InP quantum dash lasers", SPIE Photonics West, February 2022.

- S. Schaefer, R.-J. K. Obhi, C. E. Valdivia, P. J. Poole, P. Barrios, J. R. Liu, Z. G. Lu, K. Hinzer. "Investigating the effect of energy level spacing and inhomogeneous broadening on performance of quantum dash ridge-waveguide lasers at elevated temperatures", SPIE Photonics West, January 2023.

- S. Schaefer, J. Kaur, D. Paige Wilson, J. P. D. Cook, P. J. Poole, M. Rahim, J. R. Liu, Z. G. Lu, K. Hinzer. "High temperature passive optical frequency comb generation from monolithic InAs/InP quantum dash lasers", SPIE Photonics West, January 2024.

2

Semiconductor physics

2.1 Crystalline materials

Most materials relevant to optoelectronics are solids, with a crystalline or amorphous arrangement of their constituent atoms. A crystal is any material that exhibits a three-dimensional translational symmetry to this arrangement. This implies that the entire symmetry of the macroscopic crystal can be reduced to the symmetry of a single microscopic unit cell. Translation of this unit cell through space along base vectors recreates the macroscopic crystal. In contrast, in an amorphous material, small perturbations of the constituent atom positions result in this translational symmetry only existing for very short translations of a few unit cells, or collapsing altogether. For all future considerations, we will also assume we are dealing with a monocrystalline material, implying that the translational symmetry extends over the entire corpus of the material. In contrast, some materials, such as Si commonly used in solar photovoltaics, are used in a polycristalline phase where multiple spatial domains with internally consistent but no global translational symmetry exist. This introduces a variety of issues at the domain interfaces, which generally render polycrystalline materials unusable for high fidelity optoelectronics. For similar reasons, the lack of long range order in amorphous materials renders them poor candidates for optoelectronic applications where precise spatial control of material parameters is necessary to facilitate the intricate structures necessary to create devices such as a light emitting diode.

2.1.1 Crystal lattices

To use the crystalline symmetry throughout this work, we need to formalize a few concepts in the definition of crystal lattices. An easy way to define a three-dimensional crystal is via Bravais lattices: these reduce the symmetry of any crystal that spans the space into

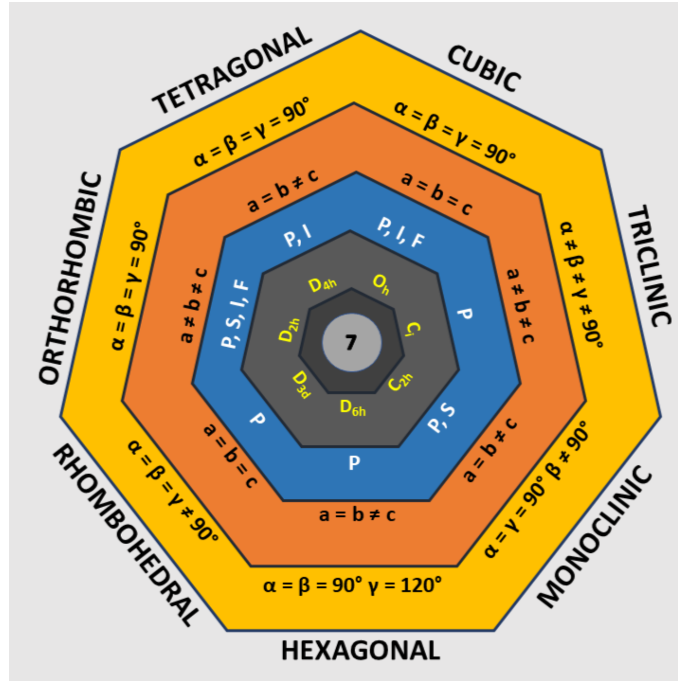

Figure 2.1: The seven Bravais crystal classes. The diagram indicates, starting from the inside, (grey) the Schönflies notation for the class, (blue) the available lattices (P=primitive, S=base-centered, I=body-centered, and F=face-centered) and lastly the relationships between the (orange) side lengths a, b, and c, and (yellow) interior angles α, β, and γ of the unit cell. Reproduced from [27] under the Creative Commons license.

one of 14 lattices, belonging to one of seven crystal classes. Their grouping and structural description can be found in Fig. 2.1 .

For any Bravais lattice, we can fill the entire volume by taking a basis set of atoms, the unit cell, and translating it along primitive lattice vectors $\vec{a}_i$ and their linear combinations. In other words, the position of a given cell in space can be described as:

$$\vec{r}_n = \sum_{i=1}^{3} n_i \vec{a}_i \tag{2.1}$$

where $n_i \in \mathbb{Z}$. We will see what these basis sets of atoms look like for common semiconductor crystal structures, but the fundamental underpinning remains the same. Using this, the position of a given lattice site in the crystal is then:

$$\vec{R} = \vec{x} + n_1\vec{a}_1 + n_2\vec{a}_2 + n_3\vec{a}_3 \tag{2.2}$$

where $\vec{x}$ is the position relative to the origin of the unit cell, and n_1, n_2, and n_3 are indices indicating the position of the reference cell in relation to the origin. In other words, we

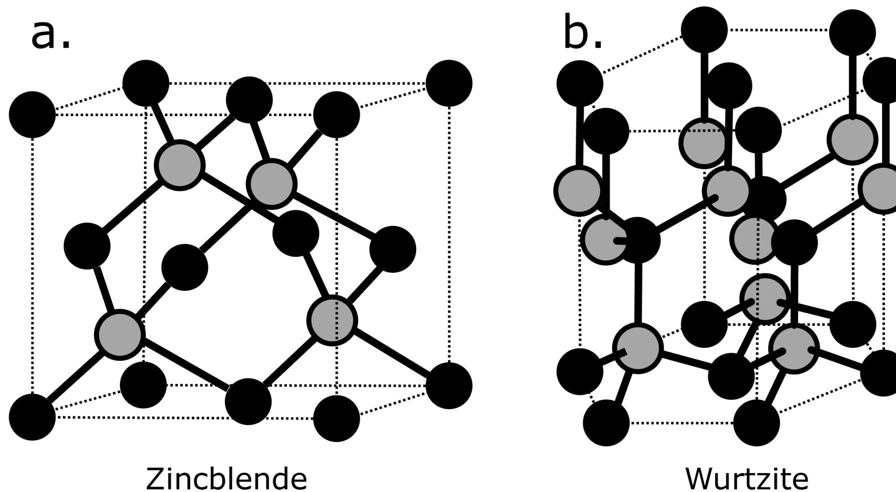

Figure 2.2: **a.** Zincblende and **b.** Wurtzite crystal structure, with the two sublattice atoms identified in blue and orange. Inspired by the lecture script of H. Foell [28]

have an aperiodic, local part ($\vec{x}$) repeated with the periodicity of the lattice ($n_i\vec{a}_i$). This is the concept that provides the opening for the Bloch theorem to deal with meso- and macroscopic crystalline structures.

2.1.2 Common crystal structures

While sufficient to describe the lattice, most common semiconductors feature Bravais lattices based on multi-atom unit cells. The most common crystal structures for commercially relevant semiconductor materials are diamond (Si, Ge), zincblende (GaAs, InAs), and wurtzite (GaN, InGaN). Zincblende and diamond both feature eight atoms in their unit cells, while wurtzite has four. We will focus our discussion of crystal structure on diamond and zincblende, as these are the only one relevant to this work.

The zincblende lattice is shown in Fig. 2.2a. It consists of two intersecting face-centered cubic Bravais lattices, offset by a Cartesian $a(\frac{1}{4}, \frac{1}{4}, \frac{1}{4})$ vector, where a is the total unit cell side length. This results in a tetrahedral coordination of each atom, as it has four equidistant nearest neighbours. It is similar to the diamond lattice, which is the zincblende structure with the same species of atoms on each sublattice.

The four-fold bonding coordination results in zincblende configurations being the lowest Gibb's free energy crystal structure under standard conditions for a lot of semiconductors based on elements, or alloys of elements, with four sp^3 hybridized electron bonding orbitals. This includes the binaries, ternaries and quarternary alloys of indium, gallium, arsenic, and phosphorus, and thereby all the materials most relevant to this study.

2.1.3 Reciprocal lattices

As the description of many aspects of the physics in crystalline systems involves periodically repeating functions, it is useful to introduce the concept of the reciprocal lattice space. While the direct lattice captures the translational and any higher order symmetries of the lattice atoms, the reciprocal lattice space describes the symmetries of periodic functions operating within the direct lattice. In analogy to the primitive lattice vectors of the direct lattice we define the primitive reciprocal lattice vectors $\vec{b}_i$:

$$\vec{b}_i = 2\pi \frac{\vec{a}_j \times \vec{a}_k}{V_p} \tag{2.3}$$

where i, j, k are the cyclically permutated indices of the primitive lattice vectors, and V_p is the volume of the primitive unit cell, used to normalize the magnitude. These vectors span the reciprocal space, so any point can be described as their linear combination:

$$\vec{G}_m = \sum_{j=1}^{3} m_j \vec{b}_j \tag{2.4}$$

with $m_j \in \mathbb{Z}$. As indicated, symmetry of the reciprocal space is related to the direct space symmetry, albeit not identical: the reciprocal space of a face-centered cubic lattice (fcc) is the body-centered cubic Bravais lattice (bcc). Since the reciprocal space is most often used for the wavenumbers k of Bloch functions, which we will encounter soon, it is also commonly referred to as k-space.

Brillouin zones

Similar to the unit cell in the direct lattice, we can use the periodicity of the reciprocal lattice to simplify the description of a given space. We just note that every point in reciprocal space can be folded back into the space spanned by the primitive reciprocal lattice vectors via translation along a linear combination of them. We therefore only need a volume defined by the bisecting planes of the primitive lattice vectors to describe every point. This representation is often called the reduced zone scheme, as we have reduced higher wavenumbers into the first Brillouin zone, or BZ. The linear coefficients m_j of the translation vector $\vec{G}_m$ that translates $\vec{k}$ into the BZ will become the band indices when we use plane waves to describe the motion of electrons in three-dimensional crystals.

2.2 Electronic band theory

Following Yu and Cardona's instructive introduction to electronic band theory, we will retrace their steps here. The original derivation can be found in [29]. The general, non-relativistic Hamiltonian describing the interactions within a defect-free crystal can be written as:

$$\mathcal{H} = \sum_i \frac{\hat{p}_i^2}{2m_i} + \sum_j \frac{\hat{P}_j^2}{2M_j} + \frac{1}{2}\sum_{j^{'},j} \frac{q^2}{4\pi\epsilon_0}\frac{Z_j Z_{j'}}{|\vec{R}_j - \vec{R}_j^{'}|} \tag{2.5}$$

$$- \sum_{j,i} \frac{q^2}{4\pi\epsilon_0}\frac{Z_j}{|\vec{r}_i - \vec{R}_j|} + \frac{1}{2}\sum_{i,i'} \frac{q^2}{4\pi\epsilon_0}\frac{1}{|\vec{r}_i - \vec{r}_{i'}^{'}|} \tag{2.6}$$

$$= V_e + V_{atom} + V_{atom,atom} + V_{e,atom} + V_{e,e} \tag{2.7}$$

where $\hat{p}_i^2$ and $\hat{P}_j^2$ are the momentum operators for the ith electron and jth nucleus, respectively, with electron mass m_i and nucleus mass M_j. The first two terms of Eq. 2.7, V_e and V_{atom}, thereby represent the kinetic energy of all electrons and nuclei within the system. Z_j is the atomic number of the jth nucleus, $\vec{R}_j$ and $\vec{r}_i$ are the position of the jth nucleus and ith electron, respectively, with q, the elementary charge. The third, fourth and fifth term thereby represent the interaction between all nuclei ($V_{atom,atom}$), the nuclei and electrons ($V_{e,atom}$), and, $V_{e,e}$, the interaction between all electrons. Summations over $j^{'}, j$ and $i^{'}, i$ exclude identical indices.
This many-particle Hamiltonian is extremely intractable and mostly serves to illustrate the components and interactions we need to take into account. There are several assumptions that need to be made in order to reduce its complexity and turn it into something that can provide meaningful predictions for the physical properties of a solid.

2.2.1 Valence electrons

The first simplification is a reduction of the number of electrons we consider: many electrons are strongly bound to their nucleus, resulting in strong localization of their wavefunction near their nucleus. These core electrons are those in filled orbitals and only show negligible interaction with the other constituents of the crystal. They can be considered in conjunction with the nuclei they are bound to as ion cores. The indices j will therefore now refer to ion cores rather than the atomic nuclei, and i will only refer to the unbound electrons, commonly referred to as valence electrons. These are electrons that reside in outer, incompletely filled shells.

2.2.2 The Born-Oppenheimer approximation

The second simplification has one of the most imposing names in physics, at least in this student's humble opinion: the Born-Oppenheimer or adiabatic approximation assumes that the large difference in masses between electrons and ion cores results in the latter responding to potential changes much more slowly. Vibrations of the ionic lattice generally exhibit frequencies below 10^{13} s^{-1}, or 10 THz, which is several orders of magnitude below the electronic response time, which is closer to 1000 THz [29]. We can therefore consider the motion of the electrons and ion cores essentially uncoupled: electrons see a stationary ionic potential, as they respond to a change in their environment long before the surrounding ion cores do. At the same time, ions can not react to each shift in electronic potential instantaneously, and thereby only interact with a time-averaged adiabatic electronic potential. The result of this approximation is therefore a split of the perfect crystal Hamiltonian into three terms, each describing one aspect of the motion and interaction of the crystal's components:

$$\mathcal{H} = \mathcal{H}_{ions}(\vec{R}_j) + \mathcal{H}_e(\vec{r}_i, \vec{R}_{j,0}) + \mathcal{H}_{e,ion}(\vec{r}_i, \delta\vec{R}_j) \tag{2.8}$$

$\mathcal{H}_{ions}(\vec{R}_j)$ describes the motion of the ionic lattice atoms moving as a result of their interactions and interactions with the time-averaged electronic potentials. $\mathcal{H}_e(\vec{r}_i, \vec{R}_{j,0})$ describes the motion of electrons due to their interaction with the stationary ion core potentials, the latter assumed to be resting in their equilibrium positions $\vec{R}_{j,0}$. The final term $\mathcal{H}_{e,ion}(\vec{r}_i, \delta\vec{R}_j)$ describes the energy relationships of electrons with infinitesimally shifted ion cores. These displacements are generally the result of lattice vibrations, referred to as phonons. Phonons are a form of collective excitation, a boson that emerges due to the quantized nature of lattice vibrations. The phonon population in a given solid is strongly correlated to its temperature, and is in fact one of the ways in which a crystalline solid can store heat. Therefore, $\mathcal{H}_{e,ion}(\vec{r}_i, \delta\vec{R}_j)$ is commonly referred to as the electron-phonon interaction.

2.2.3 The mean-field approximation

Returning to Eq. 2.7, the electronic Hamiltonian $\mathcal{H}_e(\vec{r}_i, \vec{R}_{j,0})$ contains three interactions:

$$\mathcal{H}_e(\vec{r}_i, \vec{R}_{j,0}) = \sum_i \frac{\hat{p}_i^2}{2m_i} + \frac{1}{2}\sum_{i,i'} \frac{q^2}{4\pi\epsilon_0}\frac{1}{|\vec{r}_i - \vec{r}_{i'}|} - \sum_{i,j}\frac{q^2}{4\pi\epsilon_0}\frac{Z_j}{|\vec{r}_i - \vec{R}_{j,0}|} \tag{2.9}$$

There are three terms: the first one describes the kinetic energy of every electron in the crystal, the second one the interaction between each electron and every other electron,

and the last term describes the impact of the ion core potential on electronic energy. If we examine the second term, we note its dependency on relative electronic position in relation to all other electrons, $|\vec{r}_i - \vec{r}_{i'}|$, and the third term's electronic position in relation to all ion cores $|\vec{r}_i - \vec{R}_{j,0}|$. Given that the density of atoms (and by extension of electrons) exceeds 10^{23} cm^{-3} in most solids, this Hamiltonian becomes quickly intractable even for systems on the nanoscale. Tracking the position and velocity of each electron and then performing summations over the entire ensemble is simply computationally unfeasible. Therefore, another approximation is necessary: the mean-field approximation. Also referred to as the single electron approximation, it decouples the motion of one electron from that of all other bodies within a crystal by collecting the impact of all potentials into a single term, $V(\vec{r})$. This one electron potential includes both the interaction of an electron with the ion cores of the lattice as well as its interactions with the other highly mobile valence electrons, reducing the complexity of the Hamiltonian drastically. The electronic Hamiltonian then reads:

$$\mathcal{H}_{1e}(\vec{r}) = \frac{\hat{p}^2}{2m} + V(\vec{r}) \tag{2.10}$$

There are different ways to define $V(\vec{r})$, and the choice of method defines what material properties are captured well within the model. They can be broadly categorized into two categories: ab-initio, or first principles methods, where complex atomic potentials are calculated with minimal input parameters. They are computationally intensive, but include fewer difficult to verify assumptions. The other category are simpler, albeit still highly complex, approaches. They make use of so-called semi-empirical potentials, parametrized potentials with parameter values deduced from experimental data [29, 30].

2.2.4 Electronic motion in periodic potentials

As discussed earlier, semiconductors are crystalline and as such exhibit translational symmetry of their constituent atoms. Most crystals additionally show higher symmetries, such as identity under rotation or reflection, but these are strictly speaking optional to the definition of a crystal, even though these additional symmetries affect several material properties. To reduce the problem posed by Eq. 2.10 even further, we can use the translational symmetry of the crystal. As each ion core produces a local potential, we expect this potential to repeat with the periodicity $\vec{a}$ of the lattice, where $\vec{a}$ is a lattice vector. In other words:

$$V(\vec{r}) = V(\vec{r} + \vec{a}) \tag{2.11}$$

This periodicity allows us to employ Bloch's theorem to describe the electronic states in our crystal. When trying to find solutions to the eigenvalue problem posed by the single electron Hamiltonian, we can decompose the wavefunction into two parts: a periodically

repeating part that captures the symmetry of local potentials, $u_{\vec{k}}(\vec{r})$, which modulate the propagating electron represented by a plane wave. The result is a Bloch function:

$$\psi_{\vec{k}}(\vec{r}) = u_{\vec{k}}(\vec{r})e^{i\vec{k}\vec{r}} \tag{2.12}$$

As explained above, the periodic component retains the lattice symmetry:

$$u_{\vec{k}}(\vec{r} + \vec{a}) = u_{\vec{k}}(\vec{r}) \tag{2.13}$$

where $|\vec{k}|$ is the Bloch wave number and denotes the spatial frequency of the electron. For a crystal with infinite extent there are an infinite number of potential values for k, but we can reduce the space of potential values by using the symmetry of the crystal. For a one-dimensional crystal along x with periodicity a, we postulate that k lies within the range π/a and $3\pi/a$. k can then be written as $k = (2\pi/a) + k^{'}$, with $-\pi/a < k^{'} < \pi/a$. The one-dimensional Bloch function is then:

$$\psi_k(x) = u_k(x)e^{i(2\pi/a+k^{'})x} = u_k(x)e^{i2\pi x/a}e^{ik^{'}x} = u_{k'}(x)e^{ik^{'}x} \tag{2.14}$$

where we used the periodicity in a of $e^{i2\pi x/a}$ to combine it with $u_k(x)$ into $u_{k'}(x)$. $k^{'}$ now lies within the first Brillouin zone (BZ), and every Bloch wavenumber lying outside of it can be reached by multiplying $k^{'}$ by a factor $2\pi n/a$, where n is an integer. Rewriting the Bloch functions accordingly:

$$\psi_{nk'}(x) = u_{nk'}(x)e^{ik^{'}x} \tag{2.15}$$

This reduced zone scheme has the advantage of capturing the full extent of the translational symmetry within a single cell, which can simplify calculations by only requiring solutions within the first Brillouin zone, which can then be extrapolated outwards using the crystal's symmetry.
We can now find solutions to the single electron Schrödinger equation using the Bloch functions:

$$\mathcal{H}_{1e}\phi_{n\vec{k}'}(\vec{r}) = \left(\frac{\hat{p}^2}{2m} + V(\vec{r})\right)\phi_{n\vec{k}'}(\vec{r}) = E_n\phi_{n\vec{k}'}(\vec{r}) \tag{2.16}$$

$$= \frac{\hat{p}^2}{2m}u_{\vec{k}}(\vec{r})\psi_{\vec{k}}(\vec{r}) \tag{2.17}$$

There are several different ways to define an appropriate set of basis functions to represent $\phi_{nk'}$, such as linear combination of atomic orbitals (LCAO) or tight binding models, Wannier functions, or states derived from density-functional theory. Each set of states will come with advantages and disadvantages that need to be weighed depending on the electronic property that is to be examined. As a side note, from here-on out, we will stop differentiating between $\vec{k}$ and $\vec{k}^{'}$, since we will only be referring to the reduced zone

scheme.

2.2.5 Bands of allowed energy

We established earlier that electrons interact with the potential of the ionic cores of the lattice. The plane waves used to describe the electrons' motion will undergo scattering as a result of this interaction. The scattered components will interfere, with the degree interference of interference depending on the relative phase. The combination of electronic plane wave scattering with interference is one way to conceptualize the formation of certain disallowed energies, or band gaps, to form within a material with translational symmetry. The electronic plane matter wave propagating through a crystal will scatter off the lattice ions, which are assembled in crystallographic planes. Depending on the crystal structure and the relative orientation of the electronic wave, the separation between planes experienced by the electronic wave will vary. Generally this scattering is random, and contributions from successive scattering events partially cancel. However, for specific combinations of the scattering angle and plane-to-plane separation, the scattering becomes constructive. This occurs when the Bragg condition is met:

$$n\lambda = 2a\sin(\theta) \tag{2.18}$$

Depending on the angle of incidence on the plane θ, defined by $\vec{k}$ and the orientation of the plane $\vec{G}_n$, waves reflected from the entire set of planes of a certain orientation will interfere. If the path difference is equivalent to an integer multiple of the wavelength of the electron $\lambda = 2\pi/|\vec{k}|$, the interference will be constructive, resulting in strong backscattering. For all other path differences, interference is destructive and backscattering is weak. In other words, the ion core scattering mixes waves with different $\vec{k}$. This mixing is weak unless the difference in $\vec{k}$ is equivalent to a reciprocal lattice vector $\frac{1}{2}\vec{G}_m$, at which point the aforementioned high levels of backscattering occur. Electronic states with $\vec{k} = \frac{1}{2}\vec{G}_n$ are therefore unable to propagate through the crystal lattice. Since crystal momentum is linked to energy via the single electron Hamiltonian, see Eq. 2.17, this results in a gap in energy as well. There are simply no states available for occupation at certain energies. The result is that electronic states in a crystal form continuous bands of allowed and disallowed states.

2.2.6 Quasi-particles

Many properties of solid state systems can most easily be conceptualized and modelled using quasi-particles. A quasi-particle is a perturbation of a predominantly uniform medium

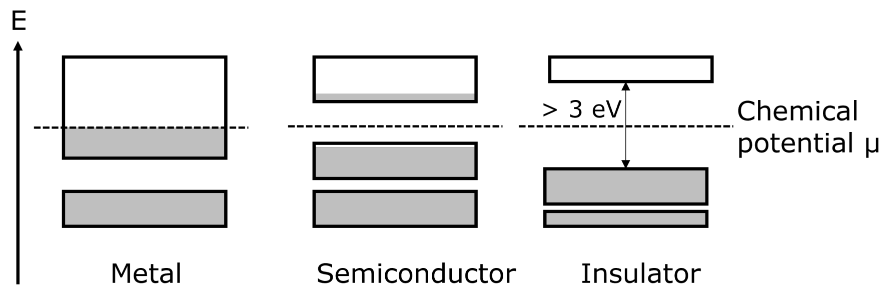

Figure 2.3: Schematic metal, semiconductor, and insulator band positions relative to the chemical potential μ.

or system, that can be treated as a particle. This quasi-particle may share characteristics of real particles, such as free electrons, like momentum, energy, spin, or polarity, but all of these properties are due to its interaction with the medium it exists in rather than intrinsic to the particle. A bubble in a glass of liquid is a useful real world analogy [31]. Without the medium of the liquid there can be no definition of the bubble, but within the medium it can be ascribed physical properties such as shape and velocity.
There is a veritable zoo of quasi-particles, but only a few are most relevant to this work, such as quantized lattice vibrations, referred to as phonons, but by far the most relevant one is the concept of the hole. So far the discussion has been centered around electronic states and their occupation by electrons. The electron in a crystal lattice is already a quasiparticle itself, as it is the concept of a free electron dressed in the potential of the crystal lattice. This alters its effective mass, a concept we will discuss more thoroughly in the section on the effective mass approximation in Ch. 4. But what happens to the electronic state that is left unoccupied when the electron is promoted to a higher energy? This vacancy, or unoccupied electronic state, is mobile and behaves like a massive particle, but with a positive charge. This concept also arises naturally from the motion of an electron at the upper edge of a band of allowed states [32]. The concept of a hole as a carrier that exists at the top of a band and carries positive mass and charge and can recombine with an electron to release energy is fundamental to conceptualizing the internal dynamics of semiconducting materials. This is especially relevant when discussing doping, a practice where carriers are introduced into a system by substituting some of the lattice atoms with species of higher or lower numbers of valence electrons. The result of doping are regions where most mechanisms are dominated by the characteristics of one charge carrier type, with profound results for the overall device behaviour.

2.2.7 Band structure for material classification

The band structure can be used to classify materials: in addition to the position of the bands, which states are occupied at the given conditions defines whether a material is a metal, semiconductor, or insulator, as indicated by Fig. 2.3. Of course, there are also more exotic states, such as semi-metals (e.g. graphene) and topological insulators (e.g. HgTe), but these are currently only of fringe interest in optoelectronic devices [33]. In order to understand the occupation, we can use the chemical potential of electrons and holes, indicating which states are occupied and unoccupied. We will expand on this concept further when discussing the density of states for a given material or nanostructure. For now it suffices to say that states up to the chemical potential are predominantly occupied, while states above it are predominantly unoccupied. The chemical potential is identical to the Fermi-energy for systems at 0 K. If the chemical potential at room temperature now happens to lie energetically exactly within a band, there are electronic states available at energies just above and below its energy. An electron that seeks a state with a different energy, possibly due to an external perturbation, such as an external applied electric field, will have a wide variety of states to occupy and therefore offer little resistance to being displaced. Materials where the chemical potential intersects a band are therefore highly conductive, and generally referred to as metals. If the chemical potential happens to fall just between two bands, there are no states that an electron seeking to occupy a higher or lower energy state can reach energetically. These materials are therefore non-conductive and labeled insulators. However, if the gap is small enough, some states will come within reach due to thermal energy sufficiently exciting electrons to bridge the gap. These are the materials are referred to as semiconductors. The exact energy at which an insulator becomes a semiconductor is poorly defined, but conventionally placed somewhere around 3 eV [32]. Due to the position of the chemical potential within the gap for semiconductors, the number of states defining the properties of a material is relatively small. This makes them ideal for material engineering, since perturbations in the form of dopants or nano-structuring are not dampened by a sea of intrinsic states.

2.2.8 Electronic dispersion

As discussed earlier, the potential an electron experiences while moving through a crystal lattice will vary depending on the relative orientation of its propagation direction $\vec{k}$ to the lattice of ionic cores. Different potentials lead to different eigenenergies, leading to the electronic dispersion $E(\vec{k})$.

Almost all technologically relevant qualities of a semiconductor are related to this dispersion relation. For the lasers examined here, the band structure defined by this relation affects every aspect of their operation, from how energy is transported to the wavelength

range in which it can operate. It is therefore paramount to understand the origins of the band structure in order to gain a deeper appreciation for its impact on the device overall. In order to obtain the band structure, Eq. 2.17 must be found. This requires finding an appropriate set of basis functions that can be used to construct $u_{n\vec{k}}$. These functions can be obtained by different methods, with a variety of options of potential basis functions. A very common approach is the use of valence electron orbitals of the isolated crystal atoms as a basis in the linear combination of atomic orbitals (LCAO) [30]. Examining the construction of Bloch functions out of atomic orbitals is illustrative in understanding the fundamentals of band structure calculations.

Assuming we have a zincblende structure, we only need to consider the interactions between the electronic wavefunctions on each of the two atoms in the primitive unit cell. For each atom $l \in [1,2]$, the Hamiltonians describing the wavefunctions of the orbitals in isolation are h_l, which act on atomic orbital wavefunctions $\phi_{ml}(\vec{r} - \vec{r}_{jl})$ constructed out of basis states that ensure orthogonality between orbitals on different atoms, called Löwdin orbitals. $\vec{r}_{jl}$ denotes the absolute position of the centre of the atom, defined as $\vec{r}_{jl} = \vec{R}_j + \vec{r}_l$, where $\vec{R}_j$ is the position of the unit cell under consideration relative to the origin and $\vec{r}_l$ is the position of the atom relative to the origin of the unit cell. The isolated atom Hamiltonian then reads as:

$$h_l \phi_{ml}(\vec{r} - \vec{r}_{jl}) = E_{ml} \phi_{ml}(\vec{r} - \vec{r}_{jl}) \tag{2.19}$$

The Hamiltonian of the full system is then combination of the unperturbed Hamiltonian $\mathcal{H}_0$ and a second term describing the interaction between the orbitals on both atoms $\mathcal{H}_{int}$:

$$\mathcal{H} = \mathcal{H}_0 + \mathcal{H}_{int} = \sum_{j,l} h_l(\vec{r} - \vec{r}_{jl}) \tag{2.20}$$

Since we are considering the electronic dispersion across the entire volume of the crystal, we create Bloch functions $\phi_{ml\vec{k}}$ based on the atomic orbital basis functions:

$$\phi_{ml\vec{k}} = \frac{1}{\sqrt{N}} \sum_j \phi_{ml}(\vec{r} - \vec{r}_{jl}) e^{i\vec{r}_{jl}\vec{k}} \tag{2.21}$$

with the number of unit cells within the crystal N. Assuming that the perturbation due to $\mathcal{H}_0$ is small, solutions to $\mathcal{H}_0$ should also represent solutions to $\mathcal{H}$. The solutions to $\mathcal{H}$ can then be written as linear combinations of these Bloch functions:

$$\psi_{\vec{k}} = \sum_{m,l} c_{m,l} \phi_{ml\vec{k}} \tag{2.22}$$

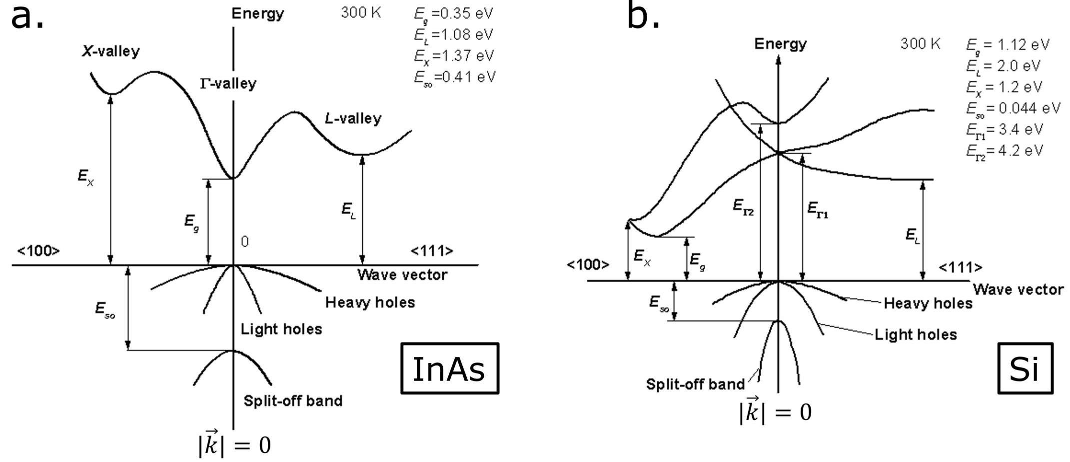

Figure 2.4: Energy momentum diagrams for **a.** InAs and **b.** Si. E_g refers to the band gap, E_X, E_{Γ_n}, and E_L to the energy gap at the X, Γ, and L points, respectively, and E_{so} denotes the energy difference between the top of the valence band and the split-off band, which is energetically depressed due to spin-orbit coupling. Reproduced from [35].

We have thereby used atomic orbitals to construct a basis set of crystal-spanning Bloch functions. These can be plugged into Eq. 2.17, which can be diagonalized to then provide us with a relationship between $\vec{k}$ and $E_{\vec{k}}$ for electrons in the semiconductor. There are other approaches to obtain appropriate basis functions as well, such as ab-initio methods based on density-functional theorem (DFT), augmented plane waves, pseudopotentials, and $\mathbf{k}\cdot\mathbf{p}$-perturbation. The choice of method will determine the accuracy and scope of the model it supports, but a thorough discussion of these methods is beyond the purview of this work. We point the reader towards [29], [34], and [30], where one can find discussion of the abilities and shortcomings of each method.

Irrespective of which method is used to obtain the solutions to Eq. 2.17, the result is a dispersion relation that links an electron's crystal momentum, expressed as $h\vec{k}$, and its energy. While there is a large number of bands m at a given momentum, most of the physical properties relevant to this work are dominated by the lowest energy band at a given momentum, which is referred to as the band edge. In a semiconductor, the band edges will define the strength and wavelength of optical transitions, and the motion of carriers under applied electric potential, among other things. This is due to the fact that carriers will generally occupy states near the band edge since there are a variety of phonon-mediated pathways for higher energy carriers to relax to these lower energy states, something that will be discussed further in the next section. These relaxations happen extremely fast, with non-band edge state lifetimes on the order of 10^{-15} to 10^{-12} s [29]. When we are concerned with the band structure of a material in the context of

Γ	Origin of reciprocal space
K	Middle of an edge between two hexagonal surfaces of the BZ
L	Centre of hexagonal surfaces of the BZ
X	Centre of square surface of the BZ
U	Middle of an edge between a hexagonal and a square surface of the BZ
W	Vertices shared by two hexagons and a square

Table 2.1: Points of high symmetry in reciprocal space for diamond and zincblende semiconductors.

optoelectronic device simulations, we are therefore most concerned with the band edge dispersion. The lowest near-fully occupied band is referred to as the valence band, while the first unoccupied band is known as the conduction band.
The band edge dispersion curves for two different semiconductors are shown in Fig. 2.4: silicon, which in its most technologically relevant phase forms a diamond lattice, and indium arsenide, which hails from the zincblende family. The dispersion curves are plotted rotating the plane wave vectors in two directions: towards $< 100 >$, the basal plane of the lattice, and $< 111 >$, the volume bisecting plane. Certain points of high symmetry are labelled. A non-exhaustive list of commonly used labels and their corresponding points in reciprocal space used for diamond and zincblende structures can be found in Tab. 2.2.8.

Direct and indirect band gaps

If we compare the energy band diagrams for InAs and Si, there are notable differences and similarities between the two semiconductors. The most obvious difference is the nature of the band gap E_g. The band gap is the smallest separation between the conduction and valence band. It is direct for InAs and indirect for Si, meaning that a carrier moving across the band gap needs to undergo a change in momentum as well as energy. This momentum difference will result in the creation or annihilation of phonons, transferring momentum into or from the lattice atoms into the electron ensemble. Naively, adding a third particle, a phonon, to a recombination process between an electron and a hole should reduce the likelihood of its occurrence, and reality bears out our naivety [29]. In the next section we will discuss the optoelectronics of semiconductors and see that whether or not a band gap is direct has profound implications for the strength and likelihood of optical transitions, with direct band gaps having a far stronger optical response than indirect band gaps. This difference in interaction strength is the motivation for Si-integrated photonics, which aims to combine the expertise in Si fabrication with materials that strongly interact with light. What is the reason for the difference between Si in InAs? The reason can be sought in the difference in ionic bonding between mono- and hetero-atomic lattices. For diamond

lattices, there is only one species of atom constituting the lattice. Using the tight binding picture, in a zeroth order approximation the Bloch functions for the electronic states are very closely related to atomic orbitals they are derived from. The four valence electrons in Si are occupying $3s^2 3p^2$ orbitals, which hybridize into sp^3. This leads to the tetrahedral bonding configuration discussed earlier. In our model picture, three of the available sp^3 orbitals will form bonding configurations with strong overlap between neighbouring atoms. These orbitals form the basis of the valence band. The last hybridized anti-bonding orbital has a much higher energy, resulting in the conduction band [29]. If the bonds now acquire a more ionic character when moving from Si to InAs, composed of two species with different electronegativities, the hybridization weakens considerably. This results in the conduction band energy near the edges of the BZ rising. This elevates the conduction band near the X- and L-points relative to the Γ-point to lead to the lowest conduction band minimum being located at Γ, the same point the valence band maximum happens to be. The band gap is now direct and carriers need to undergo no change in their linear momentum to transfer between valence and conduction band. Of course, there are severe limitations to this simplistic picture: the Bloch functions in the conduction band share much less characteristics with the underlying atomic orbitals than their valence band equivalents due to the lower effective mass of electrons resulting in a greater spread of the electronic wavefunction across multiple unit cells [32]. We will however return to this simplistic picture when discussing allowed and forbidden optical transitions, as the symmetry of the wavefunctions and therefore their ability to undergo dipole-transitions is relatively straightforward to conceptualize from their atomic orbital basis functions. All of the materials most relevant to this work are compound semiconductors in the InGaAsP family with direct band gaps, so unless specified, E_g will refer to the direct band gap of a material.

Conduction bands

While the magnitude and position of the conduction band minima is quite different for the two semiconductors, they do share a few similarities. The first is the presence of the satellite band minima, more apparent for InAs than for Si. Their energies are larger than the band gap, so in most cases these will have negligible occupation compared to the lowest energy valley, Γ for InAs and towards X along Δ for Si. They are only relevant in systems that have high hot carrier populations due to slow thermalization of electrons with energies far above the band edge. For example, this can occur if scattering is suppressed due to phonon bottlenecks or in the presence of strong electromagnetic fields [29, 36]. Under these circumstances electrons are scattered into higher energy valleys and their presence requires treatment in transport and optoelectronic models. For the lasing devices consid-

ered in this work, however, we assume that carriers are fully thermalized and reside in the lowest energy valley, allowing us to mostly ignore the higher lying valleys.
Given the origin of the band gap in both materials, the shape of the Bloch functions near the band gap is different between Si and InAs. The zincblende InAs with its band minimum near Γ has a dominant contribution from *s*-like orbitals, resulting in even symmetry of its band edge wavefunction. For Si, the underlying function are more *p*-like, lending their odd parity to the Bloch functions near X [32].

Valence bands

Comparison of the valence bands between both semiconductors shows a lot of commonality as a result of the similarity between the diamond and zincblende crystal structures, with subtle differences due to the involved species. Both semiconductors feature three valence bands in proximity to the band gap with maxima centred at Γ: the heavy, light, and split-off hole bands. There is short overview regarding the nature of each of these bands here, but the reader is encouraged to follow the excellent explanation provided in [32]. Remaining conceptually within the tight binding picture, the valence band has very strong *p*-like character, resulting in a high directionality of the bonding strength between neighbouring atoms. If a hole is to move along the direction of this bond, it will encounter only small barriers to its movement as it "hops" from atom to atom. This results in a high "hopping parameter" t, denoting a high rate of transfer between neighbouring atoms. For a hole, attempting to move in any direction not along the bond will result in a much larger barrier to motion, or a lower t. For a given orientation of the lattice one can always define a direction in-line with orbital alignment and one misaligned with the three-fold symmetry of the *p*-orbitals. This results in the non-degeneracy of the light and heavy hole bands at higher energies. The nomenclature is due to the different effective masses of the holes occupying states in either band, with the light hole band featuring a lower effective mass than the heavy hole band, albeit both are generally several times higher than the effective mass of the electron.
The origin of the split-off band lies in the spin-orbit coupling between the atomic orbitals and the nuclei of their lattice atoms. This relativistic effect couples the angular momentum of an electron to its spin, resulting in a spin-dependent correction to the energy E_{so}. The cause is the alignment of the electronic spin with the orbital momentum for the split-off band, lowering its energy relative to the misaligned light and heavy hole bands. The correction is proportional to the atomic number Z of the atom as $\approx Z^4$. We can see this borne out in the relative position of the split-off band to the top of the valence band: in Si (Z_{Si}=14), E_{so} is almost an order of magnitude smaller than for InAs (Z_{In}=49

and Z_{As}=33). In general, split-off bands are sufficiently far removed energetically to have negligible impact on the basic properties of InGaAsP-alloys, so we will generally forego their inclusion in the model for the sake of overall simplicity.

2.2.9 Density of states

Even the single electron picture from Eq. 2.17 becomes impractical when trying to derive macroscopic properties that are dependent on a large number of electrons that are only weakly interacting, such as electrical conductivity or spontaneous radiative recombination rates. Tracking the energy and wavefunction of each and every electron would be impractical. In many cases, examining the density of states as a function of energy is more useful in predicting material properties than tracking the states individually. For an arbitrary system with eigenvalues ϵ_n, the sum of all eigenvalues $N(E)$ is:

$$N(E) = \sum_n \delta(E - \epsilon_n) \tag{2.23}$$

where δ represents the Dirac delta-function. This is the total number of states of the system, and describes the spacing of states in energy space. If we want to turn this into a volumetric density of states, for example to examine the total number of states in a given volume of semiconducting material, we need the volumetric density of states, $n(E)$:

$$n(E) = \frac{N(E)}{V_{system}} \tag{2.24}$$

where V_{system} is the total volume of the system. The volumetric density of states, and sometimes its local equivalent as we will discuss later, is generally referred to as the density of states of a solid state system.

Using the Bloch theorem we arrived at the states that describe electron-like quasi-particles that move through a periodic potential. These states form bands and the relationship between crystal momentum and energy is encoded in the dispersion relation. In order to define the number of states in a given interval of energy $E + dE$, we can count the number of states available in reciprocal space that have energies lying within $E + dE$. However, we are generally interested in the volumetric density of states: for this purpose, we need to stake out the extent of the system. The periodic nature of crystals allows us to remove a segment from a perfect crystal and state that the value at opposing boundaries has to agree to be commensurate with the crystal's translational symmetry. These conditions for the boundaries of the system enforcing periodicity are referred to as periodic boundary conditions, or Born-von Karman conditions. They will be discussed in greater detail in Ch. 4. For now it suffices to say that it allows us to remove a box of side lengths L_i from our

crystal. This smaller sub-system retains all the characteristics of the macroscopic crystal, but features a well-defined system volume $V_{system} = \prod L_i$. The allowed states, denoted by their wavenumbers in reciprocal space, then span the volume from the origin at $\vec{0}$ to $\frac{2\pi}{L_i}$ along each dimension. The volume taken up by a single state in reciprocal space is $\frac{1}{(2\pi)^d}$, where d is the dimensionality of the system. The total density of states in reciprocal space, $N(\vec{k})$, is then:

$$N(\vec{k}) = 2\frac{V_{system}}{(2\pi)^d} \tag{2.25}$$

The factor of 2 is due to the fact that in addition to the momentum $\vec{k}$, each electron also has a spin $\vec{s}$, that splits each spatial wavefunction into two degenerate states, doubling the number of states at a given energy. This degeneracy can be lifted in atoms with high atomic numbers, as relativistic corrections to the orbital wavefunctions result in spin-orbit coupling (also often referred to as LS-coupling), or when a magnetic field is applied to the system. Both alter the energies of orbital eigenstates depending on the spin orientation. In semiconductors, this effect is generally relatively weak near the conduction and valence band extrema, which is where treatment using the density of states is most useful [32]. So for the purposes of this work, the most relevant contribution of electronic spin is the factor of 2 in the summation over all states.

The total number of states available in the interval $E+dE$ is then the total number of states in the interval $\vec{k}+d\vec{k}$, which is equal to the reciprocal space state density $n(\vec{k})$ multiplied by the volume covered by the interval $d\vec{k}$. It can be shown that this is proportional to $2^{d-1}\pi\vec{k}^{d-1}d\vec{k}$.

Armed with this knowledge, we now arrive at the volumetric density of states within the interval dE:

$$n(E) = \frac{N(E)}{V_{system}} = \frac{2}{(2\pi)^d}2^{d-1}\pi\vec{k}^{d-1}\frac{d\vec{k}}{dE} \tag{2.26}$$

This is the general expression for a d-dimensional density of states. Using an arbitrary dispersion relation yields the density of states of that system at the given energy [32].

In general, dispersion relations are complicated and computationally intensive to calculate. Additionally, in many use cases the regions of interest lie in the vicinity of band extrema, where the effective mass approximation holds. It is therefore often prudent to simplify the band structure prior to calculating the associated density of states. Using the parabolic approximation to the more complex shape of the band, we can use a simplified dispersion relation in the vicinity of the extremum, $E(\vec{k}) = \frac{\hbar^2}{2m^*}|\vec{k}^2|$, with the effective mass m^*. The derivative with respect to $|\vec{k}|$ then reads:

$$\frac{dE}{d|\vec{k}|} = \frac{\hbar^2}{m^*}|\vec{k}| \tag{2.27}$$

Combining with Eq. 2.26, and using $\left|\vec{k}\right| = \sqrt{\frac{2mE}{\hbar^2}}$, and setting the dimension to $d = 3$:

$$n_{3D}(E) = \frac{2}{(2\pi)^3} 4\pi \left|\vec{k}\right|^2 \frac{m^*}{\hbar^2 \left|\vec{k}\right|} = \frac{2}{(2\pi)^3} \frac{m^*}{\hbar^2} \sqrt{\frac{2m^*E}{\hbar^2}} \tag{2.28}$$

$$= \frac{\sqrt{2}}{\pi^2} \frac{(m^*)^{3/2}}{\hbar^3} \sqrt{E} \tag{2.29}$$

$$= \frac{\sqrt{2}(m^*)^{3/2}}{\pi^2 \hbar^3} \sqrt{E} \tag{2.30}$$

Here we used $\left|\vec{k}\right| = \sqrt{\frac{2m^*E}{\hbar^2}}$. This is the density of states near a band extremum for a three-dimensional crystal in the effective mass approximation and is plotted in Fig. 2.5a. The proportionality to $\sqrt{E}$ means that there are more states available far away from the band edge than close to it. Also shown are the densities for lower dimensional systems, Fig. 2.5b. through d. Note that the density of states of a system with multiple bands at a given energy is just the superposition of the density of states of each band individually. For one and zero dimensional systems, referred to as quantum wires/dashes (QDashes) and quantum dots (QDs), respectively, the DOS shows a singularity at the energy of the different subbands, and fewer states elsewhere. This concentration of states near the band edge is highly desirable in laser gain media, as we will learn later on. Lastly, it is worthwhile to consider the absolute magnitude of available states between the different dimensions: the three-dimensional DOS is several orders of magnitude higher than the two-dimensional DOS, which in turn far exceeds the one-dimensional DOS, with the zero-dimensional DOS being the lowest. Obviously one needs to take into account the fact that often there is an ensemble of dimensionally confined domains, such as QDs or QDashes, when considering volumetric densities of state, by which one needs to multiply $n(E)$ to get the absolute density of available states. Given a common QD density of $10^{10\text{-}12}$ cm^{-2}, there is still a difference of several orders of magnitude between the three- and lower-dimensional densities of states.

While considering a dimensionally reduced system, we only considered translationally invariant systems. Confining structures are abundant in semiconductor technology, so it is worthwhile to define a local density of states that takes spatially varying potentials into account. A general expression can be derived by merely scaling the density of states by the amplitude of the wavefunction $\psi_m(\vec{x})$ [32]. The expression for the local density of states then becomes:

$$n(E, \vec{x}) = \sum_m |\psi_m(\vec{x})|^2 \delta(E - \epsilon_n)$$

The local density of states is also used extensively in numerical drift-diffusion simulation, where parameters need to be spatially discretized. When modelling lower-dimensional systems and assigning carrier densities according to subband wavefunction extent, the use

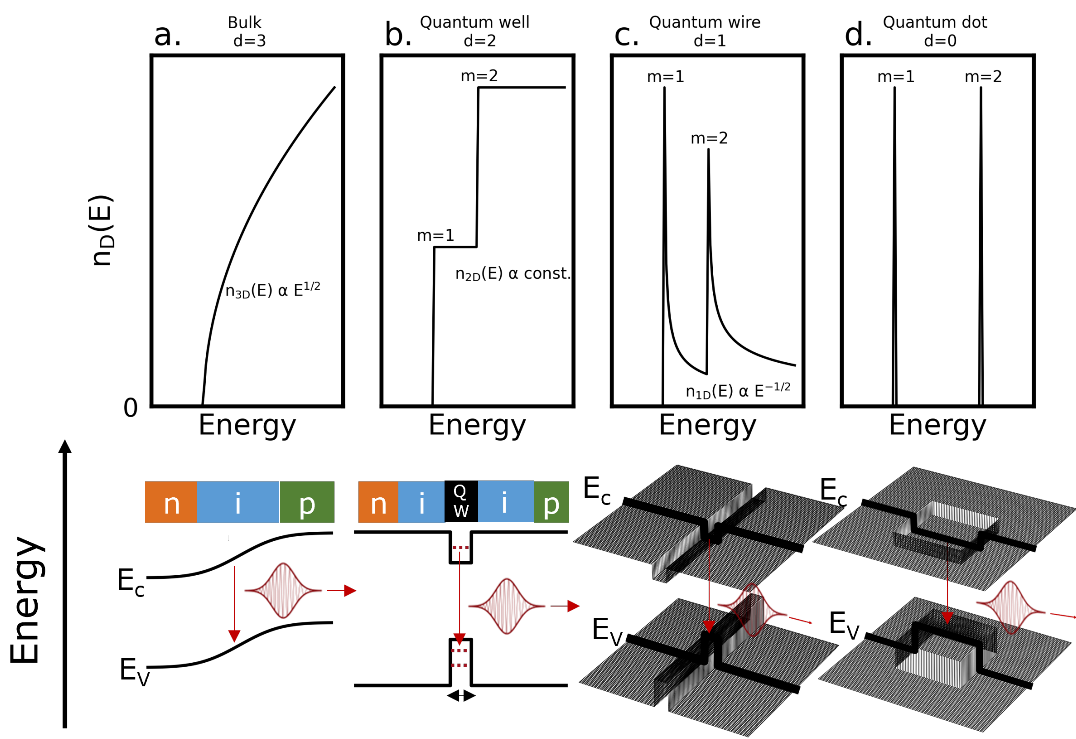

Figure 2.5: Density of states $n(E)$ as a function of dimension for a carrier moving freely in **a.** three, **b.** two, **c.** one, and **d.** zero dimensions. The lower dimensions $(d < 3)$ are plotted for multiple subbands, denoted by sub-band indices n. The lower row depicts the potential structure that will create the necessary confinement in each system.

of the local density of states allows treatment of potentials that vary over short distances compared to the extent of the wavefunction.

2.2.10 Occupation functions

The density of states provides information about the available states within a system, but no information about which of these states are occupied. In order to determine the total number of carriers and their distribution within a system, the DOS therefore needs to be multiplied by an occupation function that labels states as occupied or not. Since electrons are fermions, they follow the Pauli-exclusion principle and occupy states according to the Dirac-Fermi distribution:

$$f(E) = 1/\left(1 + \exp\frac{-(E-\epsilon_f)}{k_B T}\right) \tag{2.31}$$

where ϵ_f is the chemical potential of the fermion, k_B is the Boltzmann constant, and T is the temperature of the system under consideration. At $T = 0$ K, ϵ_f coincides with the Fermi-energy E_F. Colloquially, the chemical potential for $T > 0$ K is also often referred to as the Fermi level, which is technically incorrect, but nonetheless common practice in semiconductor physics. The eigenenergy of a state relative to the chemical potential ϵ_f defines its probability of occupation. At 0 K, this distribution is binary, with all states below ϵ_f occupied and all above unoccupied. As thermal energy increases, the $1/k_BT$ factor in the exponent smears out the carrier distribution and states on either side of the chemical potential start to flip from occupied to unoccupied and vice versa. States very close in energy to ϵ_f will flip sooner. It is important to note that T is not necessarily the temperature of the macroscopic system, but rather the temperature of the system under consideration, which is electrons. The temperature of their distribution can be different from the temperature of the lattice atoms in a semiconductor. The degree to which a semiconductor's carrier temperature can diverge from the lattice temperature depends on the efficiency of heat exchange between the lattice and the electronic ensemble, which is predominantly mediated by electron-phonon scattering. This mostly relevant when considering ultra-fast ($<10^{-14}$ s) processes or for systems with frustrated phonon relaxation pathways [29]. For our purposes, we assume thermal equilibrium between the carriers and lattice unless stated otherwise explicitly.
When modelling semiconductors, we generally operate within the two particle picture. In equilibrium, the electrons and hole populations balance each other, so that no net charge exists across the semiconductor, and ϵ_f is located exactly centred between the valence and conduction band edges. As a potential is applied, the balance of carriers shifts towards either population depending on the polarity of the local electric field. The distribution of carriers can then no longer represented by one chemical potential ϵ_f for both carrier types, but rather two potentials, $\epsilon_{f,n}$ and $\epsilon_{f,p}$, one for electrons and holes, respectively.
The carrier densities for electrons and holes, n and p, are then equal to the product of the occupation function and the density of states. We will explore the implementation used in this work explicitly in Ch. 4, which involves additional simplifications to ease numerical evaluation.

2.2.11 Effective mass

Given that we now have an idea of the distribution of carriers in a semiconductor, we can use it to gain an understanding of the carrier transport within it. This will be done in more detail in Ch. 4, where we talk about drift-diffusion modelling and the behaviour of carriers within a given material.
For a free electron, its group velocity is tied to its momentum $\vec{p}$ and wavenumber $\vec{k}$ via its

mass m_0:

$$v_{g,e}(\vec{k}) = \frac{|\vec{p}|}{m_0} = \frac{\hbar\left|\vec{k}\right|}{m_0} \tag{2.32}$$

As we will explore further in the next chapter, the group velocity is nothing but the derivative of the dispersion relation for a given material $\omega(\vec{k})$:

$$v_g(\vec{k}) = \frac{d\omega(\vec{k})}{d\vec{k}} = \frac{1}{\hbar}\frac{dE(\vec{k})}{d\vec{k}} \tag{2.33}$$

Most of this work exists within the framework of the effective mass approximation, where electrons move freely with an effective mass, which captures all the interactions between the electron and the lattice as well as other electrons. This is naturally a quite significant simplification of the complex interactions within a semiconductor, but it is surprisingly accurate and allows treatment of a wide variety of effects within semiconductors [29, 32]. We therefore replace the electron mass m_0 in Eq. 2.32 with the expression $m^*(\vec{k})$, where $m^*(\vec{k})$ is the effective mass. We can then take the derivative of Eq. 2.32, combine with 2.33 and re-arrange this expression to arrive at an expression for the mass:

$$\frac{dv_{g,e}(\vec{k})}{d\vec{k}} = \frac{\hbar}{m^*(\vec{k})} \tag{2.34}$$

$$\frac{dv_{g,e}(\vec{k})}{d\vec{k}} = \frac{1}{\hbar}\frac{d^2E(\vec{k})}{d\vec{k}^2} \tag{2.35}$$

$$m^*(\vec{k}) = \hbar\frac{1}{\frac{dv_{g,e}(\vec{k})}{d\vec{k}}} \tag{2.36}$$

$$= \hbar^2\left(\frac{d^2E(\vec{k})}{d\vec{k}^2}\right)^{-1} \tag{2.37}$$

The proportionality of the effective mass to the inverse band curvature results in lower effective masses for electrons compared to holes, whose bands generally vary more slowly with $\vec{k}$. Additionally, for low carrier densities, carriers will mostly occupy states near the Γ-valleys in zincblende semiconductors, which have approximately parabolic dispersion for small $\vec{k}$ [32]. Since $m^* \propto 1/\frac{d^2E(\vec{k})}{d\vec{k}^2}$, this means the effective mass can be approximated as constant under these conditions.

Treating the carriers in a semiconductor as freely moving with an effective mass leads us into the very simple Drude model. A carrier near the band edge will experience an acceleration due to an applied electric field $\vec{E}$:

$$\frac{d\vec{v}}{dt} = \frac{q\vec{E}}{m^*} - \frac{\vec{v}}{\tau} \tag{2.38}$$

Here q is the charge of the carrier, $\vec{v}$ is the velocity of the carrier, and τ is a phenomenological scattering time that represents the momentum relaxation time of the particle. The scattering partners, be they phonons, crystal defects, or other electrons, change as a function of temperature, doping density, and applied field. Averaged over long times, so multiple scattering events, the average velocity of carriers then becomes:

$$\bar{v} = \frac{q\left|\vec{E}\right|}{m^*} = \mu\left|\vec{E}\right| \tag{2.39}$$

$$\mu = \frac{q\tau}{m^* m_0} \tag{2.40}$$

Where μ is the mobility of a given carrier. Given the definition of current as the movement of charge over time, $\frac{dC}{dt}$, and the carrier density n, $n \cdot V$ are the carriers in a volume V moving at $\bar{v}$. Combining this with Ohm's law, we arrive at an expression for the conductivity σ of a material:

$$\sigma = \frac{nq^2\tau}{m^*} = qn\mu \tag{2.41}$$

A smaller effective mass will result in a higher mobility, and therefore a higher conductivity. In most cases, a given density of electrons will conduct more current than an equal density of holes. In areas where both carrier types are represented equally and mobilities are somewhat similar, the electrical conductivity should include both carrier types:

$$\sigma = q(n\mu_n + p\mu_h) \tag{2.42}$$

where μ_n and μ_h are the mobilities for electrons and holes, respectively. Of course, this treatment of conductivity is rather superficial, but sufficient for the purposes of this work. We recommend Yu and Cardona's discussion of electrical transport in semiconductors for a more in-depth treatment of the subject, summarized quite well by Fig. 5.11 in [29].

2.2.12 Doping

As mentioned previously, the electron and hole carrier densities in an ideal semiconductor are perfectly balanced under equilibrium conditions. However, all semiconductors divert from this idealistic picture to some degree. One important factor is chemical purity, with most semiconductors containing at least 10^{12} cm^{-3} contaminating atoms. These atoms will often have valences higher or lower than the species they replace, or be located at interstitial lattice sites, altering the surrounding bonding structure. Whatever the nature of the imperfection, the result is the same: a defect with a valence different from a regular lattice site. While these occur naturally in any semiconductor due to the nature of the smelting process, they can also be introduced deliberately, either via species introduction

during growth or post-growth using ion implantation. Irrespective of the method, they create a defect that carries a net charge. At equilibrium, this net charge will be balanced by an additional charge carrier of the opposite polarity to retain overall charge neutrality. This can be used to create regions of the device that have an excess of one type of charge carrier, if the defect densities are of a similar order of magnitude as the intrinsic carrier densities, upwards of 10^{17} cm^{-3}. The fact that there is more of one type of charge carrier at equilibrium shifts the chemical potential towards the band edge of that charge carrier. For example, adding positively charged defects would require additional negatively charged electrons, resulting on a shift of the chemical potential μ towards the conduction band edge. Negatively charged defects would similarly encourage the presence of additional holes, shifting μ towards the valence band edge. It is conventional to refer to electron- and hole-inducing defects as donors and acceptors. A semiconductor region that is engineered to predominantly have one type of defect is referred to be of n- or p-type, depending on whether or not it overwhelmingly contains donors or acceptors, and the act of altering the carrier balance in this manner is referred to as doping.

Burstein-Moss effect

One outcome of doping a semiconductor is a widening of its optical band gap, referred to as the Burstein-Moss effect. The optical band gap is the lowest energy at which significant absorption from interband optical transitions can be observed, which will be discussed in the next section. The increase in this energy is due to the filling of conduction and valence band states near the band edge at finite temperatures by dopant-induced carriers [37, 38]. An interband absorption process involves the promotion of an electron occupying a valence band state into an unoccupied conduction band state. If the valence band state is already empty, i.e. occupied by a hole, or, equivalently, the conduction band state is already filled, the transition can not occur between either of these states. Only once the energy of the photon is large enough to bridge the energetic gap between further separated states will absorption occur. This shift of the absorption is more pronounced for the conduction band, as the electronic density of states is generally lower compared to its hole counterpart due its reciprocal dependence on the effective mass, as seen in Eq. 2.30 [39].

2.2.13 Defect states

It is important to note that defects, be they added intentionally as dopants, or intrinsic to the material due to contamination with a foreign atomic species or crystallographic disordering, all break the translational symmetry of the crystal. The otherwise periodic potential of the crystal is interrupted, perturbing the Bloch wavefunctions derived for the

perfect crystal [29]. The result is a state with an energy below or above the energy of the periodic band state. Since defects generally extend the distance between neighbouring atoms, the effective ionic lattice potential in the vicinity of the defect is decreased. A lower potential results in lower eigenenergies of the local electronic wavefunctions associated with the defect; this places the energy levels of the defect states below the energy of the band edge. For holes, whose energy increases as we move below the valence band edge, this is inverted. Two defect energy levels, one for donor-like and one for acceptor-like defects, are shown in Fig. 2.6

Due to their relatively close position below the band edge, carriers in band edge states can scatter into defect states, and vice versa [40]. This trapping process has detrimental impacts on technologically relevant material parameters, such as conductivity: as carriers residing in defect states are strongly localized and therefore do not contribute to charge transport across the device. The coupling strength is proportional to the relative position of the defect state eigenenergies, which is defined by the nature of the defect [29]. Carrier-phonon scattering can provide the energy to promote carriers back into band edge states, which is why defect states, or trap states, are generally divided into two categories: deep and shallow traps. Deep traps strongly perturb the periodic potential and therefore have relative eigenenergies E_{trap} that are much larger than the average energy available through carrier-phonon scattering events. This thermal energy is approximately k_BT for complete phonon annihilation, and therefore deep traps meet the condition $E_{trap} >> k_BT$. Once a carrier is scattered into a deep trap state, a process referred to as carrier capture, its probability of being scattered into a band edge state is low. Defects that leave dangling bonds often create deep trap states, as the state associated with the dangling bond lies between both band edges. This is especially relevant at interfaces between crystals with different coordination. Since a return to the band edge is unlikely for a carrier in a deep trap, they will generally recombine with carriers of the opposite polarity and release their energy in the form of phonons. This defect mediated non-radiative recombination is named after Shockley, Read, and Hall, often abbreviated as SRH, who were the first to describe the process [40, 41]. This loss mechanism is highly undesirable, as it presents a pathway for carriers to recombine that turns their potential chemical energy into heat without doing useful work. Additionally, the heat released increases the lattice temperature which degrades other material properties, such as conductivity via higher rates of carrier-phonon scattering between band states.

If the trap energy approaches the available thermal energy, $E_{trap} \approx k_BT$, carriers are captured into and released from the trap state at a much higher rate. These traps are therefore considered shallow, and mostly act by reducing the conductivity of a given material. Their energetic proximity means they are very strongly coupled to the band states, so have rather large scattering cross-sections [29]. Most commonly used dopant

species will form shallow traps, so a common technique to avoid undue scattering between carriers and ionized traps is called modulation doping. Here the potential via alloying is graded to direct the carriers induced by the dopant to be localized sufficiently far away to avoid overlap between carrier wavefunctions and trap states [32].
Apart from affecting transport and acting as non-radiative recombination sites, carriers trapped in defect states can also undergo radiative recombination, as we will discuss in the next section. Due to the energy offset between the band edge and the defect states, the resulting transitions will occur at wavelengths greater than those of the band edge transition. Depending on the nature of the defect, they can contribute a spectrum of transitions that can be useful or detrimental. In wide-band semiconductors, such as nitrides, or diamond, defect states can allow transitions at technologically more relevant wavelengths. When building a laser however, these transitions will cannibalize carriers that can not contribute to the stimulated emission process, and are therefore another loss process that needs to be mitigated.

2.2.14 Strain

There are many mechanisms that can induce mechanical stress within a crystalline material. Defects create local stress fields which can be extensive for non-zero-dimensional imperfections such as step faults or stacking errors. Macroscopic external forces acting on the crystal translate into microscopic stress fields. The different expansion at an interface between two materials with different thermal expansion coefficients can similarly cause mechanical stress when the assembly undergoes a temperature change. Most relevant to this work, however, is mechanical stress induced during semiconductor heterostructure growth. Heterostructures are structures created by abruptly varying the composition of a semiconductor over microscopic distances. They are an important element of semiconductor technology and will be discussed in more detail in the context of optoelectronically relevant heterostructures in the upcoming section, as well as in 2.5. For now it suffices to say that during their growth process, a semiconducting material is often forced to replicate the crystal structure of a substrate. This process is referred to as epitaxy, and depending on the crystal structures of the materials involved and the growth conditions can cause mechanical stress in the deposited material. The atoms of the replicating semiconductor will attempt to match the crystal structure of the substrate. For two materials with identical crystal structures and lattice constants, this would result in a perfectly matched material without stress. If the lattice constants between the two materials differ or they preferentially grow in different crystal structures, the atoms of the deposited material will occupy positions offset from the equilibrium lattice sites at the growth interface. This is identical to the offset observed for a lattice that is subjected to external pressure. The

mismatch between the stressed and unstressed lattice is defined as strain Δa:

$$\Delta a = \frac{a_0 - a'}{a_0} \tag{2.43}$$

where a' and a_0 are the lattice constants of the stressed and unstressed material, respectively. Strain is referred to as compressive for $\Delta a < 0$ and tensile strain $\Delta a > 0$. The relevant lattice constant depends on the dimensions along which the material is strained. Since semiconductor heterostructures are commonly grown layer by layer, the relevant lattice constants lie along the growth plane. As a sidenote, depending on their crystallographic phases as well as growth conditions, there will be a maximum strain Δa that can be accommodated between two semiconductors before the strain is released in the form of a defect, such as a stacking fault, or by a growth mode change [29, 32].
Independent of the source of stress in a semiconductor, its effect will be the same: interatomic distances change. As atoms change their relative positions and the unstrained unit cell deforms, the overlap between wavefunctions changes, affecting nearly every material property. The change in wavefunction overlap alters the band structure, changing band gaps and effective masses. This has been used to increase the mobility of carriers in Si field-effect transistors and for precise tuning of the band gap to achieve optical transitions at desirable energies [42, 43]. Compressive stress will generally cause interatomic distances to shorten, which causes additional orbital overlap between neighbouring atoms, leading to an increase in energy for anti-bonding orbitals and a lowering for bonding ones. In the case of zincblende semiconductors such as InAs or GaAs, this results in a widening of the band gap under compressive strain and a narrowing for tensile strain due to bonding and anti-bonding orbitals forming the band gap near Γ shifting in opposite directions. For sufficiently high stress, this can lead to a change in the location of the band gap within the BZ, and lead to band gaps changing from direct to indirect or vice versa [29]. The strain that is commensurate with epitaxial growth is usually small enough that band energies are affected, while not fundamentally altering the location of the lowest transition within the BZ.
During epitaxial layer growth, strain predominantly occurs in the growth plane rather than perpendicular to it, leading to anisotropic stress profiles. This can reduce symmetries within crystal structures, leading to degeneracy lifting. One example is the lifting of the six-fold valley degeneracy in Si due to in-plane stress [32]. The lifting of degeneracies is also relevant at the top of the valence band for diamond and zincblende semiconductors: since light and heavy hole bands can be treated as resulting from p-orbital-like wavefunctions orientated parallel and perpendicular to $\vec{k}$, anisotropic stress will affect the light and heavy hole bands differently. Let us assume we have a semiconductor compressively stressed in the growth plane, which we will set normal to $\vec{e}_z$, with the other orientations unaffected. The p_x- and p_y-orbitals will then be compressed, leading to greater overlap

along these dimensions, decreasing their energy since p-orbitals are bonding. If they were anti-bonding, a rise of the bands would be observed instead. For electronic wavefunctions with $\vec{k}$ components parallel to $\vec{e}_z$ the result is a upwards shift of the energy of the heavy hole band and a downward shift of the light hole band. For electrons moving in the growth plane, with $\vec{k}$ components along $\vec{e}_x$ and $\vec{e}_y$, the opposite effect occurs: the light hole band rises as a result of greater wavefunction overlap of orbitals lying in the growth plane, and the heavy hole band shifts downwards. The result is broken inversion symmetry for the valence band around Γ, leading to separate light and heavy hole bands for $\vec{k} \cong 0$. The valence band ordering in the growth plane is light-heavy (top to bottom), while it is heavy-light for electrons moving normal to it. Tensile stress has the opposite effect, as it stretches the in-plane orbitals, and the order of the bands is inverted from the compressed case [32]. One of the main impacts of strain on this work is the splitting of transitions between Γ conduction band and light and heavy hole bands into two degenerate sets, with slightly different confinement for holes belonging to either band.

2.3 Semiconductor optoelectronics

Since this work is concerned with lasing devices, the attention will now shift towards the optoelectronic properties of semiconducting materials. The electronic states with the highest relevance for technological applications are the ones lying near the band edges, in the conduction and valence band. The band gap ensures that non-radiative transitions between these states are inefficient, preventing an excess of energy injected into the system to be converted into heat and lost for light generation. At the same time, the band gap also offers a strong tool for material engineering of the exact wavelength of light that the semiconductor interacts with strongly, be it emitted in the case of a laser or absorbed when creating a detector. The electronic bulk states can also be further controlled via nano-structuring, dimensionally confining carriers to achieve further control of their energetic position, absolute and relative to the rest of the device.

2.3.1 Fermi's golden rule

To consider the nature of optical transitions in semiconductors, we will first consider a simplified two-level system: a ground state ϕ_i, occupied under equilibrium conditions, coupled to an excited state, ϕ_f, via an optical transition. We are using a semi-classical approach, where the quantization of the two level system is treated while the quantization of the electric field is not. Additionally, we use the rotating wave approximation, which treats the perturbation due to the electric field as constant relative to the response of

the system. The large extent of the photon compared to the small size of the interacting medium in the semiconductor justifies these approximations. The probability of each state being occupied are f_i and f_f for the initial (ground) and final (excited) state. The coupling between the two levels depends on the nature of ϕ and ϕ_f, and is captured in the transition moment, $\langle\phi_f|\, V\, |\phi_i\rangle$. For an electronic system, the transition is pre-dominantly mediated by the linear interaction between the electronic charge and the perturbing electric field; higher order terms have negligible contributions. In this electric dipole approximation, V takes the form $\hat{e}\hat{p}$, where $\hat{e}$ and $\hat{p}$ are the polarization and momentum operator, respectively. Note that due to the symmetry of these two operators, $\langle\phi_f|\, V\, |\phi_i\rangle = \langle\phi_i|\, V\, |\phi_f\rangle$, therefore exciting and decaying transitions are equally likely. In Cartesian coordinates, the coupling operator takes the form:

$$\hat{e}\hat{p} = -i\hbar\left(e_x\frac{\partial}{\partial x} + e_y\frac{\partial}{\partial y} + e_z\frac{\partial}{\partial z}\right) \tag{2.44}$$

The symmetry of this operator also determines the strength of transitions based on the symmetry of the wavefunction and the polarization of the incoming light. The momentum operator $\hat{p}$ acts on the wavefunction by taking the gradient in all directions, flipping the parity of the wavefunction it acts upon. If we remind ourselves of the full form of $\langle\phi_f|\, V\, |\phi_i\rangle$:

$$\langle\phi_f|\, \hat{e}\hat{p}\, |\phi_i\rangle = \int \phi_f^* \hat{e}\hat{p}\phi_i d\vec{x} \tag{2.45}$$

where $\int d\vec{x}$ is an abuse of notation for the triple integral over dx, dy, and dz. The integral $\int \phi_f^*\phi_i d\vec{x}$ vanishes if ϕ_i and ϕ_f have odd parities, so one having odd parity while the other exhibits even parity. With $\hat{p}$ flipping the parity of the second wavefunction, one can therefore derive a selection rule for transitions involving the dipole operator: if the wavefunctions for the final and initial states have odd parity, Eq. 2.45 flips the parity of the initial state, resulting in even parity between both states and the integral $\langle\phi_f|\, \hat{p}\, |\phi_i\rangle$ does not vanish. This transition is therefore an allowed transition. If the initial and final state have even parity, so both odd or both even, $\langle\phi_f|\, \hat{p}\, |\phi_i\rangle$ does vanish and the transition is considered forbidden [32]. While the use of the word forbidden implies that certain transitions are impossible, the perturbed nature of most wavefunctions present in real semiconductors softens this exclusion criteria. Wavefunction symmetries are generally weakened under perturbation, and even forbidden transitions occur, however they are generally significantly weaker than their allowed counterparts due to lower magnitudes of $\langle\phi_f|\, \hat{p}\, |\phi_i\rangle$ for forbidden transitions [29]. The polarization operator modifies this condition by selecting along which orientations the symmetry relationship between the wavefunctions is probed. These symmetry considerations are important for both the Bloch wavefunctions of a bulk semiconductor and the envelope wavefunctions in dimensionally confined systems, and both need to be considered when evaluating the strength of a transition.

The s- and p-like nature of the conduction and valence band near the Γ point in the III-V compound semiconductors considered in this work mean that it is mostly the envelope wavefunction symmetries that define the selection rules for optical transitions [32].
In order to obtain light amplification in a two level system, the excited state needs to be populated from the ground state via optical or electrical excitation in a process referred to as "pumping". Carriers in the excited state will *spontaneously* return to the ground state via the aforementioned optical transition, emitting a photon with a frequency corresponding to the energy of the transition. Alternatively, a photon propagating through the semiconductor with a wavelength corresponding to the optical transition energy can stimulate the decay of the excited state to the ground state in a process referred to as *stimulated* radiative recombination. While the propagation orientation of the photon in space associated with spontaneous recombination is random assuming a spatially isotropic photon density of states in the surrounding medium, a stimulated transition will result in a photon propagating collinear with the stimulating photon. The optical transition probability between states ϕ_i and ϕ_f for a photon of energy $\hbar\omega$ using the semi-classical (quantized electron states, classical electric field) rotating wave approximation can be expressed as follows:

$$P_{if}(\hbar\omega) = \frac{2\pi}{\hbar}(\frac{qE_0}{m_0\omega})^2 |\langle\phi_f| V |\phi_i\rangle|^2 \delta(E_f - E_i - \hbar\omega) \tag{2.46}$$

where ω is the angular frequency of the photon, q is the electron charge, E_0 is the magnitude of the electric field due to the photon, m_0 is the mass of an electron, and E_f and E_i are the energies of the excited and ground state, respectively. $\delta(E_f - E_i - \hbar\omega)$ represents the Dirac delta function, indicating the resonant condition necessary for a transition to occur.
If the rate at which the excited state is pumped exceeds the combined spontaneous and stimulated recombination rate, the population of the overall system will shift towards the excited state. When the excited state population exceeds the ground state occupation ($f_f > f_i$), the system is referred to as inverted. This marks the onset of lasing in a perfectly lossless medium, as the inverted occupation results in the probability, and thereby rate, of stimulated radiative recombination exceeding the absorption rate for photon. We will illustrate this concept by returning to Eq. 2.46. We can derive a rate of the energy absorption in the system by factoring in the occupation of ground and excited state, f_i and f_f:

$$R_{if}(\hbar\omega) = \frac{2\pi}{\hbar}\left(\frac{qE_0}{m_0\omega}\right)^2 |\langle\phi_f| V |\phi_i\rangle|^2 2[f_i - f_f]\delta(E_f - E_i - \hbar\omega) \tag{2.47}$$

The factor 2 arises from the fermionic nature of electrons, resulting in two electrons of opposing spin occupying each state. Upon closer inspection of Eq. 2.47, we see that for $f_f < f_i$ there is a net loss of photons, while for $f_f > f_i$ there is a net gain. The creation

and maintenance of an inverted state population is the basis for any light-emitting device operating as a laser.

2.3.2 Optical transitions

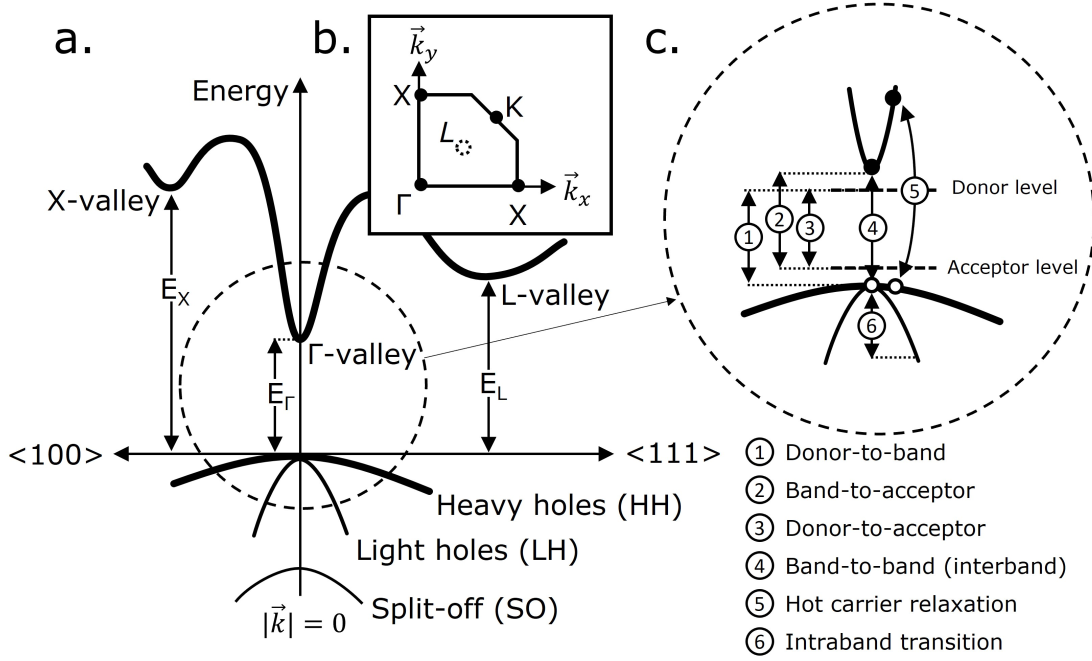

Figure 2.6: **a.** Schematic InAs conduction and valence band edge at room temperature along highly symmetrical directions. Adapted from [35]. **b.** Cut-out of first Brillouin zone, indicating points of high symmetry. Note that the L-point is located above the $\vec{k}_x$-$\vec{k}_y$ plane. Adapted from [32]. **c.** Available optical transitions for carriers near a direct band gap, excluding excitonic effects [34].

As we saw in the previous section, every optical transition occurs between an initial state ϕ_i and a final state ϕ_f. In a semiconductor, there is an abundance of states that can function as the start and end point of a radiative recombination process. Fig. 2.6 shows the schematic band structure for InAs. Ignoring defect states for now, there are three possible band-to-band, or interband, transitions due to band minima: a direct transition around Γ and two indirect transitions at the X- and L-valleys. While each of the three transitions denoted by E_Γ, E_L, and E_X are possible, the likelihood of a recombination event occurring at each band position differs greatly. The first thing to consider is the overall availability of carriers. Since it represents the lowest energetic position, carriers will generally reside near the Γ point as it is the lowest of the three valleys. The valleys are connected via scattering processes, so even carriers that end up in higher lying valleys will eventually scatter into the energetically lower lying states near Γ. With a significantly lower number of occupied initial states, transitions originating from L and X are already

strongly suppressed. Additionally, the transitions from X and L are indirect: carriers located here can only recombine while altering their momentum. Photons carry negligible linear momentum, so the transition process needs to involve the emission or absorption of phonons to conserve the overall momentum. Adding an additional particle into the process reduces its efficiency, resulting in a much weakened interaction. This is easy to see when comparing the optical absorption coefficient for the direct transition in InAs and the indirect transition in Si: while InAs has a coefficient of 910 cm^{-1} near its room temperature band gap of 0.35 eV (3540 nm), the value for room temperature Si near 1.12 eV (1108 nm) is almost two orders of magnitude smaller, at only 3 cm^{-1} [44, 45].
For any given band valley, transitions between band states are just one possible radiative recombination path of many. To illustrate this, Fig. 2.6c. shows a non-exhaustive list of optical recombination processes near a band extremum, in this case E_{Γ}. The direct transition between conduction band and valence band states, the interband transition, is denoted by 4. However, there are a variety of other possible transitions that can occur. If there are defects present, they introduce states with eigenenergies within the band gap. As discussed previously, these can capture carriers and then acts as the origin or destination of optical transitions. These are the transitions numbered 1 through 3. A special case is the donor-to-acceptor transition, which is generally less likely due to the proportionality of the dipole matrix element to the overlap of the wavefunctions. Outside of more exotic applications, such as hyperdoped semiconductors or defect complexes that exhibit both donor- and acceptor-like levels, the distances between neighbouring defects are generally much larger than the extent of the defect-bound wavefunction, reducing the likelihood of transitions between defect states significantly [29].
In case intraband carrier relaxation processes are slow and there is a significant population of carriers existing at energies above the band edge, hot carrier relaxation processes can occur (5 in Fig. 2.6c.). These are recombination processes in which an electron with an energy significantly higher than the conduction band edge recombines without first decaying to the band edge. A similar process can occur for holes with energies significantly below the valence band edge. For the devices considered in this work, we assume fast relaxation of the carriers to the band edge, resulting in carrier populations in thermal equilibrium with the lattice. There are therefore very few carriers available at any noticeable distance from the band edges.
The last group of transitions to consider are intraband transitions (6 in Fig. 2.6c). As their name suggests, they occur between initial and final states that both belong to the same band. Selection roles imposed by the dipole matrix element lower the transition likelihood for two wavefunctions with similar parities, which generally occurs near band edges. If a band is formed by states from multiple different orbital wavefunctions, so for example contains both s- and p-like orbital wavefunction contributions, the dipole moment becomes

non-vanishing. This is the case in most zincblende semiconductors, for which intraband transitions between light and heavy hole states contribute to non-negligible sub-band gap absorption [32].
Fig. 2.6c. does not contain all possible transitions for a given semiconductor, only the ones most technically relevant to the work at hand. For example, excitonic effects provide another series of transitions. Excitons are a hole-electron pair, which, due to their respective charge polarities, form a quasi-particle held together by the Coulomb force. The eigenenergy of the exciton is the sum of the eigenenergies of the electron and hole wavefunctions that form the exciton minus their binding energy, which is on the order of a few meVs for common bulk semiconductors, but can reach several 10s to 100s of meV in lower-dimensional systems. Transitions stemming from exciton decay are therefore slightly red-shifted compared to transitions of its constituting particles. The negative electron orbiting a positive hole in an exciton bears similarity to the relationship between electrons orbiting the positive nucleus of an atom, which leads to very similar wavefunctions describing both systems, with an attenuation for the exciton complex to describe the effect of the polarizable semiconductor background. This results in an excitonic fine structure, as the electron can occupy states with higher orbital angular momentum and therefore higher eigenenergies. However, due to the large amount of thermal energy available in a semiconductor via phonon interaction at finite temperatures, excitons generally decay rapidly into electrons and holes [29]. The resulting "zoo" of available optical transitions can be found via spectroscopy, e.g. [47] and [48]. The photoluminescence spectra for n- and p-doped InAs and GaAs at low temperatures, feature a multitude of features, including several defect-exciton complexes, such as D^0, X. However, as indicated by the fact that the spectra are captured at cryogenic temperatures rather than room temperature, as most of these transitions are suppressed as soon as there is sufficient thermal energy available for carriers to occupy bulk band states. We therefore generally only have to explicitly consider direct band-to-band transitions when modelling a bulk semiconductor diode laser, while the rest can generally be treated using optical scattering constants [46].

2.3.3 Refractive index

The refractive index is a material property, and is a function of many parameters that vary as a function of the current device state, such as temperature and carrier concentration. As a coarse approximation, the refractive index is a measure for the degree of polarizability of a material. The refractive index is related to dielectric function $\epsilon(\omega)$ and magnetic permeability of a material $\mu(\omega)$ [29]:

$$\bar{n}(\omega) = \sqrt{\epsilon(\omega)\mu(\omega)} \tag{2.48}$$

The magnetic permeability simplifies to the vacuum permeability $\approxeq \mu_0$ for the semiconducting materials considered in this work [32]. We therefore need to mostly concern ourselves with the dielectric function $\epsilon(\omega)$. The dielectric function connects the polarization response $\vec{P}$ of a material to the perturbing electric field $\vec{E}$, here shown for the linear response regime of the polarization:

$$\vec{P} = \epsilon_0 \chi(\omega) \vec{E} = \epsilon_0 (\epsilon(\omega) - 1) \vec{E} \tag{2.49}$$

where $\chi(\omega)$ is the electric susceptibility, and ϵ_0 is the vacuum permeability. $\epsilon(\omega)$ is a complex quantity, so we can separate it into a real and imaginary part, $\epsilon_r(\omega)$ and $\epsilon_{imag}(\omega)$:

$$\epsilon(\omega) = \epsilon_r(\omega) + i\epsilon_{imag}(\omega) \tag{2.50}$$

The imaginary part includes the generation and dissipation of energy stored in the electrical field, while the real part quantifies the modification of the propagation of the electric field in a material. The two parts are related by Kramers-Kronig relations, as the dielectric function is generally analytical. This allows determining one component if the shape of the other component is known. This relationship only holds while the material response is linear with electric field strength, a condition that is often not met within gain media [29]. Furthermore, the dielectric function is a second rank tensor in the linear regime as the polarizability is dependent on the orientation of the electric field relative to the crystal structure. However, unless we are explicitly attempting to extract material qualities related to the anisotropy of the polarizability, a medium can be treated as isotropic. This reduces the nine components of the tensor into a single function, which makes it significantly easier to handle. This simplification is relevant to keep in mind though when treating properties such as birefringence and other polarization-dependent properties in a monocrystalline material, in which the orientation of the electric field relative to the crystal structure is very much relevant [49].
As the dielectric function and refractive index are related quantities describing the same phenomena (see Eq. 2.48), the refractive index can also be broken down into real and imaginary components n_r and κ [29]:

$$\bar{n}(\omega) = n_r(\omega) + i\kappa(\omega) = \mu_0 \sqrt{\epsilon_r + i\epsilon_{imag}} \tag{2.51}$$

The term refractive index is often used ambiguously to describe the real part of the refractive index n_r, while $\kappa(\omega)$ is referred to as the extinction coefficient. $\kappa(\omega)$ is large for frequencies near oscillations of the dipoles within the material, as we discussed above, and small elsewhere. We therefore need to be mindful of $\kappa(\omega)$ inside gain media: here the frequency of the light travelling in the resonator is by design matched to the available oscillations in the medium. In other parts, such as the passive waveguiding structures

with optical band gaps far away from the lasing transitions, these losses are less relevant. For semiconductor lasers with low-dimensional gain regions, such as QW, QD, and QDash lasers, the fraction of the optical mode overlapping with regions featuring lasing transitions is often small, while the overlap with waveguiding structures, such as cladding and separate confinement heterostructures, accounts for most of the mode volume. In these cases, the effective refractive index as experienced by the optical modes is largely real [50]. The sign of the change in refractive index with wavelength is commonly used to differentiate between normal dispersion, where the index decreases with wavelength, and anomalous dispersion, where the index increases as wavelength increases [29]. Most materials will show normal dispersion in the UV to IR wavelength range, hence the name. However, laser gain media will generally exhibit anomalous dispersion in the vicinity of transitions [29]. Non-zero dispersion is detrimental to the linewidth in continuous wave lasers and broadens the pulse width in pulsed devices. Sufficient dispersion can also degrade the phase-locking mechanism underlying single section semiconductor mode-locked lasers to the point of non-pulsation. It is therefore often prudent to compensate the dispersion by adding a compensating element to the optical path [51]. The compensation can either occur internally within the cavity, or externally in the light path through components with dispersion relations of opposite sign, such as optical fibers [52].

Non-linear dispersion

As alluded to earlier, some materials, including most gain media, have a non-linear response to incident electric fields. This is requires higher order terms to be included when considering the overall polarization response of a material [49]:

$$\vec{P} = \epsilon_0(\bar{\chi}^{(1)}\vec{E} + \bar{\chi}^{(2)}\vec{E}^2 + \bar{\chi}^{(3)}\vec{E}^3 + ...) \tag{2.52}$$

Eq. 2.49 is the truncation of this power series after the classical, linear term, and applicable for low field strengths or materials with vanishing higher order susceptibilities [53]. The study and technological usage of non-linear optical effects is closely linked to the advent of the laser. The concentration of the energy into a narrow set of frequencies in a laser leads to high field strengths, leading to large higher order field terms, resulting in strong non-linear effects, since the magnitude of the higher order susceptibilities is generally much smaller than the linear response [54]. We dropped the ω dependence notation for convenience, even though each susceptibility is still very much dependent on the frequency of the perturbing electric field. The susceptibility $\bar{\chi}^{(k)}$ is a tensor of rank $k + 1$ [49]. As stated before, the classical linear regime is only concerned with the linear susceptibility $\bar{\chi}^{(1)}$, which deals with small perturbations of the equilibrium arrangement within a material. The

second order susceptibility $\bar{\chi}^{(2)}$ is zero for centrosymmetric materials, such as gasses due to their isotropy or crystals with inversion symmetry [49, 53]. Zincblende crystals are not centrosymmetric, as they lack an inversion centre [29]. However, $\bar{\chi}^{(2)}$ is generally much smaller than the third order susceptibility $\bar{\chi}^{(3)}$ in the QD and QDash gain media we discuss in this work [55]. As a side note, we could have equivalently used the dielectric function $\epsilon(\omega)$ instead of the susceptibility.

Non-linear optical materials have a profound effect on the behaviour of photons: photons as bosons are quite inefficient at interacting with one another, unless at extreme electric field strengths above the Schwinger limit or inside a non-linear medium [56]. The non-linear scaling of the polarization response can be interpreted as the interaction of multiple photons, where one photon alters the polarizability of the medium and thereby affects the interaction of the medium with a subsequent photon. This enables a wide array of non-linear processes. $\bar{\chi}^{(2)}$ is the foundation of processes such as harmonic generation and frequency mixing, the latter enabling optical parametric oscillators. $\bar{\chi}^{(3)}$ can be the source of other effects: wave-mixing, photorefractivity, self-phase modulation, phase conjugation, spatial soliton formation, and optical bistability. The third order susceptibility can also lead to self-phase modulation which in turn is results in passive mode-locking of QD and QDash lasers [57].

The non-linearity of a material can also extend to its absorption and scattering behaviour. For materials with higher order contributions to their absorption and scattering spectra, processes such as two-photon absorption and saturable absorption appear. The latter is relevant for multi-section lasers and Q-switching, where a cavity is actively driven into pulsed operation. This is highly relevant for semiconductor lasers, where the refractive index is closely tied to the carrier density.

Dielectric function and refractive index

The electric polarizability in semiconductors is a function of both the response of the ionic cores and strongly bound core electrons, and the more mobile valence electrons. While the contribution from the former is mostly unaffected by the current device state apart from thermal expansion, the carrier density can vary over several orders of magnitude depending on the bias conditions, affecting the refractive index. Amongst other effects, this interaction leads to an optical non-linearity as a result of spatial hole burning, a phenomenon we will discuss in more detail in the context of mode-locking in quantum dash lasers in 3.4.4. For now we will examine contributions to the refractive index in semiconductors and qualitatively assess the relationship between carrier densities and the refractive index of a semiconductor.

As discussed earlier, the refractive index of a material is another measure for its dielectric

function and magnetic permeability, see Eq. 2.48. Neglecting the permeability for a semiconducting material interacting with light in the UV to IR range, we can examine the different contributions to the dielectric function in a bulk semiconductor [32]. The components of the dielectric function under the assumption of a single conduction and valence band and a weak dependence of the transition dipole moment $|\langle c| V |v\rangle|^2$ on the electronic wavevector $\vec{k}$ have been derived by Yu and Cardona [29]:

$$\epsilon_r(\omega) = 1 + \frac{q^2}{\epsilon_0 m^*_{red}} \sum_{\vec{k}} \left(\frac{2}{m^*_{red} \hbar\omega_{cv}} \right) \frac{|\langle c| V |v\rangle|^2}{\omega_{cv}^2 - \omega^2} \tag{2.53}$$

$$\epsilon_{imag}(\omega) = \frac{\pi q^2}{\epsilon_0 (m^*_{red}\omega)^2} \sum_{\vec{k}} |\langle c| V |v\rangle|^2 \delta(E_c(\vec{k}) - E_v(\vec{k}) - \hbar\omega) \tag{2.54}$$

$\sum_{\vec{k}}$ is a summation over all electronic $\vec{k}$ allowed per unit volume. q is the elementary charge, $E_c(\vec{k})$ and $E_v(\vec{k})$ are the band structure for the conduction and valence band we encountered in Ch. 2, and m^*_{red} is the reduced effective mass of the conduction and valence band, as defined in Ch. 4. ω_{cv} is the angular frequency of the interband transition, $\hbar\omega_{cv} = E_c(\vec{k}) - E_v(\vec{k})$. $\delta(x)$ represents the Dirac delta function. It spikes in the vicinity of transitions, but is zero elsewhere. In a real material, this will be broadened by the dampening of the dipole oscillations and other broadening effects, as discussed in 3.3.5 [49]. Irrespective of the broadening, the imaginary part is going to be negligibly small outside of the vicinity of the transition. The propagation of an optical wave interacting with material that has no optical transitions in the vicinity of its frequency will therefore be mostly defined by the real part of the dielectric function, and by extension, the refractive index.
The real part shows an inversely proportional dependence on $\hbar\omega_{cv}$, which is effectively the optical band gap of a material. This indicates that in general, a smaller band gap will be associated with a larger dielectric function and thereby refractive index [32]. The appearance of $\omega_{cv}^2 - \omega^2$ in the denominator of the last term indicates that, analogously to the imaginary part, the interaction between the electrical field and the semiconductor will be strongest near transitions.

Correlation with carrier density

The equations for the two components of the dielectric function in Eq. 2.53 and 2.54 both include a summation over the electronic states $\vec{k}$. As carriers are injected into a material, the states included in this summation will change as electronic states near the band edge are occupied and higher lying states become available [39]. The result is a change $\Delta\kappa(\omega)$ in the extinction coefficient. Since real and imaginary parts of the refractive index are

linked via the Kramers-Kronig relation, the real part will also change. The additional carriers will also be able to react to the external stimulus via plasma oscillations, further altering the refractive index. The interaction between the carrier density, which is affected by the optical field of the cavity modes, and the refractive index gives rise to non-linear optical effects that we will examine in more detail in 3.4.4.
The refractive index due to injection n_{inj} can be split into plasma and electron dispersion related components [58, 59]:

$$\bar{n}_{inj}(\omega) = \bar{n}_0(\omega) + \Delta\bar{n}_d(\omega) + \Delta\bar{n}_p(\omega) \tag{2.55}$$

$\bar{n}_0(\omega)$ is the refractive index prior to injection. We are mostly concerned with the change in refractive index that affects the propagation of optical waves, so we will mostly concern ourselves with the real part of $n_0(\omega)$. It can be derived via Eq. 2.53 for the equilibrium occupation. $\Delta\bar{n}_d(\omega)$ and $\Delta\bar{n}_p(\omega)$ are the changes in the refractive index due to the altered dispersion as a result of state occupation and the free carrier plasma response, respectively. We can break the dispersion-related change down further:

$$\Delta\bar{n}_d(\omega) = \Delta n_d(\omega) + i\kappa_d(\omega) \tag{2.56}$$

The change in the extinction coefficient is proportional to the change in gain in the vicinity of a transition [58]:

$$\Delta\kappa_d(\omega) = -\frac{\Delta g(\omega)c}{2\omega} \tag{2.57}$$

where $\Delta g(\omega)$ is the change in the gain in the vicinity of the transition and c is the speed of light. Applying the Kramers-Kronig relations:

$$\Delta n_d(\omega) = \frac{2}{\pi}\int_0^\infty \frac{\omega'\Delta\kappa(\omega)}{\omega'^2 - \omega^2} d\omega' \tag{2.58}$$

$$= -\int_0^\infty \frac{\Delta g(\omega)c}{\omega'^2 - \omega^2} d\omega' \tag{2.59}$$

Due to the singularity at $\omega'^2 = \omega^2$, this needs to be solved using the Cauchy principal integral and separated into multiple parts for integration. Alternatively, the expression can be transformed by adding $\Delta g(\omega)c$ to the integrand [58]:

$$\Delta n_d = -\int_0^\infty \frac{1}{\omega' + \omega}\Delta g(\omega')c - \Delta g(\omega)c\omega'^2 - \omega^2 d\omega' - \Delta g(\omega)c\int_0^\infty \frac{1}{\omega'^2 - \omega^2} d\omega' \tag{2.60}$$

The second integral goes to zero, while the first term approaches the limit $\frac{2\pi c}{2\omega}\frac{d\Delta g(\omega)}{d\omega}$ [58]. $\Delta g(\omega)$ can be extracted experimentally through indirect measurements of the gain such as the Hakki-Paoli method, or numerically by evaluating the gain model and extracting the gain dispersion [59, 60].

The refractive index change due to the free carrier plasma response can be calculated using the polarization of a plasma given an applied electric field $\vec{E}$:

$$\vec{P} = -\frac{q^2}{m_0\omega^2}\left(\frac{n}{m_e^*} + \frac{p}{m_h^*}\right)\vec{E} \tag{2.61}$$

Here q and m_0 are the fundamental electron charge and mass, respectively, and m_e^* and m_h^* represent the effective masses for electrons and holes. n and p are the electron and hole densities in the active region. The total change in the real part of the refractive index due to the free carrier plasma is then [58]:

$$\Delta n_p(\omega) = -\frac{\pi c^2 r_0}{\omega^2 n_0}\left(\frac{n}{m_e^*} + \frac{p}{m_h^*}\right) \tag{2.62}$$

with r_0 as the classical radius of the electron.
The total change in refractive index is often subtle for a lasing device, usually both Δn_d and Δn_p are on the order of 10^{-2} to 10^{-3} for a bulk semiconductor at carrier densities of 10^{18} cm^{-3} [58, 59]. $\Delta n_p(\omega)$ introduces a comparatively constant decrease of the refractive index due to the $\frac{1}{\omega^2}$ dependence. $\Delta n_d(\omega)$ has slightly more structure: it is smaller in the immediate vicinity of the gain peak and increases in magnitude with detuning. The sign of $\Delta n_d(\omega)$ is negative below the gain peak and only switches sign slightly above it, showing a shape reminiscent of a Fano resonance [58].
The different DOS in lower dimensional systems has a profound impact on the gain and thereby the refractive index as well. We will discuss the gain function for QDs and QDashes in more detail in Ch. 4 and revisit this topic there, but the general impact is a decrease in the magnitude of the refractive index change with a decrease in dimensionality. The relationships are similar however, and the absolute index changes remain in the neighbourhood of 10^{-3} [61, 62].

2.4 The role of dimensionality

The first semiconductor laser diodes were based on basic p-type/n-type-interfaces, commonly known as pn-junctions, in GaAs. The spontaneous field gradient at the junction funnels and confines carriers to allow for state occupations that meet the population inversion condition. The laser active states in these initial devices were derived from bulk and defect states [63–65]. Since it is difficult to define dopant densities laterally, these interfaces tend to be extensive on the scale of an infrared photon. The resulting large overlap of the lasing mode with regions of the device that have lower current densities leads to absorptive losses, as areas of the junction that are below the population inversion condition absorb carriers rather than contributing optical amplification. Additionally, reliance on

bulk states to define lasing transitions meant that engineering a device to operate at specific wavelength required finding an alloy with a matching band gap and closely controlling its composition. Lastly, the continuum of states within a band allows for a wide band of states to participate in the transition. This broadens the lasing line, which is undesirable in frequency-resolving spectroscopic applications or in wavelength multiplexing for optical telecommunication systems [25, 49]. Additionally, especially at higher temperatures, the thermal broadening of the carrier distributions deteriorates the optical amplification at a given wavelength. As we saw in Fig. 2.5, the density of states is highly sensitive to the confinement of the particles involved. Restricting the motion of carriers results in a concentration of carrier states near the band edge. Especially for electrons that are confined to one- or zero-dimensions, such as in quantum wires or dashes and quantum dots, the majority of the available states will lie right at the band edge. This inhibits thermal broadening, as there are fewer available states for carriers to occupy at energies above the band edge, which should reduce the temperature sensitivity of the gain and gain-related parameters in lasing devices. Additionally, the total number of available states is generally reduced in dimensionally confined systems, which reduces the current density necessary for achieving population inversion and thereby positive gain. The result is a reduction in the threshold current density and phase noise as a result of lower amplified spontaneous emission rates due to an overall lower density of states in the lower dimensional system.

2.4.1 Heterostructures

A carrier is considered confined when the extent of the volume it can occupy approaches the de Broglie-wavelength of the carrier quasi-particle [66]:

$$\lambda_{\mathrm{deBroglie}} = \frac{h}{p} = \frac{h}{\frac{m^* v_g}{\sqrt{1-(v_g/c)^2}}} \tag{2.63}$$

where h is Planck's constant, m^* is the effective mass, v_g the group velocity (see Eq. 3.57), and c the speed of light in vacuum. This equation involves a relativistic correction to the denominator, which is generally not necessary for the low group velocities observed in semiconductors, and can therefore be neglected.

If any dimension starts to approach $\lambda_{\mathrm{deBroglie}}$, carriers will be severely hampered in their motion along that dimension. Since their zero-point energy can not be zero, the particle attains a quantum-mechanical confinement energy along that dimension. The higher the number of confined dimensions the higher this confinement energy will be. But how does one confine a carrier? In semiconductors, there are multiple methods for creating carrier-confining potential wells in one or more dimensions. One of the first methods discovered

employed electrical gating: electrodes apply a spatially varying electric potential that creates a planar potential well [67]. Due to the requirement for fabricating the metallic gate electrodes, the resulting confinement lengths are on the order of several tens of nanometres. Instead of using an electric potential, isolating semiconductor regions via etching of trenches and mesas can create similar confinement [68].
The most technologically relevant approach however is a semiconductor heterostructure. A heterostructure makes use of the fact that semiconductors with different band gaps will align their band edges relative to one another, which can lead to discontinuities in the conduction and valence bands at the interface. The exact alignment depends on the crystalline structure and composition of the semiconductors involved. A common method to estimate the band alignment for two semiconductors at a heterojunction is Anderson's rule, which uses the electron affinity in both semiconductors to position their conduction band edges relative to one another. The process is illustrated in Fig. 2.7a. and b. Valence band edges are positioned accordingly using the band gap. After positioning the bands, the chemical potentials, which need to be continuous at equilibrium to ensure no net current flows across the junction, are matched. Bands are then bent accordingly to arrive at the final band structure across the heterojunction [34]. While useful, this model is an oversimplification since usage of the bulk band edge for both semiconductors implicitly ignores the disruption of the crystalline translation symmetry at the junction. In reality, the interface will reconfigure itself, leading to interfacial states that need to be calculated explicitly. This, however, is complicated as it involves band structure calculations involving large numbers of atoms [32]. Anderson's rule is sufficiently useful to deliver an intuition on the alignment of two semiconductors, with heuristic approximations for band offsets ΔE_C and ΔE_V being used when quantitative accuracy is required.

Depending on the electron affinities and the chemical potential between the two semiconductors, different relative alignments are possible, outlined in Fig. 2.7c. - e. Most technologically relevant semiconductors will form interfaces of type I or type II. Type I interfaces, such as between InAs and InGaAsP alloys, lend themselves to creating carrier confining structures. For example, imagine semiconductors B and W with conduction band minima E_B and E_W. A set of layers B/W/B would confine the electron to remain within layer W. If the conduction and valence band offsets ΔE_C and ΔE_V are larger than the thermal energy $k_B T$, a carrier will be captured into the central layer and remain there until further perturbed. If we now thin the layer until its thickness approaches the de Broglie wavelength of the carrier within the semiconductor, we will start to see quantum mechanical confinement and a set of confined sub-bands replace the unconfined bulk states. This structure is referred to as a quantum well (QW) and represents a system that is confined along one dimension. Adding confinement along a second dimension results in a quantum wire, only allowing unrestricted carrier motion along one dimension. If the

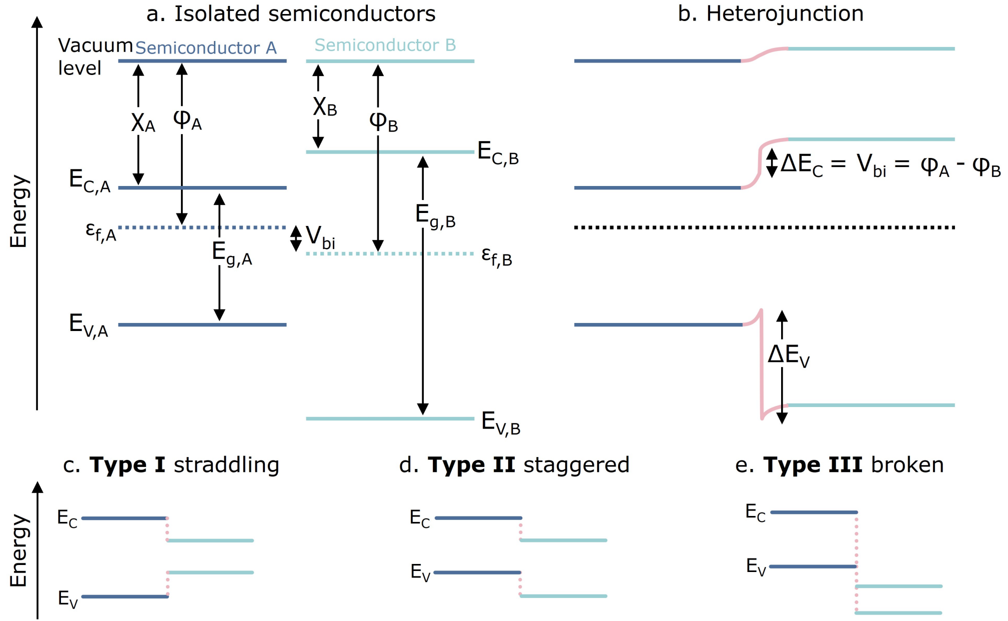

Figure 2.7: **a.** Electron affinities χ_A and χ_B, band edges for the conduction ($E_{C,A}$ and $E_{C,B}$), valence band ($E_{V,A}$ and $E_{V,B}$), and chemical potential position ($\epsilon_{f,A}$ and $\epsilon_{f,B}$) for two semiconductors in isolation. **b.** band positions and bending using Anderson's rule after semiconductors are brought into contact, with band offsets ΔE_C and ΔE_V for the conduction and valence band respectively. The distance between the vacuum level and the chemical potential in each semiconductor, also referred to as the work function, are ϕ_A and ϕ_B. They determine the conduction band offset ΔE_C, while the valence band offset follows from the magnitude of the band bending and band gap mismatch. **c.-e.** show the different types of band alignment one can obtain depending on the relative affinities and work functions.

structure is now grown to confine motion along this last dimension of free motion as well, we arrive at a quantum dot (QD). The resulting shapes of the potential and their impact on the density of states can be seen in Fig. 2.5. The quantum dash, or QDash, which is a mixture of the QD and quantum wire, resides somewhere between these two in terms of its behaviour and density of states. These dashes are generally very tightly confined in two dimensions, but only weakly along the third due to their length. We will discuss their treatment in the context of this thesis in Ch. 5, as depending on growth conditions different approaches are justifiable.

In order to calculate the energies of the states within a confined system we will make use of the effective mass approximation; otherwise we would need to consider states from every atom constituting the confined volume and its boundary. Instead, we can treat the

confined volume as a perturbation $V_{\text{conf}}(\vec{r})$ of an otherwise perfect crystal (see Eq. 2.7):

$$[\mathcal{H}_{1e} + V_{\text{conf}}(\vec{r})]\Psi(\vec{r}) = E\Psi(\vec{r}) \tag{2.64}$$

Following Luttinger and Kohn, the solution for this perturbed Hamiltonian can be written in terms of the solutions to the single-electron Hamiltonian $\phi_{m\vec{k}}(\vec{x})$, summing over states within the first Brillouin zone [69]:

$$\Psi(\vec{r}) = \sum_{m'}\sum_{\vec{k}'} \tilde{\chi}_{m'}(\vec{k}')\phi_{m'\vec{k}'}(\vec{x}) \tag{2.65}$$

with the expansion factors $\tilde{\chi}_m(\vec{k})$. Plugging this into the perturbed Hamiltonian:

$$[\mathcal{H}_{1e} + V_{\text{conf}}(\vec{r})]\sum_{m'}\sum_{\vec{k}'} \tilde{\chi}_{m'}(\vec{k}')\psi_{m'\vec{k}'}(\vec{x}) = E\sum_{m'}\sum_{\vec{k}'} \tilde{\chi}_{m'}(\vec{k}')\phi_{m'\vec{k}'}(\vec{x}) \tag{2.66}$$

Taking the inner product by multiplying by $\psi_{m\vec{k}}(\vec{x})$ and integrating over $\vec{x}$:

$$\int \sum_{m'}\sum_{\vec{k}'} \tilde{\chi}_m(\vec{k})\phi_{m\vec{k}}(\vec{x})[\mathcal{H}_{1e} + V_{\text{conf}}(\vec{r})]\tilde{\chi}_{m'}(\vec{k}')\phi_{m'\vec{k}'}(\vec{x})d\vec{x} \tag{2.67}$$

$$= \int \tilde{\chi}_m(\vec{k})\phi_{m\vec{k}}(\vec{x})E\sum_{m'}\sum_{\vec{k}'} \tilde{\chi}_{m'}(\vec{k}')\phi_{m'\vec{k}'}(\vec{x})d\vec{x} \tag{2.68}$$

$$= E\sum_{m'}\sum_{\vec{k}'} \int \tilde{\chi}_m(\vec{k})\phi_{m\vec{k}}(\vec{x})\tilde{\chi}_{m'}(\vec{k}')\phi_{m'\vec{k}'}(\vec{x})d\vec{x} \tag{2.69}$$

$$= E\sum_{m'}\sum_{\vec{k}'} \left\langle m\vec{k}\middle|m'\vec{k}'\right\rangle = E\tilde{\chi}_m(\vec{k}) \tag{2.70}$$

Due to the orthogonality of Bloch functions, the inner product over m, m', $\vec{k}$, and $\vec{k}'$ reduces along $m = m'$ and $\vec{k} = \vec{k}'$, so $\left\langle m\vec{k}\middle|m'\vec{k}'\right\rangle = \delta_{m'm}\delta_{\vec{k}\vec{k}'}$. This expression therefore simplifies to unity leaving the expansion coefficient.
On the left hand side, things simplify along similar lines:

$$\sum_{m'}\sum_{\vec{k}'} \left[\left\langle m\vec{k}\right| \mathcal{H}_{1e} \left|m'\vec{k}'\right\rangle + \left\langle m\vec{k}\right| V_{\text{conf}}(\vec{r}) \left|m'\vec{k}'\right\rangle\right] \tilde{\chi}_{m'}(\vec{k}') = E\tilde{\chi}_m(\vec{k}) \tag{2.71}$$

If the energetic separation between adjacent bands is large enough, the sum reduces to a single band index. When dealing with band edge states located near the Γ-point, this approximation should hold: for most zincblende semiconductors the separation between the band edge and the next lowest band is on the order of 1 eV [29, 32].
The second assumption follows from similar reasoning: the states we are dealing with lie

at the Γ-point near $\vec{k} = \vec{0}$. For $\vec{k} \approxeq \vec{0}$, the Bloch functions simplify to:

$$\left| m\vec{k} \right\rangle = \phi_{m\vec{k}}(\vec{r}) = u_{m\vec{k}} e^{i\vec{k}\vec{r}} \approxeq u_{m0} e^{i\vec{k}\vec{r}} = \phi_{m0}(\vec{r}) e^{i\vec{k}\vec{r}} \tag{2.72}$$

This simplification holds as long as we are dealing with Γ-valley states, and a slowly varying confined state as we are only including a narrow range of states around 0. If we are interested in confined states resulting from the L- or X-valleys, or ones that vary rapidly on the scale of the Bloch functions $u_{m\vec{k}}$, this assumption would need to be amended.
Assuming that both simplifications hold, the wavefunction for the confined state then simplifies to:

$$\Psi(\vec{r}) \approxeq \phi_{m0}(\vec{r}) \int \tilde{\chi}(\vec{k}) e^{i\vec{k}\vec{r}} \frac{d\vec{k}}{8\pi^3} \tag{2.73}$$

$$= \phi_{m0}(\vec{r}) \chi(\vec{r}) \tag{2.74}$$

Using the effective mass approximation, it appears that we can therefore separate the wavefunction of a confined state into a Bloch term derived from the band states $\phi_{m0}(\vec{r})$ modulated by an envelope term $\chi(\vec{r})$ derived from the confining potential. Another interpretation of this result is to view envelope function as an expansion of the crystal wavefunctions modulated by the perturbing potential.
If we now apply the single electron Hamiltonian to this wavefunction, we can make the assumptions stated above to arrive at a Hamiltonian more apt to describe our confined system:

$$\mathcal{H}_{1e} \Psi(\vec{r}) = \mathcal{H}_{1e} \int \tilde{\chi}(\vec{k}) \phi_{m\vec{k}}(\vec{r}) \frac{d\vec{k}}{8\pi^3} \tag{2.75}$$

$$= \phi_{m\vec{k}}(\vec{r}) \int \tilde{\chi}(\vec{k}) \epsilon_m(\vec{k}) \frac{d\vec{k}}{8\pi^3} \tag{2.76}$$

$$\approxeq \phi_{m0}(\vec{r}) \int \tilde{\chi}(\vec{k}) \epsilon_m(\vec{k}) \frac{d\vec{k}}{8\pi^3} \tag{2.77}$$

Given the often complex shape of the eigenenergies $\epsilon_m(\vec{k})$, we will replace it with a power series as a generalized approximation to the complex dispersion of electrons:

$$\epsilon_m(\vec{k}) = \sum_j a_j k^j \tag{2.78}$$

Applying this expansion to Eq. 2.77, we obtain:

$$\mathcal{H}_{1e} \Psi(\vec{r}) \approxeq \phi_{m0}(\vec{r}) \sum_j a_j \int \tilde{\chi}(\vec{k}) \vec{k}^j \frac{d\vec{k}}{8\pi^3} \tag{2.79}$$

Using the relationship between the Fourier transform and its derivative [32]:

$$\int \frac{df(x)}{dx} e^{-ikx} dx = ik \int f(x) e^{-ikx} dx = ik\tilde{f}(k) \tag{2.80}$$

This can be used to show that the inverse transform of $k^j \tilde{f}(k)$ equals $(-i\frac{d}{dx})^j f(x)$ Continuing our abuse of notation where $\int d\vec{k} = \int\int\int dk_z dk_y dk_x$, the $\frac{d}{dx}$ becomes $\boldsymbol{\nabla}$. We can then use Eq. 2.80 to rearrange the expression as follows:

$$\mathcal{H}_{1e}\Psi(\vec{r}) \approxeq \phi_{m0}(\vec{r}) \sum_j a_j \left(-i\boldsymbol{\nabla}\right)^j \chi(\vec{r}) = \phi_{m0}(\vec{r})\epsilon_m(-i\boldsymbol{\nabla})\chi(\vec{r}) \tag{2.81}$$

We can now simplify, substituting into the perturbed single electron Hamiltonian (Eq. 2.64), and using the approximation $\Psi(\vec{r}) = \phi_{m0}(\vec{r})\chi(\vec{r})$:

$$[\mathcal{H}_{1e} + V_{conf}(\vec{r})]\Psi(\vec{r}) = E\Psi(\vec{r}) \tag{2.82}$$

$$\phi_{m0}(\vec{r})\epsilon_m(-i\boldsymbol{\nabla})\chi(\vec{r}) + V_{conf}(\vec{r})\phi_{m0}(\vec{r})\chi(\vec{r}) \approxeq E\phi_{m0}(\vec{r})\chi(\vec{r}) \tag{2.83}$$

$$[\epsilon_m(-i\boldsymbol{\nabla}) + V_{conf}(\vec{r})]\chi(\vec{r}) = E\chi(\vec{r}) \tag{2.84}$$

The result is an effective Hamiltonian $\epsilon_m(-i\boldsymbol{\nabla}) + V_{conf}(\vec{r})$ describing the motion of a particle in a perturbing potential that strongly resembles the single particle Hamiltonian. There is the energy operator, $\epsilon_m(-i\boldsymbol{\nabla})$, the expansion of the band energies in $-i\boldsymbol{\nabla}$. This term can become quite complicated in itself, and therefore often needs to be approximated as well. For example, using the parabolic band approximation near a band extremum, such as the conduction band valley for example, $\epsilon_m(-i\boldsymbol{\nabla})$ can be approximated as follows:

$$\epsilon_m(\vec{k}) \approxeq E_0 + \frac{\hbar^2 |\vec{k}|^2}{2m^*} \tag{2.85}$$

$$\epsilon_m(-i\boldsymbol{\nabla}) \approxeq E_0 - \frac{\hbar^2}{2m^*}\boldsymbol{\nabla}^2 \tag{2.86}$$

$$\tag{2.87}$$

where E_0 is the band minimum, and m^* is the effective mass of the electron. In this case, we obtain the following effective Hamiltonian:

$$\left[-\frac{\hbar^2}{2m^*}\boldsymbol{\nabla}^2 + V_{conf}(\vec{r})\right]\chi(\vec{r}) = (E - E_0)\chi(\vec{r}) \tag{2.88}$$

This strongly resembles the effective mass Hamiltonian, offset by the band minimum energy E_0 and perturbed by the confining potential $V_{conf}(\vec{r})$. In order to determine the envelope function $\chi(\vec{r})$ term of a confined state within a system, we would therefore solve Eq. 2.88, with solutions resembling those for free particles [32]. This is therefore a straight-

forward approach to obtain confined states irrespective of the confinement dimensionality. However, this useful and elegant approach has several potential pitfalls, which should be highlighted. The assumption that only one band contributes significantly only really holds for the conduction band in zincblende-type semiconductors. There are two degenerate bands for the valence band, associated with the light and heavy hole, which would both need to be included. There is also a third band, the split-off band that needs to be considered in lighter semiconductors, such as Si. Furthermore, if we are dealing with a semiconductor with valley-degeneracy, such as Si, each equivalent valley will contribute to Eq. 2.72 and therefore needs to be included in the summation. Lastly, we are treating each band in isolation, when in reality, there is some intermixing between conduction and valence band states. The assumption that only states with $\vec{k} \approxeq 0$ need to be considered is therefore not fully accurate, and can lead to incorrect estimations of the confined states and their eigenenergies. The Kane model treats this intermixing and can offer higher accuracy if the coupling between bands is non-negligible. Eq. 2.88 also made use of the parabolic approximation to the band extrema, which only has acceptable accuracy over a few 100 meVs above the band edge, depending on the semiconductor. If considering very deeply confined structures, this approximation will overestimate the dispersion. Similarly, it removes the anisotropy of the light and heavy hole masses, which will result in predicted degeneracies which are in reality lifted due to the geometry of the confinement. Lastly, the derivation assumed that the effective mass m^* is uniform within the potential area. If the potential well is created by growing a heterostructure, this is incorrect, as a carrier particle's effective mass will vary depending on the surrounding crystal structure. m^* would therefore become $m^*(\vec{r})$, rendering Eq. 2.88 non-Hermitian, which would mean its solutions are not necessarily physically possible. Fortunately, a small modification to Eq. 2.88 allows the restoration of its Hermitian nature:

$$[-\frac{\hbar^2}{2}\boldsymbol{\nabla}\frac{1}{m^*(\vec{r})}\boldsymbol{\nabla} + V_{conf}(\vec{r})]\chi(\vec{r}) = (E - E_0)\chi(\vec{r}) \tag{2.89}$$

The resulting boundary conditions for the potential envelope wavefunctions at a heterojunction located at $\vec{r} = 0$ are then slightly modified:

$$\chi(0)|_A = \chi(0)|_B \tag{2.90}$$

$$\frac{1}{m_A^*}\boldsymbol{\nabla}\chi(0)|_A = \frac{1}{m_B^*}\boldsymbol{\nabla}\chi(0)|_B \tag{2.91}$$

This only works if $\chi(\vec{r})$ varies slowly in respect to the ionic potential of the lattice. Despite all these potential pitfalls, the modulated free particle model remains a powerful tool to predict the states in confined systems if precautions are taken to account for the underlying assumptions.

2.4.2 Envelope function selection rules

As discussed during the derivation of Fermi's golden rule, the symmetry of the confined state wavefunctions will affect the strength of the dipole moment coupling the states in an optical transition. Thus the optical selection rules for $\Psi(\vec{r})$ are a combination of the rules derived for $\phi_{m\vec{k}}(\vec{r})$ mixed with the envelope function $\chi(\vec{r})$. Given the form of the dipole operator, $\hat{e}\hat{p}$, let us assume the pair of states is interacting with light linearly polarized along one of the three Cartesian orientations. This means we are primarily interested in the symmetry of the wavefunctions along this direction, since the polarization vector will select the derivative along this orientation. Let us examine an example: a heterostructure quantum well in a stack of layers along $\vec{e}_z$ interacts with a photon polarized along $\hat{e}_x = (1, 0, 0)$. The product of polarization and momentum operator will then be $-i\hbar\frac{d}{dx}$. What do the states of a quantum well look like along $\vec{e}_x$? The confinement is along $\vec{e}_z$, so within the effective mass approximation we are dealing with electrons propagating freely along $\vec{e}_x$ and $\vec{e}_y$. The total state for the nth subband without normalization therefore looks something like this:

$$\varphi_{n\vec{k}}(\vec{r}) \approxeq \Psi_n(z)e^{i\vec{k}\vec{r}'} \tag{2.92}$$

with $\vec{r}' = (x, y, 0)$ and $\Psi_n(z)$ being the QW function for the nth band. If we now apply our polarization-selected momentum operator to $\Psi_{n\vec{k}}(\vec{r})$, we arrive at the following expression for an interband transition matrix element between the nth and jth state in the conduction and valence band, respectively:

$$\left\langle n\vec{k}'\right| -i\hbar\frac{d}{dx}\left|j\vec{k}\right\rangle = \hbar k_x \left\langle n\vec{k}'\middle|j\vec{k}\right\rangle \tag{2.93}$$

Since $\varphi_{n\vec{k}'}$ and $\varphi_{j\vec{k}'}$ are orthogonal, $\left\langle n\vec{k}'\middle|j\vec{k}\right\rangle = 0$. There is therefore no absorption for light polarized along $\vec{e}_x$, and similarly along $\vec{e}_y$ for a quantum well normal to $\vec{e}_z$. The QW states will not interact with light polarized along these directions. For light polarized along $\vec{e}_z$, the transition operator simplifies to $-i\hbar\frac{d}{dz}$, with the resulting matrix element:

$$\left\langle n\vec{k}'\right| -i\hbar\frac{d}{dz}\left|j\vec{k}\right\rangle = -i\hbar\int dz\int \Psi_n^*(z)e^{i(\vec{k}-\vec{k}')\vec{r}'}\frac{d}{dz}\Psi_j(z)d\vec{r}' \tag{2.94}$$

where $d\vec{r}' = dydx$. The term $\int e^{i(\vec{k}-\vec{k}')\vec{r}'}d\vec{r}'$ vanishes for $\vec{k} \neq \vec{k}'$, so the matrix element simplifies to $-i\hbar\left\langle n\right|\frac{d}{dz}\left|j\right\rangle$. Evaluating this element is slightly more complex, but necessary to arrive at the selection rules for a confined system.

As established earlier, the wavefunction for a confined state can be treated as the product of a Bloch function $\phi_{n\vec{k}}(\vec{r})$ and an envelope function $\chi_m(\vec{r})$, so $\Psi_{nm0}(\vec{r}) = \sqrt{\Omega}\phi_{n0}(\vec{r})\chi_m(\vec{r})$,

where n and m are the band and subband index, respectively, and Ω is the sample volume which will ensure that the resulting wavefunction is normalized. The matrix element for an interband transition between a conduction and valence band state, denoted by c and v, is then:

$$\langle cn| \frac{d}{dz} |vj\rangle = \Omega \int \chi_c^*(\vec{r})\phi_c^*(\vec{r})\frac{d}{dz}\chi_v(\vec{r})\phi_v(\vec{r})d\vec{r} \tag{2.95}$$

This integral can be simplified since the envelope and Bloch functions vary on two length scales: the envelope functions are slowly varying on the scale of the unit cell, while the Bloch functions vary rapidly. Eq. 2.95 can therefore be separated into two terms:

$$\langle cn| \frac{d}{dz} |vj\rangle \approxeq \Omega \sum_{w}^{cells} \chi_c^*(\vec{R_w})\chi_v(\vec{R_w}) \int_{cellw} \phi_c^*(\vec{r})\frac{d}{dz}\phi_v(\vec{r})d\vec{r} \tag{2.96}$$

The integral over a single cell is the dipole matrix element derived from Bloch functions we met earlier in Eq. 2.45. Its selection rules are based on the symmetry of the wavefunctions near the band edge. It vanishes if $\phi_c(\vec{r})$ and $\phi_v(\vec{r})$ have even parity. Introducing the band extremum dipole matrix element for Bloch functions, $\langle c| \frac{d}{dz} |v\rangle$, the expression then simplifies to:

$$\langle cn| \frac{d}{dz} |vj\rangle \approxeq \langle c| \frac{d}{dz} |v\rangle \, \Omega_{cell} \sum_{w}^{cells} \chi_c^*(\vec{R_w})\chi_v(\vec{R_w}) \tag{2.97}$$

Finally, the summation can be returned to its integral form since we have separated the two parts varying on different length scales. The final form of the interband matrix element then reads:

$$\langle cn| \frac{d}{dz} |vj\rangle \approxeq \langle c| \frac{d}{dz} |v\rangle \int \chi_c^*(\vec{r})\chi_v(\vec{r})d\vec{r} \tag{2.98}$$

If either of the terms in Eq. 2.98 vanishes, the transition will vanish. The first term imposes the previously established odd parity rule for the initial and final state Bloch functions. The second term, derived from the envelope functions, demands even parity for the envelope functions in order to be non-vanishing. So only wavefunctions with identical parity will have allowed transitions.

Given the shape of the wavefunction in a symmetrically confined system, the odd numbered envelope functions have even parity while even numbered functions will exhibit odd parity (see Fig. 10.5 in [32]). So only transitions between odd or even indices are allowed. For an infinitely deep well that is identical in conduction and valence band, this goes even further as the identical wavefunctions in both bands will result in orthogonal wavefunctions for non-matching indices, so $\Delta n = n - j = 0$. In this case, only transitions between identical band indices are allowed.

In a real heterostructure, potentials are never infinite and rarely identical for electrons and holes, so this condition is generally weaker experimentally. However, transitions for which $\Delta n = 0$ tend to be stronger than ones for which $|\Delta n| > 0$, even for finite and asymmetrical

wells.
While we derived the above rules for a QW, they extend to quantum wires, QDashes, and QDs in a straightforward manner, with the envelope function increasing in dimensionality. The result is a dipole that interacts with an increasing number of orientations of light polarization. A QD can absorb any orientation, even though the strength of the dipole may vary depending on the polarization for anisotropic confining potentials.

2.5 Semiconductor growth

While there are some naturally occurring semiconducting materials, they are too rich in impurities and other defects to be technologically viable. As explored earlier, one important characteristic of semiconductors is the ability to closely control their electrical properties. This is only possible if the material prior to fabrication is as free of defects as possible and ideally monocrystalline. This means reducing the number of impurity atoms by using high purity raw materials combined with further refinement. Structural defects are mitigated by ensuring near-equilibrium conditions during crystal growth.

2.5.1 Wafer growth

Most semiconductor wafers grown today are likely to have been manufactured using either the Czochralski, float zone, or Bridgman-Stockbarger method. The Czochralski growth of monocrystalline semiconductors employs a crucible filled with a purified semiconductor melt just below its melting point, inserting a monocrystalline seedling at the top and pulling the seedling upwards while rotating slowly. As it is pulled, liquid melt solidifies around the seedling, mirroring its crystalline phase. The temperature of the melt close to the melting point ensures proximity to equilibrium growth conditions resulting in material that is very low in defects, as atoms are sufficiently mobile to rearrange themselves into their ideal energetic positions rather than forming metastable defects. Growing semiconductor alloys with this method is possible, albeit difficult since density gradients and different formation energies can lead to stoichiometric non-uniformity and poly-crystallinity [70]. The float zone method avoids some of these shortcomings by melting a small section of a prefabricated polycrystalline ingot and allowing it to slowly cool, again making use of a seedling to initiate growth of the desired structure and orientation at one end of the ingot. Due to the sharp thermal gradient between the heated float zone and the much cooler rest of the ingot, enrichment of the melt leading to the aforementioned non-uniformity is less relevant, allowing near arbitrary alloy compositions with less risk of property deteri-

oration. The fact that it can also be conducted in a crucible-free manner further reduces contamination of the grown crystal, allowing it to achieve the lowest impurity concentrations possible in wafer growth. It also allows growing semiconductors that form highly reactive melts [71]. The third method discussed here, known as Bridgman-Stockbarger, can be seen as a mixture of the two: similar to the Czochralski-method, it grows a crystal from a continuous semiconductor melt, but rather than pulling the crystal out of the melt, a closely controlled temperature gradient along the direction of the growth induces crystallization at a specific growth speed and reduces some of the enrichment effects seen in pure Czochralski-growth. Most optoelectronic GaAs is grown via this method as it offers more control over the growth process than Czochralski growth, and is less affected by the high volatility of Ga. The InP wafers used as the growth substrates used in this work were grown in this manner. There are other methods, such as Kyropoulos and Verneuil growth methods, but they are less used for the semiconductors relevant for diode lasers. The ingot is cut into individual wafers, and each wafer lapped and polished to act as the substrate in further processing.

2.5.2 Heterostructure growth

The dimensions of the heterostructures useful for confining carriers are far to small to be created using any of the above mentioned wafer-scale methods. Instead, they require growth methods that are able to grow defect-free layers with near instantaneous compositional switching. The most common way to achieve this is to place a heated growth substrate in an isolated chamber and add small quantities of material that will adsorb unto the growth substrate and form new layers. If the new layer reproduces the crystal structure of the substrate, the growth process is referred to as epitaxy. Whether or not the grown layer will arrange itself in accordance with the substrate depends on the crystal structure of the substrate and deposited material, total thickness of the layer deposited, and the deposition conditions.

Epitaxial growth methods can generally be categorized into two groups: elemental methods that deposit elements of the layer material directly and precursor-based methods that use molecules containing the layer constituents which are decomposed at the growth interface. Molecular beam epitaxy (MBE) and physical vapour deposition (PVD) are examples of elemental methods, while metal-organic chemical vapour deposition (MOCVD) and chemical beam epitaxy (CBE) are precursor-based. Elemental methods are also always conducted under vacuum, while some precursor-based approaches may use low pressure conditions [72]. Each approach features a host of derived methods that vary slightly in their approach to deliver reactants and facilitate their decomposition, if necessary, as well as their adsorption unto the surface. A full comparison of these methods would go beyond

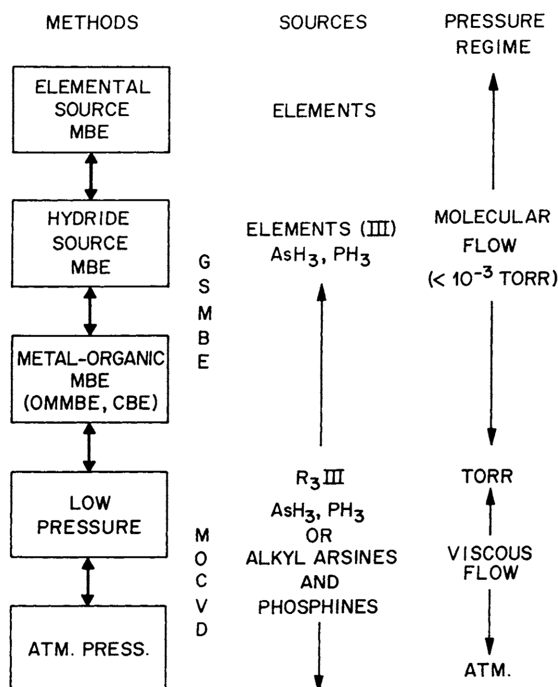

Figure 2.8: Molecular beam epitaxy (MBE) and metal-organic vapour deposition (MOCVD) methods and their source materials and pressure conditions. Chemical beam epitaxy is a subset of gas-source MBE (GSMBE) methods. Reproduced from [73].

the scope of this work, but we will quickly discuss CBE and MOCVD, as they are the growth methods used to grow the devices in this work.

Chemical beam epitaxy

Chemical beam epitaxy (CBE), also known as metal-organic molecular beam epitaxy (MOMBE or OMMBE), is the combination of MBE and MOCVD into one growth method that replaces the elemental sources used in MBE with metal-organic molecular sources similar to the ones used in MOCVD, while retaining the growth under vacuum conditions from MBE. A sample growth reactor is shown in Fig. 2.9. While the concept of gas-source MBE was initially demonstrated using hydride group V elements by Panish in 1980, a method using molecular sources for both group III and group V elements was developed by Tsang in 1984 [74, 75]. Using molecular sources for both group III and V elements has several advantages, including easier scalability, reduced source recovery time, which is especially relevant for group V sources, and more precise compositional control compared to elemental sources. The method has found widespread use in the growth of heterostructure semiconductors since it produces high quality epitaxial layers at arbitrary

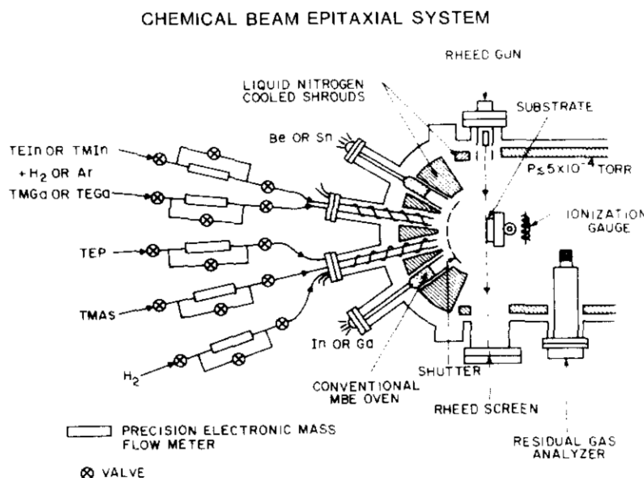

Figure 2.9: Chemical beam epitaxy system. The group III source chemicals, trimethyl- or triethylindium (TMIn and TEIn), and trimethyl or triethylgallium (TMGa and TEGa), and the group V molecules trimethylarsine (TMA) and triethylphosphine (TEP) are transported to the reaction surface using a carrier H_2 or Ar stream. Decomposition occurs at the heated growth substrate for group III molecules and in a Ta/Mo-buffered alumina tube for the group V molecules. Flow rates were controlled using electronic mass flow controllers, leading to high reproducibility of the growth rates. Since this system is a converted MBE system, elemental sources for Be, Sn, In and Ga remain. The former are useful as they are dopants that can be added during the growth process. A reflection high-energy electron diffraction (RHEED) system is used to monitor the growth process in-situ. Reproduced from [74].

compositions with sufficient abruptness to grow very thin heterostructures [72]. It is the most common technique for InGaAsP growth, a quarternary compound semiconductor which can be compositionally varied to obtain band gaps between 0.71 and 1.35 eV while maintaining a lattice match to InP, which is true if the following expression holds for the Ga fraction x and As fraction y in $In_{1-x}Ga_xAs_yP_{1-y}$ [76]:

$$x = 0.1894 * y/(0.4184 - 0.013 * y) \tag{2.99}$$

Since this range of band gaps covers several fiber optical communication bands as shown in Fig. 2.10, lattice-matched InGaAsP alloys are widely used in telecommunication systems [72]. The precursor chemicals are usually simple organo-metallic molecules, such as alkyls and hydrides, with alkyls being safer to handle [74]. The main advantage of CBE over MBE is the availability of reliable and easily reproducible sources of phosphorus, highly relevant when lattice matching InGaAsP to InP is very sensitive to the composition. Elemental phosphorus sources require frequent regeneration and are difficult to calibrate as evaporation rates are closely tied to a sources thermal history. Additionally,

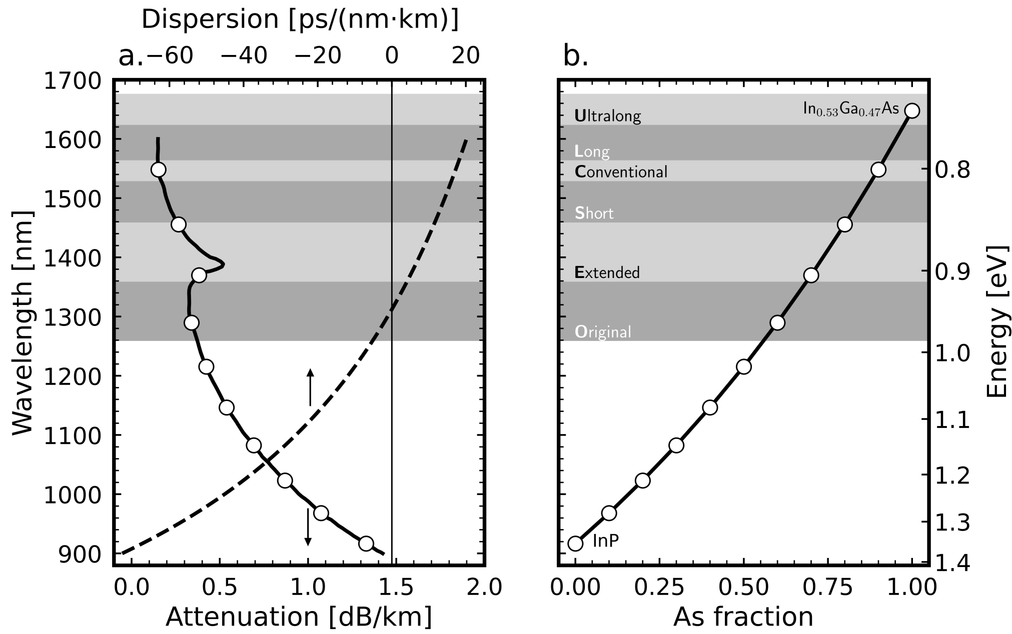

Figure 2.10: **a.** Attenuation and dispersion as a function of wavelength for Corning SMF-28 fiber, a common Ge-doped silica fiber used in optical fiber communication system [77]. **b.** band gap of InGaAsP alloys latticed matched to InP, varying from InP (0% As) to $In_{0.47}Ga_{0.53}As$ (100% As). $In_{1-x}Ga_xAs_yP_{1-y}$ is lattice matched to InP if the empirical expression Eq. 2.99 holds. The shaded regions indicate the common fiber-optical communication bands [78]. The devices studied in this work target the conventional (C)-band near the silica fiber attenuation minimum of 1550 nm.

they often deliver phosphorus allotropes that do not decompose readily on the growth substrate. Contrast this with AlGaAs/GaAs, another material highly relevant to opto-electronic heterostructures, which can grow high quality epitaxial layers using elemental sources only. It is lattice matched irrespective of composition and elemental sources are less complex to manage, which in addition to the more favourable band offsets when trying to confine carriers, led to its earlier adaptation in heterostructure lasers [72].

Comparison with MOCVD

As Fig. 2.8 indicates, MOCVD is very similar to MBE, with similar precursor chemicals used and reaction ingredients delivery via carrier gas. The main difference is the higher ambient pressure environment in MOCVD, which moves molecular motion from the ballistic to the viscous regime. As more gaseous species are present at the growth interface, interactions between reactants are more likely, introducing complexity to the source selection process. Additionally, the presence of a boundary layer above the growth substrate

can interfere with the stoichiometry and lead to spatial inhomogeneity across the growth surface. This is offset by the reduced complexity of MOCVD processes as it can occur outside of vacuum chambers, even though the toxicity of the chemicals involved still requires complex air handling equipment [74]. CBE and other GSMBE methods are also superior to MOCVD in terms of layer abruptness and achievable doping levels, at the cost of reduced growth rates [72]. For logistical reasons, MOCVD is used in the overgrowth stage of the devices fabricated for this work. The overgrowth step growths the layers constituting the ridge of the device, which is then defined via etching.

2.5.3 Quantum dot and dash formation

The self-assembled growth of QDs and QDashes in the InGaAsP/InP system are almost identical, so we will be describing the process for dots and mention the differences for dashes as they arise.

On a crystalline surface lattice matched to InP, InAs QDs will self-assemble during epitaxial growth due to strain relaxation of a layer with critical thickness t_c. The process is depicted in Fig. 2.11. The room temperature lattice constant of InP is 5.86 Å, while InAs is slightly larger at 6.06 Å and therefore experiences compressive strain when grown on InP [76]. When depositing InAs on InP, or material lattice matched to InP, the resulting epitaxial InAs layers experience a degree of strain. As the thickness of the layer increases, the elastic energy within the metamorphic InAs increases, until it is sufficient to induce a reconfiguration of the surface into separate, less strained islands on top of a strained wetting layer, as seen in step IV in Fig. 2.11. The height and shape of the resulting islands depends on the ambient conditions, including As availability, substrate crystal structure, and temperature [79, 80]. Varying the growth temperature alters the surface diffusion of As, while the crystallographic structure of the growth surface induces a strain anisotropy in the plane [81]. These two parameters are the strongest drivers in inducing the islands to elongate and form quantum dashes (QDashes) with lateral aspect ratios ranging between 1:2 and 1:20 [82, 83]. Typical dot densities are on the order of 10^{10} to 10^{11} cm^{-2}, depending on the substrate, while for dashes it usually lies closer to 10^{10} cm^{-2} [80, 82, 84, 85].

After islands have formed, dots are capped with InP. This occurs in a double-cap process, splitting the InP cap deposition into two steps, interrupted by a hold under phosphorus overpressure [80]. The hold step enables extensive As/P-exchange at the section of the dot not covered by the first InP deposition. This reduces the height variability between different dots and thereby the degree of inhomogeneous broadening of transitions [86, 87]. By altering the height of the first InP deposition step, the final height of the dots can be tuned, allowing precise control over the transition energies in the dot [88, 89].

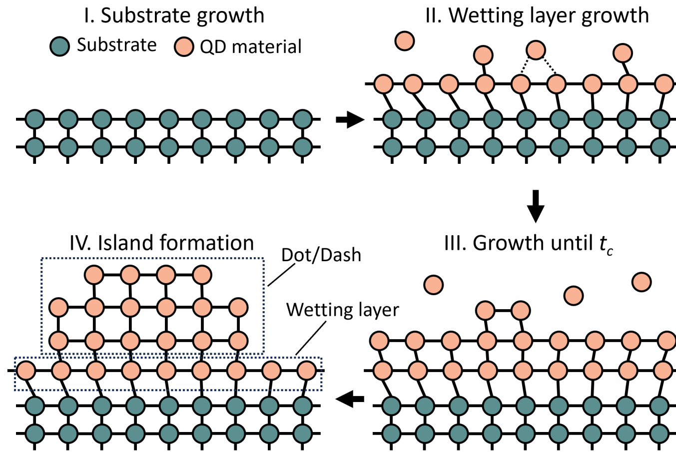

Figure 2.11: QD formation due the Stranski-Krastanov, also referred to as layer-island, growth mode. **I.** A substrate is grown with a lattice constant different from the QD material. **II.** The QD material is deposited, forming a continuous layer across the surface that is referred to as the wetting layer. Due to the mismatch in the lattice constants between substrate and dot material, the wetting layer is slightly strained. **III.** The wetting layer continues increasing in thickness, continuing the strained structure induced by the substrate. The layer will grow in thickness until it reaches a critical thickness t_c. This is often on the order of a few monolayers of material. **IV.** The strain is released via island formation. The crystal structure within the island is less strained and therefore energetically favourable. A thin wetting layer remains.

2.5.4 Size fluctuations

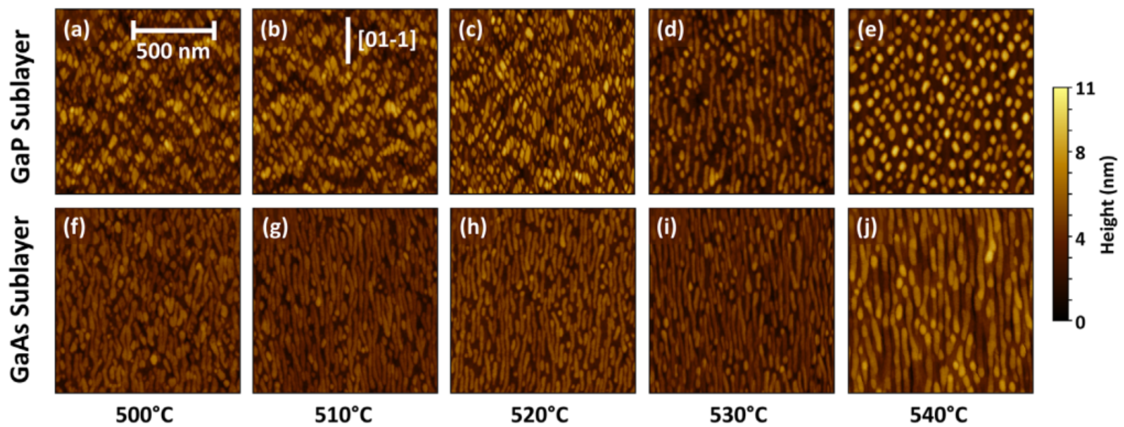

Figure 2.12: AFM images detailing the differences in nanostructure morphology as a function of sub-layer and growth temperature. Reproduced from [83].

Since QDs and QDashes are self-assembled, their shapes and sizes will vary and be subject to some degree of variation across the extent of the active region. This is illustrated by Fig. 2.12, which shows the nanostructure morphology as a function of sub-layer composition

and growth temperature [83]. The dashes used in this work were grown under conditions nearly identical to Fig. 2.12h. Assuming a lasing device of 1500 µm length with an approximately circular mode of diameter 2 µm, the optical mode volume encompasses around 10^5 to 10^6 QDs or QDashes in a single layer. A typical devices will feature three or more layers, further increasing the size of the nanostructure ensemble that is contributing to the light emission from the cavity. As we established in the previous section, the energy levels of a nanostructure are closely linked to its spatial extent. Any variation in shape and size will therefore inevitably translate into a variation in sub-band structure [90]. Not all dimensions are equally relevant for this fluctuation however. Assuming isotropic effective masses, the shortest dimension will have the largest impact on the overall energy level since confinement is the strongest. For QDs and QDashes, with heights that are significantly smaller than their lateral extent, keeping the height uniform across the ensemble will reduce the energy level spread more than controlling diameter or length in the case of QDashes. This is the motivation for the double-capping process discussed earlier [86, 91]. For shorter quantum dashes, which have non-negligible quantization energies along the longitudinal direction, the relationship between length and sub-band position varies depending on the shape of the wavefunction in the dash cross section. Higher order states will show a higher sensitivity to length than the ground state [92]. We will discuss these size fluctuations in more detail when discussing the linewidths of QD- and QDash-based gain media.

A last thing to mention when discussing quantum dashes is the large variability in lengths: Fig. 2.12 illustrates how the transition between QD and QDash formation is not step-like with temperature, but rather a smooth transition from one morphology to another. QDash layers will therefore often include short dashes reminiscent of dots in shape and size, as well as long dashes that resemble quantum wires in their extent. The treatment of QDash layers then requires mixing the qualities of zero-dimensional QDs with one-dimensional quantum wires, with a large fraction of the sample falling somewhere in between. We chose to treat QDashes as elongated QDs with minimal longitudinal quantization due to the technological capabilities of the Schrödinger solver attached to the numerical simulation environment used. This is most relevant when considering the optical gain function, where the DOS plays a strong role and the largest variation between wire- or dot-like treatment exists. A more thorough discussion of this choice can therefore be found in the explanation of the gain models used in Ch. 4.

2.5.5 Barrier composition

While the composition of the dash itself is generally InAs, even though InGaAs dashes have been explored, there are two material systems commonly used for the barrier material

between dashes: InAlGaAs and InGaAsP. The band offset between InAs and InAlGaAs is larger, leading to greater confinement and reduced thermionic carrier escape. Lattice matching is also less complicated, as InAlGaAs is lattice matched for all combinations of its constituents, while InGaAsP is only matched for certain compositions (see Eq. 2.99), which complicates the growth process in requiring precise control of the group V source [93]. Additionally, the absence of phosphorus means that there are no As/P exchange effects to alter the composition or shape of structures post-growth in unforeseen or undesirable ways. However, the lattice mismatch between InAs and InGaAsP alloys latticed-matched to InP is smaller than for InAlGaAs, allowing for larger dot sizes as the relaxation energy is reduced. For devices targeting the L- and U-bands at 1570 nm and beyond, InGaAsP barrier materials are therefore potentially less cumbersome to grow [94].

3

Laser fundamentals

The laser (Light Amplification by Stimulated Emission of Radiation) has contributed to technological progress in numerous fields since its development in the late 1950s [95, 96]. Laser light emitting devices have contributed to medicine by way of corneal laser ablation or thermal cancer treatment, to process technology by laser-based ablation and welding methods, and to telecommunications as one of the key components in enabling optical fiber networks, networks which form the backbone of the internet [4, 97, 98]. Lasers have also had a catalytic effect on a variety of sciences, be it astronomy by enabling the study of minuscule shifts in gravitational fields, environmental science by providing the tools to study cloud formation, or material science where lasers enabled even closer scrutiny of the optoelectronic properties of a variety of materials [49, 99, 100]. This is especially relevant for semiconductors, a group of materials that have played a pivotal role in the accelerating rate of human technological progress. The existence of the laser also created entirely new fields of science and engineering, as it provided a comparatively accessible test bed for many quantum mechanical effects and allowed their integration into novel technologies, such as quantum metrology [49]. The usage of lasers has grown ubiquitous, affecting every field of technology. The focus of this work is on lasers designed for telecommunication applications, which are generally in the near infrared, coinciding with the attenuation or dispersion minima of silica fiber. Single- and multi-mode fibers constitute the majority of modern optical network infrastructure, but with ever increasing data transfer demands the limitations of current signal sources will soon be reached. There is therefore a need to create new light sources that can extend the capacity and thereby lifetime of existing infrastructure by increasing the data rates per fiber [4]. We will therefore start by examining the fundamentals of lasing devices, and then dive into the theory underpinning mode-locked lasers which offer higher data rates.

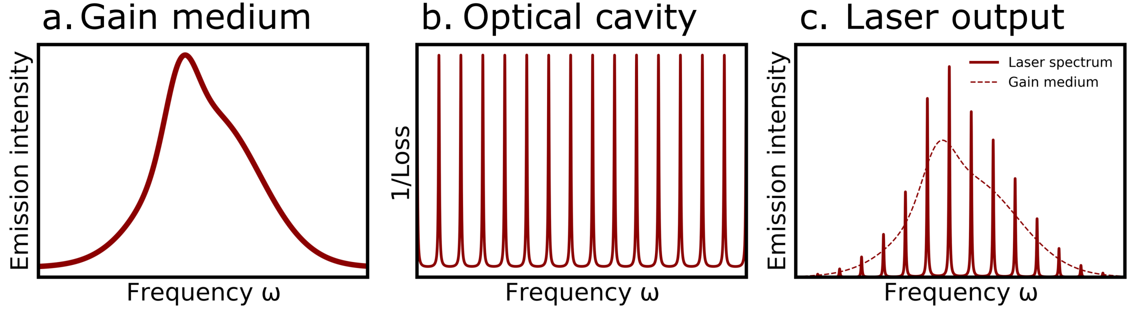

Figure 3.1: Defining spectral characteristics of the components of any lasing device **a.** emission spectrum of the gain medium, **b.** inverse loss spectrum for the optical cavity (in this case an idealized Fabry-Perot cavity) and the **c.** resulting laser emission spectrum as a combination of both. This is a simplified analogy, where several complicating factors, such as gain competition between modes, are ignored.

3.1 Characteristics of a laser

Presume an extended source of light that is emitting into a space. If the phase difference is constant at a given point in space P between arbitrary times t_1 and t_2, the light source is considered temporally coherent. If the phase difference between point P_1 and P_2 is also constant as a function of time, the light is also considered spatially coherent. Varying degrees of coherence are usually quantified using the coherence time Δt_c, which is defined as the maximum time difference for which the phase difference $\Delta\phi$ varies by $\leq \pi$:

$$\Delta t_c = t_2 - t_1,\ \Delta|\phi(t_2) - \phi(t_1)| \leq \pi \tag{3.1}$$

From Δt_c we can calculate a coherence length Δl_c:

$$\Delta l_c = c\Delta t_c \tag{3.2}$$

Light emitted from a laser has both temporal and spatial coherence [49, 54]. Additionally, the photons emitted from a laser once the lasing condition is met will change their energetic probability distribution from chaotic Bose-Einstein statistics to an approximate Poisson distribution (see Fig. 3.8b.), with important implications for metrological applications [101]. Lastly, laser light is significantly more intense in terms of intensity per unit of frequency due to its concentration of optical energy into a small number of near-discrete modes. This concept is taken further in pulsed lasers, that additionally concentrate the input of energy in time, leading to peak powers of several hundred TW and possible pulse widths in the 10^{-15} s regime [54, 102]. These properties are directly related to the design of a lasing device, which consists of an optical gain medium and a resonator. The gain

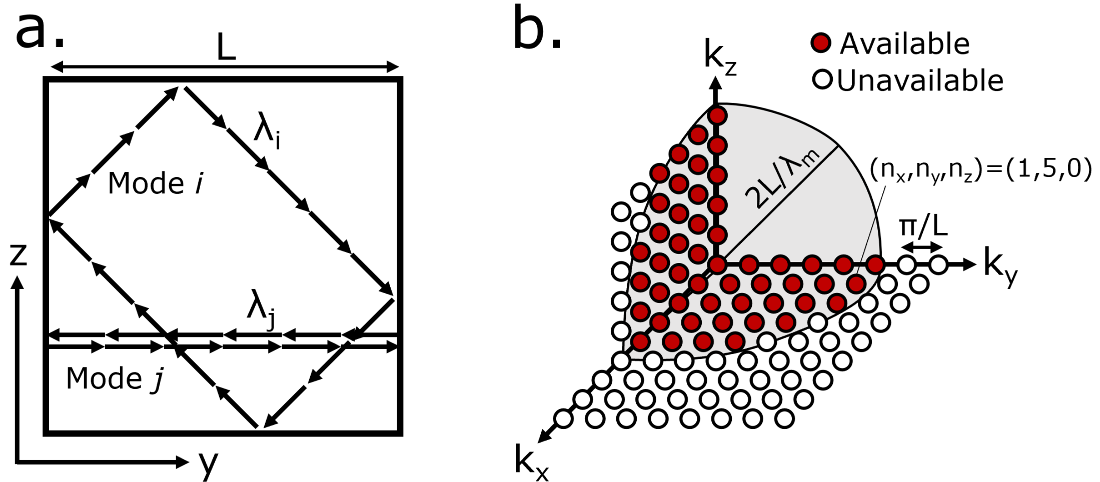

Figure 3.2: **a.** Two valid cavity modes inside a cubic resonator and **b.** possible modes in wave vector space. Each site indicates a potential mode, with only modes within the grey sphere being accessible given the properties of the resonator.

medium can be any material providing two or more energetic levels coupled by an optical transition which can be excited through the supply of external energy. The resonator, or resonant cavity, is selected to show minima in optical loss at wavelengths corresponding to optical transition energies of the gain medium. The result is a self-amplifying standing wave within the cavity, of which a fraction is coupled out representing the emission from the device. The resonator suppresses emission with random phases in favour of in-phase processes that result in the coherence characteristics observed at the laser output [49]. We will now discuss both components of the laser in more detail.

3.2 Optical resonators

The main role of the optical resonator is the creation of a set of low-loss electromagnetic standing waves at frequencies that coincide with desirable transitions in the gain medium. The standing waves are the modes of the resonator, with their spectral and spatial shape defined by the design and reflectivity of the resonator. The key characteristic for resonators suitable for use with an active medium to form a laser is strong feedback for cavity modes and strong suppression everywhere else. Resonators are also often referred to as cavity resonators or optical cavities as a result of borrowed terminology from the field of microwave radiation, and we will be using the terms resonator and cavity interchangeably.

3.2.1 Cavity modes

To understand the modes for any cavity, let us start with a simple cubic sample cavity. It is at a uniform temperature T and it has side lengths L, and its yz-plane is depicted in Fig. 3.2a. Given the thermal equilibrium, every wall of the cavity acts as a black body emitter and therefore has to emit and absorb equivalent amounts of electromagnetic radiation to maintain the dynamic balance of energy, or $P_{abs}(\omega) = P_e(\omega)$, where $P_{abs}(\omega)$ and $P_e(\omega)$ are the absorbed and emitted energy within the cavity. The result of this energy exchange within the cavity is a stationary, spatially varying electric field $\vec{E}(\vec{r})$:

$$\vec{E}(\vec{r}) = \sum_n \vec{A}_n e^{i[\omega_n t - \vec{k}_n \vec{r}]} + \vec{A}_n e^{-i[\omega_n t - \vec{k}_n \vec{r}]} \tag{3.3}$$

It is the linear superposition of transverse plane waves with amplitude $\vec{A}_n$ and wave vectors $\vec{k}_n$ related to their angular frequencies ω_n as $\left|\vec{k}_n\right| = \frac{\omega_n}{v_p}$, where v_p is the phase velocity we will discuss in more detail later (see Eq. 3.57). Assuming reflective interior walls, waves within the cavity will interfere if their wave vectors $\vec{k}$ fulfil the resonance condition:

$$\vec{k} = \frac{\pi}{L}(n_x, n_y, n_z) \tag{3.4}$$

where $n_{(x,y,z)} \in \mathbb{N}_0$. This condition states that only waves for which the total optical path length along each dimension, which is twice the cavity side length L for the cubic cavity, is an integer multiple of its wavelength will form standing waves. From this we can derive a condition for the magnitude of the mode wave vectors:

$$\left|\vec{k}\right| = \frac{\pi}{L}\sqrt{n_x^2 + n_y^2 + n_z^2} \tag{3.5}$$

This is depicted in Fig. 3.2b: each site indicates an integer multiple of $\frac{\pi}{L}$, but only red sites indicate viable modes given the cavity length and cut-off wavelength λ_m. This translates into conditions for the wavelength λ and angular frequency ω of the cavity modes:

$$\lambda = \frac{2L}{\sqrt{n_x^2 + n_y^2 + n_z^2}} \tag{3.6}$$

$$\omega = \frac{\pi v_p}{L}\sqrt{n_x^2 + n_y^2 + n_z^2} \tag{3.7}$$

Since we used plane waves to construct the original electric field $\vec{E}(\vec{r})$, $\vec{A}$ will always be perpendicular to $\vec{k}$ and can be restated as a superposition of two orthogonal polarization components $\hat{e}_1$ and $\hat{e}_2$:

$$\vec{A} = a_1\hat{e}_1 + a_2\hat{e}_2 \tag{3.8}$$

Since each cavity mode can be treated as consisting of two linearly polarized modes interfering, each triplet of indices (n_x, n_y, n_z) actually denotes two cavity modes with orthogonal polarizations. Since any stationary electric field needs to be expressed in terms of standing waves in order to retain its time-independence, and the modes from Eq. 3.5 and 3.7 are the only viable standing waves, any stationary field can be expressed as a superposition of the cavity modes.

The total number of cavity modes accessible depends on the maximum attainable frequency in the system, ω_m, or a minimum attainable wavelength λ_m. To determine the total number of modes we merely need to sum over all mode indices that result in modes with ω_n between 0 and ω_m. For the optical cavities we are interested in this work, the condition $L >> \lambda_n$ holds, as cavities are on the order of $10^{2\text{-}3}$ µm, while optical wavelengths in the near-infrared region we are most interested in are on the order of 1 µm. $\frac{\pi}{L}$ is therefore very small and the summation over all indices can be approximated as an integral to determine the volume of accessible mode space. For the octant of accessible mode space depicted in Fig. 3.2b, we therefore only need to calculate the volume of a sphere for which $\omega_n^2 \leq \omega_m^2$:

$$N(\omega_m) = 2\frac{1}{8}\frac{4\pi}{3}\left(\frac{L\omega_m}{\pi c}\right)^3 = \frac{\omega_m^3 L^3}{\pi^2 c^3} \tag{3.9}$$

The factor of 2 arrives as a result of the two available polarization modes per index triplet, and the factor of $\frac{1}{8}$ is a result of forward and backwards propagation being degenerate, hence we are only interested in the positive octant of the sphere.

Due to the interaction with optical transitions which are located at specific frequencies and location, one is generally less invested in the total number of modes within a cavity and rather the total number of modes per unit volume in a given spectral interval. We therefore define the spectral mode density $n_{ph}(\omega)$:

$$n_{ph}(\omega)d\omega = \frac{d}{d\omega}\frac{N(\omega)}{L^3}d\omega = \frac{\omega^2}{\pi^2 c^3}d\omega \tag{3.10}$$

From this we can also formulate at the spectral energy density $\rho_{ph}(\omega)$ using the mean energy per mode $\overline{W_{ph}}$:

$$\rho_{ph}(\omega)d\omega = n_{ph}(\omega)\overline{W_{ph}}d\omega = \frac{2\omega^3 n_r^3}{\pi c^3}N_{ph}(\omega) \tag{3.11}$$

Determining the mean energy per mode requires knowledge about the occupation of each mode, which is related to photon emission and absorption and will be discussed in the next section when exploring different gain media and concepts of quantifying coupling between optical transitions and cavity modes.

3.2.2 Quality factor

In order to obtain lasing emission from a resonator, only a comparatively small number of modes can be allowed to have significant photon occupation. These modes will then be further amplified via stimulated emission. All other modes need to be suppressed to prevent their parasitic depletion of the gain medium excited state population. This concentration of energy into a small number of modes requires a resonator with strong loss contrast between desirable modes with low loss and undesirable modes with very high loss. In order to quantify this feedback, let us take a look at the change in energy stored within the nth mode:

$$\frac{d}{dt}W_n = -\beta_n W_n \tag{3.12}$$

The change in stored energy W_n is the product of the already accumulated energy multiplied by the loss factor β_n. The quality factor of this mode is then the ratio of the energy stored to the energy lost per oscillation:

$$Q_n = -\frac{2\pi\nu W_n}{\frac{d}{dt}W_n} = -\frac{2\pi\nu}{\beta_n} \tag{3.13}$$

The quality factor for a given mode n is related to the cavity lifetime t_n by the following relation [103]:

$$Q_n = \omega_n t_n \tag{3.14}$$

The role of the cavity is to produce a series of modes with high Q_n, which are the modes that will be preferably amplified by the gain medium.

3.2.3 Mode shape

For optical resonators, there are two relevant mode shapes: the spectral and the spatial mode shapes. The spectral shape is required to quantify the overlap with optical transitions of the gain medium. The spatial mode shape defines the near- and far-field pattern of the light emitted from the resonator and the spatial distribution of the optical mode for gain media with spatially non-uniform emission and absorption characteristics. Both spectral and spatial mode shape are dependent on the type of resonator used. The devices studied in this work are monolithic semiconductor diode lasers. The resonator is formed by near total internal reflection at the interface at the semiconductor and air interfaces creating a Fabry-Perot resonator. The discussion will therefore be focussed on the mode structure inside these resonators.

Spectral mode shape

As we discussed in the previous section, cavity modes are a result of standing waves related to the geometry of the cavity. In an idealized resonator, the spectral mode shape would be a discrete line located at the frequency of the mode ω_n, but imperfections of the resonator will broaden this line into a narrow range of frequencies around ω_n, referred to as the linewidth.

In order to understand the linewidth of the Fabry-Perot cavity, let us conceptualize the modes within it as a result of interference between waves. Homo-dyne waves, that is waves with the same frequency, will interfere constructively if they are in phase and destructively if they are not. Let us analyze a sample system, an absorption-free transparent plate of thickness t, made of a material with refractive index n_r, and partially reflective parallel surfaces. An incoming wave $E_0 = A_0 e^{i(\omega t - kx)}$, incident at angle α to the surface, will create two resultant beams: a reflected beam with intensity $A_R = A_i\sqrt{R}$ and a transmitted component $A_T = A_i\sqrt{1-R}$. A_i is the amplitude of the incoming wave at the first surface and R the reflectivity of the interface. The reflectivity $R = \frac{I_R}{I_i}$ is a function of α, the polarization of A_i, and the refractive index of the plate n_r. The refractive index of the surrounding medium is relevant when determining refracted angle, and we will assume the plate is surrounded by air, so $n_{ambient} \approxeq 1$. At the lower surfaces, the beam is scattered again, resulting in a reflected component with amplitude $A_i\sqrt{1-R}\sqrt{R}$ and a transmitted component $A_i\sqrt{1-R}\sqrt{1-R} = A_i(1-R)$. The reflected component will intersect the first surface again, splitting into two beams via reflection and transmission. This process continues, resulting in a series of parallel reflected and transmitted beams with decreasing amplitude. In general, the absolute amplitudes of the successor to the jth wave reflected at the top surface $A_{R,j+1}$ or transmitted through the bottom surface $A_{T,j+1}$ will be as follows:

$$|A_{R,j+1}| = R|A_{R,j}| \tag{3.15}$$

$$|A_{T,j+1}| = R|A_{T,j}| \tag{3.16}$$

The path difference Δl between two successive reflected waves is dependent on the angle of incidence and refractive index of the plate:

$$\Delta l = \frac{2n_r t}{\cos(\beta)} - 2t\tan(\beta)\sin(\alpha) \tag{3.17}$$

where β is the refracted angle inside the plate. The incident and refracted angles are connected via Snell's law, $\sin(\alpha) = n_r \sin(\beta)$ and Eq. 3.17 simplifies to:

$$\Delta l = 2n_r t\cos(\beta) = 2n_r t\sqrt{1-\sin^2(\beta)} \tag{3.18}$$

The phase difference φ as a result of the path difference Δl is equal to:

$$\varphi = \frac{2\pi\Delta l}{\lambda} + \Delta\varphi \tag{3.19}$$

$\Delta\varphi$ accounts for any phase changes at the plate surface. For example, if the ambient refractive index is $< n_r$ and $n_r > 1$, the reflected wave will undergo a phase change of π when getting reflected at the top surface while moving from the ambient medium with low refractive index into the higher refractive index plate. At the bottom surface, the phase change would be 0 for the reflected wave.
The total amplitude of the reflected wave A_R is a summation over all reflected wave components, $A_{R,j}$, including the phase-shifts $\Delta\varphi_i = (j-1)\pi$:

$$A_R = \sum_{j=1}^{N} A_j e^{i(j-1)\pi\varphi} \tag{3.20}$$

$$= -\sqrt{R}A_0 + \sqrt{R}A_0(1-R)e^{i\varphi} + \sum_{j=3}^{N} A_j e^{i(j-1)\varphi} \tag{3.21}$$

$$= -\sqrt{R}A_0 \left[1 - (1-R)e^{i\pi} \sum_{j=0}^{N-2} R^j e^{ij\varphi} \right] \tag{3.22}$$

If A_i is incident at $\alpha \approxeq 0$ and the extent of the plate is much larger than the incident beam, so there are no diffraction losses, we can assume a near-infinite number of reflections, $N \to \infty$. Eq. 3.22 then resembles the geometric series and we can use its limit as $N \to \infty$ [104]:

$$\lim_{N\to\infty} 1 - (1-R)e^{i\pi} \sum_{j=0}^{N-2} (Re^{i\varphi})^j = \frac{1-e^{i\varphi}}{1-Re^{i\varphi}} \tag{3.23}$$

$$A_R = -\sqrt{R}A_0 \frac{1-e^{i\varphi}}{1-Re^{i\varphi}} \tag{3.24}$$

The intensities of the reflected and transmitted waves I_R and I_T are then:

$$I_R = A_R^* A_R = I_0 R \frac{4\sin^2(\frac{\varphi}{2})}{(1-R)^2 + 4R\sin^2(\frac{\varphi}{2})} \tag{3.25}$$

$$I_T = A_T^* A_T = I_0 \frac{(1-R)^2}{(1-R)^2 + 4R\sin^2(\frac{\varphi}{2})} \tag{3.26}$$

With the incident intensity $I_0 = c\epsilon_0 |A_0|^2$. We used the trigonometric identities $e^{i\varphi} = \cos(\varphi) + i\sin(\varphi)$ and $\sin(2\varphi) = 2\sin(\varphi)\cos(\varphi)$ [49]. The two expressions in Eq. 3.26 are known as the Airy formulas and they are often stated using the coefficient of finesse

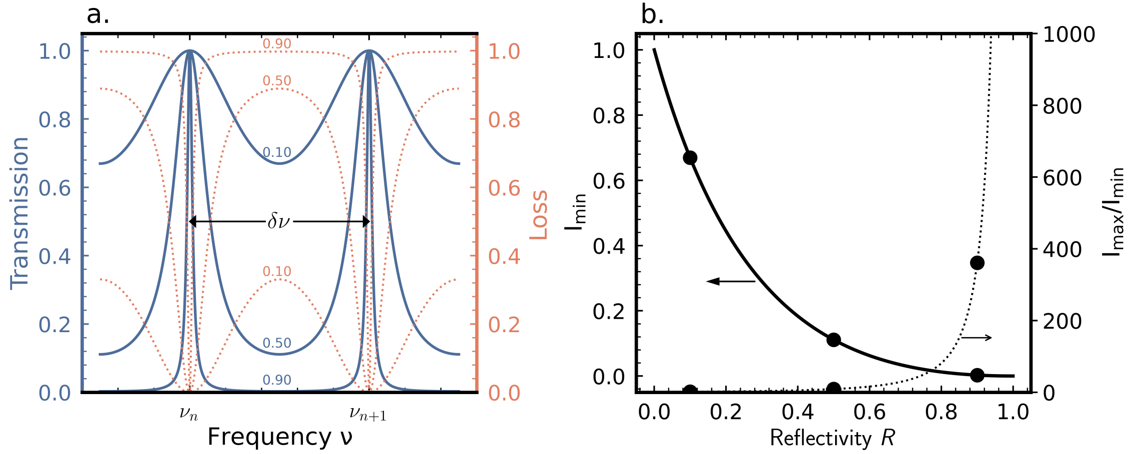

Figure 3.3: **a.** Transmission and loss spectrum for a parallel plate Fabry-Perot resonator. The fractions indicate the interface reflectivity. Shown is also the free spectral range $\delta\nu$ between the two adjacent mode peaks. **b.** The minimum intensity in the resonator I_{min} and the ratio between on peak and off peak intensities I_{max}/I_{min} as a function of interface reflectivity R.

$F = \frac{4R}{(1-R)^2}$ of a given resonator rather than its reflectivity:

$$I_R = I_0 \frac{F \sin^2(\frac{\varphi}{2})}{1 + F \sin^2(\frac{\varphi}{2})} \tag{3.27}$$

$$I_T = I_0 \frac{1}{1 + F \sin^2(\frac{\varphi}{2})} \tag{3.28}$$

The result of this is a set of peaks in the transmitted intensity I_R and a set of troughs in the reflected intensity I_T. The higher the magnitude of F due to higher interface reflectivity, the narrower these peaks will be in terms of φ. It also affects the minima between adjacent resonance peaks, as the interference condition becomes more strict and therefore destructive interference more dominant as F increases:

$$I_{min} = \frac{1}{1+F} = \left(\frac{1-R}{1+R}\right)^2 \tag{3.29}$$

Translating these results into the realm of laser resonators, the plate of thickness t becomes a cavity of length L, and the transmitted and reflected waves become the viable cavity lasing modes and the resonator's loss spectrum, respectively.

The resulting spectral mode structure in a parallel plate resonator is shown in Fig. 3.3a. It shows the light distribution and loss spectrum for a given resonator for different interface reflectivities R. For an idealized, absorption-free resonator with no surface reflectivity, there is no loss at any frequency. However, as the reflectivity increases, equivalent to increasing the refractive index n_r within the cavity, the spectral mode structure emerges.

Regions of destructive interference result in high losses as light is coupled out of the cavity. Regions of constructive interference, located at ν_n and ν_{n+1} in Fig. 3.3a, appear and then narrow as more light is reflected at the interfaces. In order to ensure lasing, the loss contrast between modal frequencies and intermodal regions needs to be strong enough to suppress the spontaneous emission into intermodal parts of the spectrum. If not suppressed, this emission can in turn get amplified by the gain medium. Since this amplification will reduce the degree of population inversion, amplification of intermodal light will reduce the gain at the desirable modal frequencies and is therefore an optical loss mechanism in a lasing device. This contrast can be quantified using the quotient of the intensity of the loss-less regions of the spectrum and the high loss regions, $\frac{I_{max}}{I_{min}}$, plotted as a function of reflectivity in Fig. 3.3b. As the reflectivity increases, the intensity of light between mode peaks I_{min} decreases, and the ratio $\frac{I_{max}}{I_{min}}$ increases. The magnitude of the contrast necessary to achieve lasing depends on the shape of the gain and desired lasing spectrum. A higher contrast will result in a better performing laser in almost all aspects: reduced threshold current, higher efficiencies, reduced emission linewidths, and reduced intensity noise. It therefore not an uncommon practice to add anti-reflective facet coatings that maximize the reflectivity in the operating wavelength range of the laser. These coatings can also act as mode selective elements within the cavity [46].

The spacing between resonator modes $\delta\nu$ is schematically illustrated in Fig. 3.3a. Since the path difference between ν_n and ν_{n+1} is constant, the spacing between modes, referred to as the free spectral range $\delta\nu$ of a resonator, is also a constant. Using the path difference Δl, we can state:

$$\delta\nu = \frac{c}{\Delta l} = \frac{c}{2L\sqrt{n_g^2 - \sin^2(\alpha)}} \tag{3.30}$$

where n_g is the group index, which is equivalent to the refractive index in a dispersion-free medium. For the parallel interface Fabry-Perot cavity, $\alpha = 0$, and the expression for the free spectral range reduces to:

$$|\delta\nu| = \frac{c}{2n_g L} \tag{3.31}$$

Note the dependence on the cavity length L is highly relevant: if we recall the condition for wavelength multiplexing, certain channel spacings were required. This is the first reminder, how ideally, a laser design keeps its final application throughout the development process. A common method for stating the width of a broadened line is its width at half its maximum intensity, referred to as full-width half-maximum (FWHM). In the FWHM of a peak as a result of multi-beam interference in phase is $\frac{4}{\sqrt{F}}$ for $R \approxeq 1$, from which we can derive the FWHM in frequency units $\Delta\nu$ as follows:

$$\Delta\nu = \frac{4}{\sqrt{F}}\frac{\delta\nu}{2\pi} = \frac{c}{2\pi n_g L}\frac{1-R}{\sqrt{R}} \tag{3.32}$$

The ratio between the resonator linewidth $\Delta\nu$ and free spectral range $\delta\nu$ is often referred to as the finesse $\mathbb{F}$, and reduces as follows using Eq. 3.32:

$$\mathbb{F} = \frac{\delta\nu}{\Delta\nu} = \frac{\pi\sqrt{R}}{1-R} = \frac{\pi\sqrt{F}}{2} \tag{3.33}$$

This equation varies from the exact finesse of an non-ideal resonator when absorption is included, but only slightly in the limit of $R \to 0$. Interested readers are referred to the work by Suter and Dietiker [105].
So far we have assumed perfectly flat and entirely parallel aligned surfaces defining the ends of the cavity. In reality, imperfections and misalignment between the two surfaces defining a cavity will result in a reduction of the finesse compared to the finesse calculated from reflectivity alone. The total finesse for a resonator can therefore be approximated as follows:

$$\frac{1}{\mathbb{F}^2} = \sum_i \frac{1}{\mathbb{F}_i^2} \tag{3.34}$$

where $\mathbb{F}_i^2$ are the finesse due to the reflectivity, surface flatness, surface alignment, and other properties of the cavity affecting the wave phase. The resulting broadening of the interference peak can be used to associate a finesse. Other than facet reflectivity, the other non-negligible contributions to the overall finesse in a monolithic Fabry-Perot cavity are the facet flatness and the relative facet alignment, as well as diffraction losses [49]. For flatness and alignment we can use the variation from the average flatness, Δs, to estimate the resulting cavity finesse:

$$\mathbb{F}_{flat} = \frac{2\lambda}{\Delta s} \tag{3.35}$$

Usually the flatness is quoted in $\Delta s/\lambda$. The surface roughness $\Delta s_R/\lambda$ has a magnitude below 10^{-3} for high quality monolithic cavities, as cleaving produces facets with near atomic flatness in most monocrystalline semiconductors [106, 107]. The path difference due to facet misalignment by an angle θ, Δs_θ is a function of the wedge between them across the extent of the beam. Assuming we have a circular aperture with diameter a, the path difference between the centre and edge of the aperture is then:

$$\Delta s_\theta = \cos(\theta) a \tag{3.36}$$

Since the monolithic laser diodes of this work are cleaved along crystallographic planes, the facet misalignment is near negligible. More important are diffractive losses: however, these are highly dependent on the design of the cavity and the resulting aperture as well as the lateral shape of the mode [49]. We will therefore return to these losses in the next section when we derive the spatial mode shape perpendicular to the axis of the resonator.

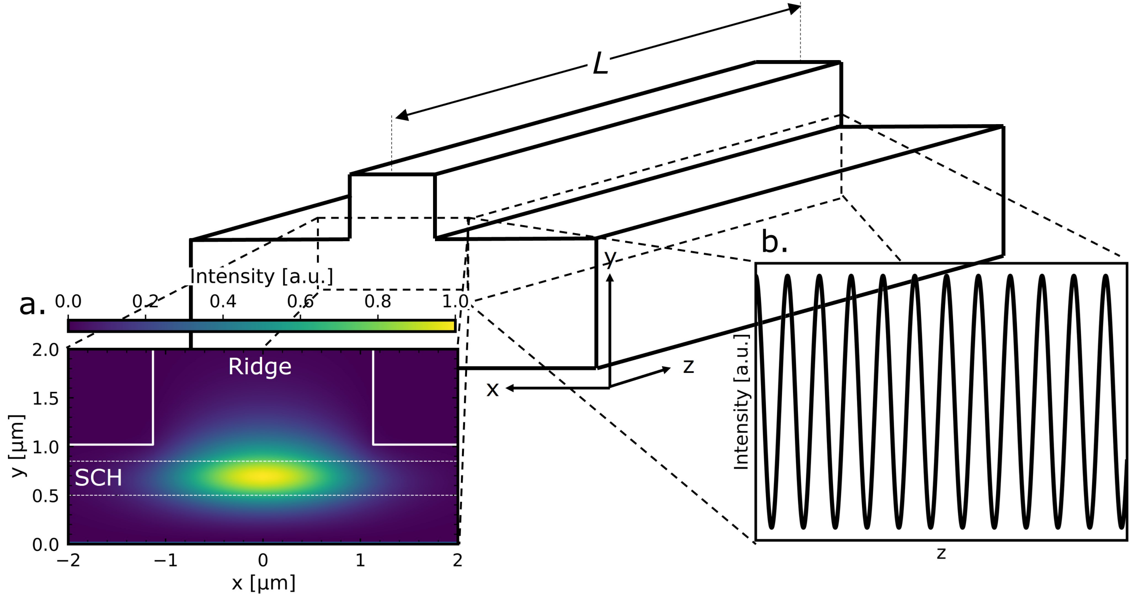

Figure 3.4: Spatial mode shape **a.** perpendicular and **b.** parallel to the cavity axis for a ridge waveguide Fabry-Perot cavity.

Spatial mode shape

For a Fabry-Perot cavity, the mode shape along the cavity axis is defined by the wavelength, producing a series of nodes and anti-nodes terminating at the cavity facets. This is the standing wave condition we arrived at in Eq. 3.5 and Eq. 3.7. For the semiconductor cavities in this work, the length of the cavity L is significantly greater than its height and width. It is therefore convenient to separate the modes into longitudinal modes along the length of the cavity axis, and lateral modes in the plane perpendicular to the cavity.
The lateral shape of the mode is defined by diffraction losses, which are dependent on the aperture. For a starting spatially uniform plane wave, successive passes through the resonator will eventually result in a non-uniform field distribution. Let us assume we have a cavity axis along $\hat{z}$, which places the lateral mode shape $A(x, y)$ in the xy-plane. For the plane mirror Fabry-Perot cavity, we can represent the path of the beam for multiple passes as a series of circular apertures with diameter a through which the beam has to pass N times. The beam pattern after the Nth pass is then the beam pattern after the previous pass, $N-1$, modified by the diffraction due to the aperture:

$$A_N(x, y) = -\frac{i}{\lambda}\int\int A_{N-1}(x', y')\frac{e^{-ik\rho}}{\rho}cos(\zeta)dx'dy' \tag{3.37}$$

Here λ and k are the wavelength and wavenumber of the diffracted wave, $\rho = L^2 + (x - x')^2 + (y - y')^2$, and $cos(\zeta) = L/\rho$. After a number of passes, we reach an equilibrium, where the beam pattern between successive apertures only varies by a constant, diffraction

loss dependent factor:

$$A_N(x,y) = CA_{N-1}(x,y) \tag{3.38}$$

with the amplitude attenuation factor C:

$$C = \sqrt{1-\gamma_D}e^{i\phi} \tag{3.39}$$

ϕ is the phase shift due to diffraction and γ_D is the fractional energy loss due to diffraction, which can be estimated using the Fresnel number $N_{Fresnel}$ for a plane mirror resonator [49]:

$$N_{Fresnel} = \frac{a^2}{\lambda L} \tag{3.40}$$

Here a is the diameter of the aperture, and L is the length of the cavity. The stationary amplitude in the plane is then:

$$A(x,y) = -\frac{i}{\lambda\sqrt{1-\gamma_D}e^{i\phi}} \int\int A(x',y')\frac{e^{-ik\rho}}{\rho}cos(\zeta)dx'dy' \tag{3.41}$$

This equation has no analytical solutions, so several approximations exist [54, 108]. For approximately quadratic mirrors of area $4a^2$, it can be split into integrals along both x and y, if $a << (L^3/\lambda)^{1/4}$ holds [49]. For a monolithic cavity similar to the one used in this work, $a \approx 10$ µm and $L = 1500$ µm, designed for operation at $\lambda = 1550$ nm, this approximation holds. The solutions to Eq. 3.41 can then be represented by Hermite-Gaussian functions [108]:

$$A_{mp}(x,y,z) = C^* H_m(x^*)H_p(y^*)e^{-r^2/w^2(z)}e^{-i\phi(z,r,R)} \tag{3.42}$$

The solutions are the product of Hermite polynomials H_m and H_p of mth and pth order, respectively, and a Gaussian function e^{-r^2/w^2} multiplied by a phase factor, with $r^2 = x^2 + y^2$ The in-plane coordinates x and y are modified by the radial intensity distribution measure $w^2(z)$:

$$w^2(z) = \frac{\lambda L}{2\pi}\left[1 + \frac{4z}{L^2}\right] \tag{3.43}$$

$$x^* = \frac{\sqrt{2}x}{w} \tag{3.44}$$

$$y^* = \frac{\sqrt{2}y}{w} \tag{3.45}$$

The resulting field distributions can be found in various works, such as Fig. 18 in Fox and Li [108] or Demtröder Fig. 5.9 [49]. The modes are designated as transverse electric standing waves (TE$_{mp}$), with the mode indices m and p representing the number of nodes along x and y. The fundamental mode for rectangular waveguides is the mode for which

$m = 1$ and $p = 0$, so TE_{10}. Most conventional semiconductor laser diodes are designed to have low loss for the fundamental lateral mode and high loss for all higher order modes. Similar to the longitudinal modes concentrating the energy from the gain medium into a small set of modes in the emission spectrum, this design philosophy concentrates the light emitted from the cavity into a single spatial mode that can be designed to ensure high coupling efficiencies with other photonic components [46]. The intensity distribution of the fundamental mode I_{00} is proportional to $A_{00}A_{00}^*$, and for $m = p = 0$ the Hermite polynomials along each dimension simplify to 1, leaving us with a Gaussian beam shape:

$$I_{10}(x, y, z) = I_0 e^{-2r^2/w^2(z)} \tag{3.46}$$

This will be the emission profile for our semiconductor laser, even though higher order modes are possible if the loss for several lateral modes is similar.

3.3 Gain media

In its most general definition, a gain medium can be any material which has two or more states connected via an optical transition that is more likely than non-radiative decay. Due to the requirement of efficient coupling with the electric field, these states are electronic states which are coupled via electric multipole transitions. One example are the electron and hole band states in a semiconductor, which were discussed in the previous chapter. Other systems are conceivable and see extensive use as well, and Tab. 3.3.1 provides an overview of common laser gain media. As we saw in the discussion of the ideal two level system (Ch. 2.3.1), the likelihood of an optical transition is proportional to the inversion factor, i.e. the system shift from equilibrium to a condition where the excited state has a higher population than the ground state, or $f_f > f_i$. This condition is referred to as population inversion and a technologically relevant system needs to be capable of maintaining population inversion easily. In the semiconductor example this would mean a conduction band state filled with electrons and a coupled valence band state occupied by holes. If a given material has a sufficiently slow non-radiative or parasitic radiative decay of the excited state, either due to a small number of available decay paths or by virtue of each available path being extremely slow, it will be comparatively easy to maintain the population inversion and ensure that there are sufficient excited states available for light amplification. If there are highly efficient parasitic decay paths, with decay rates greater than the optical transition rates, maintaining the excited state and thereby consistent light output from the gain medium will be impossible.
We will use a simple rate model to get a basic understanding of gain before we dive into the underlying principles that affect gain, and especially the gain in semiconductor

nanostructures. Presume we have a semiconductor laser with a single transition between a conduction and a valence band state. Carriers in the conduction band will recombine either radiatively while emitting a photon, via spontaneous or stimulated emission, or non-radiatively through one of the many mechanisms discussed in Ch. 2. The number of carriers in the conduction band state N_c is a measure for the available excited state population which is capable of further light amplification. The number of photons in a single optical mode matching the transition energy between the conduction and valence band state is N_{ph}. The rate of change in both of these populations is then [109]:

$$\frac{dN_c}{dt} = \frac{J_{bias}}{qd_{gain}} - \frac{N_c}{\tau_{tot}} - g(N_c)N_{ph} \tag{3.47}$$

$$\frac{dN_{ph}}{dt} = g(N_c)N_{ph} - \frac{N_{ph}}{t_p} + \frac{\beta N_c}{\tau_c} \tag{3.48}$$

J_{bias} is the bias current density, q is the elementary charge, d_{gain} is the thickness of the gain medium, τ_{tot} and t_p are the carrier and photon lifetimes, respectively, and β is the fraction of the spontaneous emission that is coupled into this specific optical mode. We will encounter most of these parameters again when discussing the lasing condition. Note that τ_{tot} is the total carrier lifetime in this simplistic model, so it includes both radiative and non-radiative processes. We will discuss the different processes' contribution to this lifetime when examining the Einstein coefficients for an idealized two level system. The most important contributions to Eq. 3.48 from the gain medium are τ_c and $g(N_c)$. Both are strongly material and device dependent, and take some effort to extract experimentally. There are various forms of the gain function $g(N_c)$, as different material systems will have vastly different broadening and optical interaction characteristics [49]. We will provide a brief overview over the different classes of materials that have seen usage as gain media, discuss some general characteristics of an optical medium such as dispersion and its Einstein coefficients, and finalize our discussion by examining the gain and other laser relevant characteristics of nanostructure semiconductor lasers.

3.3.1 Materials for gain media

Due to the nature of condensed matter, any potential host for the idealized two level system will be subject to a myriad of perturbations, resulting in a gain medium featuring a number of levels far greater than the idealized two discussed previously. Real-world gain media feature a set of optically active transitions, which are either spaced sufficiently far apart that they can be excited selectively or have low enough state densities that population inversion can be achieved on multiple transitions concurrently. Generally, gain media will have properties that combine both characteristics to varying degrees.

Laser type	**Examples**	**Pump method**	**Advantages**
Gas	He-Ne, Ar, CO_2	Electrical discharge	High damage threshold
Crystals	Nd:YAG, Ti:sapphire, Er-doped fiber	Optical absorption	Low background absorption and high gain [110]
Ceramic	Nd:YAG	Optical absorption	Similar to crystals, but lower cost [111]
Free electron	LCLS@SLAC, FLASH	High energy electron beam	Access to extreme IR and UV [112]
Dye	Rhodamine 6G, Fluorescein	Optical absorption	Wavelength range flexibility [111]
Diode	GaN, InGaAsP, AlGaAs	Carrier injection	Cost, size, and photonic integration
Nuclear	OKUYaN, IKAR	α-particles; neutron collision	Access to X-ray lasing [113]

Table 3.1: Table of common gain media. *Optical absorption* refers to the absorption of light at a higher energy (shorter wavelength) than the light eventually emitted from the gain medium. Abbreviations used: Nd:YAG = neodymium-doped yttrium aluminum garnet; LCLS@SLAC = Linac Coherent Light Source @ Stanford Linear Accelerator, FLASH = Free electron laser in Hamburg

Types of gain media

There are a wide variety of materials that have been used for the purpose of amplifying light, in various physical states, ranging from gasses and plasmas (e.g. He-Ne mixtures), to liquids (e.g. dye-solutions) and solids, the latter being the most prolific source for telecommunication applications. A non-exhaustive list of gain media and their most relevant advantages and disadvantages are shown in Tab. 3.3.1. The most important aspect of each gain medium is the shape of its gain. This defines the wavelength range for which it can produce lasing emission, and determines the minimum width of optical pulses it can form. Beyond that, almost all gain media share some other common properties: relatively high quantum efficiency of the pump process to achieve reliable population inversion, transparency to reduce the overall optical losses, chemical stability to avoid medium degradation over time, and a high optical damage threshold to handle the intense concentration of the electromagnetic field within the cavity [111]. The high field strengths will also result in non-linear optical effects within the cavity, so a material's optical dispersion and the higher order susceptibilities are important factors for consideration [57, 114]. For pulsed lasers, the gain recovery time also becomes relevant [115, 116].

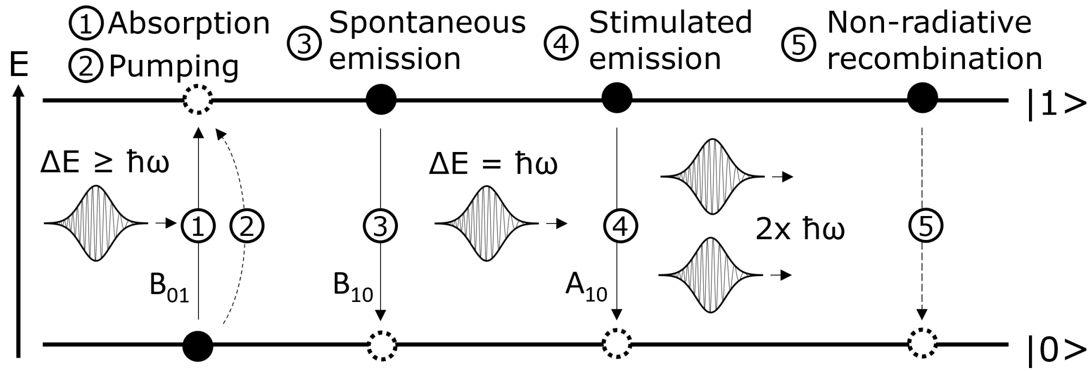

Figure 3.5: Relevant absorption and recombination processes inside a two-level system. B_{10}, B_{01}, and A_{10} denote the Einstein coefficients for the radiative processes.

3.3.2 Einstein coefficients

There are several processes in dynamic equilibrium in each lasing device. They are outlined in Fig. 3.5. In order to maintain conditions necessary for lasing, the system needs to be in population inversion, so a greater population of electrons in an excited state $|1\rangle$ than in the ground state $|0\rangle$. This is achieved through pumping, shifting electrons from the ground into the excited state. The addition of this potential energy is most commonly achieved optically via absorption of higher energy light or electrically through injection of carriers, even though other methods are possible (see Tab. 3.3.1). For semiconductor diode lasers, electrical injection creates a population of electrons in conduction band states and holes in the valence band that are available for radiative recombination processes. Given the presence of the ground state, every excited state will eventually decay into the ground state spontaneously. The decay time is proportional to the coupling between the states. If the states are coupled via the electronic multipole operator, the energy difference between excited and ground state can be released in the form of light, a photon with energy $\hbar\omega = \Delta E$. This is the first of the two fundamental radiative recombination processes. The other is stimulated radiative recombination, which follows a similar radiative decay from the excited state to the ground state, but stimulated by an incoming photon rather than occurring spontaneously. This has three important consequences: first, it allows the amplification of a light particle, providing the light amplification aspect within a lasing device. Second, the phase and wavevector of the stimulating and emitted photon will be identical, resulting in coherence between the two and every subsequent photon they stimulate. This is the origin of the temporal and spatial coherence of light emitted from a laser. And lastly, this process preferentially stimulates photons with frequencies matching the stimulating photon, resulting in the necessary feedback to obtain light that originates from a small set of discrete modes rather than a continuum [49]. The last process in a

gain medium is non-radiative decay. This process is in competition with radiative decay paths and therefore represents a loss channel. The exact nature depends on the type of gain medium. For semiconductor gain media, we examined a few parasitic recombination mechanisms such as Shockley-Read-Hall and Auger recombination in the previous chapter. While strongly material and device design dependent, Auger recombination processes will generally be the dominant non-radiative loss channel in semiconductor materials at the carrier concentrations necessary for lasing operation [46]. If non-radiative decay rates are significantly faster than radiative recombination rates, achieving population inversion and thereby lasing is impossible. It is therefore necessary to understand the rates at which these transitions occur in a given system, for which one generally employs the Einstein coefficients.

The strength of an optical transition and its coupling to propagating electromagnetic modes can be quantified using the Einstein A and B coefficients. They are dependent on the the transition matrix element between the initial and final state $|i\rangle$ and $|f\rangle$, $\langle f|\,\hat{e}\hat{p}\,|i\rangle$, which we encountered first in Eq. 2.45 [29, 49]:

$$B_{if}^{(\omega)} = \frac{1}{g_i}\frac{\pi}{3\epsilon_0\hbar^2}|\langle f|\,\hat{e}\hat{p}\,|i\rangle|^2 = \frac{g_i}{g_f}B_{fi}^{(\omega)} \tag{3.49}$$

$$A_{if}(\omega) = \frac{1}{g_f}\frac{\omega^3}{3\pi^2\epsilon_0\hbar c^3}|\langle f|\,\hat{e}\hat{p}\,|i\rangle|^2 = \frac{2\omega^3 n_r^3}{\pi c^3}B_{if}^{(\omega)} \tag{3.50}$$

With the degeneracy factors for the initial and final state g_i and g_f, the refractive index of the gain medium n_r, the vacuum permeability ϵ_0, the speed of light c, and the reduced Planck coefficient $\hbar$. g_i and g_f are relevant when considering systems with multiple degenerate levels acting as the ending and starting point of an transition. In a semiconductor gain medium, this would be relevant for higher dimensional states, so transitions in bulk and QW gain media, where multiple equivalent final states can be reached from a single initial state. B_{if} and B_{fi} are referred to as the Einstein coefficients of absorption for $E_i < E_f$ and induced emission for $E_i < E_f$. A_{fi} describes the spontaneous radiative decay of an excited state into a ground state, so is commonly referred to as the Einstein coefficient of spontaneous emission. The two coefficients are correlated by the photon energy density $\rho_{ph}(\omega)$ from Eq. 3.11 divided by the number of photons at given frequency, $N_{ph}(\omega)$.

For a system in thermal equilibrium, this would relate to the total emission rate from a given set of states as follows:

$$R_{if}(\omega) = A_{if}(\omega) + B_{if}^{(\omega)}\rho_{ph}(\omega) = A_{if}(\omega)\,[1 + N_{ph}(\omega)] \tag{3.51}$$

This rate dictates the rate at which radiative recombination occurs, and thereby the maximum allowable rates for non-radiative decay mechanisms [96]. The limited radiative re-

combination rate is the reason why solid state gain media with internal crystal boundaries, such as sintered optical ceramics, took multiple decades to become viable gain media. The interfacial states at grain boundaries are efficient non-radiative recombination centres that diminish the excited state population [111].

3.3.3 The lasing condition

As mentioned previously, in order for sustained lasing to occur, photon generation must match and outpace photon loss in a given mode. From Eq. 3.51, the total rate of emission from a single two level emitter is $R_{if}(\omega)$, giving the excited state a radiative lifetime of $\tau_{if}(\omega) = \frac{1}{R_{if}(\omega)}$. These photons are emitted into a frequency range $\Delta\omega$, as the linewidth of any transition is broadened at least homogeneously as a result of de-phasing during the finite transition time [29]. If there are p potential cavity modes within $d\omega$, the spontaneous emission would be split into these modes and the total emission per emitter per mode would be $\frac{1}{p\tau_{if}(\omega_p)}$ per unit time. For stimulated emission, this is modified by the number of photons $N_{ph,n}$ already present in mode n that can stimulate further emission. The total stimulated emission into mode n is then $\frac{N_{ph,n}}{p\tau_{if}(\omega_n)}$.
We now consider the inversion factor we discussed earlier. Assuming there are N_{emit} emitters, with a fraction f_f in the upper excited state and f_i in the lower ground state. The total photon generation rate into mode n is then [54]:

$$R_{ph,n} = N_{emit}(f_f - f_i)\frac{N_{ph,n}}{p\tau_{if}(\omega_n)} \tag{3.52}$$

If the lifetime of the mode in the cavity p is t_p, with the photon loss rate $\frac{N_{ph,p}}{t_p}$, lasing starts if photon generation exceeds photon loss and the laser feedback is positive. This is the lasing condition:

$$N_{emit}(f_f - f_i)\frac{1}{p\tau_{if}(\omega_n)} > \frac{1}{t_n} \tag{3.53}$$

The disappearance of $N_{ph,p}$ indicates that lasing can occur at any photon generation rate. Since the cavity lifetime t_n is related to the quality factor via Eq. 3.14, we could alternatively use the quality factor of the cavity for mode n Q_n:

$$t_n = \frac{\omega_n}{Q_n} \tag{3.54}$$

Given the mode spacing $\delta\nu$ for a Fabry-Perot resonator and assuming the mode spacing and linewidth of the cavity resonance are much smaller than the transition linewidth, $\Delta\nu << \Delta\omega$. We can then state the mode density $p = \frac{\Delta\omega}{2\pi\delta\nu}$, and the lasing condition in a

given mode due to a single homogeneously broadened transition becomes:

$$N_{emit}(f_f - f_i)\frac{2\pi\delta\nu}{\Delta\omega\tau_{if}(\omega_n)} > \frac{1}{t_n} \tag{3.55}$$

Eq. 3.53 and 3.55 can give us some basic insight into the functionality of the device. first of all, lasing can only occur once population inversion is achieved, since otherwise $(f_f - f_i) < 0$ and the equality can not be satisfied. Additionally, increasing the resonator quality factor will reduce the threshold for lasing, as raising Q_n will increase t_n. Also, reducing the linewidth or increasing the modal spacing will generally reduce the lasing onset, since it reduces the competition between modes from a given transition. Lastly, increasing the number of emitters is only useful if the product with the population inversion $N_{emit}(f_f - f_i)$ increases. So a higher number of emitters may not be beneficial due to a lower population inversion since more carriers need to be injected to achieve a similar f_f. All of this is good intuition to carry forward when examining the different parameters that affect the overall operation of the laser.

3.3.4 Optical dispersion

All gain media will exhibit some degree of dispersion, so the refractive index varies as a function of frequency ($n_r \to n_r(\omega)$). We therefore need to differentiate between the group velocity v_g and the phase velocity v_p:

$$v_p = \frac{\omega(k)}{k} = \frac{c}{n_r(\omega)} \tag{3.56}$$

$$v_g = \frac{d\omega(k)}{dk} = \frac{c}{n_g(\omega)} \tag{3.57}$$

where $\omega(k)$ is the dispersion relation, $k = \frac{2\pi}{\lambda}$ is the wavenumber, c is the speed of light in vacuum and $n_r(\omega)$ and $n_g(\omega)$ are the real part of the refractive index and the group refractive index of the medium, respectively. For a dispersion-free medium, $\omega(k)$ is directly proportional to k and $v_p = v_g$, resulting in the envelope of a pulse and its components travelling at the same speed. If $\omega(k)$ is linearly dependent on k, but there is a non-zero offset, a wave packet envelope will travel at v_g while its individual components will travel at v_p. The wave packet will stay coherent, identical to the dispersion-free case; the pulse will experience no "chirping" where high or low frequency components will travel at different velocities and stretch the pulse. Chirping occurs if $\omega(k)$ is non-linear, which is the case for most gain media, including semiconductors [54].

3.3.5 Transition linewidths

Every transition is inherently broadened due to the finite timescale of the transition process. This will cause de-phasing, which leads to a broadening of the transition in frequency space. Since this de-phasing is identical for each emitter in a gain medium, it is referred to as *homogeneous* broadening, and the resulting linewidth is sometimes referred to as a transition's natural linewidth. The resulting lineshape around a transition frequency ω_{if} then takes a Lorentzian shape [49]:

$$I_{homo}(\omega) = I_0 \frac{1}{2\pi} \frac{\Delta\omega_{if}}{(\omega - \omega_{if})^2 + \left(\frac{\Delta\omega_{if}}{2}\right)^2} = I_0 L(\omega, \omega_{if}, \Delta\omega_{if}) \tag{3.58}$$

where $\Delta\omega_{if}$ is the full-width at half maximum and I_0 is the total intensity $\int I_{homo}(\omega) d\omega$. The strength of the de-phasing and thereby the magnitude of $\Delta\omega_{if}$ is a function of the dampening of the dipole oscillation of an emitter. Stronger dampening will result in a broader linewidths, as the difference in oscillation frequency between subsequent oscillations is greater [49]. Since every oscillator in a real material will experience some degree of dampening, natural broadening is unavoidable. Natural broadening can also be thought of as the effect of spontaneous emission: albeit small compared to the stimulated emission rate, spontaneous emission into lasing modes does occur. The emitted light alters the environment of its surroundings instantaneously, leading to a small phase jump of the optical field within the cavity. This is identical to the de-phasing described previously [117]. However, in addition to the instantaneous phase change, there is also a delayed phase change due to the change in field intensity when the photon is emitted spontaneously. The field intensity and phase are coupled through the carrier density, which alters both the real and imaginary parts of the refractive index [58, 59]. The spontaneous emission displaces the system from its steady-state, leading to relaxation oscillations which cause a temporary change in the gain $\Delta g(t)$ proportional to the change in the imaginary part of the refractive index $\Delta\kappa(t)$ from its steady-state value:

$$\Delta g(t) = -\frac{2\omega}{c} \Delta\kappa(t) \tag{3.59}$$

The ratio between the total change in the real and imaginary parts of the refractive index $\Delta n_r(t)$ during the spontaneous emission process can be used to quantify the broadening due to the phase delay [117]:

$$\alpha_H = \frac{\Delta\kappa}{\Delta n_r} \tag{3.60}$$

The change in the refractive index immediately after spontaneous emission and resulting phase delay cause further significant homogeneous broadening. The final linewidth of the transition will then be Lorentzian in shape, but broadened by the linewidth enhancement

factor $1+\alpha_H^2$ [117]. The value for the α factor is usually around 5 for a typical semiconducting laser, but smaller and sometimes even negative for QD and QDash lasers. Apart from the often undesirable broadening of a continuous laser's linewidth, this broadening also lowers the efficiency of some non-linear effects, such as four-wave mixing, which in turns reduces the mode-locking stability. Additionally, it drives other non-linear effects, such as giant Kerr non-linearities and leads to self-frequency modulation [118].
In addition to the homogeneous broadening, there are other broadening mechanisms that affect each emitter differently, and are therefore referred to as *inhomogeneous* broadening mechanisms. For gas lasers, this would be something like Doppler broadening based on the velocity distribution of emitting molecules [49]. In QD and QDash-based lasers, the dominant inhomogeneous broadening mechanism is the size variation across the population of dots or dashes [90, 92, 119]. As discussed in Ch. 2, these nanostructures self-assemble under the certain growth conditions. However, the exact conditions such as temperature and availability of reactants vary on the length scale of the average laser, leading to dots and dashes with slight dimensional variability. Since a nanostructure's dimensions, especially its height, strongly affect its sub-band positions, the inevitable variation in size across the ensemble of all nanostructures within the laser will lead to transitions in the vicinity of the average transition energies [92, 120]. The impact of size fluctuations is discussed in more detail in 2.5.4. While beneficial in applications where an extremely broad gain spectrum is useful, such as optical amplifiers or ultrashort pulsed lasers, size broadening negatively affects the modulation bandwidth of QD and QDash lasers, due to decreased differential gain [119]. Size broadening can be treated as an inhomogeneous broadening mechanism, since each nanostructure is affected differently. The resulting line shape is generally Gaussian, rather than the Lorentzian line profile observed for homogeneous broadening [90]:

$$I_{inhomo}(\omega) = \frac{1}{\sqrt{2\pi}\delta} e^{-\frac{1}{2\delta^2}\left(\frac{\omega-\omega_{if}}{\omega_{if}}\right)^2} \tag{3.61}$$

where δ is the variation in energy due to the size fluctuation, and ω_{if} represents the average transition frequency for an ensemble of emitters. The order of magnitude for $\hbar\delta$ is generally 10s of meV, depending on whether or not the system in question features QDs or QDashes [90, 92]. This means it is generally much broader than the natural linewidth.

3.3.6 Gain saturation

The relationship between the ensemble of emitters determines more than just the linewidth, however: a gain medium pumped to above threshold will experience gain saturation. The saturation occurs due to the positive feedback between increased photon occupation of a mode and the stimulated emission into it. If the gain medium is now pumped harder, the

additional carriers will be converted into photons immediately rather than increasing the gain any further. If a gain medium only features a single type of homogeneously broadened emitter, this will result in a uniform depression of the gain across the entire spectrum. The gain is essentially pinned at the lasing threshold value, something referred to as gain saturation [49]. The resulting, saturated homogeneous gain $g_{sat}^{homo}(\omega)$ can be calculated using the unsaturated gain function $g(\omega)$:

$$g_{sat}^{homo}(\omega) = g(\omega)\frac{1}{1+\beta} \tag{3.62}$$

Here β is a parameter reflecting the degree of mode competition in the device.
For inhomogeneously broadened gain media, such as QDs and QDashes, not all emitters can participate in a given transition wavelength. The pinning of the gain is therefore limited to the extent of the homogeneously broadened linewidth of a given sub-ensemble of emitters, $\delta\omega$. Other transitions sufficiently far removed from the first transition experience no saturation effect. The resulting gain profile is shown in Fig. 3.8a, where the dips in the curve labelled IV. indicate the parts of the spectrum that are pinned. The width of these dips reflects the homogeneously broadened transition linewidth, which grows with increased bias (Eq. 3.58). Eventually, neighbouring sub-ensembles are broad enough to contribute to nearby resonator modes, resulting in an increase in gain. However, this is balanced by the mode competition between the modes now coupled together by homogeneous broadening, resulting in a overall reduction of the gain that is reduced compared to an exclusively homogeneous gain medium:

$$g_{sat}^{inhomo}(\omega) = g(\omega)\frac{\sqrt{1+\beta}}{1+\beta} \tag{3.63}$$

We will discuss the specific gain functions used in this work in more detail in Ch. 4, where we will also discuss the gain saturation parameters used.

3.4 Semiconductor diode lasers

The lasers we are concerned with in this work are semiconductor diode lasers, which means they are electrically injected lasing devices with a gain medium based on bulk or nanostructured semiconductor materials. All diode lasers share some fundamental characteristics irrespective of the specific design and dimensionality of the gain region, which we will briefly examine here.

3.4.1 Waveguide design

Semiconductor lasers have several intrinsic advantages over other laser designs in terms of ease of fabrication. As discussed earlier, the large refractive index difference between the laser and the surrounding medium will result in comparatively high facet reflectivities even for bare, uncoated facets. Additionally, the cleaving dynamics lead to smooth facets. One more advantage is their refractive index: as it is significantly higher than air, optical modes originating within a semiconductor material will remain within the semiconductor material through index guiding [121]. Semiconductor stacks are therefore their own waveguides as well.

One of the most basic designs for a semiconductor laser is the stripe laser, which is a stack of semiconducting layers with a metallic contact down the length of the stack. The stack is separated into a n- and a p-doped half, separated by an undoped, intrinsic region, usually the SCH, between them. The stripe laser, like most laser diodes, is therefore a pin-diode. The semiconductor stack is cleaved along the growth direction to create a cavity, with the cleaved facets acting as the cavity mirrors. Carriers are injected below the stripe, leading to higher carrier concentrations in this region. Since gain increases with carrier density, lasing will first start in the region below the stripe.

Stripe lasers are also referred to as gain guided lasers, as there is no confinement along

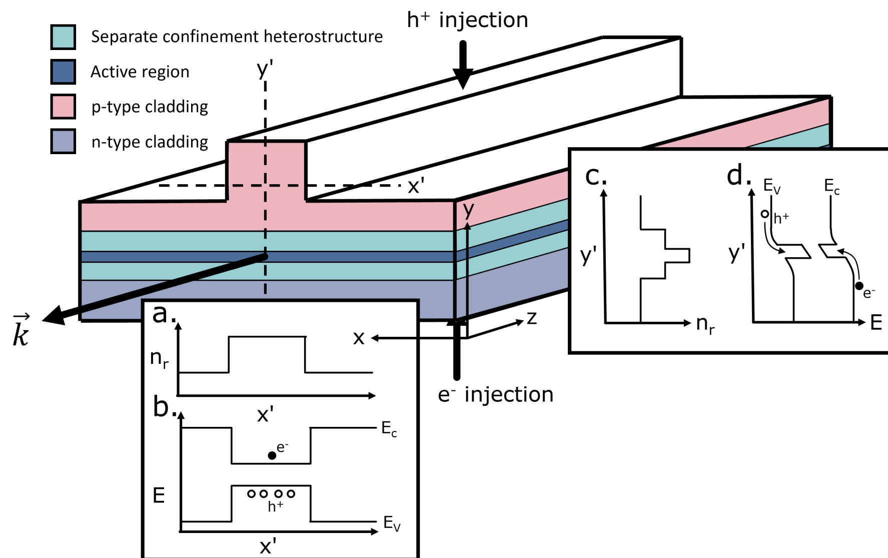

Figure 3.6: Basic layout for a ridge waveguide laser diode, including cross-sections of the **a.** and **c.** refractive index and **b.** and **d.** band structure.

x and the optical mode is only confined by the decrease in local gain as the mode extends outwards from below the stripe. While easy to fabricate, this confinement method has several drawbacks: significant lateral carrier leakage reduces the injection efficiency, and

thereby increases the threshold current while reducing the slope efficiency of the devices. It can also lead to higher order lateral modes achieving positive gain [50]. Modern semiconductor lasers therefore generally exhibit some form of lateral gain guiding within the waveguide. The most effective method is by reducing the active region laterally, removing most of the active region and leaving only the material below the top contact. The etched area is then re-grown using a material with a lower refractive index, generally another semiconductor with a larger band gap to obtain carrier confinement in addition to the optical confinement. Due to the enclosed nature of the active region, lasers featuring the active region etching and regrowth are referred to as buried heterostructure lasers. They improve on the gain guided stripe laser in all aspects: apart from lower threshold currents and higher efficiencies, they generally produce more symmetric lateral mode shapes, free of higher order modes. They are also less susceptible to temperature affecting their performance and capable of outputting significantly higher power than comparable striped devices. Unfortunately, they are also rather complex to fabricate due to the etch and growth steps [122]. A compromise between the two designs is the ridge waveguide laser, schematically illustrated in Fig. 3.6. It features an isolated ridge of material that works to both confine the mode and injected carriers laterally, as shown by the profile of the refractive index and band structure along x' in Fig. 3.6a. and b. These devices can be grown in a single process and only require etching afterwards to define the ridge. This is more economical to process due the elimination of the complex regrowth step over a non-planar substrate leading to overall higher fabrication yields [123]. The performance of a ridge waveguide laser will generally be slightly worse than a comparable buried heterostructure device in nearly all quantifiable metrics [123–125]. However, the added complexity of carrier leakage and parasitic capacitance in the regrown material can lead to significant underperformance in buried heterostructures [126].

The device shown in Fig. 3.6 shows a common diode laser design pattern. The design starts with n-type cladding at the bottom, since these devices are commonly grown on n-type substrates due to their higher conductivity, making thicker layers less punishing in terms of series resistance losses. The next layer in the semiconductor stack is the separate confinement heterostructure (SCH). It has the role of confining the mode vertically, so its refractive index should be greater than the indices of the surrounding cladding. These layers are also referred to as optical confinement layers (OCLs). Additionally, the band gap within the SCH should be smaller than the band gap in the cladding layers to confine carriers in the vicinity of the active region and prevent carrier leakage across the active region. Nestled within this confinement structure lies the active region. The band edge diagram in Fig. 3.6d. shows a double heterostructure region as an example, but this could just as easily be a MQW, QD or QDash gain region. Ideally we would like most of the carriers injected into the device to enter this region and recombine here via stimu-

lated radiative emission since the optical transitions in this region are designed to couple to the optical modes of the cavity. The relative position of the active region within the separate confinement heterostructure depends on the desired mode shape and absolute gain of the device. Since p-doped semiconductors will generally have higher scattering coefficients than n-doped material, it is desirable to minimize the overlap of the optical mode with the p-type cladding to reduce optical losses. Additionally, the ridge etching process can lead to ridge sidewall roughness, which increases scattering and thereby losses further [127, 128]. At the same time, increasing the distance between the bottom of the ridge and the gain region will reduce the degree of lateral confinement. This can lead to undesirable lateral mode shapes, and even result in higher order lateral modes achieving positive overall gain for active regions with very high gain. Larger separation also increases the distance between the p-side contact and the active region, introducing further resistive loss. The correct placement of the active region is therefore a careful trade-off between different characteristics, and also highly application specific. We examine the impact of the separation between ridge and active region for our devices in 6.2.7. The entire device is covered in a layer of an insulating dielectric material followed by a metallization that acts to both confine the mode and act as the top contact through a small window in the dielectric at the top of the ridge. This is the positive top contact for hole injection into the device. The bottom, electron injecting contact can be achieved via another bottom-up metallization step or by placing the device on a conductive medium.

3.4.2 Voltage, power, and current characteristics

The general behaviour of a laser diode in terms of the relationship between voltage, current, and optical power is shown in Fig. 3.7. Please note that this is only a qualitative illustration and the relationships between the bias range and on-set of different regimes will be different in a real device. Also, the light power output prior to threshold is indicated much larger than it would be in a real device. This graphic is only intended to highlight the different operating regimes of a laser diode without any meaningful quantitative relationships.

The most basic performance parameters are a laser's diode voltage V_d , resistance R , threshold current I_{th} , and slope efficiency n_d . They can be extracted from the current-voltage (IV) and laser power-current (LI) characteristics. For the purpose of this work, the stated diode voltage V_d is the intercept of the linear fit to the high forward bias regime of the IV curve, while the resistance R is its inverse slope. Similarly, we extract the threshold current I_{th} from the linear fit to the linear, or small signal, regime of the LI curve, and use its slope as the quoted slope efficiency n_d of the device. Note that we are generally

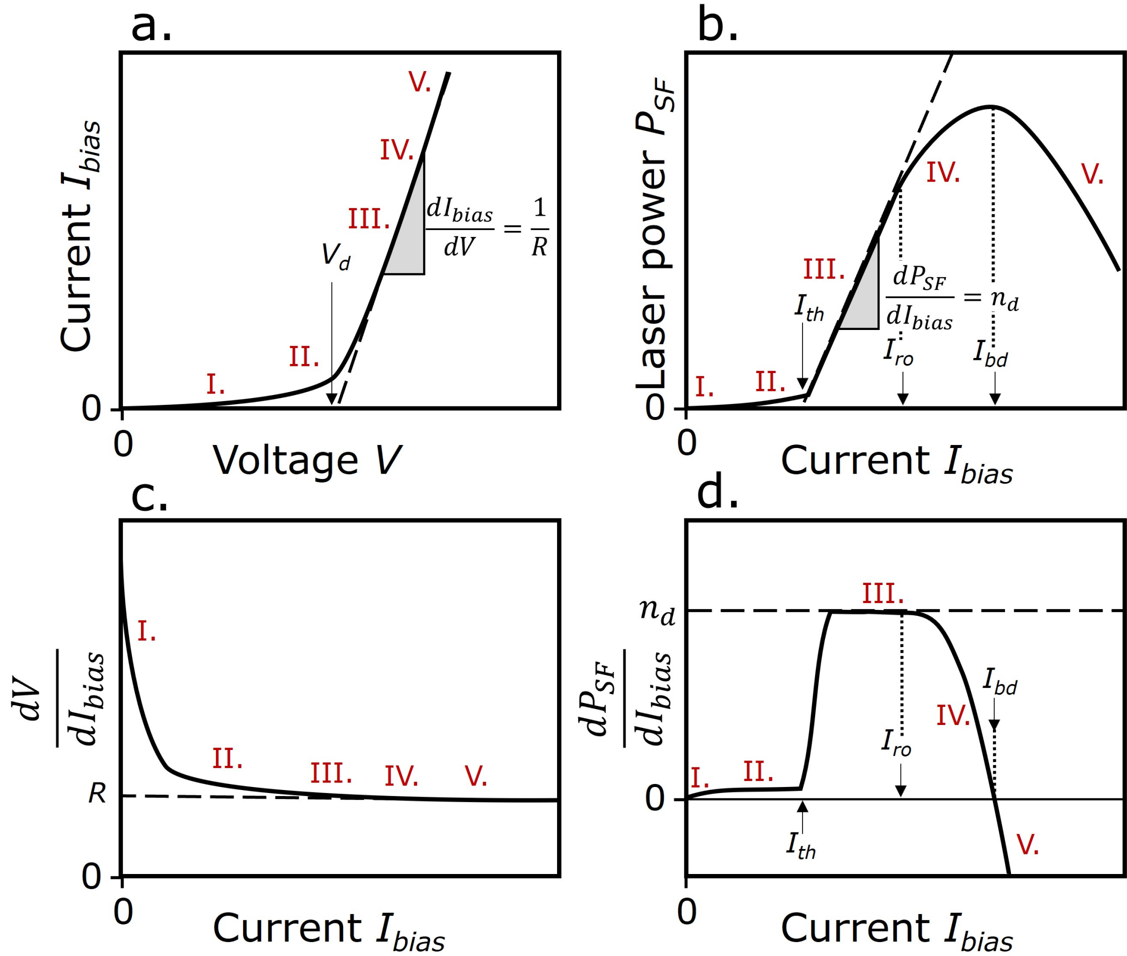

Figure 3.7: Schematic **a.** current-voltage (IV) and **b.** laser power-current (LI) characteristic for a diode laser. The diode voltage V_d and the threshold current I_{th} are indicated. The dashed lines illustrate the fit to linear sections of the characteristics which are used to extract the resistance R and slope efficiency n_d . **c.** and **d.** show the derivative with respect to current of the two characteristics. Roman numerals indicate the different operating regimes of a diode laser and are discussed in the text.

measuring the single facet laser power of a device, rather than the total power emitted. Since all devices tested in this work featured as-cleaved, uncoated facets, the emission should be perfectly symmetric between both facets. Indeed, measuring the power from both facets to verify this assumption showed negligible facet variability within the small subset of devices tested in this manner.

There are five different laser operating regimes we identify for each plot in Fig. 3.7. While some are clearly delineated by step-like changes in certain parameters, the transition between a few is a more continuous process with less clear boundaries. The first regime (I.) is

the current blocking regime. Since a laser diode is a diode, it has a built in potential that prevents meaningful current flow across the junction. While a small leakage current exists, it is orders of magnitude below the threshold current. There is no significant current flow until the applied bias voltage gets into the vicinity of the built-in potential, which we refer to as a device's bias voltage V_d throughout this work.
This is the second regime (II.), where the voltage is sufficient to cause the current across the junction to increase by several orders of magnitude, while still remaining below the threshold current I_{th} . Due to the higher carrier densities in the active region as a result of the increasing injection current, light begins to be emitted from the cavity. This is predominantly spontaneous emission, combined with amplified spontaneous emission (ASE) into resonator modes [50]. The emission spectrum is a broad band of light at all available transition wavelengths within the medium. The light also has neither spatial nor temporal coherence and is emitted uniformly into space, albeit limited by the aperture of the cavity design.
As the bias current is increased further, the population inversion $f_f - f_i$ increases, and with it the fraction of stimulated emission in the emitted light from the cavity. The transition between regime II. and III. occurs when the lasing condition is met: as soon as stimulated emission matches the round-trip losses of a single cavity mode, positive feedback sets in. Photons in this mode will stimulate more photons being emitted into it, which in turn will stimulate further emission into the mode. The device is now lasing and we are in the linear lasing regime. In an ideal device, the chemical potentials for electrons and holes in the regions of the material that are contributing to the lasing mode are now pinned: any additional carriers injected into the mode region will be converted into photons, resulting in no change in the carrier density in the active region. The gain at and in the vicinity of resonator modes will stay at the threshold condition. In reality, lateral carrier spreading will lead to more and more carriers getting injected into regions that are below the lasing threshold, resulting in a change of occupation until the lasing condition is met there as well. For devices with multiple weakly-coupled emitting layers, such as QWs of different thicknesses or QD and QDash layers with vastly different morphologies between layers, pinning can occur in multiple steps. However, this does require significant differences between energy levels in different layers, otherwise luminescent coupling will lead to uniform chemical potentials between all active regions.

The light coupled out of the cavity is now almost Poissionian and almost entirely in the lowest loss mode [101], as shown in Fig. 3.8. The broad spontaneous emission background remains, but is dwarfed in intensity by the lasing mode emission. The spectral shape and spatial distribution of the gain varies as a function of carrier density and core temperature, since they affect both carrier injection and distribution. The altered gain may increase sufficiently to allow other modes, both lateral and longitudinal, to match the

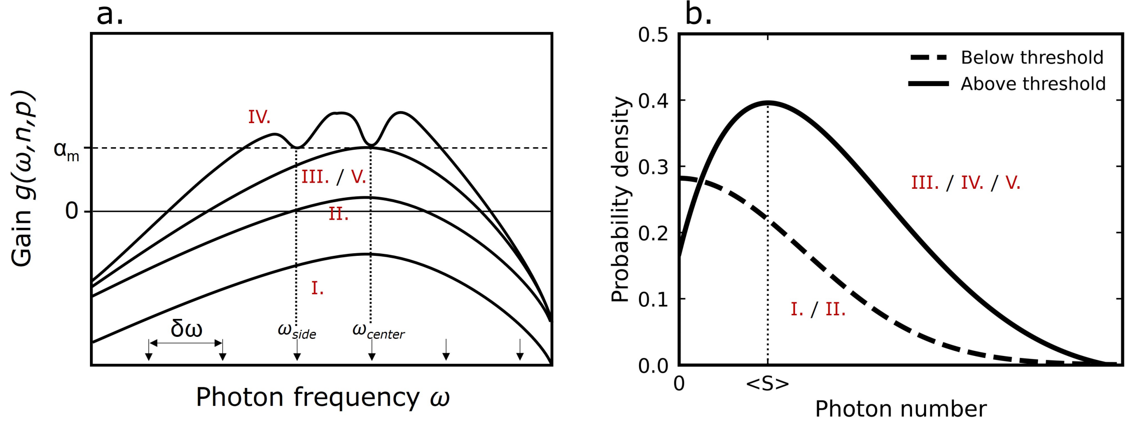

Figure 3.8: **a.** Schematic gain curves in the laser diode operating bias regimes outlined in Fig. 3.7. This is a sample gain function for an inhomogeneous gain medium since $g(\omega, n, p)$ is highly material and device specific. α_m represents the total optical modal loss in the cavity, while $\delta\omega$ represents the resonator mode spacing (see Eq. 3.7). **b.** Statistical distribution of emitted photons as a function of number of photons in a single mode laser. $< S >$ is the average occupation of the mode.

lasing condition. This is indicated by the second dip in the gain profile at ω_{side}, where the gain changes sufficiently to overcome the gain threshold.
If the carrier density is raised further by increasing the injection current density significantly above I_{th} , the device will start to roll off in IV. due to different mechanisms reducing the efficiency of optical conversion within the device. These mechanisms are generally related to an increase in the carrier density or the core temperature of the device, with non-radiative recombination and resistive heating due to both carrier transport and sub-band gap absorption providing the thermal energy for the temperature increase, as discussed in 4.8. As we will discuss in 3.4.5, raising the temperature degrades the operation of a device in multiple ways, predominantly by broadening the carrier distribution and thereby reducing the peak gain. However, the dominant mechanism is an increasing fraction of carriers recombining non-radiatively, mostly via Auger recombination which scales with the carrier density product np, while stimulated recombination scales approximately linearly with n or p. Auger recombination also becomes more efficient with temperature. This creates a feedback loop where core temperature rises due to non-radiative recombination, leading to a higher fraction of carriers recombining in this manner, raising the temperature even higher. The end result is a reduction in the energy conversion efficiency, apparent as the deviation in Fig. 3.7b. from the dashed linear slope. The two regimes are easily differentiated in the derivative of the output power in Fig. 3.7d., where the linear regime appears as a straight line at n_d , while roll-off is delineated by the departure towards 0. This work will examine the onset of roll-off for devices, for which we use the

roll-off current I_{ro}. The definition used through this work is the current at which the slope efficiency has decreased to 95% of its value in the linear regime.
If the device bias is increased still further, its lasing will break down as non-radiative recombination overtakes stimulated recombination in magnitude. This is the final regime V., the lasing breakdown regime, where additional bias current entered will result in less overall light being emitted. The cause of this is merely a continuation of the dynamics that drive roll-off. The beginning of the break down is marked by the slope efficiency turning negative, again easily legible from the plot of differential efficiency in Fig. 3.7. The definition of the lasing breakdown current, I_{bd}, used in this work is based on the bias at which the differential efficiency switches sign. Some devices will never enter this regime, as they will undergo thermal breakdown as a result of the high field intensities within the cavity much before the necessary carrier densities. This breakdown is mostly observed in shorter cavities, where high carrier densities and low absolute gain prevent an optically induced material breakdown.

3.4.3 Continuous wave and pulsed lasers

It is now time to start differentiating between lasers that emit a continuous stream of light and those which emit a train of light pulses. The former are referred to as continuous wave, or cw, lasers, while the later are intuitively referred to as pulsed lasers. The formation of pulses either occurs spontaneously due to a combination of lasing on multiple modes and phase-coupling between them, or can be introduced deterministically by introducing additional components into the cavity to turn a continuous laser oscillation into a train of pulses separated by T_{pulse}, with width $\Delta\tau_{pulse}$. $\frac{1}{T_{pulse}}$, which is the rate of pulse emission, is referred to as the repetition rate.

Actively driven pulsation

There are multiple ways to actively drive a cavity into emitting a train of pulses. A simple approach is to modulate the pump at the desired repetition rate, which will cause the laser to drift in and out of the lasing regime, resulting in pulsations. For an electrically driven semiconductor laser, the repetition rate is limited by the carrier transport and the time constant to establish the population inversion and necessary mode occupation within the cavity, which can take several ns, depending on the emission rates. Reliable pulsation can therefore only be achieved for repetition rates of a few MHz [49].
Another method of inducing pulsations is via Q-switching, where Q refers to the quality factor of the cavity as described in Eq. 3.13. As we explored in the context of the lasing

condition, the quality factor is a metric for the average photon lifetime within the cavity. By introducing an element into the optical path that can alter the quality factor over short timescales, the lasing threshold can be varied as a function of time. The continuously pumped gain medium will build up a significant population inversion which will not be depleted due to the low quality factor hindering the build-up of a significant self-amplifying photon population in any resonator mode. If the quality factor is then switched into the low loss regime, several modes in the resonator are now far exceeding the lasing condition. A pulse forms that depletes the built-up population inversion. Afterwards, the cavity is switched back into the high loss regime and the inversion is replenished. There are many methods of varying the quality factor of a cavity, usually based on electro-optical or acousto-optical modulators combined with a polarization selective element. The modulator alters the polarization state of the mode within the cavity, which results in varying degrees of loss at the polarization filter. The repetition rates obtained in this manner are generally limited by the bandwidth of the modulators, which generally lie in the 100s of kHz [49, 129].

Mode-locking

For single mode lasers, there is usually the need to include frequency-selective elements such as narrow bandpass reflective coatings or distributed Bragg reflectors to select one of multiple resonator modes that match or exceed the lasing condition and introduce sufficient loss to suppress the rest. The output spectrum from a lasing device without these mode-selecting optical elements will generally contain multiple, mutually incoherent modes [49].

This incoherence between modes arises due the transitions contributing to the device gain being inhomogeneously broadened, resulting in no defined phase relationship between the different emitters in the medium. While there is no relationship between the phases of the quantum mechanical states underlying the optical transitions, the different resonator modes can be brought into coherence via an optical phase coupling mechanism. This will introduce a fixed phase relationship between the modes, which results in a coherent superposition of the amplitudes of the different lasing modes: the laser is now mode-locked. The output will be a pulse train with pulse widths which are much narrower and repetition rates that are much higher than what can be achieved in actively pulsated lasers without coherent modes.

We can separate mode-locking into active and passive mode-locking, where one is the result of active external stimulation while the other is due to intrinsic interactions between different regions of the device. The concept of active mode-locking is illustrative in under-

standing how non-linear optical effects can have similar effects. We will therefore begin our discussion by understanding the phenomenon of active mode-locking.
Presume a monochromatic light wave, with $\vec{k} \parallel z$ and $\vec{E} = (E_x, E_y)$:

$$\vec{E} = \vec{A}_0 cos(\omega_0 t + \left|\vec{k}\right| z) \tag{3.64}$$

If this wave is now amplitude-modulated at a frequency $\Omega << \omega_0$, it will generate two additional waves with frequencies $\omega_0 + \Omega$ and $\omega_0 - \Omega$. Introducing some terminology borrowed from early radio-frequency systems, ω_0 is referred to as the carrier while $\omega_0 \pm \Omega$ are its upper and lower sidebands. The modulator produces a transmission that is a

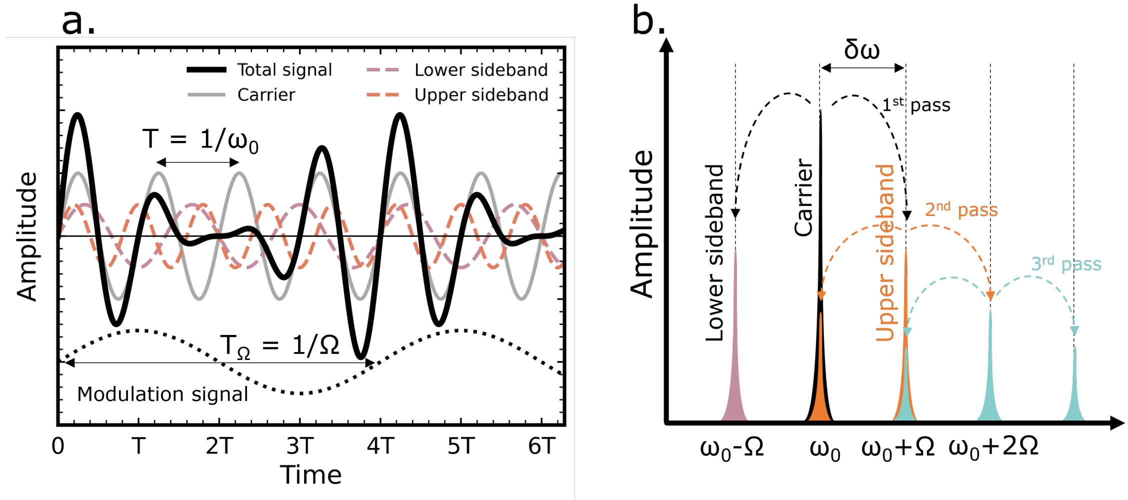

Figure 3.9: Sideband generation due to an amplitude modulating element. **a.** Time-domain signal with carrier and lower and upper side band. The modulation signal is also depicted. T is the oscillation period of the carrier. **b.** Frequency-domain transform of the signal. $\delta\omega$ is the mode spacing in the resonator, which is matched to the modulation frequency Ω. Only the upper side-band is cascaded through multiple resonator passes for clarity, even though the process is symmetric about ω_0.

function of time t, modulation frequency Ω, and modulation amplitude $a \leq \frac{1}{2}$:

$$T(t) = T_0 \left[1 - a(1 - \cos(\Omega t))\right] = T_0 \left[1 - 2a \sin^2(\frac{\Omega}{2} t)\right] \tag{3.65}$$

where we used the trigonometric identity $cos(2x) = 1 - 2\sin(x/2)$. The new, modulated amplitude of the nth monochromatic wave, an approximation of the resonator modes, is

then [49]:

$$\vec{A}_n(t) = T\vec{A}_{n,0}\cos(\omega_n t) = T_0 A_{n,0}\left[1 - 2a\sin^2(\frac{\Omega}{2}t)\right]\cos(\omega_n t) \tag{3.66}$$

$$= T_0\vec{A}_{n,0}\left[(1-a)\cos(\omega_n t) + \frac{a}{2}[\cos((\omega_n+\Omega)t) + \cos((\omega_n-\Omega)t)]\right] \tag{3.67}$$

This is the sideband generation via amplitude modulation depicted in Fig. 3.9. For $\Omega = \frac{\pi v_g}{L} = \delta\omega$ the modulation frequency is matched to the mode-spacing of the resonator from Eq. 3.7. The sidebands will then match the lasing condition and participate in stimulated emission in neighbouring modes. As stimulated emission preserves the phase relationship, the emission injected by the sidebands start to drive the ensemble of modes into a coherent state [29]. The strength of this phase-coupling mechanism can be estimated from the injected amplitude into the adjacent modes $n+1$:

$$\vec{A}_{n+1} = \frac{\vec{A}_0}{2}T_0 a\cos(\omega_{n+1}) \tag{3.68}$$

For N modes above lasing threshold, phase-locked by the modulation, the output signal is the linear superposition of all modes:

$$\vec{A}(t) = \sum_{n=-m}^{m}\vec{A}_0\cos((\omega_0+n\Omega)t) \tag{3.69}$$

Here we assumed that the gain is symmetric about ω_0, so $m = \frac{N-1}{2}$ and that the amplitudes for each mode are equal $\vec{A}_n = \vec{A}_0$. The gain profile will rarely be perfectly flat, so the latter condition is rather weak. However, making these assumptions allows us to determine the time-dependent intensity profile at the output port of the modulated laser:

$$I(t) \propto \left|\vec{A}_0\right|^2\frac{\sin^2(\frac{N\Omega t}{2})}{\sin^2(\frac{\Omega t}{2})}\cos^2(\omega_0 t) \tag{3.70}$$

For time-independent $\vec{A}_0$, this results in a series of pulses separated by a cavity-length L dependent period T_{pulse}:

$$T_{pulse} = \frac{2L}{v_g} \tag{3.71}$$

The resulting pulse width depends on the N, the number of modes phase-locked together. Since N increases with the gain bandwidth $\delta\omega_{gain}$ for a fixed resonator mode spacing, a broader gain shape will result in narrower pulses [49]:

$$\Delta\tau_{pulse}^{ideal} = \frac{2\pi}{(2m+1)\Omega} = \frac{2\pi}{N\Omega} = \frac{1}{\delta\omega_{gain}} \tag{3.72}$$

Of course, we made several assumptions to arrive at this result, which may or may not be accurate. We will re-examine the realistic limitations to pulse width in 3.4.4.
Using active amplitude modulation to introduce a fixed phase relationship between the different cavity modes is experimentally difficult, as it requires the integration of a modulator into the cavity. Especially for monolithic semiconductor lasers, for which the ease of fabrication is a significant consideration, introducing a microscopic modulator reduces the appeal.
Fortunately, there are passive methods of introducing phase-locking modulation into the cavity, allowing for passive mode-locked devices that will produce a train of pulses under constant excitation. There are multiple approaches, one being a saturable absorber that is introduced at either end of the cavity. This absorber with transitions lying in the gain band has a strongly non-linear, saturating absorption: as intensity increases, absorption decreases. Due to random fluctuations, the cavity will produce amplified emission pulses at near-random times. A strong pulse will experience less loss in the saturable absorber than a weaker pulse, and therefore be attenuated less. This allows the strong pulse to pick up more intensity in the gain section of the device, which will further reduce its attenuation in the saturable absorber. A positive feedback loop is established that selects one pulse out of the random fluctuations and amplifies it while suppressing the rest. Once the pulse has built up sufficient intensity to deplete the population inversion, no other pulses exist within the cavity and mode-locking has been established [49].
An alternative way to think about this process is by picturing the saturable absorber as an amplitude-modulating element, which operates at the repetition rate.
The effectiveness of passive mode-locking relies on a balance between the relaxation times of the absorber section and gain recovery times in the gain sections of the laser. The saturable absorber must return to its high absorption regime shortly after the intense pulse has passed to ensure weaker pulses are suppressed effectively. The decay times τ_{sat} of the states involved in the absorbing transitions therefore need to be much shorter than the cavity round-trip time:

$$\tau_{sat} << T_{pulse} \tag{3.73}$$

The gain recovery time τ_{gain}, on the other hand, should ideally be close to the round-trip time to ensure that only one pulse experiences significant amplification:

$$\tau_{gain} \approxeq T_{pulse} \tag{3.74}$$

If it is too short, other pulses may deplete some of the inversion before the mode-locked pulse arrives. On the other hand, if the gain recovery time is too long, the maximum gain may fluctuate over time, leading to inconsistent pulse energies.
The realization of a saturable absorber in a monolithic semiconductor laser is quite simple:

by separating the top contact into multiple sections that are electrically independent, bias can be applied selectively to different sections. Since absorption is tied to the population inversion (see Eq. 2.46), which can be controlled via electrical bias, this allows for a tunable saturable absorption. Saturable absorber sections are generated by applying a reverse bias, which can be tuned to optimize for short pulse creation [130]. Absorbers can be separated into two categories: fast absorbers with $\tau_{sat} << \Delta\tau_{pulse}$ and slow absorbers with $\tau_{sat} \geq \Delta\tau_{pulse}$ [115]. Most semiconductor saturable absorbers fall into the latter category [114, 115]. Note that the pulse width is generally much larger than the pulse period, so $\Delta\tau_{pulse} << T_{pulse}$ and Eq. 3.73 holds even for slow absorbers. Faster absorbers will allow for narrower pulse widths, as the degree of coherence is greater due to a narrower phase-matching window. However, there are other interactions that can result in narrow pulses far below τ_{sat} from slow absorbers [114, 115, 130].

One more effect that should be mentioned is the Kerr effect [131]. Driven by the third-order non-linearity induced by the refractive index change, it can lead to mode-locking in systems with a high contrast in diffraction losses depending on beam sizing. The Kerr effect leads to a spatial lensing effect that focusses the mode profile at high intensities. Using a spatial filter to create the required diffraction loss contrast, this self-lensing rejects low intensity, unfocused components. It can therefore act as an effective saturable absorption mechanism, where reduced diffraction losses take the place of optical transparency in the mechanism discussed earlier [132].

The final pulse shape of passively mode-locked laser, irrespective of underlying locking mechanism, is the result of complex interactions between different mechanisms in the gain medium. The pulse shape in Eq. 3.70 using the idealized assumption of equal mode amplitudes $\vec{A}_n$ is a good starting point to get an intuition about the behaviour of a pulsed device, but lacks granularity when trying to describe realistic performance. Real gain media have non-negligible gain dispersion and may experience saturation, which affects its time dependent behaviour due to coupling with the refractive index [130]. This is the case for semiconductors as we showed in Eq. 2.48. There is also the general dispersion of the group refractive index $n_g(\omega)$ to consider, which alters the pulse shape due the different travel times of varying spectral components and can weaken phase-matching phenomena [133]. Lastly, phase noise can interfere with phase-locking mechanisms, leading to jitter (variation of pulse period over time) or preventing stable mode-locking altogether [115]. All of these factors are heavily material dependent, so we will now discuss the relevant mechanisms in the context of mode-locking in quantum dash lasers.

3.4.4 Mode-locking in quantum dash lasers

The inhomogeneous broadening in quantum dot and dash gain media as a result of the growth-induced size fluctuation causes very broad gain bandwidths, making them prime candidates for both amplification and generation of mode-locked pulses [94,130,134]. Both QDs and QDash devices that are passively mode-locked using saturable absorbers have been shown [135–138].

Mode-locking in these devices can occur in the absence of a saturable absorber as well, in so called single section devices, which were shown in InAs-InP as early as 2005 [136, 139]. The mechanism driving the phases into coherence here is based on a non-linear effect: four wave mixing. As indicated by the name, four wave mixing (FWM) mixes three optical signals through a third order non-linearity, resulting in a fourth output frequency [140,141]. There are 12 possible output frequencies ω_4, which are all available linear superpositions of the incoming frequencies ω_0, ω_1, and ω_2 [142]:

$$\omega_4 = \pm\omega_0 \pm \omega_1 \pm \omega_2 \tag{3.75}$$

We recommend the technical report by Thiel for a more in-depth treatment of four-wave mixing [141]. In a semiconductor laser above threshold, the input frequencies will be the resonator modes ω_n, which means that the difference between any two modes is an integer multiple of the resonator mode spacing $\delta\omega$. The resulting frequency ω_4 will therefore also lie on a resonator mode. Given the fact that the differences between frequencies $\delta\omega$ will be very small compared to the actually modal frequency ω_n, the output frequency will be nearly degenerate with the input frequencies; this type of FWM is therefore generally referred to as nearly degenerate FWM (ND-FWM) [143]. This process is strongest when phases between input fields are matched, so the amplitude of the output wave ω_4 is strongest when ω_{1-3} are in-phase [141, 144]. Similar to the effect of sidebands introduced via amplitude modulation discussed earlier, the sidebands are now generated via ND-FWM. This results in cross-talk between the different modes due to the mutual injection of phase-matched photons. The system is therefore driven into a coherent, mode-locked state.

The effect is quite strong in QDash gain media [145, 146]. The origin of this strong four wave mixing lies in SHB, depicted in Fig. 3.10a. The longitudinal spatial optical field $I_n(z)$ of mode n generates nodes and anti-nodes, with the latter resulting in a localized depletion of the carrier densities n and p through increased stimulated emission. Since the refractive index n_r changes with carrier density (see Eq. 2.55), longitudinal structure in the carrier density translates into gain and refractive index structure. Given that the inhomogeneity arises as a result of anti-nodes of the optical field, the modulation of the carrier density and thereby gain and refractive index occurs at the mode wavelength [147]. The

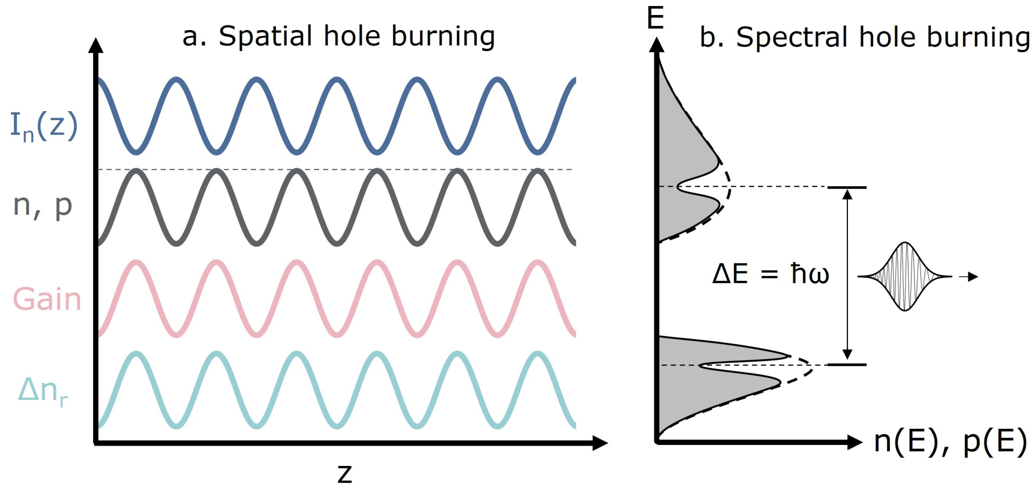

Figure 3.10: **a.** Spatial hole burning for laser with its cavity axis along z. The four parameters shown are the longitudinal intensity profile for the nth mode $I_n(z)$, the electron and hole carrier densities n and p, the optical gain, and the change in refractive index due to injected carriers Δn_r. **b.** Spectral hole burning. The carrier distribution pictured schematically matches a bulk semiconductor with a laser active state above the band gap E_g, with the equilibrium distribution indicated by the dashed line.

gain grating encourages multi-mode lasing by reducing the gain of the dominant mode in favour of sidebands [148]. ND-FWM, on the other hand, is primarily driven by the index grating [143]. In this way SHB first creates an ensemble of modes via the gain grating, which are then phase-locked by the index grating [148].

There are two conditions for this mechanism to work effectively: first, the recombination dynamics in semiconductors are sufficiently fast to allow multiple waves to interact via the refractive index change. The relevant time scale is the beat frequency $\Omega = \delta\omega$, which are the harmonics in the polarization generated via FWM. As the resonator mode spacing usually lies in the range of 10^{10} Hz and carrier lifetimes for semiconductors are in range of 10^{-10} s, this condition is met in most semiconductors [141,149,150]. Secondly, the spatial carrier density grating needs to persist and not get washed out by carrier drift. The gradient in carrier density will induce an electric potential opposed to it (see Ch. 4). This potential induces a current reducing the non-uniformity. The ratio between the magnitude of this current and the stimulated emission rate leading to the hole burning therefore defines the maximum achievable contrast for the density grating. The high in-plane carrier mobilities in bulk and QW regions lead to efficient carrier transport into the carrier-depleted regions, washing out the induced density structure. The strong confinement in QDs and QDashes lead to inefficient lateral coupling and low in-plane mobilities. This is why mode-locking is significantly stronger in QD and QDash gain media [148,151,152].

Another effect in semiconductors that can lead to FWM as well is spectral hole burning, depicted in Fig. 3.10b. Here a process that is significantly faster than the intraband relaxation time will cause the occupation of a state to deplete rapidly, causing a hole in the occupation function. This can extend the mechanism of spatial hole burning into the THz range, as the index change behind the third order susceptibility is no longer limited by the carrier lifetime but rather the time scale of intraband mechanisms. As these occur at the sub-ps scale, this can enable mode-locking in short cavities with large mode-spacing or high refractive indices [149]. Significant spectral hole burning was predicted for QDs due to a phonon bottleneck limiting scattering into dots, but these estimates were later proven to be overly pessimistic [153]. For this work, we are operating in the regime of strong spatial hole burning where spectral hole burning is less relevant.

3.4.5 Temperature dependence of laser performance

All of the mechanisms that underlie a material's ability to produce stimulated emission of light are dependent on temperature, either directly or indirectly. In general, a higher device temperature will lead to a degradation of laser performance in terms of efficiency and noise characteristics. The current flow through the laser diode as well as all non-radiative recombination processes will intrinsically elevate the temperature within the gain region of a semiconductor lasing device anywhere from 10s to 100s of degrees above ambient temperatures, depending on device geometry and heat shedding ability [154].

Band gap narrowing

There are several material parameters that show relatively large changes across the common operational laser range of 100-150°C. For most devices, the largest impact will arise from the band gap narrowing as temperatures increase. A common empirical estimate of band gap narrowing can be derived using the Varshni formula:

$$E_g(T) = E_g(0K) - \frac{AT^2}{B+T} \tag{3.76}$$

where T is the local temperature, and A and B are non-zero, phenomenological parameters that are fit based on experimental data. For the common semiconductor alloys, these are well known and have been tabulated as a function of constituent composition. The narrowing results in a red-shift of the gain, either directly via band edge shifting in the case of bulk gain media, or indirectly in the case of quantum-confined systems. For these systems, the change in band structure as a function of temperature alters the potential

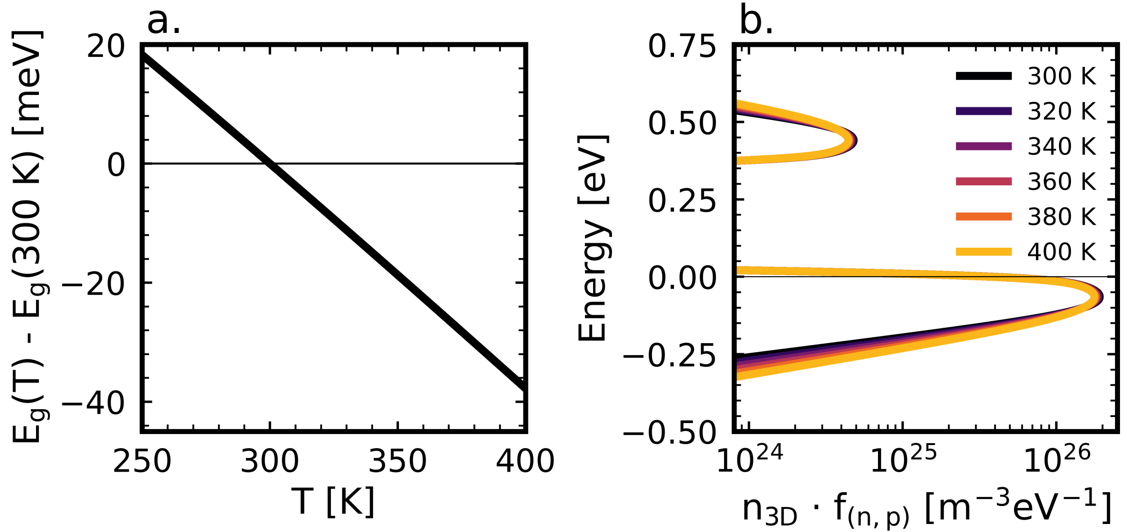

Figure 3.11: **a.** Band gap as a function of temperature for the *ingaasp_xyt* material macro in PICS3D, which was used for InP, InGaAsP, and InAs throughout the model. The dependence is based on [76]. **b.** Density of occupied states for InAs, n_{3D}, for an idealized effective mass approximation bulk density of states g_{3D}. An inhomogeneous broadening of 10 meV was assumed for both electrons and holes.

environment for the confined carriers. This affects the envelope wavefunctions, and leads to a mediated shift of the sub-bands. This is one of the contributing factors to reduced red-shift in quantum-confined laser gain media when compared to equivalent bulk materials [46]. The band gap for semiconductor alloys relevant to this work are shown in 3.11a. For devices where the lasing wavelength is determined by the gain medium, such as devices featuring Fabry-Perot cavities, band gap narrowing will directly red-shift the lasing emission. For highly spectrally sensitive parts of the device, such as anti-reflective coatings, distributed Bragg reflectors, or other strongly phase-sensitive components, this will lead to a significant decrease in device performance. For single-mode lasers, this is due to reduced light extraction efficiency and ineffective side-band suppression resulting in broader linewidths and increased intensity noise.

Carrier distribution broadening

With increasing device temperature, the energy available to individual carriers increases as well. As more thermal energy becomes available, carrier distributions broaden, as more states become energetically accessible. This can be seen in 3.11b., where we see a broadening of the occupation and a slight decrease in the occupation density at the peak of the distribution. For a bulk gain medium, this will broaden the gain, reducing the available

material gain at the band edges. Quantum-confined systems will behave differently. Depending on the relative position of the occupation density maximum and the sub-bands of the lower dimensional system, there are two possible scenarios. If the energetic difference between the distribution peak and the sub-bands is low initially, or the sub-bands are detuned towards the band extrema, the broadening of the energy distribution and the shift of the distribution peak will reduce the gain. Alternatively, if the misalignment is detuned away from the band extrema, gain will increase while detuning between sub-bands and the distribution peak decreases. Gain will decrease once the thermal shift exceeds the red-shifted sub-band detuning [155].

Apart from reducing the carrier occupation in states available for stimulated optical transition, the distribution broadening also has other effects that negatively impact device performance. Carriers near the high energy tails are in closer energetic proximity to band edges of confining barriers and are therefore more likely to undergo thermionic promotion into states within the barrier. While a fraction of these carriers is recaptured, this increases the carrier density in non-lasing parts of the device, leading to higher levels of parasitic recombination, either via spontaneous radiative recombination at wavelengths away from the laser operation range or non-radiative mechanisms such as Shockley-Read-Hall or Auger recombination. The thermionic promotion mechanism is phonon mediated and therefore increases with temperature, as more lattice phonons become available for carrier-phonon scattering.

Non-radiative recombination mechanisms

Since a lot of non-radiative recombination processes in semiconductors are mediated by lattice phonons, these processes generally show a strong dependence of their efficiency on temperature. This is true for Shockley-Read-Hall processes, and to an extent as well for Auger mechanisms.

Other effects

There are also, weaker effects that come into play as temperature increases. The increasing number of lattice phonons results in higher intrinsic carrier concentrations, leading to more minority carriers and thereby promoting non-radiative recombination mechanisms. The impact of this effect is generally small, however, as thermally promoted minority carrier concentrations are generally dwarfed by either extrinsic carriers due to defects or carrier influx due to leakage across the active region.

As phonon modes become more occupied with temperatures, the probability of carrier-phonon interactions increases, leading to a decrease in mobility. This decrease is generally

quite slight however, and without a noticeable decrease in conductivity, since the mobility decrease is compensated by an increase in majority carrier densities with temperature.

3.5 Mode-locked quantum dash lasers

As the last part of this chapter, we will summarize the literature findings for quantum dash lasers. We follow and supplement the two comprehensive review papers by Khan and Ooi on the subject, as well as the earlier work by Reithmaier et al [94, 156, 157].
The benefits of reducing the dimensionality of a gain medium to zero to improve the characteristics of the laser it supported were first postulated by Arakawa and Sakaki in 1982. The idea was that a reduced density of states would in turn reduce the degree of thermal distribution broadening, leading to better performance at elevated temperatures [158]. This proved to be correct for QWs, which were already being investigated, and even more so for self-assembled quantum dots, which had received less scientific interest at this point due to the relative infancy of advanced semiconductor growth methods [157]. QDs demonstrated several other desirable qualities as well: low room-temperature threshold currents, small linewidth enhancement factors as a result of reduced spontaneous emission, wide, bias-tunable wavelength ranges, combined with reduced sensitivity to optical feedback, and reduced threshold current increase and lasing wavelength shifting with temperature [159–171]. The carrier dynamics were also found to be sufficiently fast to support narrow pulse formation for potential mode locking [130, 172]. Lastly, the reduced in-plane mobility due to carrier localization within dots allowed for patterning of the active region without introducing significant surface recombination at the etched interfaces [173]. The first devices were based on InAs and InGaAs dots lattice-matched to GaAs, which emit into the O-band near 1300 nm. For long haul fiber communications, minimizing optical losses maximizes the distance between repeaters, hence emission into the C-band near 1550 nm is desirable, as shown in Fig. 2.10. However, the large lattice mismatch of 7 % between InAs and GaAs leads to significant compressive stress within the InAs QDs. This leads to band gap widening, while also hindering the self-assembled growth of large dots, which makes dot emission around 1550 nm difficult to achieve in this material system [85, 157]. Alternative growth strategies using metamorphic buffers proved to be difficult and saw limited uptake due to high defect densities [157, 174]. Especially since switching material systems proved to be a path of less resistance. The lattice mismatch between InAs and InP is significantly smaller at 3 % than the 7 % observed for InAs-GaAs, resulting in InAs-InP QDs being more easily tuned towards C-band emission than their GaAs and InGaAs counterparts. The first lasers featuring InAs-InP QDs were grown by Saito et al. in 2001 [175]. These initial devices were grown on InP(311)B miscut substrates: the non-baseplane growth surface facilitates island formation, leading to higher

dot densities to counter the higher island formation energy in InAs-InP due to the reduced lattice mismatch. The different substrate orientation also resulted in QD ensembles with less size dispersion, and with reduced QD wavefunction symmetry compared to InP(001) substrates [176]. However, they later fell out of favour when reliable high density growth could be achieved on InP(001) substrates due to the added complexity in device processing for miscut substrates [157].

When using InP(001) substrates, a curious effect was observed: under the correct growth conditions and given the right buffer layers, QDs would elongate along the $(0\bar{1}1)$ crystallographic orientation during the island formation process, forming wire like structures that were dubbed quantum dashes (QDashes) as they resembled a combination of both dots and dashes, putting them in the regime of quasi-0D dimensionality [85, 177]. This had been observed earlier in other material systems, but proved to be a preferred growth mode in InAs-InP [94]. The self-assembled dashes far outperformed earlier top-down fabricated dashes that suffered from processing related limitations with regards to dash orientation, surface quality, and dash density [85, 178]. The first laser based on this new generation of InAs-InP quantum dashes was demonstrated by Wang et al, using InAs sandwiched between InAlGaAs barriers emitting between 1600 and 1660 nm [85]. Gain media based on QDashes offer similar advantages to QDs when compared with bulk and QW gain media, and even outperform QDs in certain other aspects [157]. The differences between QDs and QDashes are mostly related to the in-plane carrier mobility and changed density of states. QDashes generally produce a higher and broader optical gain profile than equivalent QDs: the higher peak gain leads to lower threshold currents, while the larger gain bandwidth is beneficial in broadband amplification and the formation of narrow pulses [130, 172]. QD-based gain media on the other hand exhibit lower phase noise, which is excellent for stable mode-locking over wide spectral bands [179]. They are therefore often employed as active regions in passively mode-locked lasers [136]. These produce an optical frequency comb, as discussed in 3.4.4, which find application in spectroscopy, clock recovery for all-optical signal processing, wavelength multiplexing, and mm-wave generation over fiber [25, 82, 94, 156, 179–184]. Additionally, QDs and QDashes are resilient to defects and strain, making them ideal candidates for monolithic integration into silicon photonics, which offers both flexibility and scalability [185, 186].

4

Numerical and experimental methodology

The purpose of this chapter is to explain the methodology used to derive the results presented in this work. This work combines experimental characterization with numerical simulation to provide a comprehensive analysis of the properties of quantum dash lasers. This chapter starts with a short discussion of the details of the device growth, which was conducted at the National Research Council of Canada and the Canadian Photonics Fabrication Centre. We then describe the various experimental methods that were used to characterize the devices. The chapter concludes with a thorough discussion of numerical optoelectronic device simulation, examining the methods, models, and assumptions that underpin Crosslight PICS3D, the commercial solver that was used for this work.

4.1 Device growth

The devices in this work were not fabricated by the candidate, but instead provided by collaborators at the National Research Council of Canada, with parts of the growth done by the Canadian Photonics Fabrication Centre (CPFC). The layers up to the etch stop were grown on 3" wafers using chemical beam epitaxy (CBE, see 2.5) by P. J. Poole. The layers comprising the ridge were then grown using metal-organic chemical vapour deposition (MOCVD) at the CPFC, which also handled patterning, etching, and cleaving fully processed wafers into lasing bars of different lengths. While in theory the device design explored here could be grown in a single step, the two-step process was used due to the relative cost of InP growth for both systems and the higher interface quality achieved. The dopants used were Zn and Si for p- and n-type, respectively. A detailed description of the fabrication process can be found in [187] and [188], with the details of the QDash growth explained in [84].

4.2 Experimental methods

Given the simplifications and assumptions necessary to facilitate the model, it is important to have a comparison with experimental data to get an intuition how the model predictions compare to physical reality. For this purpose we compare devices simulated at different cavity lengths and temperatures with data derived from fabricated devices. While different device designs were simulated and tested, only results for the baseline design are presented here. chapter Ch. 6 includes further comparison between simulated predictions and experimental results for different device designs.

4.2.1 Note on origin of data

Not all of the experimental data in this work was captured by the author. If any data was captured by a person other than the author, it will be credited in the caption of the graph or table. Significant contributors were Ping Zhao, who conducted all measurements on the semi-automated bar testing setup, and Ras-Jeevan K. Obhi, who conducted AFM studies of the dashes and was part of the photoluminescence measurements. The different contributions to this work are

4.2.2 Photoluminescence

Figure 4.1: Photoluminescence measurement setup.

The photoluminescence was measured using the setup shown in Fig. 4.1. It features several lasers, of which we used the 532 and 1064 nm devices in this work. The setup operates in a confocal geometry, with a biconvex lens acting as the focusing and collection optic. The detector used is a Horiba Synapse InGaAs/Symphony II unit, cryogenically cooled to liquid nitrogen temperatures, mounted on a Horiba spectrometer with 300 to 1200 g/mm gratings.

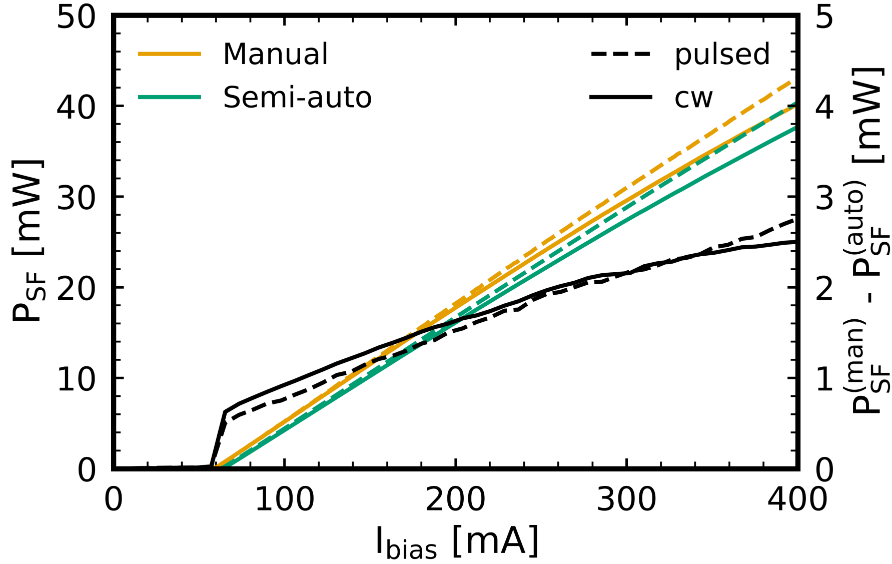

Figure 4.2: Comparison between LI characteristic measured using the semi-automatic and manual measurement setups for both pulsed and continuous bias of a 2000 µm cavity at 293 K. The semi-automatic data was measured by Ping Zhao.

4.2.3 LI and IV characteristics

Two different setups, both located at the NRC, were used to characterize the LI and IV characteristics for the devices. After growth and fabrication, wafers were cleaved into bars featuring approximately 30 devices each. A semi-automatic setup was used to characterize these devices. The device is contacted from above by two probes and grounded via the brass sample mount. A thermoelectric cooler (TEC) keeps the devices at a set temperature. The TEC is controlled by a Keithley 2510-AT TEC controller, while the diode is controlled by a Keithley 2520 Pulsed Laser Diode System.The light out is collected by a Ge photodetector, which is aligned with the centre of the bar and remains static throughout the measurement. The probes then move automatically between the different devices on the bar, collecting an LI and IV characteristic for each device. Due to the extent of the beam and the distance between the lasing device and the detector, some of the light output of the device is not captured, leading to an underestimation of the power output and thereby the slope efficiency of devices measured in this setup.
In addition to the semi-automatic measurements, we therefore also conducted manual LI characterization measurements. These use a similar setup, however the top probes are aligned manually. A second Ge detector with an active area significantly larger than the expected beam diameter is placed in close physical proximity to the device-under-test (DUT). It therefore captures a larger portion of the light than the semi-automatic setup, with a difference between the two setups of approximately 7 %, as shown in Fig. 4.2. The

manual setup also features a TEC, capable of maintaining temperatures of up to 80°C. Most of the data in this thesis was captured using this setup.
The bias current supplied to the laser being tested can either be applied continuously or in short pulses. The former represents the operating conditions of the device more accurately, while the latter avoids heating effects. While the model is capable of reproducing self-heating, as outlined in 4.8. Unless explicitly mentioned, all data in this thesis therefore reflects measurements conducted using biases pulsed with 3 μs periods and 0.5% duty cycles. The difference in results obtained for the same 2000 µm cavity between the two measurement setups used, as well as a comparison between pulsed and continuous (direct current) bias measurements is shown in Fig. 4.2.

4.2.4 Spectral measurements

The spectral characteristics of the devices were assessed in three ways: the detector in the semi-automatic setup can be replaced by a fiber-coupling lens, which couples the light output of the laser into an optical spectrum analyzer (OSA) via single mode (SM) fiber. This setup was used to get an initial idea of the spectra emitted across a given laser bar. In order to do temperature sweeps and obtain higher resolution spectra, a second setup was used additionally, which also uses a lens-coupled fiber collimation to send light into a Yokogawa AQ6370D OSA. The power supply used was a Tektronix PS2521G and the diode and TEC were controlled by an ILX Lightwave LDC-3722 laser diode controller. The light was switched between an optical power meter and the OSA using a JDS Uniphase SC-series fiber-optical switch. Given the slightly different sample mount geometry and the TEC used, this setup was only capable of reaching temperatures around 50°C reliably, hence there is no spectral data at higher temperatures.
Since the devices we are investigating are mode-locked lasers, a third setup was used to assess the degree of mode-locking. For this, the laser output was fiber-coupled using a lens, and then split between an OSA, an Anritsu MS9740A, and a 100 GHz bandwidth Finisar XPDV4120R photodiode connected to a signal analyzer (SA), a Keysight Model-N9030A with a bandwidth of 50 GHz. Different parts of the spectrum could be selected for either path by adding a fiber-coupled mechanically adjustable Fabry-Perot filter cavity.

4.2.5 Dispersion

The last relevant measurement setup used the setup pictured in Fig. 4.3a. It was used to assess the group velocity dispersion (GVD) of the cavity, by allowing measurement of the group refractive index by comparing the delay between two pulses travelling along optical paths with different lengths. By comparing the delay between spectral components of

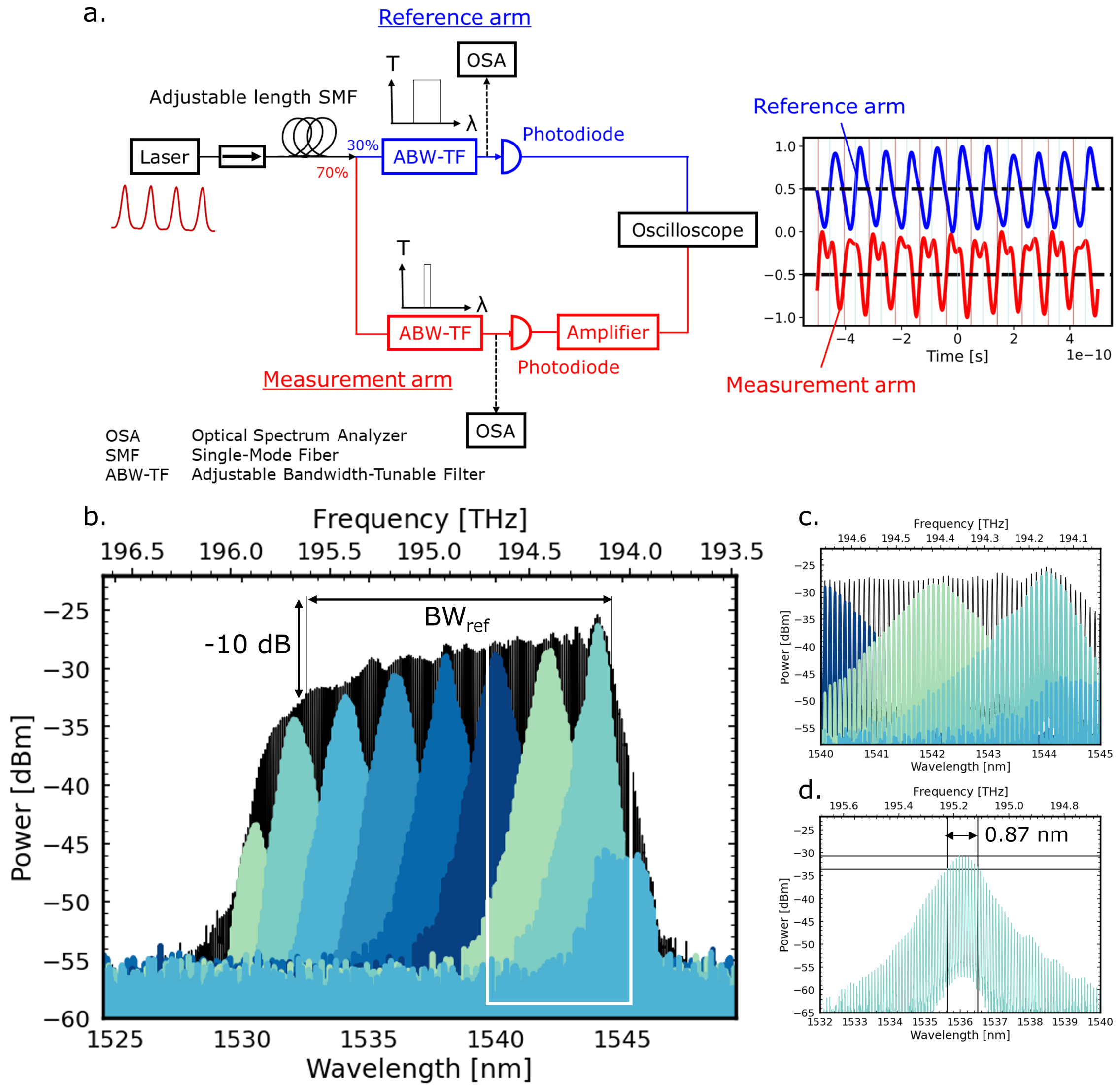

Figure 4.3: **a.** Setup used for measurement of the dispersion compensation. **b.** Complete lasing spectrum (black) and 1 nm slices from the measurement arm adjustable bandwidth-tunable filter (ABW-TF) used for quantifying the group velocity dispersion (shades of blue), with **c.** close up near the peak of the lasing spectrum. **d.** spectrum after the reference arm ABW-TF, with the 0.87 nm 3 dB bandwidth indicated.

the pulses received at the end of both paths, the group refractive index could be inferred. Two adjustable bandwidth tunable filters (ABW-TFs) with 3 dB bandwidths around 1 nm were used to select different parts of the spectrum in reference and measurement arm. The reference arm was kept near the centre of the comb at 1537 nm, while the measurement arm was tuned to different parts of the spectrum. The wide bandwidth meant that somewhere between 7 to 8 longitudinal modes were fell within the 3 dB window, as shown in Fig.

4.3d. This measurement is based on the experiment described by Faugeron et al [51]. The setup was slightly modified, by moving the adjustable fiber into the shared path prior to the beam splitter. The delay can still be compensated in this manner, and it allows the measurement of devices with greater temporal drift without having to add fiber to both paths. As the path difference between both arms remains small, the time of emission between pulses arriving at each photodiode is small. Each path is terminated by a large bandwidth photodiode, 30 and 50 GHz for reference and measurement arm, respectively, with the signal combined into a 30 GHz bandwidth oscilloscope. The tunable filters were adjustable Fabry-Perot filter cavities.

4.3 Numerical methods

There are many ways to model semiconductor diode lasers, which can be grouped into one of two archetypes: analytical and numerical models [115]. Analytical models generally take the form of rate equation-based models which abstract a device into sets of interacting carrier populations. These rate equations often include phenomenological constants to capture the effect of device geometry, such as injection efficiencies and mode overlaps. Numerical models are often spatially- and/or temporally-resolved representations to capture effects related to spatial carrier inhomogeneities over time. The evolution of the system as parameters are varied relies on solving partial differential equations (PDEs) over a discretized representation of the physical system, which allows to treat more complex geometries self-consistently without using stand-in phenomenological constants. The cost is often complexity, as the solution of PDEs over large matrices comes with a computational penalty that often calls for more severe approximations than rate equations models will [46]. One approach is not inherently superior to the other and they both have their appropriate use cases.
One of the objectives of this work is building an understand of how the geometry of a mode-locked laser relates to its performance. The device we are trying to emulate is therefore more appropriately represented using a spatially-resolved approach based on a Finite Element Mesh (FEM). We used a commercial semiconductor simulation software, *Crosslight PICS3D*, which is a tool to define complex semiconductor structures, spatially discretize them into meshes, and then solve drift-diffusion equations on these meshes which can be coupled to secondary sets of equations, such as self-consistent optical mode and heat generation and transport calculations. We will now examine the different components of the numerical simulation of devices in the formalism used within PICS3D.

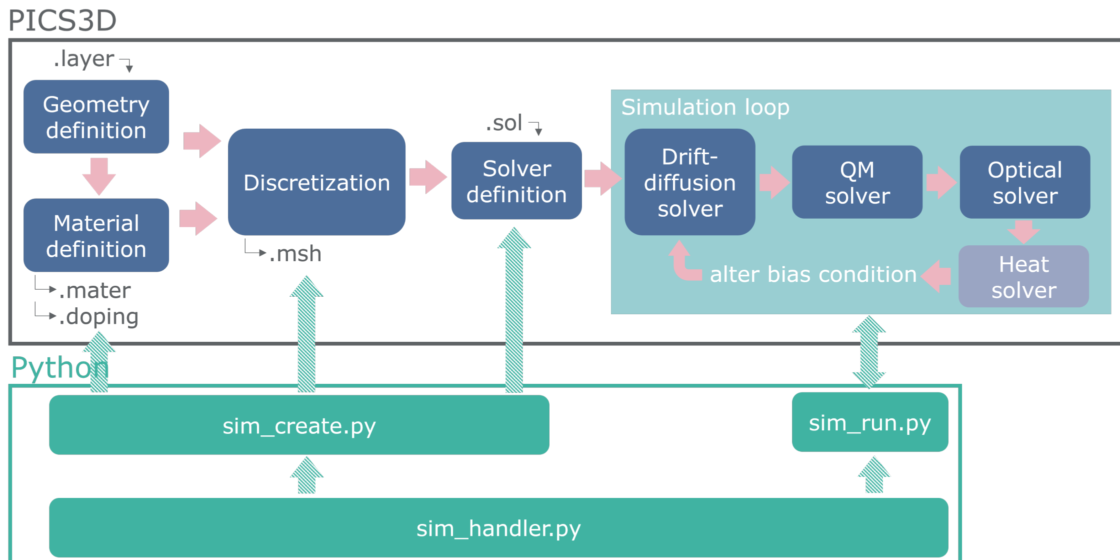

Figure 4.4: Simulation flow in PICS3D and Python wrapper.

4.4 Simulation flow

The process of device simulation in PICS3D is outlined in Fig. 4.4. The first step is the definition of the device geometry by defining the device layer by layer, specifying the material each layer is composed of. The geometry is then spatially discretized, resulting in a mesh with each node of the mesh associated with a specific material. The material definition occurs by specifying material macros, which we will discuss in 4.4.2. The discretization in PICS3D creates triangular elements in the xy-plane, that are then extruded along z into prisms. The xy-plane mesh used in the this work is shown in Fig. 4.5. With

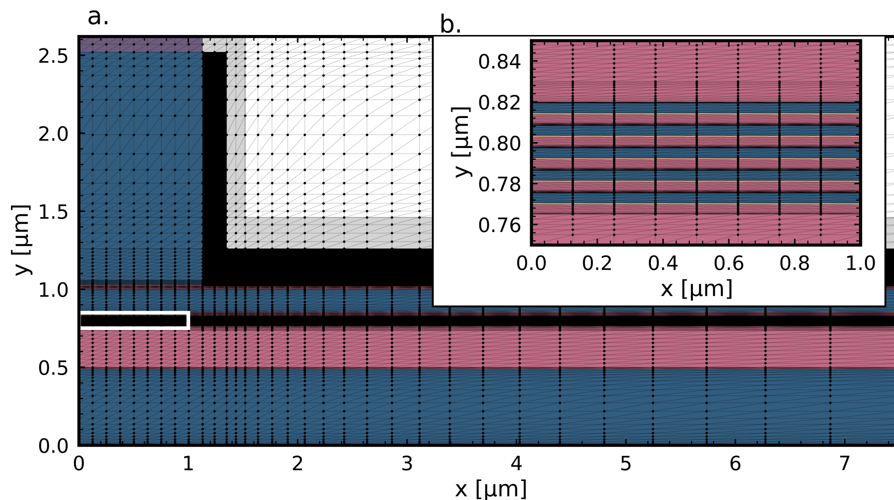

Figure 4.5: Mesh used in the simulation, **a.** full device and inset **b.** active region.

the geometry defined and discretized, the next step is setting up the solvers. There are three separate solvers that are called in a PICS3D device simulations: a drift-diffusion solver which handles the transport, generation, and recombination of charge carriers, a quantum mechanical (QM) solver that calculates confined states for any two-dimensional confinement regions in the device, and an optical solver that treats the interaction between the optical field and carrier population in the device. There is also an optional heat solver that gets called to reproduce the effects of self-heating in the device. The different solvers are called in the order shown in Fig. 4.4: after the bias is varied, the carrier distribution and potential are re-evaluated by the drift-diffusion solver. After a solution within the error margin is found, the QM solver is called, recalculating the QW states due possible shifts in the band edge position as a result of applied bias. Note that only QW states are recalculated, while QD and QDash states are treated as static. After the self-consistent quantum mechanical states are found, the optical solver is called. The solver determines spatial and longitudinal modes based on the altered quantum mechanical states and carrier distributions. If self-heating effects are to be included, the final step of the solver subroutine will then calculate heat generation and flow given the optical field and carrier profiles calculated in the previous steps. Once this solver has successfully converged on a solution within the margin of error as well, the bias step is considered complete. The bias is then altered, and each solver is called again, using the previous solution as its initial state.

The separation of the calculations into separate steps of the solution means that the final result is not entirely self-consistent, as the feedback between the different solvers is delayed to the subsequent solver step. However, the bias is altered in steps that are small relative to the absolute bias, which means the lack of direct feedback is unlikely to converge to a solution that is different from a truly self-consistent model. And the separation of solvers decreases the complexity of the problem by orders of magnitude, making it a worthwhile trade-off [189].

4.4.1 Simulation setup

While there is support for running simulations in batches in PICS3D, it is limited in its ability to significantly alter the underlying simulation beyond changing a few basic parameters. One contribution of this thesis was the development of a more sophisticated interface to interact with PICS3D. The interface was done in Python, a third generation object oriented programming language, but it also makes use of CMAKE and the C-language pre-compiler to conduct basic logic operations within the simulation support files required by PICS3D. The CMAKE/precompiler approach was originally developed by Matt Wilkins, and incorporated into the Python interface as these tools offer powerful

internal consistency and file handling capabilities that would have been difficult to build ab-initio.
Before making use of the interface, a simulation skeleton needs to be created. PICS3D requires a .layer file that specifies the layers and materials used, including thickness, composition and doping. Other required files, such as .geo, .msh, .mater, and .doping are generated from this .layer file using layer3d.exe, a tool provided by PICS3D. The second user-defined file required is a .sol file that instructs the solver on what kind of simulation to run on the given geometry and contains additional parameters defining the device. Lastly, a .plt file defines which parameters should be extracted from the solver results in the post-processing stage. The skeleton simulation needs to contain these three files, .layer, .sol, and .plt. Any parameter that is to be exposed to the interface needs to be given a unique variable name in the file. The variable name will then be replaced by a context-sensitive value based on user input in the pre-processing stage of simulation creation.
The core of the Python interface is *sim_create* . This object handles the creation and execution of simulations, as well as post-processing and archiving. *sim_create* needs to be called with directions to locate the predefined skeleton simulation, a directory in which to store simulation files during the calculations, and where to archive the simulation once completed. Additionally, a *dict*-instance can be passed, which contains parameters that are to be varied for the specific simulation at hand. This dict has two functions: keywords matching variable names defined in the simulation skeleton will be replaced by the value matching that keyword during the simulation processing stage. The second function is to provide inputs to simulation sub-modules. Before running the full simulation, *sim_create* can be provided with a list of sub-modules to run at any stage of the simulation. These sub-modules are Python modules following a standard template that instructs *sim_create* when and how to execute their contained code. These sub-modules contain a variety of capabilities, from ensuring that the separate confinement heterostructure height matches a certain value when quantum dash layer numbers or barrier widths are altered, to running a separate quantum mechanical pre-calculation prior to full device simulation to allow parameters sweeps across different QD designs. To ease integration of additional modules the sub-module manager integrated into *sim_create* contains functionality to ensure that they are executed in a manner that ensures that two modules altering the same parameter avoid race conditions.
When *sim_create* is called, it creates a new directory with an unique name based on the provided simulation parameters in the specified calculation directory. It then copies all the files from the skeleton simulation into the new directory. After ensuring all files were moved successfully, simulation sub-modules which are flagged as pre-processing modules are run. Once completed, variables in the simulation skeleton files matching keywords in the simulation parameter dictionary are replaced. Sub-modules flagged as post-processing

are then run. The simulation is now ready for calculation, and PICS3D is called by *sim_create* to run the simulation.
While the simulation is running, the command line output produced by the solver is read out and interpreted. Different parameters, such as current error on various parameters, center wavelength, and peak gain are plotted continuously to allow the user to monitor the status of the calculation.
Once the simulation has run its course, the simulation directory is cleaned to remove temporary simulation files that contain no relevant information and the simulation is archived.
In addition to *sim_create* , the suite of Python tools written for PICS3D also includes *SimData* , *SimShepherd* , and *opti* . *SimData* allows post-processing of simulation results, most notably it allows read-out and compression of the binary results created during simulation. This is useful, as it allows for advanced insight into device performance, such as localized recombination maps to identify sources of loss within the devices. *SimShepherd* is a tool that creates a "flock" of agents that can run simulations independently and in parallel to use of distributed computing resources efficiently. It also enables *opti* , an interface for optimization algorithms to interact with PICS3D. *opti* can instruct the simulation agents created by *SimShepherd* and analyse the results, comparing them with a pre-defined objective function. *opti* currently only includes a stochastic optimization algorithm, but it could be easily extended to arbitrary optimization algorithms, such as genetic functions or other machine learning approaches.

4.4.2 Material macros

As indicated previously, the material definition in PICS3D occurs via material macros. A material macro is a bundled set of parameters that generally reflect one specific material, such as Ti, Ag, or air, or compound semiconductors, such as InAs, GaAs, or InGaAsP. It will contain material parameters relevant for the simulation, such as the band gap, carrier mobilities, effective masses, and refractive indices. While there is a vast collection of material parameters fro semiconductors in the scientific literature, they have been mostly determined for binary semiconductor alloys such as GaAs. Even for technologically relevant compound semiconductors such as InGaAsP, the sheer size of the parameter space renders experimental determination of the parameters for every possible composition prohibitively resource-intensive. The material parameters for quarternary semiconductors are therefore commonly inferred based on an interpolation of the parameters of the constituent binary compounds. This interpolation is approximately linear for most parameters in InGaAsP, with a slight deviation referred to as "bowing" for some parameters [76]. We will not elaborate on the specific material models used, as most parameters are based on the standard values provided by PICS3D, which are primarily derived from [76]. The specific

Parameter	InAs	InP	1.15Q	InAlAs	InGaAs
E_g [eV]	0.352 [190]	1.31	1.08	1.45 [191]	0.477
Δ_{so} [eV]	0.500 [192]	0.108	0.23	-	0.15
$\frac{m_e^*}{m_0}$	0.023 [193]	0.08	0.07	0.049	0.01
$\frac{m_{hh}^*}{m_0}$	0.41 [193]	0.531 [194]	0.47	-	-0.145
$\frac{m_{lh}^*}{m_0}$	0.027 [194]	0.121 [194]	-	-	0.02

Table 4.1: Band structure related material parameters at room temperature used in the single band model. Band gap E_g and heavy-split-off hole splitting Δ_{so}, as well as effective masses m_e^* and m_{hh}^* are evaluated at the Γ-point along [100]. The effective hole masses are for the parabolic approximation to the heavy hole band. The parameters for $In_{0.815}Ga_{0.185}As_{0.405}P_{0.595}$ are a result of interpolations between the properties for the binary constituent compounds. All parameters are stated at 293 K. If not citation is provided, parameters are from [76].

values used in this work can be found in Tab. 4.1.
For active regions, which are regions that interact with the optical field strongly, a second type of macro needs to be provided. These are called complex macros and contain additional material parameters, relevant to the calculation of quantum mechanical states and optical transitions. These macros will also contain additional band structure parameters, such as the band offset for X/L-band states near Γ, and parameters that feed into a 8x8 k·p calculation of confined states. It should be noted that PICS3D only supports k·p state calculations for quantum wells, while quantum dashes and dots states are based on parabolic bands as discussed in 4.6. The complex macros also set a flag for the quantum mechanical and optical solver to consider regions using the macros in their calculation step.

4.5 Drift diffusion simulation

At the heart of each spatially resolved semiconductor simulation lies the Poisson equation:

$$-\nabla \frac{\epsilon_0 \epsilon_{DC}}{q} \nabla \vec{V} = -n + p + (p_{conf} - n_{conf}) + N_D(1 - f_D) - N_A f_A + \sum_j N_{tj}(\delta_j - f_{tj}) \quad (4.1)$$

We have dropped the dependence on position $\vec{r}$ for all parameters as a matter of convenience, and will continue to do so in this chapter unless explicitly mentioned otherwise. On the left side, we have the vacuum permittivity ϵ_0, the low-frequency component of the dielectric function ϵ_{DC}, the fundamental charge q, and the local electric potential $\vec{V}$. n and p are the electron and hole concentrations in bulk states, while p_{conf} and

n_{conf} are carriers located in QDashes. N_A and N_D are the acceptor and donor densities, with the occupied acceptor and donor fractions f_A and f_D. Assuming shallow impurities, $\left|E_{(c,v)} - E_{(D,A)}\right| \leq k_B T$, all doping atoms should be fully thermalized:

$$f_D = \frac{1}{1 + \frac{1}{g_D} e^{\frac{E_D - \epsilon_{f,n}}{k_B T}}} \tag{4.2}$$

$$f_A = \frac{1}{1 + \frac{1}{g_A} e^{\frac{\epsilon_{f,p} - E_A}{k_B T}}} \tag{4.3}$$

with the degeneracy factors $g_A = 4$ and $g_D = 2$ due to the spin degeneracy, combined with the light and heavy hole bands for acceptors. E_D and E_A are the absolute energetic positions of the donor and acceptor state, while $\epsilon_{f,n}$ and $\epsilon_{f,p}$ are the chemical potentials, also referred to as the quasi-Fermi levels, for electrons and holes.
The last term in Eq. 4.1 includes the presence of different trap states, denoted by j, which are deep within the band gap compared to the more shallow donors, $\left|E_{(c,v)} - E_{tj}\right| >> k_B T$. N_{tj} is then the density of trap states of species j, and f_{tj} is its occupation fraction:

$$f_{tj} = \frac{c_{n,j} n_{1,j} + c_{p,j} p}{c_{n,j}(n + n_{1,j}) + c_{p,j}(p + p_{1,j})} \tag{4.4}$$

Here $c_{n,j}$ and $c_{p,j}$ are the capture coefficients for electrons and holes of the jth trap species and $n_{1,j}$ and $p_{1,j}$ are the concentrations of trapped electron and holes when $\epsilon_{f,(n,p)}$ coincides with the energy level of the trap state [195]. δ_j is either 1 or 0, depending on whether or not the jth trap is negatively or positively charged in its unoccupied state [189].
The inclusion of The Poisson equation describes the electric potential that arises in a device which is trying to maintain charge balance between the different charge-carrying entities within it. Given that charge must be preserved overall, a set of continuity equations arises:

$$\frac{1}{q}\boldsymbol{\nabla}\vec{J}_n - \sum_j R_n^{(tj)} - R_{rad,spon} - R_{rad,stim} - R_{Auger} + G_{opt}(t) - \frac{1}{q}(J_{n,in} - J_{n,out}) \tag{4.5}$$

$$= \frac{\partial n}{\partial t} + N_D \frac{\partial f_D}{\partial t} \tag{4.6}$$

$$\frac{1}{q}\boldsymbol{\nabla}\vec{J}_p + \sum_j R_p^{(tj)} + R_{rad,spon} + R_{rad,stim} + R_{Auger} - G_{opt}(t) + \frac{1}{q}(J_{p,in} - J_{p,out}) \tag{4.7}$$

$$= -\frac{\partial p}{\partial t} + N_A \frac{\partial f_A}{\partial t} \tag{4.8}$$

The change in local carrier density over time is the sum of the change in local electron and hole current densities $\vec{J}_n$ and $\vec{J}_p$, the Shockley-Read-Hall recombination rate $R_{(n,p)}^{(tj)}$ due to the trap states j, the spontaneous and stimulated radiative recombination rates

$R_{rad,spon}$ and $R_{rad,stim}$, and the optical generation rate $G_{opt}(t)$. As we will examine in 4.7, the radiative recombination rates are the connection between the drift-diffusion carrier transport model and the generation of laser light from the device. The last term on the right hand side represents the interaction of the mobile carrier population and the carriers that are captured into and escaped from the confined states. These states interact with the larger drift-diffusion simulation via the electron and hole capture and release currents $J_{(n,p),in}$ and $J_{(n,p),out}$. We will discuss their impact in 4.6. The two terms on the right side include the immobile donor and acceptor atoms represented by N_A and N_D and the free carrier densities n and p which are mobile and can therefore contribute to currents directly. The currents $\vec{J}_n$ and $\vec{J}_p$ are proportional to the potentials their respective carriers are subjected to, denoted by the gradient in their respective chemical potentials:

$$\vec{J}_n = qn\mu_n \boldsymbol{\nabla}\epsilon_{f,n} = \sigma_n \boldsymbol{\nabla}\epsilon_{f,n} \tag{4.9}$$

$$\vec{J}_p = qp\mu_p \boldsymbol{\nabla}\epsilon_{f,p} = \sigma_p \boldsymbol{\nabla}\epsilon_{f,p} \tag{4.10}$$

Where μ_n and μ_p are the electron and hole mobilities, q is the elementary charge, and σ_n and σ_p the conductivities discussed in Ch. 2.

4.5.1 Hydrodynamic model

The equations Eq. 4.1, 4.8, and 4.10 are sufficient to describe the basic movement of charge carriers and their creation via optical absorption and annihilation due to various recombination mechanisms. However, this approach does not track the occupation function of the carriers, it just tracks the carrier densities and implicitly assumes that carriers are distributed according to Fermi-Dirac statistics. This assumption is valid if we assume that our intraband dynamics are sufficiently fast to always return to a perfectly thermalized distribution of carriers. The relevant timescale for comparison is the characteristic time of the processes we are most interested in. In a laser, these processes are optical transitions, which have lifetimes in the ns range [149]. As we explored in the section on spectral hole burning in 3.4.4, intraband dynamics are generally much faster than this in the sub-ps range [149, 153]. In most scenarios, the assumption of perfect thermalization is therefore valid.

A problem arises when carriers are scattering between systems with different dimensionalities: the coupling between the separate confinement heterostructure (SCH), the wetting layer (WL) and the ensemble of dots is often much slower than the interaction of carriers in the same band in a bulk semiconductor [196–198]. There are therefore often two or more carrier populations existing in parallel: one in the lowest energy configuration, which has undergone thermalization, and one at a higher energy that exists as a result of

the mismatch between thermalization and carrier injection rates. In these cases, there is the need to track different carrier occupations existing at different energies. The chemical potential $\epsilon_{f,(n,p)}$ can be converted into an energy by dividing it by the Boltzmann constant k_B, to yield a Fermi temperature of the distribution T_f. Since the higher energy carrier population will be described by a greater chemical potential, associated with a higher temperature, non-thermalized carriers are also referred to as hot carriers. They can be included in the three equation formalism by introducing two more equations that describe the intraband dynamics for electrons and holes when deviating from Fermi-Dirac statistics [199, 200]:

$$\nabla\vec{S}_n + R_n\vec{w} - \nabla E_c \cdot \vec{J}_n + \frac{n(\vec{w}-\vec{w}_0)}{\tau_w} = -\frac{\partial(n\vec{w})}{\partial dt} \quad (4.11)$$

$$\nabla\vec{S}_p + R_p\vec{w} + \nabla E_v \cdot \vec{J}_p - \frac{p(\vec{w}-\vec{w}_0)}{\tau_w} = \frac{\partial(p\vec{w})}{\partial dt} \quad (4.12)$$

With the electron and hole energy flux densities $\vec{S}_n$ and $\vec{S}_p$:

$$\nabla\vec{S}_n = -\frac{5}{3}\vec{J}_n\vec{w} - \frac{10}{9}\mu_n m\vec{w}\nabla\vec{w}\nabla\vec{S}_p \qquad = \frac{5}{3}\vec{J}_p\vec{w} + \frac{10}{9}\mu_p m\vec{w}\nabla\vec{w} \quad (4.13)$$

The driving force of the hydrodynamic carrier current is the carrier energy $\vec{w}$, which is a displacement from the equilibrium carrier energy $\vec{w}_0 = \frac{3k_BT}{2}$. The T in this case refers to the lattice temperature, which is the final temperature for fully thermalized carriers. τ_w is an energy relaxation time that describes the characteristic time for carriers to scatter from the hot carrier population towards the cooler population in thermal equilibrium with the lattice [199].

Adding hydrodynamic carrier transport to the model means solving Eqs. 4.12, plus a modification to the current densities:

$$\vec{J}_n = \mu_n\left[-n\nabla\psi + \chi + \gamma_n + \frac{2}{3}\nabla(n\vec{w}) - n\vec{w}\nabla ln(m_n^*)\right] \quad (4.14)$$

$$\vec{J}_p = \mu_p\left[p\nabla\psi + \chi + E_g + \gamma_p - \frac{2}{3}\nabla(p\vec{w}) - n\vec{w}\nabla ln(m_p^*)\right] \quad (4.15)$$

Where m_n^* and m_p^* are the effective electron and hole masses. ψ here is the electric potential in units of energy (multiplied by q), χ the electronic affinity, and γ_n and γ_p reflect a correction to the Fermi-Dirac distribution:

$$\gamma_n = k_BT\ln\left(\frac{F_{1/2}(\frac{E_c-\epsilon_{f,n}}{k_BT})}{e^{\epsilon_{f,n}-E_c}/k_BT}\right) \quad (4.16)$$

$$\gamma_p = k_BT\ln\left(\frac{F_{1/2}(\frac{\epsilon_{f,p}-E_v}{k_BT})}{e^{\epsilon_{f,n}-E_c}/k_BT}\right) \quad (4.17)$$

We will describe the Fermi-Dirac integral $F_{1/2}$ in the next section in the context of carrier distribution. PICS3D generally makes use of the hydrodynamic model whenever hot carriers are considered, which will mostly be in the regions of the device that are most relevant to its operation. These are the active regions, which we will discuss in the next section.

4.5.2 Active and passive device regions

In order to reduce the computational overhead, PICS3D separates the device into active and passive regions. For regions that have a large bearing on the functionality of the device, multiple bands are modelled and their relative occupation tracked. The calculations done to arrive at their band structure are also more complex, using up to 8 band $k \cdot p$-derived bands rather than a single parabolic band, as we will explore in the next section. For a laser, these regions are generally the gain medium, surrounding barriers, and the SCH. Since the gain medium is the only part of the device that (ideally) actively participates in optical processes, these regions are referred to as a active. Active regions feature more detailed model representations, which comes at an increased computational cost. Other parts of the device, such as the substrate or cladding layers, require less detail to capture their impact to on the overall behaviour. Since there are no optical transitions actively participating in the light emission from from these regions, they are referred to as passive. Passive regions forego detail to ensure reasonable overall calculation time. The choice of whether or not a region is active or passive is provided by the user indirectly, by selecting certain material macros that provide additional parameters necessary to carry out the more detailed calculation.
An explicit list of which regions of the device are considered active and passive is provided in Ch. 5, where we discuss the specifics of the geometry of the device and its representation.

4.5.3 Band structure

There are a few inherent physical approximations in the treatment of band structure: first and foremost, the single band model is employed everywhere in the device outside of the active regions. This means a truncation of the number of bands considered to one conduction and two valence bands. Since the lowest energy band gap exists at the Γ-point for all zincblende crystals considered here, we are using its energy as the conduction and valence band edge. For the conduction band, the assumption is that other band minima, such as L- or X-valley are far enough removed in terms of energy and momentum that they are largely inaccessible for carriers injected into the Γ-valley [29]. Similarly, we assume

that the split-off band for holes is sufficiently far from the band edge that it has negligible occupation compared with the degenerate heavy hole band. Given the energy splitting for the split-off band $\Delta_{so,InAs}$ of 0.5 eV (Tab. 4.1) this assumption seems appropriate. While the light and heavy hole bands are degenerate, or nearly degenerate for unstressed zincblende semiconductors near Γ (see Ch. 2), the effective density of states (DOS) is much smaller for light compared to heavy holes, due to DOS scaling with effective mass. The effective mass used is a reduced mass based on light and heavy hole masses m_{lh} and m_{hh}:

$$m_r^* = (m_{lh}^{3/2} + m_{hh}^{3/2})^{2/3} \tag{4.18}$$

The reduced mass is dominated by heavy holes. Due to the band and spin degeneracies, the valence band DOS is multiplied by a factor of four rather than the two for the conduction band. This leads to a much higher effective density of states for holes than electrons.

Within active regions, two additional bands are considered: the electronic L-band as well as the light hole band. We only treat strain empirically as an effect that alters the band gap, and forego its impact on other band parameters such as the effective mass. While these models are available in PICS3D, they add computational overhead. The additional bands have the highest relevance for the confined states calculated in the microscopic sub-simulation, as discussed in 4.6: the additional bands result in additional confined states in the vicinity of the barrier band edge, as pictured in Fig. 5.6c. Outside of the dashes the additional bands are less relevant, for the reasons stated earlier when justifying the single band approximation. We do not observe any confined states, as we will discuss in more detail in 5.4.

As we discussed in Ch. 2, when bringing two semiconductors into contact, there is the potential for band discontinuities. The most relevant discontinuity in our work is the offset between InAs, $In_{0.815}Ga_{0.185}As_{0.405}P_{0.595}$, and InP, as this defines the most significant barriers in the baseline device. We used a split of the band gap discontinuity ΔE_g of 60/40, meaning the offset in the conduction band $\Delta E_c = 0.6\Delta E_g$, while $\Delta E_v = 0.4\Delta E_g$. This is based on values commonly used in the field [76, 92, 155].

4.5.4 Carrier mobility

The mobilities for carriers for materials are defined explicitly in PICS3D, and not directly linked to the effective mass, as one would expect from Eq. 2.37. They are provided as part of the material parameters for both active and passive regions. Since the mobility is strongly dependent on the impurity density via impurity scattering, the expressions for

the mobility include an impurity correction term:

$$\mu_{n,0} = \mu_{n,1} + \frac{\mu_{n,2} - \mu_{n,1}}{1 + \left(\frac{N_D + N_A + \sum_j N_{tj}}{N_{n,r}}\right)^{\alpha_n}} \tag{4.19}$$

$$\mu_{p,0} = \mu_{p,1} + \frac{\mu_{p,2} - \mu_{p,1}}{1 + \left(\frac{N_D + N_A + \sum_j N_{tj}}{N_{p,r}}\right)^{\alpha_p}} \tag{4.20}$$

Here $\mu_{n,1}$, $\mu_{n,2}$, $N_{n,r}$, and α_n are phenomenological fitting constants based on experimental data.

However, we also need to take into field effects, which can lead to velocity saturation [29]. We therefore plug the expressions for $\mu_{n,0}$ and $\mu_{p,0}$ into an additional set of equations.

The hole mobility can simply be split into two regimes: a low-field, constant mobility regime where the value is the field-independent $\mu_{p,0}$ and equal to the value calculated above. At higher field intensities, drift velocity saturation sets in, which presents as a $1/\left|\vec{E}\right|$ dependency, where $\left|\vec{E}\right|$ is the local electric field. The overall expression for the hole mobility then reads:

$$\mu_p = \begin{cases} \mu_{p,0} & \text{for } |\vec{E}| < E_{p,0} \\ \mu_{p,0}\frac{E_{(n,p)}}{|\vec{E}|} & \text{for } |\vec{E}| \geq E_{p,0} \end{cases} \tag{4.21}$$

Where $E_{p,0}$ is a reference field that defines the onset of the saturation regime.

For electrons, the approach is a little bit more complex, taking into account the scattering between valleys that can occur if the fields get sufficiently large [29]. The expression for the electron mobility μ_n is then:

$$\mu_n = \frac{\mu_{n,0} + (\mu_{n,0}\frac{v_{n,sat}}{E_{n,0}})\left(\frac{|\vec{E}|}{E_{n,0}}\right)^3}{1 + \left(\frac{|\vec{E}|}{E_{n,0}}\right)^4} \tag{4.22}$$

Where $v_{n,sat}$ is the saturation velocity, which can be approximated as $\mu_{n,0}E_{n,0}$.

During initial calibration of the model, we found that the conductivity for p-type InP was far below what we estimated from experiments. An alternative hole mobility model that included a temperature dependence of the hole mobility as well was therefore implemented. PICS3D enables this via the import of value tables, which we used to substitute the hole mobility for p-type InP and InGaAsP. The model was based on work by Benzaquen et al. for Zn-doped InP [201]. It includes terms for hole scattering on ionized impurities, longitudinal and transverse acoustic phonons as well as polar and non-polar optical phonons, as well as piezoelectric phonons. The extensive parametrization is well laid out in [201] and shall not be repeated here.

4.5.5 Carrier distributions

The carrier distributions in PICS3D are treated to varying levels of detail, depending on how pertinent the regions are to the overall device behaviour. We will therefore split the discussion of the carrier distributions between active and passive regions.

Passive device regions

In order to evaluate carrier distributions throughout the device, PICS3D uses a density of states based on a single, parabolic band for all passive semiconductor regions. The electron and hole carrier densities n and p at a given point within the device are then:

$$n = N_c^{3D} F_{\frac{1}{2}} \left(\frac{E_c - \epsilon_{f,n}}{k_B T} \right) \tag{4.23}$$

$$p = N_v^{3D} F_{\frac{1}{2}} \left(\frac{\epsilon_{f,p} - E_v}{k_B T} \right) \tag{4.24}$$

$\epsilon_{f,n}$ and $\epsilon_{f,p}$ are the local chemical potentials for electrons and holes, respectively, E_c and E_v are the conduction and valence band edge, k_B is the Boltzmann constant, and T is the local temperature. The impact of dopants is reflected in the altered positions of $\epsilon_{f,n}$ and $\epsilon_{f,}$, which move close to the conduction and valence bands as dopant densities are increased. N_c^{3D} and N_v^{3D} are the effective, three-dimensional densities of state for the conduction and valence band, and defined as follows:

$$N_c^{3D} = \frac{1}{\sqrt{2}} \left[\frac{m_e^* k_B T}{\pi \hbar^2} \right]^{\frac{3}{2}} \tag{4.25}$$

$$N_v^{3D} = \frac{1}{\sqrt{2}} \left[\frac{m_h^* k_B T}{\pi \hbar^2} \right]^{\frac{3}{2}} \tag{4.26}$$

With the effective masses for electron and holes, m_e^* and m_h^*. Lastly, $F_{\frac{1}{2}}$ is the complete Fermi-Dirac integral of order $\frac{1}{2}$, generally defined as follows [202]:

$$F_j(x) = \frac{1}{\Gamma(j+1)} \int_0^\infty \frac{t^j}{e^{t-x}+1} dt \tag{4.27}$$

With the gamma function $\Gamma(j+1)$:

$$\Gamma(j+1) = \int_0^\infty t^j e^{-t} dt \tag{4.28}$$

In the case of order $\frac{1}{2}$, this is equal to:

$$F_{\frac{1}{2}}(x) = \frac{1}{\Gamma(\frac{3}{2})} \int_0^\infty \frac{t^{\frac{1}{2}}}{e^{t-x}+1} dt \tag{4.29}$$

This is rather unwieldy, but can be approximated as proposed by Bednarczyk and Bednarczyk [203] into something more numerically convenient:

$$F_{\frac{1}{2}}(x) \approx \frac{1}{e^{-x} + \Psi(x)} \tag{4.30}$$

$$\Psi(x) = \frac{3}{4}\sqrt{\pi}\nu(x)^{-\frac{3}{8}} \tag{4.31}$$

$$\nu(x) = x^4 + 50 + 33.6x\left(1 - 0.68e^{-0.17(x+1)^2}\right) \tag{4.32}$$

Our expressions for the carrier concentrations then read as follows:

$$n = \frac{1}{\sqrt{2}}\left[\frac{m_e^* k_b T}{\pi\hbar^2}\right]^{\frac{3}{2}} \left[e^{\frac{E_c - \epsilon_{f,n}}{k_B T}} + \frac{3}{4}\sqrt{\pi}\left[\left(\frac{E_c - \epsilon_{f,n}}{k_B T}\right)^4 + 50 + 33.6\frac{E_c - \epsilon_{f,n}}{k_B T}\left(1 - 0.68e^{-0.17(\frac{E_c - \epsilon_{f,n}}{k_B T}+1)^2}\right)\right]^{-\frac{3}{8}}\right]^{-1} \tag{4.33}$$

$$p = \frac{1}{\sqrt{2}}\left[\frac{m_h^* k_b T}{\pi\hbar^2}\right]^{\frac{3}{2}} \left[e^{\frac{\epsilon_{f,p} - E_v}{k_B T}} + \frac{3}{4}\sqrt{\pi}\left[\left(\frac{\epsilon_{f,p} - E_v}{k_B T}\right)^4 + 50 + 33.6\frac{\epsilon_{f,p} - E_v}{k_B T}\left(1 - 0.68e^{-0.17(\frac{\epsilon_{f,p} - E_v}{k_B T}+1)^2}\right)\right]^{-\frac{3}{8}}\right]^{-1} \tag{4.34}$$

The resulting carrier concentrations as a function of relative quasi-Fermi level position, $\epsilon_{f,n} - E_c$ and $E_v - \epsilon_{f,p}$ are plotted in Fig 4.6. The effective masses are based on InP, and can be found in 8.1.

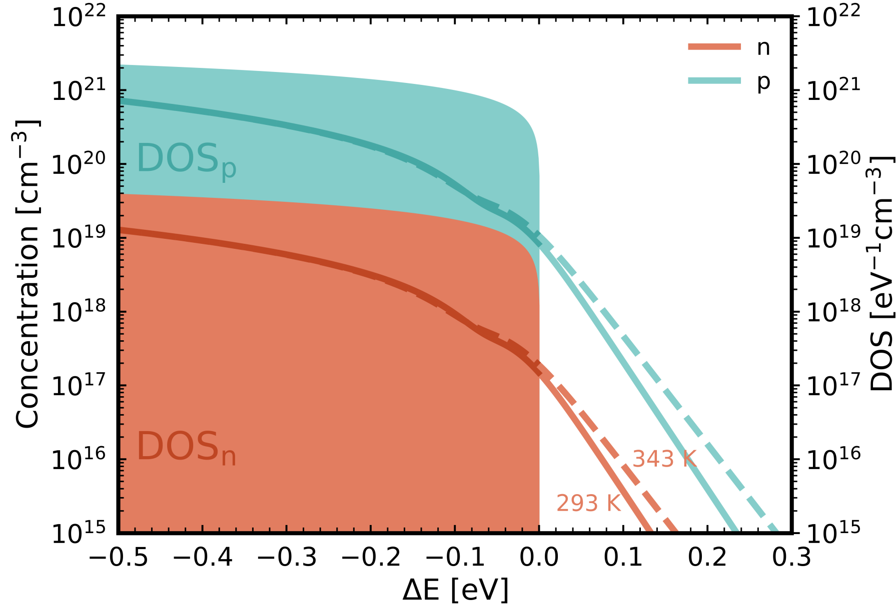

Figure 4.6: Lines: electron and hole concentrations n and p as a function of separation between band edges $\Delta E = E_c - \epsilon_{f,n} = \epsilon_{f,p} - E_v$ at 293 (solid) and 343 K (dashed). The filled areas indicate the idealized DOS for a bulk semiconductor in the single band approximation, matching the right hand side of the graph. Effective masses are based on InP (Tab. 4.1) [76].

Active device regions

Carrier densities in areas of the semiconductor that are designated active and therefore modelled in terms of their optical transitions are approached differently than passive regions. PICS3D was designed with bulk and MQW lasers in mind. The general approach is therefore to solve for one-dimensionally confined quantum mechanical states, forming sub-bands that span the entire extent of the active region in question. The density of states is then a two-dimensional density of states as discussed in 2.2.9, rather than the bulk expressions mentioned before. When no confined states can be found, the model defaults to the bulk carrier distributions described in the previous section. For an active region with confined states j, the expression for the two-dimensional density of states then reads:

$$n^{(2D)}(x,y) = \frac{1}{h_{well}} \sum_j \rho_j^{(2D)} k_B T \ln\left(1 + e^{\frac{\epsilon_{f,n}(x,y) - E_j}{k_B T}}\right) \tag{4.35}$$

Where h_{well} is the thickness of the QW, $\rho_j^{(2D)}$ is the two-dimensional density of states for the jth confined state, with $E_j(x,y)$ being its absolute energy. $\epsilon_{f,n}(x,y)$ is the local chemical potential for electrons. An equivalent expression can be written for holes. Further details on this matter can be found in Ch. 8 of [189].

As we will discuss in 4.6, the treatment of dots and dashes in PICS3D adds additional states

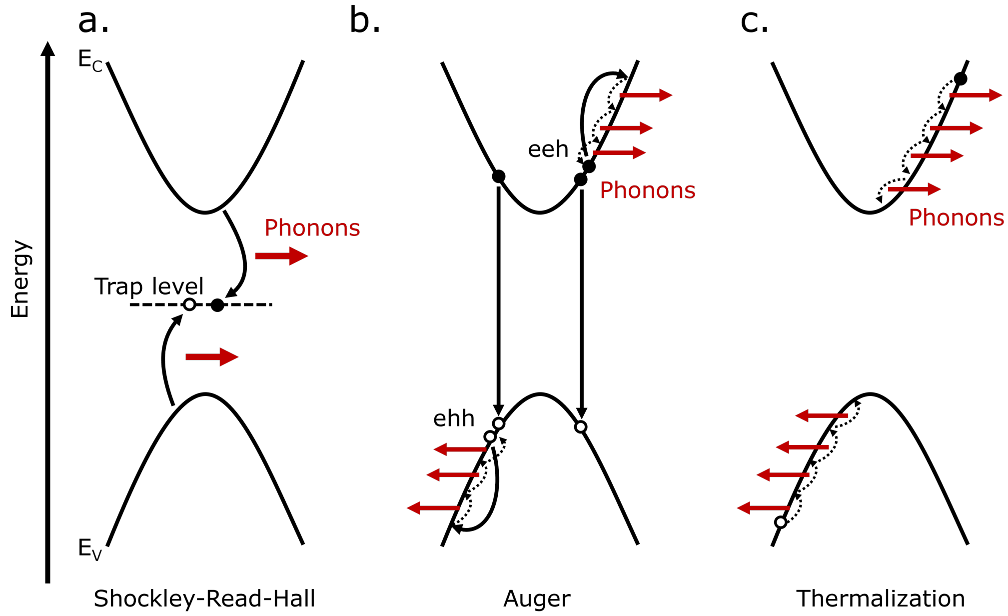

Figure 4.7: **a.** Shockley-Read-Hall and **b**. Auger recombination, showing both the momentum transfer to a hole (ehh) and electron (eeh). **c.** thermalization to the band edge via phonon scattering.

to a designated hosting layer, reflecting the presence of embedded confined structures. The interaction between these states and the surrounding layers is described in that section at length as well.

For both types of systems, the carrier density is still the product of the density of states and respective conduction and valence band occupation functions. The density of states is the only variation between the two.

4.5.6 Recombination

Apart from radiative recombination, three other forms of recombination are considered in PICS3D: Auger recombination due to carrier-carrier scattering, Shockley-Read-Hall recombination due to mid-gap defects, and surface recombination due to interfacial states.

Shockley-Read-Hall

Shockley-Read-Hall (SRH) recombination, shown in Fig. 4.7a., requires deep traps to facilitate a non-radiative interband transition, so it is intimately linked to the deep trap density N_{tj} we encountered earlier. The recombination rates for electrons and holes are then a

combination of the density of traps, their effectiveness at capturing carriers quantified by their capture coefficients $c_{(n,p),j}$, and their occupation f_{tj}:

$$R_n^{(tj)} = c_{n,j} n N_{t,j}(1 - f_{tj}) - c_{n,j} n_{1,j} N_{tj} f_{tj} \tag{4.36}$$

$$R_p^{(tj)} = c_{p,j} p N_{t,j} f_{tj} - c_{p,j} p_{1,j} N_{tj}(1 - f_{tj}) \tag{4.37}$$

With the definition of the capture coefficients $c_{(n,p),j}$:

$$c_{n,j} = \sigma_{n,j} \bar{v}_n = \sigma_{n,j} \sqrt{\frac{8 k_B T}{\pi m_n^*}} \tag{4.38}$$

$$c_{p,j} = \sigma_{p,j} \bar{v}_p = \sigma_{p,j} \sqrt{\frac{8 k_B T}{\pi m_p^*}} \tag{4.39}$$

The capture coefficients can be related to the SRH lifetimes of the carrier due to the jth trap state:

$$\frac{1}{\tau_{SRH,(n,p),j}} = c_{(n,p),j} N_{tj} \tag{4.40}$$

For multiple deep trap states simultaneously present, the total SRH lifetime is a summation over all traps [29]:

$$\frac{1}{\tau_{SRH,(n,p)}} = \sum_j \frac{1}{\tau_{SRH,(n,p),j}} \tag{4.41}$$

The occupation of the traps is naturally linked, as scattering of a carrier into a trap occupied by a carrier of the opposite charge will annihilate the carrier pair and result in the trap becoming available for future carrier capture:

$$N_{tj} \frac{\partial f_{tj}}{\partial t} = R_n^{(tj)} - R_p^{(tj)} \tag{4.42}$$

From which naturally, arises the steady state occupation ($\frac{\partial f_{tj}}{\partial t} = 0$) in Eq. 4.4, with $R_{SRH} = \sum_j R_n^{(tj)} = \sum_j R_p^{(tj)}$. This trap formalism is also used to treat recombination due to interface states. Interfaces between materials will often introduce a variety of states that are located near the centre of the band gap, making them efficient non-radiative recombination centres. In PICS3D, a surface population of states can be defined, that then add to the local recombination rate via Eq. 4.37.

Auger recombination

Auger recombination is a three-particle process where the recombination energy is transferred to a tertiary carrier, either an electron (eeh) or hole (ehh) [204, 205]. These processes will also sometimes be named using the semiconductor bands involved: for example,

a CHCC process involves a conduction band electron (C) recombining with a heavy hole (H), with the energy transferred into a third conduction band electron (C) that is elevated into an excited Auger state within the conduction band (C) [206]. The recombination can occur with or without momentum conservation between the carrier depending on whether it occurs directly or indirectly with phonon involvement. It can also make use of intermediary states, so for example a recombination between a split-off hole, conduction band electron resulting in a light hole entering an excited state within its band [207].
The standard Auger model included in PICS3D uses carrier specific Auger recombination coefficients $C_{aug,(n,p)}$ to capture the complicated electron-electron and electron-phonon interactions. This approach does not treat the Coulomb enhancement due to carrier attraction at high carrier densities and instead assumes non-interacting quasi-free carriers to maintain ease of treatment [205, 207]. The simplified Auger recombination rate is then:

$$R_{Auger} = (C_{aug,n}n + C_{aug,p}p)(np + n_i^2) \tag{4.43}$$

Where n_i is the intrinsic carrier density. The Auger coefficients are temperature and material dependent due to the effect of band structure and especially band gaps on the efficiency of the scattering process [208, 209]. This is reflected in a material-specific definition of the Auger coefficients in PICS3D, as well as a temperature dependence of the Auger-coefficient:

$$C_{aug,(n,p)} = C_{aug,(n,p),0} e^{-\frac{E_{aug,(n,p)}}{k_B T}} \tag{4.44}$$

Where $C_{aug,(n,p),0}$ is a reference Auger coefficient. This dependence reflects the fact that Auger recombination becomes more efficient at higher temperatures, another driver of laser performance degradation at elevated temperatures.
The formula in Eq. 4.43 is appropriate for bulk semiconductors and was shown to be adequately accurate to represent the mechanism inside QWs [210]. For QDs and QDashes however, carriers are strongly localized which means the overlap between wavefunctions of carriers in different dashes is small. Recombination can therefore only occur between carriers in the same dot [198]. The result is a change in the overall recombination mechanics [211]. For example, Auger scattering can couple the WL carrier population with confined states, adding another channel for populating QDs and thereby actually improving device efficiency [212]. However, there is experimental evidence for InAs-InP QDashes that a cubic dependence on carrier density for the Auger mechanism persists at room temperature and above [213]. Coupling between dots and the WL is thought to be sufficiently high at these temperatures that WL carriers become available to support Auger recombination similar to the bulk scenario. Eq. 4.43 is then a valid approximation, especially for dots with high degeneracy of its states, which fits the description of QDashes [214, 215]. This is confirmed by Dogonkin et al., who calculate the Auger coefficients for InGaAsP

quantum wires and find an expression that supports usage of Eq.s 4.43 and 4.44, at least for temperatures above 200 K [215].
While there is not method for redefining the Auger recombination rate calculation in PICS3D, another model can be substituted when an external gain table is imported. PICS3D then supports the additional import of externally calculated Auger recombination rates, which can be interpolated as a function of carrier density, *pn*-ratio, temperature, and electric field strength. This would allow the import of a gain model different from Eq. 4.43 for the active region. While this was not done in the context of this thesis, Python scripts to write PICS3D readable gain tables including Auger rates can be found in the appendix.

4.6 Treatment of quantum dots and dashes

While PICS3D supports self-consistent calculation of quantum-mechanical states for QWs during the full drift-diffusion simulation, QDs and QDashes are integrated statically. For QDs and QDashes, states are calculated prior to the full simulation in a separate definition and calculation step. They are then placed in the full device simulation using a reference layer with added quantum mechanical states. Changes in the states due to a change in the band structure as a result of the dynamic conditions within the cavity are therefore not captured by this approach. However, given the work by Obhi et al. that developed the dash model that the states used in this thesis are based on, we expect the overall change to be minimal compared to the inhomogeneous broadening as a result of size fluctuations [83].

4.6.1 Calculating confined states

The confined states that are embedded into the full device simulation are obtained via an implementation of an effective refractive index-like (ERI-like) method for the Schrödinger equation. This method delivers quantum mechanical states based on the confining potential of a single quantum dot or dash in isolation [216].
Assuming that there is no interaction between electronic motion along different dimensions, the wavefunction for a particle can then be split into three components, one along each axis. The single particle wavefunction can then be written as:

$$\Psi_{c,n_x,n_y,n_z} = \chi_{c,n_x}(x)\chi_{c,n_y}(y)\chi_{c,n_z}(z) \tag{4.45}$$

where the subscript c indicates that these are conduction band states, and $\chi_{c,n_x}(x)$, $\chi_{c,n_y}(y)$, and $\chi_{c,n_z}(z)$ are the envelope functions along x, y, and z, respectively. n_x,

n_y, and n_z are sub-band indices along each dimension. An analogous function Ψ_{c,m_x,m_y,m_z} can be written for holes in the valence band. The decomposition along different axes is most appropriate when the extent of the structure varies greatly along each dimension, so $L_y << L_x << L_z$ in the coordinate system used throughout this work [69]. With typical dash dimensions of $3 \times 20 \times 300$ nm^3, this condition is well met by the system under investigation [83].
We state the time-independent, one-dimensional Schrödinger equation for the conduction band particle along the orientation with the strongest confinement, y in our problem:

$$\left[-\frac{\hbar}{2m_e^*}\frac{\partial^2}{\partial y^2} + V_c(y)\right]\chi_{c,n_y}(y) = E_{c,l}\psi_{c,n_y}(y) \tag{4.46}$$

Here $V_c(z)$ is the potential in the conduction band and E_{c,n_y} is the eigenvalue of the nth sub-band for electrons along y. For a simple symmetric well of depth $\Delta E_{c,y}$, extending from $-L_y/2$ to $+L_y/2$, the conduction band potential is then:

$$V_c(y) = \begin{cases} 0, & |y| \leq L_y/2 \\ \Delta E_{c,y} & |y| > L_y/2 \end{cases} \tag{4.47}$$

We can then approximate the envelope functions as follows:

$$\psi_{c,l}(y) = \begin{cases} A\cos\frac{\sqrt{2m_{e,well}^* E_{c,n_y}}y}{\hbar} & |y| \leq L_y/2 \text{ and } l = \text{even} \\ A\sin\frac{\sqrt{2m_{e,well}^* E_{c,n_y}}y}{\hbar} & |y| \leq L_y/2 \text{ and } l = \text{odd} \\ Be^{-|y|\sqrt{2m_{e,bar}^*(\Delta E_{c,y} - E_{c,n_y})}/\hbar}, & |y| > L_y/2 \end{cases} \tag{4.48}$$

$m_{e,well}^*$ is the effective mass within the well, while $m_{e,bar}^*$ is the barrier effective mass. A and B are normalization constants.
The energy levels can then be solved using:

$$\sqrt{\frac{m_{e,well}^*}{m_{e,bar}^*}\frac{(\Delta E_{c,y} - E_{c,n_y})}{E_{c,n_y}}} = \begin{cases} \tan\left(L_y\sqrt{2m_{e,well}^* E_{c,n_y}}/\hbar\right) & n_y = \text{even} \\ -\cot\left(L_y\sqrt{2m_{e,well}^* E_{c,n_y}}/\hbar\right) & n_y = \text{odd} \end{cases} \tag{4.49}$$

Once the eigenenergies along y have been calculated, the next strongest confinement is along the width of the dash, which happens to be x in our choice of coordinates. The well depth along x, $\Delta E_{c,x}$, is modified by the eigenenergy along y, resulting in the following potential:

$$V_c(x) = \begin{cases} 0, & |x| \leq L_x/2 \\ \Delta E_{c,x} - E_{c,n_y} & |x| > L_x/2 \end{cases} \tag{4.50}$$

We find the eigenstates along x using a similar approach to Eq.s 4.48 and 4.49, resulting in the nth conduction band state eigenenergy along x, E_{c,n_x}. Using this energy, we then arrive at the final potential along the least confined dimension z. The potential is modified using both the eigenenergies along y and x:

$$V_c(z) = \begin{cases} 0, & |z| \leq L_x/2 \\ \Delta E_{c,z} - E_{c,n_y} - E_{c,n_x} & |z| > L_z/2 \end{cases} \tag{4.51}$$

After determining E_{c,n_z}, the final eigenenergy of the state with quantum numbers n_x, n_y, and n_z is then just the superposition of the three:

$$E_{c,nlm} = E_{c,n_x} + E_{c,n_y} + E_{c,n_z} \tag{4.52}$$

The process for holes is analogous, using the valence band edges to define the potentials. In reality, the potential for the dashes treated in this work have a more complex shape: there is a GaAs sublayer at the bottom and the barrier layers are $In_{0.815}Ga_{0.185}As_{0.405}P_{0.595}$ (also referred to as 1.15Q) below the dash and InP above it, leading to an asymmetric well overall. Instead of the analytical states in Eq. 4.48, the states in PICS3D are therefore derived numerically. The potential along each dimension is discretized, and then solved in a manner similar to the solution to the lateral mode problem discussed in 4.7, with the band structure replacing the effective index.
The calculated electron and hole states are exported into a file that lists the energy of each state (ϵ_n for electrons and ϵ_m for holes in Fig. 4.8) in relation to a conduction or valence band reference energy $E_{(c,v),ref}$. The reference band energy is the energy of the first barrier layer from the bottom. This reflects the intended implementation of QD and QDash states in PICS3D, which are integrated into the device simulation via a hosting layer whose band edges will become the new reference energies.
While PICS3D has the capability to use up to 8x8 k·p based quantum mechanical states when QWs are considered, the model used for QDashes is much simpler: it assumes isolated, parabolic bands for both conduction and valence bands. The lifted degeneracy for light and heavy hole bands in InP-lattice matched InAs is treated by conducting separate calculations for the light and heavy hole band confinement potentials. The usage of parabolic bands implicitly neglects the in-plane effective mass anisotropy due to the anisotropic strain, which would introduce a correction to the calculated state energies.

4.6.2 Integration with the full device simulation

The integration of QDashes into a full laser simulation in PICS3D is facilitated by treating the calculated dash states as subbands within the full device. The states are calculated

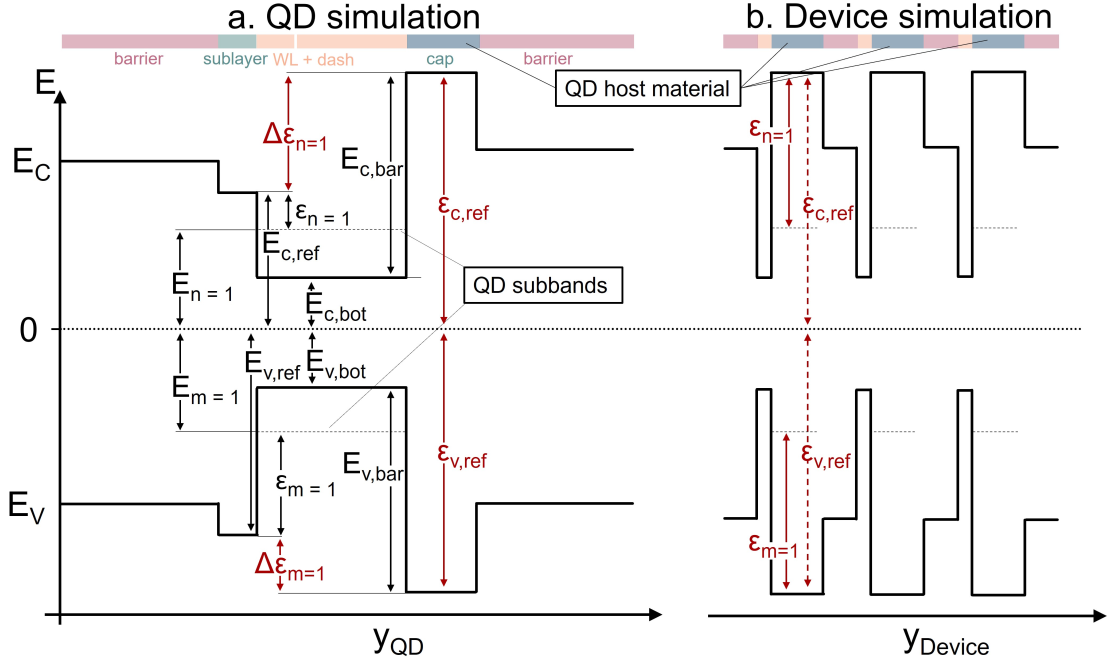

Figure 4.8: Connection between energies in the **a.** QD and **b.** device simulation in PICS3D.

prior to the full device simulation in a separate numerical model and are not varied as a function of dynamic simulation parameters. To place the subbands both spatially and energetically within the full device simulation, they are assigned a hosting layer. The states due to the QDashes are embedded within this layer, adding to its density of states. All states are associated with a broadening energy, $\Delta\epsilon_{inhomo}$ that reflects the inhomogeneous broadening due to size fluctuations. The connection between the microscopic simulation of a single QD and the full device simulation are outlined in Fig. 4.8. The various energies referenced in the reference file output by the Schrø"dinger solver in PICS3D are shown within a schematic QD or QDash device structure. $E_{(c,v),ref}$ are the *Ref. energy* for the conduction and valence band, respectively, while $E_{(c,v),bot}$ and $E_{(c,v),bar}$ map to *Potential bottom* and *Barrier height* for their respective bands. The absolute position of the QDash subbands depends on the relative eigenenergy of the state, E_n for electron and E_m for hole states, plus the reference energy $\epsilon_{(c,v),ref}$:

$$\epsilon_{(n,m)}^{(dev)} = E_{(c,v),host} + \epsilon_{(c,v),ref} + E_{(n,m)}^{(QDash)} \tag{4.53}$$

where $E_{(c,v),host}$ is the conduction or valence band edge of the host material. Other parameters that are needed to calculate the optical transition strength, such as the effective mass or the dipole moment, are supplied via a second material macro which defines the material of the QDash. Bulk parameters are generally assumed for these parameters,

rather than conducting a full quantum mechanical calculation.
An issue arises due the asymmetry of the layer structure (wetting layer/dash/capping layer) of the dashes used in this work. The hosting layer has to be considered active, so either be a quantum well or part of complex multi-quantum well. PICS3D states in the manual that it allows the integration of embedded layers into hosting layer defined using a symmetric-type macro. These macros are used to implement symmetric QWs with a barrier/well/barrier structure, with the well hosting the QD subbands. The barrier material used during the QD simulation is expected to match the barrier material in the device simulation. This allows integration of the common dot-in-well (DWELL) and dot-in-bar (DBAR) structures, but unfortunately can not replicate asymmetrical structures, such as the barrier/wetting layer/dash/capping layer/barrier structure we are examining in this work. To circumvent this problem, a complex multi-quantum well macro was used, with the QD states embedded into the capping layer. While an error flag is printed to the simulation log when forcing it to add embedded states to an unsupported asymmetrical MQW structure, the results indicate a correct integration of the embedded levels. This asymmetrical structure using the complex MQW structure is used whenever a wetting layer is include in the model.
There is also an issue when using states calculated based on a QD structure that is not exactly replicated in the full device structure. For the devices examined in this work, the GaAs sublayer beneath the InAs wetting layer was not included in the full device simulation. Since the reference energy is based on the first layer that uses a complex material macro in the microscopic model, its absence in the full device simulation can result in energy levels being placed incorrectly. This has been rectified by altering the reference energy, with $\epsilon_{(c,v),ref}$ in Fig. 4.8a. indicating the altered reference energy. A Python script to implement this shift is included in *laser_tools*
pics3d.

QDash states effect on carrier density

As the states due to the presence of QDashes gets added to a hosting layer, the approach for PICS3D to combine the densities of states into one total density. The resulting carrier density for the QDL is then a combination of the carriers within the hosting layer $n_{QW}^{(2D)}$ and the carriers captured into the QDashes $n_{QDash}^{(2D)}$:

$$n_{host}^{(2D)} = n_{QW}^{(2D)} + n_{QDash}^{(2D)} \tag{4.54}$$

An analogue equation could be written for holes. These are two-dimensional carrier densities, so they will later need to be translated into three-dimensional densities to interact

with the bulk carrier densities n and p treated by the drift-diffusion solver. The total concentration of carriers in the QDashes is calculated using the surface density of QDashes, N_{QDash}, and the Fermi occupation functions $f_{(c,v)}$ (see Eq. 2.31):

$$n^{(2D)}_{QDash} = 2 \sum_n \sum_s N_{QDash}(s) f_c(E_{n,s}) \tag{4.55}$$

where n is the quantum number of the dash state, s denotes a size counting parameter that reflects the size broadening of a given dash and the factor 2 appears as a result of the spin degeneracy. Again, an analogue equation for holes could be written using the hole occupation function $f_v(E_{m,s})$. Note that this treatment assumes QDashes can be treated as elongated QDs. We will examine this assumption in more detail later when comparing the gain functions for QDs and QDashes. The difference in the DOS for treatment of the structures as zero- vs one-dimensional quantum confined systems is shown in Fig. 5.6d. A broadening of the states of 40 meV is assumed for both dimensionalities. The density of states for dots is much smaller than for dashes, while the shapes are very similar, even without considering the occupation function. The density of states is difficult to examine experimentally, as it is most commonly measured using scanning tunneling microscopy. This involves approaching a surface using a conductive tip until tunneling transport occurs. As dashes are capped and then covered in a barrier material, which both result in a change to the electronic confinement and thereby alter the density of states, this measurement is exceedingly difficult for the dash ensemble we are interested here. We therefore opted to scale the density of states and observe how it affects the overall device behaviour.

4.6.3 Carrier capture and escape

An important aspect of the operation of QDash devices is the intralayer coupling between dashes as well as the coupling between the dashes and the unconfined carriers in the separate confinement heterostructure (SCH). As explained above, the QDash states are embedded within a hosting layer. The coupling between the dash states and the device at large is reflected in the rate of exchange between carriers in the hosting layer and surrounding barriers and the ones confined within the dashes. If coupling is strong, the difference will be small as carriers can easily move into and out of the dash states. If it is weak, and carriers are confined within the dash, and they will follow a different occupation function than the hosting layer carriers. It assumes strong coupling between dashes, either direct or mediated by a wetting layers. We therefore assume an even and fully thermalized carrier population within the dash ensemble. The dash and hosting layer states are then treated as one level each of a two-level system. The hosting layer states represent hot carriers, which move across the hosting layer without interacting with the dash states.

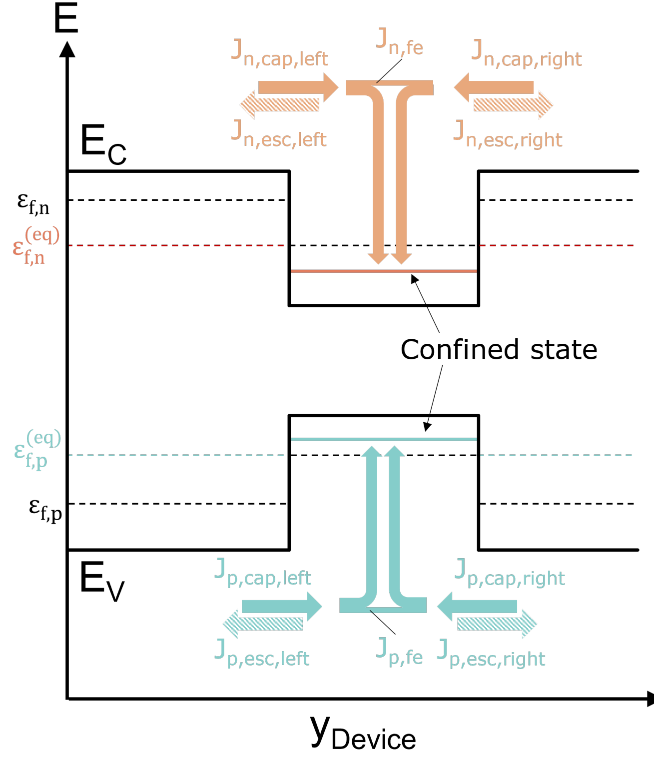

Figure 4.9: Carrier capture and escape into the quantum dash layer. $\epsilon_{f,n}$ and $\epsilon_{f,p}$ are the chemical potentials for electrons and holes at arbitrary bias, while $\epsilon_{f,n}^{(eq)}$ and $\epsilon_{f,p}^{(eq)}$ are the potentials at equilibrium. Other variables are defined in the text.

The dash ensemble itself represents the fully thermalized state. The rate of change of the electron density within the dash ensemble n_{QDash}, is then [217]:

$$\frac{dn_{QDash}}{dt} = -\frac{n_{QDash}}{\tau_{interband}} + J_{n,in} + J_{n,out} - J_{n,hot} \tag{4.56}$$

This is also depicted in Fig. 4.9. Here we turned the two-dimensional electron density we examined in the previous section into a three-dimensional quantity using the thickness of the hosting layer. $\tau_{interband}$ is the interband recombination time, which depends on the available recombination paths from the confined level. J_{in} and J_{out} are the thermionic in- and out-flowing currents from the two-level system of hosting layer states and dash ensemble into the surrounding semiconductor. These currents can be defined in terms of

capture and escape currents into the barrier to the left and right of the hosting layer:

$$J_{n,in} = J_{n,cap,left} + J_{n,cap,right} \tag{4.57}$$

$$= \gamma_{n,left}\bar{v}_{n,left}n_{left} + \gamma_{n,right}\bar{v}_{n,right}n_{right} \tag{4.58}$$

$$J_{n,out} = J_{n,esc,left} + J_{n,esc,right} \tag{4.59}$$

$$= \gamma_{n,left}\bar{v}_{n,left}n_{left}^{(eq)} + \gamma_{n,right}\bar{v}_{n,right}n_{right}^{(eq)} \tag{4.60}$$

$\gamma_{n,left}$ and $\gamma_{n,right}$ are phenomenological capture coefficients; these coefficients represent the effect of carrier scattering at the quantum well interfaces. $\bar{v}_{n,left}$ and n_{left} are the thermal velocity and density for electrons in the left barrier region, while $\bar{v}_{n,right}$ and n_{right} are the equivalent parameters for the right interface. The average thermal electron velocities in the barriers, $barv_{n,left}$ and $barv_{n,right}$, reflect the energetic distribution of carriers on either side of the well. They are defined as [189]:

$$\bar{v}_{n,(left,right)} = \sqrt{\frac{k_B T}{2m^*_{e,(left,right)}\pi}} \tag{4.61}$$

where $m^*_{n,(left,right)}$ are the effective masses in the left and right barrier, respectively. In order to extract the current density of electrons escaping, the equilibrium carrier densities $n_{left}^{(eq)}$ and $n_{right}^{(eq)}$ are used, representing the density of electrons when the chemical potentials of hosting layer and barrier layers are in equilibrium.
The last term in Eq. 4.56, $J_{n,hot}$ represents the partial electron current that remains "hot", so moves across the hosting layer without scattering:

$$J_{n,hot} = \frac{F_{n,esc}n_{QDash}v_{n,esc}}{h_{host}} \tag{4.62}$$

where $F_{n,esc}$ is the fraction of electrons escaping from the dashes as a function of total carrier density, while $v_{n,esc}$ is an escape velocity based on the effective mass and thickness of the hosting layer:

$$v_{n,esc} = \frac{2\pi\hbar}{dm^*_e} \tag{4.63}$$

From this an "escape time" for electrons, after which they will be thermalized on average, can be calculated:

$$\tau_{n,esc} = \frac{h_{host}}{v_{n,esc}F_{n,esc}} \tag{4.64}$$

All the equations in this section were written for electrons, but are applied analogously to holes.
In addition to the fundamental thermionic model, there a variety of additional leakage models that can be activated in PICS3D. These effectively add a further contribution to the escape current from the confined states, attempting to capture other carrier leakage

mechanisms, primarily due to Auger-related carrier excitation above the confining barrier. There are three implementations that ship with PICS3D: a combination of Auger and thermionic emission, as well as direct and indirect Auger carrier excitation. All three add another contribution to $J_{n,out}$:

$$J_{n,\mathrm{Auger}} = qv_{eff}n_{\mathrm{above}} \approxeq qv_{\mathrm{eff}}\beta n_{\mathrm{conf}} \tag{4.65}$$

where an identical equation could be written for holes. n_{above} is the fraction of confined electrons above the barrier, which is approximated by a fraction β of the total confined electron population n_{conf}. This factor is actually a constant, even though in reality it should vary as a function of bias as the distribution of carriers shifts. All three models deliver different expressions for the effective escape velocity v_{eff}, which fulfills a similar role to the thermal capture velocity v_{th} described earlier. Since these processes are Auger mediated, they increase in efficiency super-linearly with carrier density [189].

4.7 Optical calculations

In order to represent the propagation of waves within the laser, we use the semi-classical approach of quantum mechanical electron levels and classical electromagnetism for the electrical field. The following sections largely restate the formalism employed by PICS3D as outlined in the manual [189]. Further explanations were added to parts of the derivation of the formalism to provide further context.

4.7.1 Maxwell's equations

For such a classical electromagnetic wave, the relationship between its electric and magnetic field components $\vec{E}$ and $\vec{H}$ are represented by the Maxwell equations [50] for the electric and magnetic field $\vec{E}$ and $\vec{H}$:

$$\boldsymbol{\nabla} \times \vec{H} = \frac{\partial \vec{D}}{\partial t} + \frac{\partial \vec{P}}{\partial t} + \sigma \vec{E} = \epsilon\epsilon_0 \frac{\partial \vec{E}}{\partial t} + \frac{\partial \vec{P}}{\partial t} + \sigma \vec{E} \tag{4.66}$$

$$\boldsymbol{\nabla} \times \vec{E} = -\frac{\partial \vec{B}}{\partial t} = -\mu_0 \frac{\partial \vec{H}}{\partial t} \tag{4.67}$$

with the displacement field $\vec{D}$, the polarization density $\vec{P}$, the electrical conductivity σ, and the dielectric function ϵ, as well as the magnetic induction $\vec{B}$ and vacuum permeability μ_0. Here we used the following expression for the displacement field:

$$\vec{D} = \epsilon_0 \vec{E} + \vec{P} \tag{4.68}$$

Its gradient, $\nabla \cdot \vec{D}$, is equal to the charge density ρ:

$$\nabla \cdot \vec{D} = \rho \tag{4.69}$$

This is equivalent to Poisson's equation in Eq. 4.1.
The magnetic field $\vec{H}$ and the magnetic induction are linked by the magnetization $\vec{M}$:

$$\vec{H} = \frac{1}{\mu_0}\vec{B} - \vec{M} \tag{4.70}$$

Since the magnetization of the zincblende semiconductors we are interested with in this work is negligible, $\vec{M} \approxeq 0$. We are then left with a reduced set of Maxwell's equations:

$$\nabla \vec{E} = \frac{1}{\epsilon_0}(\rho - \nabla \vec{P}) \tag{4.71}$$

$$\nabla \vec{B} = 0 \tag{4.72}$$

$$\nabla \times \vec{E} + \frac{\partial \vec{B}}{\partial t} = 0 \tag{4.73}$$

$$\nabla \times \vec{B} - \epsilon_0 \mu_0 \frac{\partial \vec{E}}{\partial t} = \mu_0 \left(\vec{J} + \frac{\partial \vec{P}}{\partial t} \right) \tag{4.74}$$

Since we are interested in the electrical field at optical frequencies, the net charge transport via current $\vec{J}$ is negligible. For an electric field and magnetic induction oscillating at angular frequency ω, we can introduce the time dependence by appending the factor $e^{-i\omega t}$:

$$\vec{B}(t) = \vec{B}_0 e^{-i\omega t} \tag{4.75}$$

$$\vec{E}(t) = \vec{E}_0 e^{-i\omega t} \tag{4.76}$$

$$\vec{P}(t) = \vec{P}_0 e^{-i\omega t} \tag{4.77}$$

Eq.s 4.74 then simplify further into:

$$\nabla \times \vec{E} + i\omega \vec{B} = 0 \tag{4.78}$$

$$\nabla \times \vec{B} - i\omega \epsilon_0 \mu_0 \vec{E} = i\omega \mu_0 \vec{P} \tag{4.79}$$

The polarization can be split into an electric field induced polarization term and a contribution from spontaneous emission, something which we touch upon in 3.2.3 when discussing the homogeneous broadening of a transition. The total polarization $\vec{P}$ then reads as:

$$\vec{P} = \epsilon_0(\epsilon_{tot} - 1)\vec{E} + \vec{P}_{spon} \tag{4.80}$$

$\vec{P}_{spon}$ is driven by random spontaneous emission events, which is unrelated to the present optical field $\vec{E}$. Re-arranging Eq. 4.79 and 4.80 allows substituting for $\vec{B}$:

$$-\nabla \times \nabla \times \vec{E} + \omega^2 \epsilon_0 \epsilon_{tot} \mu_0 \vec{E} = -\mu_0 \omega^2 \vec{P}_{spon} \tag{4.81}$$

Assuming an electrically neutral semiconductor on the length and time scale of the oscillation, $\boldsymbol{\nabla}\vec{E} = 0$ and $-\nabla \times \nabla \times \vec{E} = \boldsymbol{\nabla}^2 \vec{E}$. Using $c = \frac{1}{\epsilon_0 \mu_0}$, we then arrive at a vector wave equation describing the interaction between the optical field and the semiconducting material:

$$\boldsymbol{\nabla}^2 \vec{E} + \frac{\omega^2}{c^2} \epsilon_{tot} \vec{E} = -\mu_0 \omega^2 \vec{P}_{spon} \tag{4.82}$$

Most of the interaction between the optical wave and the material is captured by the dielectric function ϵ_{tot}, which incorporates absorptive losses and gain amplification in addition to the dampening of the electric field due to polarization [189]. A more thorough discussion of the dielectric function can be found in 2.3.3. The random nature of the spontaneous emission affecting $\vec{P}_{spon}$ results in Eq. 4.82 being a stochastic differential equation. Given its random nature, we expect $\left\langle \vec{P}_{spon} \right\rangle = 0$. It then fulfills all criteria for a Langevin force $\vec{F}_\omega$ [218]:

$$\vec{F}_\omega = -\mu_0 \omega^2 \vec{P}_{spon} \tag{4.83}$$

With this force defined, we can state the wave equation for the electric field as used by PICS3D:

$$\boldsymbol{\nabla}^2 \vec{E} + \frac{\omega^2}{c^2} \epsilon_{tot} \vec{E} = \vec{F}_\omega \tag{4.84}$$

We will now use it to get a feeling for how it relates to the computations done by PICS3D at every step of the optical solver.

4.7.2 The scalar wave equation

The electric field is a vectorial quantity. However, the orientation of the transition dipoles responsible for stimulating laser emission generally favour emission along a certain axis. This leads to a linear polarization, and we can therefore collapse $\vec{E}$ into a scalar quantity E with an implied orientation along the linear polarization axis. With y as the growth direction, which is the normal to the substrate plane, the light emitted from the cavity via stimulated emission will predominantly be polarized along y. For now however, we will only assume that the linear polarization lies in the xy-plane.
The scalar wave equation is just Eq. 4.84 reduced to one dimension:

$$\nabla^2 E + \frac{\omega^2}{c^2} \epsilon_{tot} E = F_\omega \tag{4.85}$$

The waveguide design we are interested in is a Fabry-Perot cavity which is confined transversally and extends along the longitudinal direction. As a result, the mode will be comprised of a longitudinal component $E(z)$ and a transverse component $\phi(x, y)$ (see Ch. 3 for a more thorough discussion). We will also assume that we are dealing with a monochromatic wave with angular frequency ω, as the resonator linewidth $d\omega$ is small ($\approx 10^9$ Hz) compared to the frequency of the light oscillation ($\approx 10^{14}$ Hz).
Building on the discussion outlined in 3.2.3, we assume there is a complete set of orthogonal transverse modes $\phi_n(x, y)$ that satisfy the following equation:

$$\left[\frac{\partial^2}{\partial x^2} + \frac{\partial^2}{\partial y^2} + \frac{\partial^2}{\partial z^2}\right] \phi_n(x, y) + \frac{\omega^2}{c^2}\epsilon_{tot}\phi_n(x, y) = k^2(z)\phi_n(x, y) \tag{4.86}$$

Using the wavenumber along z, $k(z)$:

$$k(z) = \frac{\omega}{c} n_{eff}(z) \tag{4.87}$$

$n_{eff}(z)$ is the z-dependent effective refractive index, which simplifies the complex lateral structure into a single quantity that varies with mode shape. It also incorporates effects such as longitudinal spatial hole burning that occur along the length of the cavity.
If $\phi_n(x, y)$ are orthogonal and form a complete set, which we assumed earlier, the final lateral mode $\phi(x, y)$ can be written as a linear superposition of modes $\phi_n(x, y)$:

$$\phi(x, y) = \sum_n A_n \phi_n(x, y) \tag{4.88}$$

with the linear coefficients A_n:

$$A_n = \frac{\int \phi_n^*(x, y)\phi(x, y) d\vec{r}}{\int \phi_n^*(x, y)\phi_n(x, y) d\vec{r}} = \frac{\langle \phi_n|\phi\rangle}{\langle \phi_n|\phi_n\rangle} \tag{4.89}$$

Using the combined scalar electric field $E(x, y, z) = E(z)\,|\phi\rangle$ in Eq. 4.85 then yields:

$$\left[\frac{\partial^2}{\partial x^2} + \frac{\partial^2}{\partial y^2} + \frac{\partial^2}{\partial z^2}\right] E(z)\,|\phi\rangle + \frac{\omega^2}{c^2}\epsilon_{tot}E(z)\,|\phi\rangle = F_\omega \tag{4.90}$$

Here a weak z-dependence of the lateral mode shape is assumed, $\frac{\partial^2}{\partial z^2}\,|\phi\rangle \approxeq 0$. Similarly, $E(z)$ is invariant along x and y, so $\frac{\partial^2}{\partial x^2}E(z) = \frac{\partial^2}{\partial y^2}E(z) = 0$. We can then split the first term into two parts using the [product rule ($\frac{\partial}{\partial x}\left[g(x)f(x)\right] = g(x)\frac{\partial f(x)}{\partial x} + \frac{\partial g(x)}{\partial x}f(x)$):

$$E(z)\left[\frac{\partial^2}{\partial x^2} + \frac{\partial^2}{\partial y^2}\right]|\phi\rangle + |\phi\rangle\,\frac{\partial^2}{\partial z^2}E(z) + \frac{\omega^2}{c^2}\epsilon_{tot}E(z)\,|\phi\rangle = F_\omega \tag{4.91}$$

We can rearrange this to resemble the lateral mode condition in Eq. 4.86:

$$|\phi\rangle \frac{\partial^2}{\partial z^2}E(z) + E(z)\left(\left[\frac{\partial^2}{\partial x^2} + \frac{\partial^2}{\partial y^2}\right] + \frac{\omega^2}{c^2}\epsilon_{tot}\right)|\phi\rangle = F_\omega \tag{4.92}$$

Substituting the linear superposition for $|\phi\rangle$:

$$|\phi\rangle \frac{\partial^2}{\partial z^2}E(z) + E(z)\left(\left[\frac{\partial^2}{\partial x^2} + \frac{\partial^2}{\partial y^2}\right] + \frac{\omega^2}{c^2}\epsilon_{tot}\right)\sum_n A_n |\phi_n\rangle = F_\omega \tag{4.93}$$

$$|\phi\rangle \frac{\partial^2}{\partial z^2}E(z) + E(z)\sum_n A_n\left(\left[\frac{\partial^2}{\partial x^2} + \frac{\partial^2}{\partial y^2}\right]|\phi_n\rangle + \frac{\omega^2}{c^2}\epsilon_{tot}|\phi_n\rangle\right) = F_\omega \tag{4.94}$$

$$|\phi\rangle \frac{\partial^2}{\partial z^2}E(z) + E(z)\sum_n A_n k^2(z)|\phi_n\rangle = F_\omega \tag{4.95}$$

where we used the lateral mode condition from Eq. 4.86 for $|\phi_n\rangle$.
Multiplying both sides by $\langle\phi_n|$, we can start towards reducing the dependence to one dimension:

$$\langle\phi_n|\phi\rangle \frac{\partial^2}{\partial z^2}E(z) + E(z)\sum_n A_n k^2(z)\langle\phi_n|\phi_n\rangle = \langle\phi_n| F_\omega \tag{4.96}$$

$$\langle\phi_n|\phi\rangle \frac{\partial^2}{\partial z^2}E(z) + E(z)k^2(z)\langle\phi_n|\phi\rangle = \langle\phi_n| F_\omega \tag{4.97}$$

$$\langle\phi_n|\phi\rangle\left[\frac{\partial^2}{\partial z^2}E(z) + k^2(z)E(z)\right] = \langle\phi_n| F_\omega \tag{4.98}$$

The Langevin force is a vector $|F_\omega\rangle$, so we undertake one last rearrangement:

$$\langle\phi_n|\phi\rangle\left[\frac{\partial^2}{\partial z^2}E(z) + k^2(z)E(z)\right] = \langle\phi_n|F_\omega\rangle \tag{4.99}$$

$$\frac{\partial^2}{\partial z^2}E(z) + k^2(z)E(z) = \frac{\langle\phi_n|F_\omega\rangle}{\langle\phi_n|\phi\rangle} = f(z) \tag{4.100}$$

We therefore have a problem that is split into two parts: a lateral solution that interacts with the lateral waveguide structure via $\langle\phi_n|F_\omega\rangle$ and a longitudinal solution that is affected by the effective refractive index along z integrated into $k^2(z)$. As we have assumed that the second derivative of the lateral solution with respect to z is negligible, this approach primarily holds for longitudinal waveguides with slowly varying longitudinal index profiles. Armed with this solution, we will now look at the solution approach using Green's function.

4.7.3 Green's function

A common method of solving partial differential equations that has found applications in all parts of physics and especially solid state physics employs the Green's function to solve equations of the following form [219, 220]:

$$\mathcal{L}u(z) = f(z) \tag{4.101}$$

where $\mathcal{L}$ is a linear differential operator and $f(z)$ is an arbitrary function. It has solutions $u(z)$:

$$u(z) = \int f(z_s)\mathcal{G}(z, z_s)dz_s \tag{4.102}$$

with the Green's function $\mathcal{G}(z, z_s)$:

$$\mathcal{G}(z, z_s) = \delta(z - z_s) \tag{4.103}$$

with the delta function $\delta(z - z_s)$. The Green's function method allows building the desired function, $u(z)$ in this case, by evaluating $f(z)$ at a continuous set of points z_s and arriving at partial solutions $\mathcal{G}(z, z_s)$. Via integration these partial solutions can then be combined into a formal solution of the whole problem. This works well for the longitudinal waveguide problem, as we can expend the solution from one location unto the whole device. Using the boundary conditions, a solution can be determined in one location, like a facet, and then extended across the entire waveguide.
For the mode problem we considered in the previous section, we arrived at a differential equation in Eq. 4.100. It featured a linear operator acting on the longitudinal electric field $E(z)$. We restate the problem, rewriting it in a manner that makes the resemblance more apparent:

$$\mathcal{L}u(z) = \left[\frac{\partial^2}{\partial z^2} + k^2(z)\right] u(z) = f(z) \tag{4.104}$$

There are multiple ways to continue this solution process, with PICS3D implementing an approach using the Wronskian $\mathcal{W}$ to arrive at solutions for $u(z)$ from a known solution determined via boundary conditions.

4.7.4 The Wronskian

Assuming we have two differentiable functions $w(z)$ and $v(z)$, we can write a square matrix using the original functions and their derivatives $w'(z)$ and $v'(z)$. The Wronskian $\mathcal{W}$ is

then the determinant of this square matrix:

$$\mathcal{W}(z) = \det \begin{bmatrix} w(z) & w'(z) \\ v(z) & v'(z) \end{bmatrix} = w(z)v'(z) - v(z)w'(z) \tag{4.105}$$

The determinant has the property that it vanishes if $w(z)$ and $v(z)$ are linear dependent on one another. This is a useful criterion to find orthogonal functions. Additionally, if the two functions are independent, but both represents solutions for a homogeneous equation such as $\mathcal{L}u(z)$, the z-dependence of $\mathcal{W}$ vanishes:

$$\mathrm{d}z\, \mathcal{W}(z) = w(z)v''(z) - v(z)w''(z) = 0 \tag{4.106}$$

Given that $\frac{\partial^2}{\partial z^2} u(z) = -k^2(z)u(z)$, we find that this conditions holds for Eq. 4.104.
This is very useful if one solution is already known. Assuming we have found $w(z)$ using $\mathcal{L}w(z) = 0$, the Wronskian allows determining a second independent solution $v(z)$:

$$\mathcal{W} = w(z)v'(z) - v(z)w'(z) \tag{4.107}$$

$$= w^2(z) \frac{\mathrm{d}}{\mathrm{d}z} \frac{v(z)}{w(z)} \tag{4.108}$$

A second, independent solution to $\mathcal{L}$ can then be found using the constant value for $\mathcal{W}$ and integrating:

$$v(z) = \mathcal{W} w(z) \int_{z_0}^{z} \frac{1}{w^2(a)} da \tag{4.109}$$

This can now be employed to find formal solutions to Eq. 4.104. Substituting $u(z) = w(z)v(z)$, we obtain the following equation:

$$v\mathcal{L}w(z) + w(z)v''(z) + 2w'(z)v'(z) = f(z) \tag{4.110}$$

We can substitute $Z_1(z)$ for $w(z)$, where $Z_1(z)$ is the solution to $\mathcal{L}Z_1 = 0$:

$$v''(z) + 2\frac{Z_1'(z)}{Z_1(z)} v'(z) = \frac{f(z)}{Z_1(z)} \tag{4.111}$$

We now multiply this equation by $\frac{d}{dz}\left(\frac{Z_2(z)}{Z_1(z)}\right) = \left(\frac{Z_2(z)}{Z_1(z)}\right)'$:

$$v''(z) \left(\frac{Z_2(z)}{Z_1(z)}\right)' + 2\frac{Z_1'(z)}{Z_1(z)} \left(\frac{Z_2(z)}{Z_1(z)}\right)' v'(z) = \frac{f(z)}{Z_1(z)} \left(\frac{Z_2(z)}{Z_1(z)}\right)' \tag{4.112}$$

Using the equality in Eq. 4.108, we can find an expression for $\mathcal{W}$, also substituting $Z_2(z)$ for $v(z)$:

$$\frac{d}{dz}\left(\frac{Z_2(z)}{Z_1(z)}\right) = \frac{\mathcal{W}}{Z_1^2(z)} \tag{4.113}$$

$$\frac{d^2}{d^2z}\left(\frac{Z_2(z)}{Z_1(z)}\right) = \frac{d}{dz}\left(\frac{\mathcal{W}}{Z_1^2(z)}\right) \tag{4.114}$$

$$= \mathcal{W}\frac{d}{dz}\frac{1}{Z_1^2(z)} = \mathcal{W}\left(-2\frac{Z_1'(z)}{Z_1^3(z)}\right) = -2\frac{\mathcal{W}}{Z_1^2(z)}\frac{Z_1'(z)}{Z_1(z)} \tag{4.115}$$

Where we used the z-independence of $\mathcal{W}$ again. This can be arranged to arrive at an expression for the middle term in Eq. 4.112. First, we substitute $\frac{\mathcal{W}}{Z_1^2(z)} = \left(\frac{Z_2(z)}{Z_1(z)}\right)'$:

$$\left(\frac{Z_2(z)}{Z_1(z)}\right)'' = -2\left(\frac{Z_2(z)}{Z_1(z)}\right)'\frac{Z_1'(z)}{Z_1(z)} \tag{4.116}$$

We then rearrange and multiply by $v'(z)$:

$$2\frac{Z_1'(z)}{Z_1(z)}\left(\frac{Z_2(z)}{Z_1(z)}\right)'v'(z) = -\left(\frac{Z_2(z)}{Z_1(z)}\right)''v'(z) \tag{4.117}$$

Eq. 4.112 then reads as following:

$$v''(z)\left(\frac{Z_2(z)}{Z_1(z)}\right)' - \left(\frac{Z_2(z)}{Z_1(z)}\right)''v'(z) = \frac{f(z)}{Z_1(z)}\left(\frac{Z_2(z)}{Z_1(z)}\right)' \tag{4.118}$$

The left hand side clearly implies the quotient rule, so we can collapse it into the following expression:

$$v''(z)\left(\frac{Z_2(z)}{Z_1(z)}\right)' - \left(\frac{Z_2(z)}{Z_1(z)}\right)''v'(z) = \left[\left(\frac{Z_2(z)}{Z_1(z)}\right)'\right]^2\frac{d}{dz}\frac{v'(z)}{\left(\frac{Z_2(z)}{Z_1(z)}\right)'} \tag{4.119}$$

The right hand term in Eq. 4.118 can also be simplified, using $\mathcal{W}^2 = Z_1^4(z)\left[\left(\frac{Z_2(z)}{Z_1(z)}\right)'\right]^2$:

$$\frac{f(z)}{Z_1(z)}\left(\frac{Z_2(z)}{Z_1(z)}\right)' = \frac{f(z)}{Z_1(z)}\left(\frac{\mathcal{W}}{Z_1^2(z)}\right) \tag{4.120}$$

$$= \frac{f(z)}{\mathcal{W}}\left(\frac{\mathcal{W}^2}{Z_1^3(z)}\right) \tag{4.121}$$

$$= \frac{f(z)Z_1(z)}{\mathcal{W}} \tag{4.122}$$

The second order inhomogeneous equation can then be written in an equivalent first order form:

$$\frac{d}{dz}\frac{v'(z)}{\left(\frac{Z_2(z)}{Z_1(z)}\right)'} = \frac{f(z)Z_1(z)}{\mathcal{W}} \tag{4.123}$$

We can then arrive at an expression for $v'(z)$ via integration:

$$v'(z) = \left(\frac{Z_2(z)}{Z_1(z)}\right)' \int \frac{f(z)Z_1(z)}{\mathcal{W}}\,\mathrm{d}z \tag{4.124}$$

Lastly, we notice the similarity to the product rule for the right hand side:

$$\frac{d}{dz}\left[\frac{Z_2(z)}{Z_1(z)}\int \frac{f(z)Z_1(z)}{\mathcal{W}}\,\mathrm{d}z\right] = \left(\frac{Z_2(z)}{Z_1(z)}\right)' \int \frac{f(z)Z_1(z)}{\mathcal{W}}\,\mathrm{d}z + \frac{Z_2(z)}{Z_1(z)}\frac{f(z)Z_1(z)}{\mathcal{W}} \tag{4.125}$$

$$= \left(\frac{Z_2(z)}{Z_1(z)}\right)' \int \frac{f(z)Z_1(z)}{\mathcal{W}}\,\mathrm{d}z + \frac{f(z)Z_2(z)}{\mathcal{W}} \tag{4.126}$$

By adding $\frac{f(z)Z_2(z)}{\mathcal{W}}$ to both sides of Eq. 4.124, we obtain an expression for one part of the solution to the Green's function $u(z) = Z_1(z)v(z)$:

$$v'(z) + \frac{f(z)Z_2(z)}{\mathcal{W}} = \frac{d}{dz}\left[\frac{Z_2(z)}{Z_1(z)}\int \frac{f(z)Z_1(z)}{\mathcal{W}}\,\mathrm{d}z\right] \tag{4.127}$$

$$v(z) = \frac{Z_2(z)}{Z_1(z)}\int_{z_1}^{z} \frac{f(z)Z_1(z)}{\mathcal{W}}\,\mathrm{d}z + \int_{z}^{z_2} \frac{f(z)Z_2(z)}{\mathcal{W}}\,\mathrm{d}z \tag{4.128}$$

The complete solution is then:

$$u(z) = Z_1(z)v(z) = Z_2(z)\int_{z_1}^{z} \frac{f(z)Z_1(z)}{\mathcal{W}}\,\mathrm{d}z + Z_1(z)\int_{z}^{z_2} \frac{f(z)Z_2(z)}{\mathcal{W}}\,\mathrm{d}z \tag{4.129}$$

z_1 and z_2 can be regarded as the starting and ending points of the longitudinal cavity, making $Z_1(z)$ and $Z_2(z)$ the functions describing the longitudinal optical field propagating into the cavity from each facet. $Z_1(z)$ satisfies the boundary condition at z_1, while $Z_2(z)$ satisfies it at z_2. Using $u(z)$, we can then build the Green's function using $f(z) = \delta(z - z_s)$:

$$\mathcal{G}(z, z_s) = Z_2(z)\int_{z_1}^{z} \frac{\delta(z - z_s)Z_1(z)}{\mathcal{W}}\,\mathrm{d}z + Z_1(z)\int_{z}^{z_2} \frac{\delta(z - z_s)Z_2(z)}{\mathcal{W}}\,\mathrm{d}z \tag{4.130}$$

$$= \frac{1}{\mathcal{W}}\left[Z_1(z)Z_2(z_s)\Theta(z_s - z) + Z_2(z)Z_1(z_s)\Theta(z - z_s)\right] \tag{4.131}$$

With the Heaviside step function Θ. From this we can arrive at the longitudinal electric field $E(z)$:

$$E(z) = \int f(z_s)\mathcal{G}(z, z_s)dz_s \tag{4.132}$$

where $f(z_s)$ is the spontaneous emission noise at z_s as stated in Eq. 4.100.
As we will discuss in Ch. 5 when examining the assumptions underlying this simulation work, the use of this Green's function formalism prevents PICS3D from representing the ultrafast dynamics underlying mode-locking. This approach breaks down if the boundary conditions for the two facets of the longitudinal cavity are vastly different. They therefore need to be in equilibrium for the solution derived via integration of $\mathcal{G}(z, z_s)$ to be appropriate. This is true for slowly varying time transients, as one would observe when pulsing the applied bias for example. For a modulation in the kHz to MHz range, the cavity round trip time (see Eq. 3.71) is small enough that a new equilibrium between facets can be established over a negligible fraction of the modulation period. The cavity perturbation is varying sufficiently slowly for the cavity to follow. During passive mode-locking processes, the cavity conditions vary on the same time scale as the round trip time. The facets are therefore not in equilibrium and the solutions derived via the Green's function method are unfortunately invalid. We will justify the use of PICS3D irrespective of this limitation in Ch. 5.

4.7.5 Langevin forces and spectral diffusion coefficients

Due to the random nature of spontaneous emission, the expectation values for the Langevin forces over both space and time are zero, as the quantum fluctuations driving the emission are entirely uncorrelated. The correlation function between the driving force at two different frequencies and locations is therefore:

$$\left\langle F_\omega(\vec{r}) \middle| F^*_{\omega'}(\vec{r}') \right\rangle = 2D_{FF^*}(\vec{r})\delta(\vec{r}-\vec{r}')(\omega-\omega') \tag{4.133}$$

Note, that unlike the previous section where we denoted the derivative using the prime symbol, here it just denotes a frequency or position different from the original one. As previously, we will assume that we are dealing with a monochromatic wave, so we can drop the dependency on ω. Given that the linear energy density is [189]:

$$s_\omega \hbar\omega = 2\epsilon_0 \bar{n} n_g \left\langle |E(z)|^2 \right\rangle \int\int |\phi(x,y)|^2 dydx \qquad = 2\epsilon_0 n n_g \left\langle |E(z)|^2 \right\rangle \tag{4.134}$$

Where ϵ_0 is the vacuum permittivity, $\bar{n}$ is complex refractive index, and n_g is the group refractive index at ω. s_ω is the photon density at ω, reduced to a linear density along z. We combine this with another expression for the linear energy density, derived using the solutions to the Green's function for a cavity with perfectly reflective facets [189]:

$$\left\langle |E(z)|^2 \right\rangle = \frac{2D_{FF*}(z)}{8|k|^2\kappa} \tag{4.135}$$

where k is the wavenumber along z, which we presume to be uniform and κ is the imaginary part of the refractive index. A more thorough derivation of this result can be found in D7 of [189]. Combining the two expressions, we arrive at an expression for the noise power in the nth mode P_n due to spontaneous emission:

$$P_n = v_g s_\omega \hbar\omega = 2 v_{g,n} \epsilon_0 \bar{n} n_g \frac{2D_{FF*}(z)}{8|k|^2 \kappa} \tag{4.136}$$

where $v_{g,n}$ is the group velocity for the nth mode, see Eq. 3.57. However, this noise power P_n can also be derived using the average mode occupation number $\langle n_\omega \rangle$:

$$P_n = \frac{\hbar\omega \langle n_\omega \rangle}{2\pi} \tag{4.137}$$

Setting the two expression for the noise power into the nth mode equal, we can arrive at an expression for the spectral diffusion coefficient:

$$D_{FF^*}(z) = \frac{|k|^2 \hbar\omega\kappa \langle n_\omega \rangle}{\pi c \epsilon_0 \bar{n}} \tag{4.138}$$

Here we will make two important substitutions: first of all, we use the relationship between the local longitudinal gain function $g(z)$ and the complex part of the refractive index to replace $\kappa = -\frac{1}{2}(\hbar\omega, z)$. Then we assume that the change in $|k|$ over z is small due to negligible loss, so we can replace $|k|^2$ with $\frac{\bar{n}^2}{\omega}^2 c^2$. The resulting expression for the diffusion coefficient is then:

$$2D_{FF^*}(z) = -\frac{\hbar\omega^3 g(\hbar\omega, z) \langle n_\omega \rangle}{\pi c^3 \epsilon_0} \tag{4.139}$$

Finally, we need an expression for the mode occupation:

$$\langle n_\omega \rangle = \left(e^{\frac{\hbar\omega - qV_F}{k_B T}} - 1 \right) \tag{4.140}$$

where V_F is the chemical potential for the photons. Using a relationship between the spectral gain $(\hbar\omega, z)$ and the bulk spontaneous recombination rate $r_{spon}(\hbar\omega)$ in a medium, allows replacing the right side:

$$g(\hbar\omega, z) = \frac{r_{spon}(\hbar\omega)}{v_g D(\hbar\omega)} \left[1 - e^{\frac{\hbar\omega - qV_F}{k_B T}} \right] \tag{4.141}$$

with the photon mode density $D(\hbar\omega)$:

$$D(\hbar\omega) = \left(\frac{\bar{n}}{c} \right)^3 \frac{\omega^2}{\hbar\pi^2} \tag{4.142}$$

The product $g(\hbar\omega, z) \langle n_\omega \rangle$ can then be used to eliminate the photon potential V_F:

$$g(\hbar\omega, z) \langle n_\omega \rangle = -\frac{r_{spon}(\hbar\omega)}{v_g D(\hbar\omega)} \tag{4.143}$$

The result is an expression for the diffusion coefficient that looks something like this:

$$D_{FF^*}(z) = \frac{\hbar\omega r_{spon}(\hbar\omega)\pi\hbar}{2\bar{n}^2 v_g \epsilon_0} \tag{4.144}$$

This can be simplified further by introducing the integral $\int\int \phi_n^*(x, y) r_{spon}(\hbar\omega)\phi_n(x, y)dydx$, which is equal to $\langle\phi_n| r_{spon}(\hbar\omega) |\phi_n\rangle$. This accounts for a simplification we have made: $r_{spon}(\hbar\omega)$ is a local variable, which varies both longitudinally and across the cross-section of the laser. The integral allows eliminating the transverse dependence, as the magnitude of the lateral optical mode is used to arrive at z-dependent spontaneous emission rate. Removing this inconsistency we used until now, we arrive at the final spectral diffusion coefficient, the driving force for random noise in the lasing modes:

$$D_{FF^*}(\hbar\omega, z) = \frac{\hbar^2\omega\pi \langle\phi_n| r_{spon}(\hbar\omega) |\phi_n\rangle}{2\bar{n}^2 v_g \epsilon_0} \tag{4.145}$$

with now have an approach for determining the lateral optical modes $\phi_n(x, y)$ from the vectorial wave equation in Eq. 4.84 and corresponding longitudinal optical fields $E(z)$ via the Green's function in Eq. 4.101. Without too much technical detail, we will now briefly examine how to numerically find solutions to either problem.

4.7.6 Numerical approach

Throughout this section, we will assume we are dealing with transverse electric (TE) modes of the form $\vec{E} = (E_x, E_y, 0)$. The lateral modes can be determined using the vectorial wave equation, which we examined earlier:

$$\boldsymbol{\nabla}^2\phi_n(x, y) + k_0(\epsilon_{opt}(x, y) - n_{eff}^2)\phi_n(x, y) = 0 \tag{4.146}$$

$\epsilon_{opt}(x, y)$ is the high frequency dielectric constant and n_{eff} is the effective index, specific to mode $\phi_n(x, y)$. PICS3D offers multiple ways of calculating this effective index, including an effective index method (EIM) and purely analytical approximations using Gaussian mode profiles. The effective index method is relevant as it works as the foundation of the Schrödinger solver used to calculate the confined states of isolated QDs and QDashes. Eq. 4.146 is solved using a restarted Arnoldi iterator which operates on the sparse matrix constructed from the mesh nodes. Its technical details go beyond the scope of this work and we point the reader to texts such as Saad et al. for further details [221]. In essence,

it will iteratively alter n_{eff} and $\phi_n(x, y)$ until Eq. 4.146 is satisfied.
Once lateral mode solutions are found, and n_{eff} is known, the Green's function approach that we outlined previously is used to find partial solutions to $E(z)$. The approach employed by PICS3D computes a round trip gain, $g_{RTG}(\omega)$. This is a complex quantity, which captures all the amplitude- and phase-altering effects that light travelling within the cavity is subjected to during one round trip. The abstract formulation of the problem then reads as follows:

$$W(\omega) = 1 - g_{RTG}(\omega) \tag{4.147}$$

The local minima to this equation are the longitudinal modes on which light is emitted from the cavity [222]. PICS3D finds these zeroes using the previously calculated n_{eff} due to the lateral modes combined with the longitudinal gain.
This is a natural transition to the next section: the accurate description of a laser requires an accurate description of its gain. Gain is generally described using the gain function, which links internal states of the semiconductor with its ability to amplify light. We will now examine three gain functions that apply to this work: one for quantum wells, one for quantum dots, and lastly, an attempt at introducing a gain function specific to quantum dashes.

4.7.7 Gain calculations

The gain function is strongly dependent on a variety of material parameters. Some of these parameters are a function of bias, most notably the quasi-Fermi levels $\epsilon_{f,n}(\vec{r})$ and $\epsilon_{f,p}(\vec{r})$, which determine the inversion factor and thereby the strength of light amplification. Since the inversion factor for a given carrier density varies strongly with the shape and magnitude for the DOS, different degrees of dimensional confinement result in vastly different gain functions. There are therefore three relevant models we will discuss: first, there is the internal model for quantum well transitions, relevant for transitions in any thin piece of semiconductor in the active region, i.e. the barriers and the wetting layer. Secondly, the quantum dot model used for some parts of the work where we treat quantum dashes as elongated dots. The last gain model we will discuss is based on Gioannini's development of a quantum dash gain functions in the InAs/InAlGaAs system, which we attempted to recreate and alter for the InAs/InGaAsP system [92, 192]. We do not succeed, but share our progress in the interest of potential future research.

Gain model for quantum wells

As QDs are treated as embedded states in a QW, the resulting gain functions contains contributions from both the QW and the QDs:

$$g_{host} = r_{QW} g_{QW} + g_{QD} \tag{4.148}$$

Here g_{QW} and g_{QD} are the gain functions for the QW and the QDash, respectively, with r_{QW} denoting the area fraction of the wetting layer compared to the QDashes. The hosting layer in the model is the InP capping layer, which has a band gap around 1.32 eV at room temperature, far greater than the transition energy of the QDashes around $\approxeq 0.8$ eV [76]. The gain contribution from the hosting layer is therefore negligible.
For the wetting layer, however, comprised of InAs and with heights of $\approxeq 1$ nm, can be relevant. Transitions between confined wetting layer states can lie closer to the dash state transitions, even though the expectation value would still be for a transition that is $\approxeq$ 100 meV removed from the ground state transition of the dashes [223]. Depending on the degree of broadening, the wetting layer may then have an impact on transitions between higher lying states.
Assuming no band mixing and parabolic bands, the gain function for quantum wells can be stated as:

$$g_{QW}(\hbar\omega) = \sum_i \sum_j \delta_{ij} g_{ij}(\hbar\omega) \frac{\tau}{\hbar} L(\hbar\omega - E^0_{ij}, \frac{h}{\tau}) \tag{4.149}$$

where $g_{ij}(\hbar\omega)$ is the gain between the jth conduction and ith valence band state, E^0_{ij} is the optical transition energy between them, and τ is a time constant reflecting the degree of homogeneous broadening. δ_{ij} is the Dirac delta function, which appears for symmetry reasons we discussed in Ch. 2. $L(\hbar\omega - E^0_{ij}, \frac{\hbar}{\tau})$ is a Lorentzian broadening function, which we first encountered in Eq. 3.58. The gain for a given set of states $g_{ij}(\hbar\omega)$ can be written as:

$$g_{ij}(\hbar\omega) = \frac{2\pi}{\hbar} |H_{ij}|^2 (f_j(\hbar\omega) - f_i(\hbar\omega)) \frac{\epsilon_r}{n_r c} \rho_{ij}(\hbar\omega) \tag{4.150}$$

$\rho_{ij}(\hbar\omega)$ is the joint density of states between the ith and jth state, while n_r and ϵ_r are the real parts of the refractive index and dielectric function, with c being the speed of light [224]. $|H_{ij}|^2$ is another variant of the transition matrix element we encountered before, which we can expand into [189]:

$$|H_{ij}|^2 = \left(\frac{q}{m_0}\right) \left(\frac{2\hbar\omega}{4\epsilon_1 \epsilon_0 \omega^2}\right) M^2_{ij} \tag{4.151}$$

M^2_{ij} are the interband dipole moments, for which PICS3D uses a formulation based on Yamada et al [225]. $(f_j - f_i)$ is the inversion factor, which we calculate using the chemical

potentials for electrons and holes:

$$f_j(\hbar\omega) - f_i(\hbar\omega) = \left[1 + e^{\frac{E_j^0 - m_{ij}/m_j(\hbar\omega - E_{ij}^0) - \epsilon_{f,n}}{k_B T}}\right]^{-1} - \left[1 + e^{\frac{E_i^0 - m_{ij}/m_i(\hbar\omega - E_{ij}^0) - \epsilon_{f,p}}{k_B T}}\right]^{-1} \tag{4.152}$$

Where $1/m_{ij} = 1/m_i + 1/m_j$. This is the fundamental gain model used by

Gain model for quantum dots

The quantum dot gain model included in PICS3D is largely based on work by Dikshit and Pikal, which was developed for pyramidal InAs/InGaAs dots [226]. The gain function for a QD is the sum of the contributions from all electron and hole states denoted by n and m:

$$g_{QD}(\hbar\omega) = \sum_{n,m} \frac{\pi q^2 M_b^2 N_{QD}}{\omega \epsilon_0 c m_0^2 n_r h_{host}} \beta_{cp} \langle m|n\rangle \, G_s(\hbar\omega - E_{n,m})[f_c(\hbar\omega) - f_v(\hbar\omega)] \tag{4.153}$$

The summation $\sum_{n,m}$ is actually a double summation over all possible combinations of n and m. Other variables are the elementary charge q, the speed of light in vacuum c , the reduced Planck constant $\hbar$, the vacuum permittivity ϵ_0, is the electron mass m_0, is the real part of the refractive index n_r, and h_{host} is the thickness of the hosting layer. The transition dipole element from Eq. 2.45 is split into an absolute transition moment M_b^2 and the overlap integral $\langle m|n\rangle$, both assuming that the dependency on the electronic wavefunction wavevector $\vec{k}$ is weak. N_{QD} is the surface density of QDs, while β_{cp} is the dot coupling factor:

$$\beta_{cp} = \frac{1}{N_{coupled}} \tag{4.154}$$

where $N_{coupled}$ is the number of dots coupled into one quantum mechanical state, either vertically between layers with thin barriers, or within a layer due to close proximity of dots. This factor prevents counting the same state multiple times. The Gaussian broadening function $G_s(\hbar\omega - E_{n,m,s})$ represents the inhomogeneous size broadening:

$$G_s(\hbar\omega - E_{n,m}) = \frac{1}{\sigma_{inhomo}\sqrt{2\pi}} e^{-\frac{(\hbar\omega - E_{n,m})^2}{2\sigma_{inhomo}^2}} \tag{4.155}$$

where σ_{inhomo} is the inhomogeneous broadening energy, usually on the order of a few 10s of meVs for self-assembled QDashes [92, 227]. PICS3D uses an equivalent inhomogeneous

scattering time τ_{inhomo} instead:

$$\tau_{inhomo} = \frac{\hbar}{\sigma_{inhomo}} \tag{4.156}$$

The spontaneous recombination rate is very similar to the gain function, and reads as follows for the QD:

$$R_{spon,QD} = \sum_{n,m} \int \frac{\omega q^2 n_r M_b^2 N_{QD}}{\pi \epsilon_0 m_0^2 c^3 h_{host}} |\langle m,s|n,s\rangle|^2 G_s(\hbar\omega - E_{n,m,s}) f_c[1-f_v] d\omega \tag{4.157}$$

Eq. 4.153 is the gain function used for QDs in PICS3D and the gain model used when embedded states are used without calling an external gain model. It implicitly assumes that the homogeneous broadening is insignificant compared to the inhomogeneous broadening. The dimensionality factors in through the occupation factors for the conduction and valence band, f_c and f_v. The position of the chemical potentials, or quasi-Fermi levels, $\epsilon_{f,n}$ and $\epsilon_{f,p}$, depends on the position and density of available states and the injected carrier density. For a material with a lower number of available states, i.e. lower density of states, the chemical potentials respond stronger as current is injected. This means inversion is obtained more easily. The correct representation of the density of states is therefore important to accurately capture the carrier dynamics in a device. PICS3D allows altering the density of states using the *dos_reduction_factor* option in the *qdot_material* command that defines the details of the QD integration. It allows linearly scaling the density of states of the QDs, which was used in this work to obtain a threshold current and slope efficiency that matches experimental results.

Gain model for quantum dashes

While PICS3D does not allow access to the density of states (DOS) of the QD, it allows the import of externally calculated gain functions. This is done via gain tables, which tabulate the gain as a function of photon energy, temperature, carrier density, electron-hole ratio, and applied field. The values from the table act as reference points between which PICS3D interpolates the local gain value to use based on the local variables. This can be combined with an externally defined relationship between chemical potentials and carrier density, allowing the indirect integration of a custom density of states.
To gain model we choose as a one-dimensional stand in is based on work done by Gioannini on InAs/InP dashes with InAlGaAs barriers [192]. It poses that there is a degree of mixing between wetting layer and dash states, resulting in three different contributions to the gain due to transitions between confined states, transition between confined and mixed dash-wetting layer states, and wetting layer transitions. These terms are $g_{conf}(\hbar\omega)$, $g_{mixed}(\hbar\omega)$,

and $g_{WL}(\hbar\omega)$, respectively:

$$g_{conf}(\hbar\omega) = \frac{C_g}{\hbar\omega} \sum_{j}^{N_{Wire}} P_{wire,j} \int M_b^2 |\langle n|m\rangle|^2 \rho_{wire,j}(\epsilon) \left[f_n(E_n) - f_p(E_m)\right] L(\hbar\omega - \epsilon, \sigma) d\epsilon \tag{4.158}$$

$$g_{mixed}(\hbar\omega) = \frac{C_g}{\hbar\omega} \int\int \frac{\Delta x_{wire}}{2\pi^2 \bar{A}} M_b^2 |\langle n|m\rangle\,(k_y)|^2 \left[f_n(E_n) - f_p(E_m)\right] L(\hbar\omega - \epsilon, \sigma) dk_y dk_z \tag{4.159}$$

$$g_{WL}(\hbar\omega) = \frac{C_g}{\hbar\omega} \int M_b^2 |\langle l|w\rangle|^2 \frac{m_{2D_r}}{\pi\hbar^2 h_{WL}} u[\epsilon - (E_l - E_w] \left[f_n(E_l) - f_p(E_w)\right] L(\hbar\omega - \epsilon, \sigma) d\epsilon \tag{4.160}$$

where σ is a broadening energy that includes both homogeneous and inhomogeneous broadening. With C_g [92]:

$$C_g = \frac{\pi\hbar q^2}{m_0^2 \epsilon_0 n_r c} \tag{4.161}$$

m_{2D_r} is a reduced effective mass:

$$\frac{1}{m_{2D_r}} = \frac{1}{m_e^*} + \frac{1}{m_h} \tag{4.162}$$

The total gain is then:

$$g_{tot}(\hbar\omega) = \Gamma_{Wires}[g_{conf}(\hbar\omega) + g_{mixed}(\hbar\omega)] + \Gamma_{WL} g_{WL}(\hbar\omega) \tag{4.163}$$

Here $u[\epsilon - (E_l - E_w)]$ is a step function, and $\rho_{wire,j}$ is the one-dimensional joint density of states:

$$\rho_{wire,j}(\epsilon) = \frac{1}{\pi\bar{A}} \sqrt{*} \frac{2m_r}{\hbar^2} \frac{1}{\sqrt{\epsilon - (E_n - E_m)}} \tag{4.164}$$

where E_n and E_m are confined electron and hole states within the dash, while E_l are E_w states within the wetting layer. The energy variable ϵ represents the transition energy, which is defined as follows:

$$\epsilon = \epsilon_e + \epsilon_h + E_g \tag{4.165}$$

$$\epsilon_e = E_{(n,l)} + \frac{\hbar^2}{2m^*_{e,(wire,WL)}} \vec{k}^2 \tag{4.166}$$

$$\epsilon_h = E_{(m,w)} + \frac{\hbar^2}{2m^*_{h,(wire,WL)}} \vec{k}^2 \tag{4.167}$$

For confined states, the momentum dependence due to the last term is dropped. Other parameters are defined in [192].

4.8 Adding thermal effects

There are several heating mechanisms active within the device, which raise the device temperature and thereby alter the flow of carriers by changing the band structure and other material properties. The change in the temperature profile at a position $\vec{r}$ within a material is a combination of transport and generation [228]:

$$\frac{dT(\vec{r})}{dt} = \frac{1}{\rho(\vec{r})C(\vec{r})}(\kappa_T \nabla^2 T(\vec{r}) + Q(\vec{r})) \tag{4.168}$$

where ρ is the density of a material, $C(\vec{r})$ is its specific heat capacity, κ_T is the thermal conductivity, ∇^2 is the Laplace operator, and $Q(\vec{r})$ a local heating term. We will explore this heating term in the next section.
Before we dive into the different heating contributions, we also need to keep in mind that thermal gradients induce a thermoelectric current, proportional to the local thermoelectric powers $P_n(\vec{r})$ and $P_p(\vec{r})$, for electrons and holes respectively:

$$P_n(\vec{r}) = \frac{k_B}{q}\left[-\frac{5}{2} - \nu + \ln\left(\frac{n}{N_c^{3D}}\right)\right] \tag{4.169}$$

$$P_p(\vec{r}) = \frac{k_B}{q}\left[-\frac{5}{2} - \nu + \ln\left(\frac{p}{N_v^{3D}}\right)\right] \tag{4.170}$$

$$\tag{4.171}$$

with the Boltzmann constant k_B, the carrier densities n and p, the effective carrier densities for the conduction and valence band N_c^{3D} and N_v^{3D}, and the field-dependent carrier relaxation factor ν, which we will assume to be equal to $-\frac{1}{2}$ throughout this work [189,229]. The resulting thermal carrier currents are then:

$$\vec{J}_{n,thermal} = -q\mu_n P_n \boldsymbol{\nabla} T \tag{4.172}$$

$$\vec{J}_{p,thermal} = -q\mu_p P_p \boldsymbol{\nabla} T \tag{4.173}$$

These currents move opposite the thermal gradient. Since we expect the core of the laser cavity to be hotter than the contact regions, this current will oppose the bias current.
The main contributions to $Q(\vec{r})$ are non-radiative recombination releasing phonons, Joule heating due to both the DC current bias and the dissipation of optical energy via intraband absorption, as well as Thomson and Peltier heating terms due thermoelectric power gradients:

$$Q(\vec{r})) = Q_{non-rad}(\vec{r}) + Q_{Joule}(\vec{r}) + Q_{Thomson}(\vec{r}) + Q_{Peltier}(\vec{r}) + Q_{rad}(\vec{r}) \tag{4.174}$$

Note this expression also includes $Q_{rad}(\vec{r})$, a term that includes the cooling effect of the light emission out of the cavity, both due to spontaneous and stimulated radiative recombination:

$$Q_{rad}(\vec{r}) = -\int (R_{spon}(\omega,\vec{r}) + R_{stim}(\omega,\vec{r}))\hbar d\omega \tag{4.175}$$

where $R_{spon}(\omega,\vec{r})$ and $R_{stim}(\omega,\vec{r})$ are the spontaneous and stimulated radiative recombination rates, and ω is the frequency of the emitted light. In practice, the spectral dependency of these rates is ignored and the integral approximated with $R_{spon}(\omega,\vec{r}) + R_{stim}(\omega,\vec{r}))\hbar\omega$. We are assuming that the average emitted photon has energy $\hbar\omega \approxeq \mu_n(\vec{r}) - \mu_p(\vec{r})$. $\mu_n(\vec{r})$ and $\mu_p(\vec{r})$ represent the chemical potentials for electrons and holes in this context.
Regarding the heating terms, the heating due to non-radiative recombination is dependent on the overall fraction of injected carriers recombining in this manner, which varies throughout the device. The energy converted into heat $Q_{non-rad}(\vec{r})$ is then proportional to the local difference in chemical potentials $\Delta\mu(\vec{r})$ multiplied by the non-radiative recombination rate $R_{non-rad}(\vec{r})$, assuming no hot carriers in the device [230, 231]:

$$Q_{non-rad}(\vec{r}) = R_{non-rad}(\vec{r})\Delta\mu(\vec{r}) \tag{4.176}$$

The non-radiative recombination rate depends on the local carrier densities, temperature, and density of defects, as discussed previously. Auger recombination benefits from both the increase in carrier densities and an overall higher efficiency of its carrier-carrier scattering mechanism, leading it to become the dominant recombination mechanism most devices at high bias and therefore the primary source of recombination heat [154, 198].
The other source of heat is Joule heating. Joule heating occurs as a result of carrier scattering events with other carriers and the lattice, all releasing phonons and thereby raising the temperature of the lattice. The heat produced is proportional to the product of the local current density $\vec{J}$ and electric field $\vec{E}$, which can be simplified to include the electrical conductivity $\sigma(\vec{r})$ via $\vec{J} = \sigma(\vec{r})\vec{E}$:

$$Q_{Joule}(\vec{r}) = \vec{J}\cot\vec{E} = \frac{1}{\sigma(\vec{r})}\vec{J}^2 \tag{4.177}$$

Since the conductivity at low frequencies is vastly different than conductivity at high frequencies, we will therefore separate the Joule heating into two terms: a DC term $Q_{Joule,DC}(\vec{r})$ for the current induced heating and a high frequency term $Q_{Joule,optical}(\vec{r})$ due to optical absorption. The DC term in a semiconductor will see contributions due to both the electron and hole currents $\vec{J_n}$ and $\vec{J_p}$:

$$Q_{Joule,DC}(\vec{r}) = \frac{1}{qn\mu_n}\vec{J}_n^2 + \frac{1}{qp\mu_p}\vec{J}_p^2 \tag{4.178}$$

where n and p are the electron and hole densities, respectively, and μ_n and μ_p their mobilities.
The optical part is related to the intraband losses, which are captured by the background absorption coefficient α_i [189]:

$$Q_{Joule,optical}(\vec{r}) = \frac{S(\vec{r})\hbar\omega^2 n_r \alpha_i}{2\pi k_0} \frac{\left|\vec{E}(\omega)\right|^2}{\int \epsilon_r(\omega)\left|\vec{E}(\omega)\right|^2 d\omega} \tag{4.179}$$

where $S(\vec{r})$ is the photon density, $\left|\vec{E}(\omega)\right|^2$ is the intensity of the optical electric field, n_r is the real part of the refractive index, and k_0 is the wave number of the central mode in vacuum [189]. This expression assumes that the spread of relevant frequencies around the central lasing frequency is small, and therefore we can ignore the spectral dependence of $S(\vec{r})$ the photon density, and the refractive index n_r.
The last two heating terms are due to the variation of the thermoelectric power due to temperature ($Q_{Thomson}(\vec{r})$) and carrier density ($Q_{Peltier}(\vec{r})$):

$$Q_{Thomson}(\vec{r}) = -T(\vec{J_n}\frac{\mathrm{d}P_n(\vec{r})}{\mathrm{d}T}\boldsymbol{\nabla}T + \vec{J_p}\frac{\mathrm{d}P_p(\vec{r})}{\mathrm{d}T}\boldsymbol{\nabla}T) \tag{4.180}$$

$$Q_{Peltier}(\vec{r}) = -T(\vec{J_n}\frac{\mathrm{d}P_n(\vec{r})}{\mathrm{d}n}\boldsymbol{\nabla}n + \vec{J_p}\frac{\mathrm{d}P_p(\vec{r})}{\mathrm{d}p}\boldsymbol{\nabla}p) \tag{4.181}$$

(4.182)

We now have an expression for all the contributions to the local heat generation within an arbitrary device. The next step is to examine the boundary conditions at the edges of the simulation to define insulating or thermally conductive boundaries. PICS3D supports three types of conductive boundaries: type I has a defined temperature that will remain unchanged, representing an infinite heat bath such as a thermoelectric cooler (TEC). Type II specifies a specific heat flow that can be extracted from this contact per unit time, a scenario that is similar to a heat spreader with an inelastic heat dissipation. The last boundary type, type III, represents a boundary at fixed temperature, but with its own thermal conductivity. This boundary is useful when trying to represent a device with poor thermal contact with the TEC [189].

4.9 Version control

Since Crosslight PICS3D is a commercial software package it is subject to updates and changes to its operation. Throughout this work, three different yearly releases of the software were used: 2020, 2021, and 2022. Versions below 0.6.0 are based on the 2020

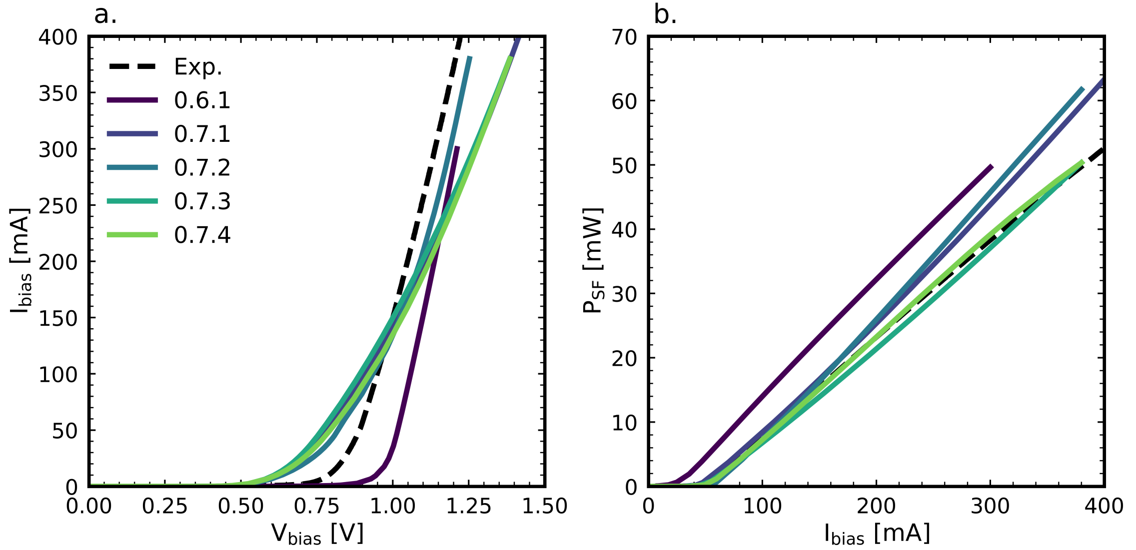

Figure 4.10: Comparison of the prediction of various model versions for a 1500 µm cavity at 293 K.

release, versions between 0.6.0 and 0.8.0 are based on the 2021 release and everything ≥0.8.0 uses the 2022 version. Unfortunately the only way to maintain access to the software was by using the latest version, which resulted in this yearly change. The data presented in this work is from versions 0.7.1, 0.7.2, 0.7.3, and 0.7.4 based on the 2021 version. As new versions are published, implementation details are changed. The most important change occurred in the complex multi-quantum well implementation for the 2022 version, which resulted in the previously functional integration of the QDashes into an asymmetrical MQW structure breaking. This thesis was completed using the 2021 version for which the wetting layer integration was still functional. A comparison between the results prediction by different version of the simulations is shown in Fig. 4.10.
Some of the simulation data presented in Chapter 6 is based on model version 0.6.1, which is an earlier iteration of the model, which did not use a wetting layer. A comparison with version 0.7.1 is shown in Fig. 4.10. The main difference between v0.7.1 and v0.7.2 is a different definition of the MQW, where layers are re-arranged to separate each QDL into its own separate MQW structure rather than one structure encompassing all QDLs. The change to the 0.7.3 version is additional functionality, with additional PICS3D parameters being exposed to the Python wrapper, and the wetting layer was removed temporarily. 0.7.4 reverts to a an all encompassing MQW structure, and introduces fixed electron and hole capture time constants. Various other material parameters are also adjusted between versions; a complete list of changes can be found in the *ridge_laser* simulation directory.

5

Model development and calibration

5.1 Baseline laser design

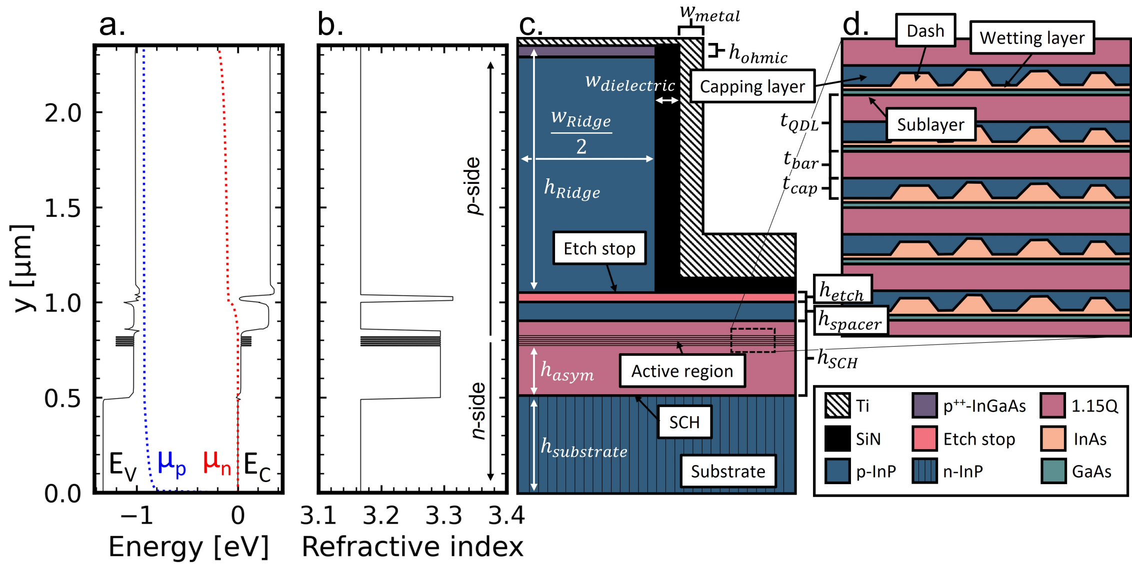

Figure 5.1: **a.** Vertical linecut at $x = 0$ of band edges E_c and E_v, with the chemical potential for electrons and holes, $\epsilon_{f,n}$ and $\epsilon_{f,p}$, and **b.** refractive index at $I_{bias} = 100$ mA for a 1500 μm cavity length device at room temperature. **c.** shows a schematic cross-section of a halved device, with specific regions and dimensions of the device labelled. The device is symmetric across x. The green lines indicate the extent of the top and bottom contact. The cut-out **d.** shows the active region with five QDLs. Note that the long axis of the dashes is actually perpendicular to the cavity length.

There are a variety of device designs that were simulated, grown and characterized within the context of this work. They were all based on a baseline design, of which a schematic cross-section is shown in Fig. 5.1c., with a cut-out of the active region in Fig. 5.1d. The values for each dimension can be found in 5.1. Only half the design is shown, as

Region	Dimension	Value [nm]
Ridge	h_{ohmic}	100
	h_{ridge}	1600
	w_{metal}	200
	$w_{dielectric}$	220
	w_{ridge}	2260
Etch	h_{etch}	30
Spacer	h_{spacer}	160
SCH	h_{SCH}	350
	h_{asym}	265
Active	h_{QDL}	11
	h_{bar}	6
	h_{cap}	5
Substrate	$h_{substrate}$	500
	w_{device}	7350

Table 5.1: Dimensions for the baseline design

it is perfectly symmetric about x. Only half the device was simulated as well to reduce the numerical complexity. The laser design of all the devices examined in this work is a ridge waveguide laser. The ridge waveguide serves two purposes: provide lateral optical confinement, as the ridge width is close to the desired width of the optical mode, and reduce lateral current spreading. The optical cavity is formed by the semiconductor material, with the semiconductor/air interfaces at the facets acting as cavity mirrors. Current enters the device through the substrate and from the top of the ridge. Ridge waveguide laser diodes are described in more detail in 3.4.1.

5.1.1 Substrate

The devices are grown on n-type (100) InP substrates, with (100) $\parallel x$. The substrate is thinned to allow better thermal contact between device and heat sink. It is useful for future discussion to divide the device into a n- and a p-side, depending on which carrier type is in the majority. In this model, we modelled a substrate thickness of 500 nm, which we found to be sufficiently thick for all electric field components of the optical mode to fully dissipate. Due to the high mobility of electrons in n-doped InP, the series resistance of the substrate was negligible compared to the active region and p-side cladding, resulting in thicker substrates not contributing significantly to overall device resistance.

5.1.2 Active region

The boundary between the n- and p-side is the active region, the part of the device where stimulated emission provides optical gain to the lasing mode. We will consider everything below it to be part of the n-side of the device, and everything above it p-side. For the baseline design, the active region consists of five layers of QDLs (shown in Fig. 5.1d.), spaced $t_{QDL} = 11$ nm apart. Each layer consists of a GaAs sublayer, roughly one monolayer thick. This layer's primary purpose is adding stress to the following layers. However, its thinness and the high growth temperature result in strong intermixing with nearby layers. This layer is therefore only included as a Ga-rich section of the barrier. On top of the sublayer, an InAs wetting layer (WL) is grown. While several monolayers (4-5) are deposited, the exact thickness of the layer after the capping process is unclear due to the complex growth dynamics for As/P, which were discussed in Ch. 5.4. The release of the accumulated stress leads to QDash formation via island growth, a complex process that is discussed more thoroughly in 2.5. These dashes are essentially elongated QDs, with their elongated axis oriented perpendicular to the cavity axis, as this maximizes optical gain [238, 239]. The layers are capped with $t_{cap} = 5$nm InP. Due to the implementation of QD and QDashes in PICS3D, this layer functions as the hosting layer for the dot levels and dash subbands. The QDL sandwich is completed with another barrier, with a thickness $t_{bar} = 6$ nm. This barrier is thinned to make space for the wetting layer in our model.

5.1.3 Separate confinement heterostructure

The active region is nestled within a separate confinement heterostructure (SCH), sometimes also referred to as an optical confinement layer (OCL). It consists of $h_{SCH} = 350$ nm of $In_{0.815}Ga_{0.185}As_{0.405}P_{0.595}$, which confines both carriers and the optical mode. Since $In_{0.815}Ga_{0.185}As_{0.405}P_{0.595}$ is a quarternary compound lattice matched to InP, with a bulk bandgap of 1.08 eV, corresponding to an optical transition wavelength of 1.15 µm, therefore $In_{0.815}Ga_{0.185}As_{0.405}P_{0.595}$ is also commonly referred to as 1.15Q. The alignment of the bands between 1.15Q and n- or p-doped InP leads to the formation of a barrier for minority carriers. This can be observed in Fig. 5.1a., where we see a barrier for electrons in the conduction band E_c at around 0.75 µm, and for holes in the valence band E_v at 0.5 µm. This prevents their respective spillage into the opposing majority carrier type regions, where they would function as minority carriers, increasing recombination losses. The second function of the SCH is optical confinement: it has a higher refractive index than the InP cladding (see Fig. 5.1b.). This confines the optical mode vertically and reduces its overlap with the p-cladding or the metallization layer, which are both sources of increased scattering and thereby optical loss [121]. p-doped InP has a much higher free carrier absorption coefficient than n-doped InP and the dielectric and metallization layers

are sources of surface roughness and plasmons scattering the optical mode field. As we will discuss in the context of the spacer layer thickness, minimizing mode overlap with these regions while balancing transport losses is therefore paramount to optimizing device performance. The active region is offset towards the p-side of the device to reduce the transport loss of holes within the SCH. While this does increase hole injection efficiency, it decreases optical gain slightly, as overlap between the optical mode and the active region is reduced. The offset therefore needs to be balanced carefully.

5.1.4 Spacer

On top of the SCH sits a thin spacer region of p-doped InP, with $h_{spacer} \approx 160$ nm. Its thickness is a trade-off between different loss mechanism again, and it will be discussed in more detail in Ch. 6.2.7. In short, a thinner spacer will reduce lateral current leakage and recombination losses, but increase scattering due to the increased overlap of the optical mode with the p-doped InP and the metallization layer. If optical losses for the fundamental lateral mode are too large as a result of this, multimode lasing can be observed, as higher order lateral modes see sufficient gain to compete with the fundamental mode. This is undesirable for multiple reasons, both related to detrimental efficiency and noise characteristics, as we will explore in 6.2.7. The spacer is doped to $N_a = 5 \cdot 10^{17}$ cm^{-3} .

5.1.5 Etch stop

In order to define the ridge, an etch needs to be performed that selectively removes material. While using a highly anisotropic etch to select for a vertical rather than lateral etch process, calibrating the etch depth precisely is difficult. Composition and doping levels of the layers make a process based on timing alone difficult, as each of these will alter the amount of etch time in a sometimes difficult to predict manner. In order to prevent "punch-through", an etch that removes material from deeper within the device than desired, an etch stop is introduced at the bottom of the ridge. This is an alloy that has a slower etch rate than the etch target material (in this case p-InP and p^{++}-InGaAs) to prevent small variances in etch time from removing material from below it. For the baseline device, the etch stop is composed of $In_{0.815}Ga_{0.185}As_{0.405}P_{0.595}$, the same 1.15Q alloy that is used to define the SCH. The thickness of the etch stop is 10 nm, with a 10 nm grading layer on each side due to an assumed intermixing between the 1.15Q and the adjacent InP, making for a total etch stop thickness of 30 nm. The band edge structure of the etch stop can be seen at $y = 1$ µm in Fig. 5.1a. It represents a thin barrier for holes, and confining well for electrons. As we will see when we do a thorough analysis of

the carrier densities within the device, the etch stop efficiently collects minority electrons, leading them to recombine in the etch stop rather than elsewhere on the p-side. Since they were already the result of leakage across the active region, this has no significant detrimental effect on the device behaviour.

5.1.6 Ridge

The ridge itself consists of $h_{ridge} = 1600$ nm p-doped InP, with $h_{ohmic} = 100$ nm of heavily p-doped InGaAs at the top to facilitate an ohmic contact to the Ti:Au metallization. The doping level throughout the ridge is uniform, slightly higher than the spacer at $N_a = 1{\cdot}10^{18}$ cm^{-3} , rising to $2{\cdot}10^{19}$ cm^{-3} in the ohmic contact layer. The ridge is covered in $w_{dielectric} = 220$ nm silicon nitride, which electrically isolates it from the metallization. The metallization, in these devices an Ti:Au alloy, allows the electrical connection of the devices through the top contacts and acts as a heat sink. The thickness of the metallization varies as a result of the asymmetry of the deposition, but can be assumed to be around $w_{metal} = 200$ nm.

5.2 Model assumptions

As indicated in Ch. 4, in order to perform numerical simulations over extended device areas, significant simplifications need to be made in order to minimize computation time. There are therefore several assumptions that were made to simulate the devices in this work. Some are a direct result of the usage of PICS3D, as its implementation makes some implicit assumptions with regards to the semiconductor physics treated. Some of these approaches were outlined in the previous chapter (Ch. 4) where we discussed the modelling approach in PICS3D, and we will therefore only include pointers to the relevant sections here. Other assumptions were made by us with respect to material or structural parameters that were inaccessible experimentally, or to simplify the model whenever possible to limit the computation time.

5.2.1 Time independent simulation of a pulsed device

The largest assumption made during this work was using a PICS3D steady-state model to represent the pulsed behaviour of a mode-locked laser. PICS3D does not support modelling modelling due to the computational approach taken by the software. The assumptions justifying the usage of the Green's method, which is employed to solve the partial differential equations for the optical modes, require time-scales that are greater

than several cavity round trip times T_{pulse} (see Eq. 3.71). It assumes an established mode shape that satisfies the boundary conditions at both ends of the cavity. This means that a comparatively slow modulation of a device at RF frequencies in the kHz to low MHz range could be represented, while anything above can not be represented [189].
The dynamics driving mode-locking, active or passive, occur on shorter time-scales, as the modulation frequency has to match the cavity mode-spacing $\delta\omega$, which is in the GHz range (see 3.4.4). Representing the full dynamics of mode-locking in PICS3D is therefore not possible. However, insights can still be gained from the steady-state representation of the device that are translatable into the pulsed domain.
The approach of this work is therefore as follows: treating the steady-state model as a time averaged representation of the pulsed device, we aim to extract fundamental operational parameters, such as resistance, diode voltage, threshold current, and slope efficiency, internal modal loss, and internal efficiency as a function of device design parameters. As energy conservation must hold irrespective of the time-dependence of the underlying mechanisms, we aim to understand the flow of energy within the device and where losses occur due to geometric and material limitations.
Naturally, this approach limits the reliability of its predictions. The largest discrepancy arises due to the difference in light intensity distribution within the cavity between the mode-locked pulsed device and the steady-state representation. Due to the lack of a well-defined phase relationship, the intensity profile is relatively uniform, lacking the short range localization observed in mode-locking. This results in several differences between the two states: the higher peak intensity of the pulse results in much stronger optical non-linearities, reflected in a reduced refractive index change for the steady state. The effects related to spatial hole burning are therefore also weakened. The most relevant effect is the gain non-linearity, which reduces the sideband suppression and is much weaker for the steady than the pulsed state. This results in an overestimation of the gain in the model presented here.
Another discrepancy is due to the occupation of higher lying dash states. For device with several transitions of roughly equal dipole moment, the gain will be maximized at the transition energy of states with the maximum population inversion. Generally, for a steady state device, this will be the ground state, or an excited state very close to the ground state, depending on the carrier dynamics within one dash. In a pulsed device with short gain recovery times ($\tau_{gain} << T_{pulse}/2$), carriers are allowed to build up within the active region. These carriers will occupy higher lying states within the quantum dash. This leads to a gain shape that is broader, with increased flatness at the top.
As a final note, and as we will discuss in the final chapter, a more self-consistent approach includes a time-dependent model that captures these effects implicitly. Several of these models can be found in literature, e.g. [148, 240, 241]. While they are able to reflect lon-

gitudinal spatial non-uniformity, they generally forego lateral variation of the waveguide. The device geometry is only included abstractly, using phenomenological parameters such as capture constants, current spreading, and injection efficiencies. Using the laterally resolved steady-state model, these parameters can be extracted directly rather than used as fitting parameters or estimated from references. Especially when looking to optimize the device geometry, the impact on these parameters due to a design change can be examined accurately. Data from the steady-state model can therefore be used to enhance the accuracy of a time-dependent model to provide a more self-consistent picture of the full device and all aspects of operation.

5.2.2 Lateral optical modes

For most simulations, we assume that there is only a single lateral mode (TE_{10}) with higher order lateral modes experiencing negligible gain and therefore remaining below the lasing threshold. To ensure this condition is fulfilled, we modelled the inclusion of higher order modes for the baseline design for a $L = 1500$ µm cavity at different temperatures. The results are shown in Fig. 5.2. While all modes are contributing to the light output below I_{th} , once lasing sets in the fundamental TE_{10} mode (Mode 1 in Fig. 5.2e.-h.) dominates. Spontaneous emission into other modes remains, but its fraction of total device emission decreases and becomes negligible with increasing overall device output. At elevated temperatures, the contribution from higher order modes to the overall light emission remains more relevant, but even then it never exceeds more than 40% of the overall light output. Since the operational window of these devices is generally at injection current densities exceeding $2J_{th}$, higher order lateral modes have negligible impact on overall device behaviour. This justifies the inclusion of only a single lateral mode in the lateral mode search. Only when parameters that alter the waveguide, or the position of the gain section within it, are varied will a check for higher order modes be performed, as it results in a significant increase in the computation time of the model. We will explicitly indicate whenever multi-mode operation is considered. Including higher order modes is most relevant when the spatial gain or loss profile is altered significantly, for example when varying the relative position of the SCH to the bottom of the ridge.

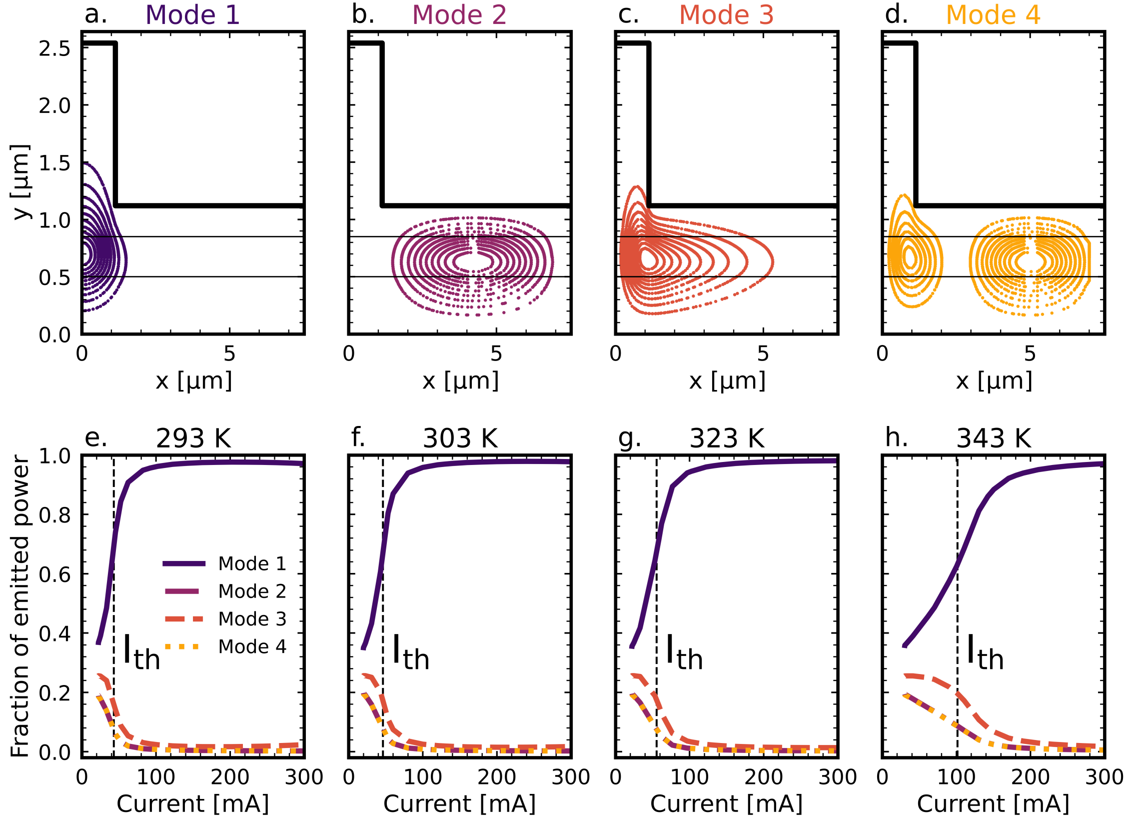

Figure 5.2: **a. - d.** Contour lines for the lateral mode shape. The thick black line indicates the lower edge of the ridge dielectric, while the thinner lines show the extent of the SCH. **e. - h.** Fractional contribution to the overall light output by mode as a function of injection current. The dashed vertical line indicates the threshold current I_{th} .

5.2.3 Boundary conditions

We assume a Neumann boundary condition for the left boundary; derivatives of the electric field eigenfunctions are assumed to be negligible here. This selects for optical modes with even symmetry, such as the fundamental transverse electric mode, TE_{10}. Given the perpendicular orientation of the QDashes relative to the cavity axis and thereby propagation direction of the optical mode, we can also exclude transverse magnetic modes (TMM), as the orientation of the QDash dipole suppresses emission into magnetic modes.

5.2.4 Ohmic contacts

PICS3D assumes that there is little to no contact resistance at the interface. This is ensured by introducing an extremely high acceptor dopant density of $2{\cdot}10^{19}$ cm^{-3} at the top contact, combined the usage of a Ti:Pt:Au alloy that produces very low contact resistances.

The resulting resistivity from literature suggests values below 10^{-5} Ωcm^{-2} [242,243]. Using these values, we can calculate an absolute contact resistance R_c using the contact area A_c:

$$R_c = \rho_c A_c \approxeq 10^{-5} \cdot Lw_{(ridge,device)} \tag{5.1}$$

For $L = 1.5{\cdot}10^{-3}$ m, the resulting contact resistances are below 10^{-13} Ω, with total device resistances $\approxeq 1\ \Omega$. Treating the contacts as ohmic is therefore justified.

5.2.5 Fixed refractive indices in passive regions

Both the real and imaginary parts of the refractive index of a bulk semiconductor are strongest in the vicinity of its optical transitions, as outlined in the discussion of Eqs. 2.53 and 2.54. The real part scales with $\frac{1}{\omega_{cv}^2-\omega^2}$ while the imaginary part features an even stronger proximity dependence in the Dirac delta function dependent on the separation between the field and dipole oscillations. We will therefore make the assumption that only the real components of the refractive index are relevant outside of the active region of the device. The passive regions of the lasing device, such as the n- and p-cladding, and the SCH, all feature band gaps above the operating regime of the laser, and we assume only negligible densities of optically active defects within the gap. The large relative distance between transition and modal frequencies also means the factor $\frac{1}{\omega_{cv}^2-\omega_n^2}$ varies little for different modal angular frequencies ω_n, so we assume n_r to be a frequency-independent quantity. We will therefore treat them as isotropic media with a loss-less linear response to the optical fields in the cavity. This assumption is baked into PICS3D and can not be circumvented.

5.2.6 Interface grading

During heterostructure growth, compositional changes can occur with near atomistic abruptness as we briefly outlined in 2.5. However, some degree of intermixing at an interface is inevitable given the high thermal energy available under normal semiconductor growth conditions around 500°C. Species from the growth interface will diffuse into the material, with the exact rate of intermixing dependent on the precise growth conditions. Most interfaces in heterostructures will therefore feature a compositional gradient between adjacent layers rather than an abrupt, step-like profile. And even if the interface is atomically smooth, the material properties will vary across the interface due to the broken symmetry. As the translational symmetry is broken by the compositional change, many of the assumptions underpinning the solid state physics we discussed in chapter Ch. 2 break down. The result are properties that are unique to the interface rather than the two materials interfacing [32].

In the discretized numerical representation, truly abrupt interfaces are the default. As mesh nodes are assigned a specific material, the change in material properties can vary abruptly. While unrealistic, this is often unproblematic if the change is minimal, but can lead to convergence issues for the numerical solver since it can result in large variable gradients.

The unrealistic interface abruptness also has a large impact when two heavily-doped materials with identical dopant polarity interface. The abrupt change in the affinity and band gap leads to a large discontinuity in the band structure. This induces a depletion region that blocks current flow. The depletion region presents as a large resistance at low injection currents, leading to an overestimation of V_d in the model. The solution to overcome this issue is the introduction of a graded region, that blends one composition into another. The larger spatial extent of the band structure changes prevents the formation of a deeply depleted interface region, reducing the V_d of the device.

We use this grading between several layers: the interface between the substrate and the SCH, the SCH and the spacer, the spacer and the etch stop, and the etch stop and the ridge material are all graded with a grading length of $h_{grading} = 10$ nm. While much larger than the length over which physical intermixing at the interfaces is expected, it represents the long range alteration of the material properties due to the aforementioned symmetry break at the interface. Additionally, carrier tunnelling would reduce the impact of the depletion zone, which is not represented in the model outside of active regions [32, 189]. Interface grading is therefore a compromise that captures the impact of both physical effects at heterojunctions outside of the active region.

5.2.7 Static quantum-mechanical states

As explained in 4.6, the QDash states used in this model are calculated prior to the full device simulation and do not change as a function of bias and temperature. This assumption is reasonable if the change in level positions is negligible compared to the the size broadening of a $\approxeq 40$ meV.

5.2.8 Absence of self-heating

While we discuss the mechanisms driving self-heating in the device in this section, we would like to note that the versions of the model used to produce the results presented in this work did not use this self-heating formalism. Initial testing revealed a severe underestimation of the core temperatures compared to literature [155]. This could be due to a variety of causes. Careful re-examination of the simulation results and further experimental work is required to ascertain how to correct this discrepancy. We therefore chose to not

include self-heating in the current version of the model. When elevated temperatures are simulated, the temperature is varied uniformly across the device and further heating of any specific region is ignored. As we compare the predictions of the simulation primarily with results from pulsed measurements, in which heating effects should play a secondary role, this should be a valid assumption to make.

5.3 Comparing numerical results with experimental data

To conduct meaningful quantitative modelling, access to experimental results is incredibly important. Comparing numerical prediction with experimental truth allows validation and verification of the plethora of assumptions and simplifications that were made in order to be able to obtain a numerical representation of the device. The following sections will therefore compare the predictions of the model with experimental results to highlight areas where the model can provide useful information to inform device design, and areas where additional work and auxiliary models are required to provide useful insight.
There were certain material parameters which were difficult to obtain experimentally, such as the exact size and shape of the dots, and thereby the density of states, or the degree of tunneling across the QDLs. These parameters were used as fitting parameters to obtain matching with experimental data.

5.4 Wetting layer inclusion

The growth of InAs quantum dashes studied in this work occurs in multiple steps, as described in 2.5, one of which is the deposition of an InAs wetting layer. It facilitates the self-assembled formation of quantum dashes, and is partially consumed during the island formation and subsequent capping process. The fraction of wetting layer that is consumed in these two steps, either by incorporating into the dashes or by being integrated into the cap is unclear and difficult to assess experimentally. The initial deposition only amounts to a few monolayers, resulting in a thickness below 2 nm generally. This is difficult to accurately characterize experimentally, due to the proximity of the thickness of the remaining layer to the resolution limit of highly resolved transmission electron microscopy (HR-TEM) [86, 232]. From a volumetric standpoint, full strain relaxation of the wetting layer into the dashes leaves excess material, since the dashes can not accomodate the entire InAs material deposited. This points towards a wetting layer remaining between the sublayer and dashes themselves. There is however very strong As/P-exchange, which converts InAs into InP as a result of the comparatively higher volatility of As. This process is very sensitive to the growth conditions, especially temperature and phosphorus partial

pressure [233, 234]. While As/P-driven material removal at the top of the dash has been studied intensely due to its reduction of dash height variability and thereby inhomogeneous broadening, the dynamics between the dashes are less well studied [86, 88, 235, 236]. Both a complete removal and large fraction are feasible given the growth conditions.
Given the difficulty of examining the wetting layer's existence and thickness directly, an indirect characterization method is required [237]. Since the wetting layer is effectively a QW, it creates a series of confined states, which are optically coupled and will therefore have a spectroscopic fingerprint. The simplest way to observe this fingerprint is using luminescence, which will show additional emission due to radiative recombination on wetting layer transitions [80, 87]. Unfortunately, depending on the energetic proximity of the wetting layer transitions to the quantum dash levels and the coupling strength between the two, wetting layer transitions may be drowned out in both electro- and photo-luminescence spectroscopic characterization by emission from QDash states, especially at higher temperatures [80].

Fig. 5.3 shows PL spectra taken from a reference sample which featured a QDL stack

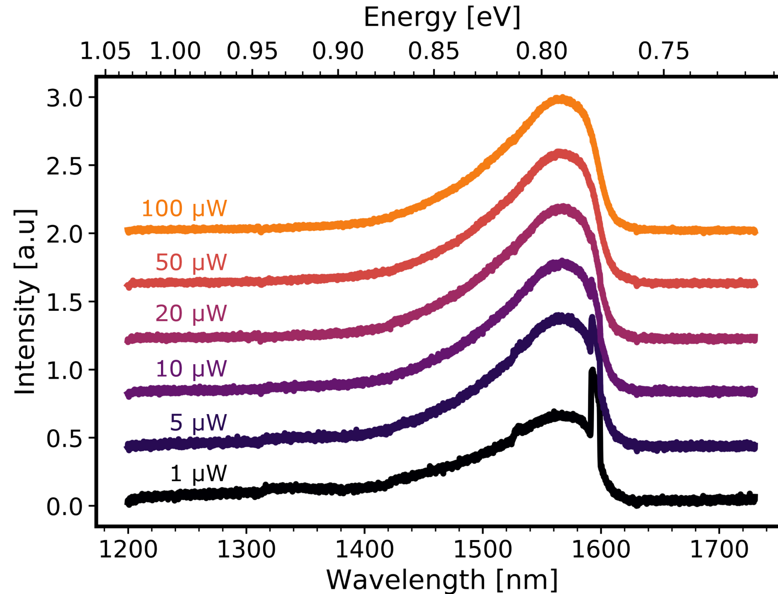

Figure 5.3: Photoluminescence power spectra for a reference QDL stack. The measurements were done at 298 K, using a 532 nm diode laser as the pump.

grown in an identical manner to the ones used throughout this work. We do not observe any notable transition from the wetting layer. The peak near 1600 nm is an artifact due to the pump laser. There are two potential explanations for the lack of change: either the wetting layer is not present due to the As/P exchange process discussed earlier or the wetting layer is strongly coupled to the dash population, resulting in negligible emission from these states compared with QDash emission.

Lacking definitive experimental data on the existence and extent of the wetting layer, we chose to model devices both with and without a wetting layer to observe its impact on the overall device behaviour. The inclusion of the wetting layer in PICS3D is difficult, as the software is designed around symmetric wetting layers as found in DBAR or DWELL structures [238]. For the devices in this work, the wetting and barrier layers are composed of different materials, InAs and 1.15Q, which complicates their inclusion in PICS3D. This process is discussed in more detail in 4.6. All models other than those used in versions 0.6.1 and 0.7.3 include a wetting layer, as it results in a significantly better match between experiment and simulation.

5.4.1 Calculated quantum dash states

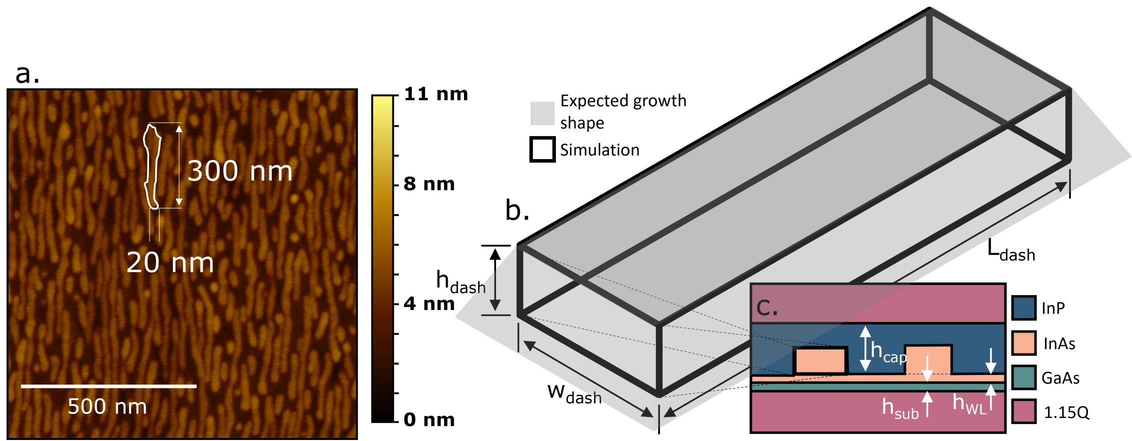

Figure 5.4: **a.** Rectangular prism dash with relevant dimensions, **b.** quantum dash layer structure with sub-layer, wetting and capping layer sandwiched between two 1.15Q barrier layers, and **c.** AFM image of uncapped quantum dashes with dimensions of single dash added.

For this work, the dashes were based on simulations done in the context of R.-J. K. Obhi's work, published in [120] and [83]. There were several simplifications made in order to be able to treat the dashes in PICS3D. The AFM image shown in Fig. 5.4a. shows that there are a variety of different dash morphologies that appear as a result of the self-assembled formation process, ranging from short dashes with low lateral aspect ratios resembling dots to long dashes resembling wires with very high aspect ratios. The majority of dashes additionally exhibit a non-uniformity of their cross-section along their length. The cross-section of dashes after deposition of the capping layer was not analyzed for this work, but the surface growth dynamics of dash formation in InAs/InP favour a slight angle of the dash facets [91]. However, we found the integration of angled facets had no meaningful impact on the resulting dash states. In order to treat these dashes meaningfully within

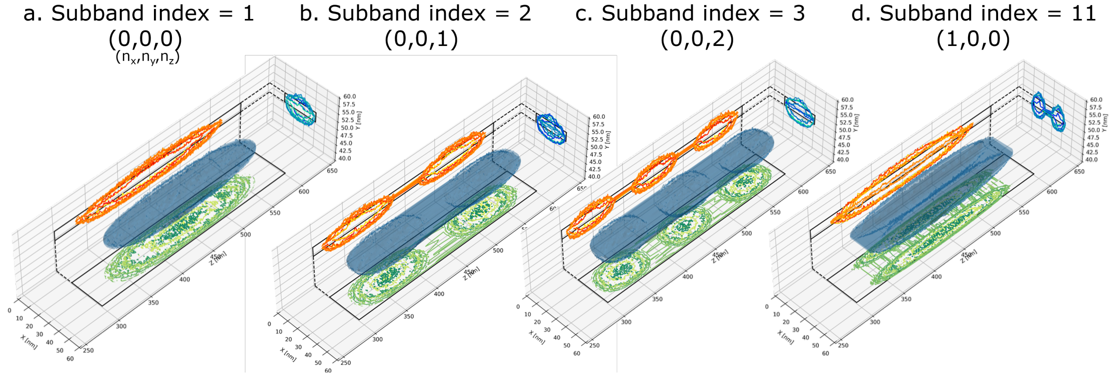

Figure 5.5: Spatial extent of electronic wavefunctions in the conduction band at 20% of the highest probability density for four different subbands and their respective quantum indices.

PICS3D, we reduce the wide assortment of dashes to a single representative dash, which we approximate as a rectangular prism shown in Fig. 5.4b. with dimensions $h_{dash}{\cdot}w_{dash}{\cdot}L_{dash}$ of 1.5·20·300 nm^3. We treat the variation in dash length and cross-section along said length by applying a Gaussian broadening function to the energy levels derived from the representative dash. Similar results were found by others for InAs/InAlGaAs dashes [192]. The material surrounding the dash is shown in Fig. 5.4c. The dash is grown on top of a GaAs sub-layer and InAs wetting layer and is capped by an InP layer. The thicknesses of the different layers used in the representative dash are listed in Tab. 5.2.

The calculation of quantum mechanical states in PICS3D is described in 4.6. The re-

Dimension	Value [nm]
h_{cap}	5
h_{dash}	1.5
w_{dash}	20
L_{dash}	300
h_{WL}	0.6
h_{sub} 0.3	

Table 5.2: Dimensions for the representative quantum dash used in this work. See Fig. 5.4 for definitions of parameters.

sults for the reference dash are shown in Fig. 5.5. Each figure shows the surface of the wavefunction at 20% of the maximum probability density for states at different subband indices.

Due to the low longitudinal confinement, increasing subband indices map to increasing longitudinal quantum numbers. This trend holds for both electron and hole states. Higher order modes along x only start to appear at higher energies. For electronic subband indices above 11 increasing subband indices hail from both $n_x = 0$ with high n_z, and $n_x = 1$

with low n_z. The large contrast in confinement energies along y compared to the other dimensions results in no higher order modes along y appearing within the 33 lowest energy states probed. The pattern is similar for holes, but due to the higher hole mass, the transition occurs at a comparatively higher energy offset.

The full spectrum of electron and hole states near the Γ valley are shown in Fig. 5.6a and

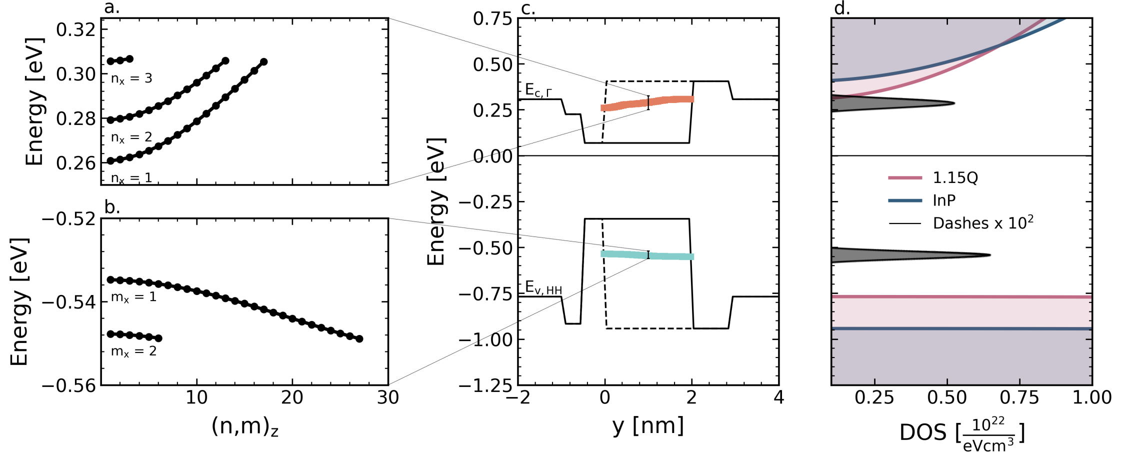

Figure 5.6: Calculated confined states for **a.** electrons (n_x, n_y, n_z) and **b.** hole states (m_x, m_y, m_z). The level position is shown as a function of longitudinal dash index n_z for electrons and m_z for holes. $n_y = m_y = 0$ for all shown states are for . **c.** band edge potential for a cut through the centre of a dash along the growth direction y. The solid line reflects the band edges within dashes, while the dashed line reflects the profile in a barrier region. The coloured lines show the position of the confined states within the dash potential. **d.** density of states (DOS) for the quantum dashes, barrier and capping material. Note that the DOS for the dashes has been multiplied by a factor of 10^2 .

b. The higher lying L band as well as the deeply confined light hole band are not shown. The predicted states were 100 meV (electrons) and 150 meV (holes) removed from the lowest energy Γ state, sufficiently far to not contribute meaningfully to the overall gain profile near the design wavelength of 1550 nm. For the electronic states, the L-band levels are also very close to the barrier band edge, resulting in shallow confinement and enabling significant carrier escape via these states.

For electrons, the first 33 states separate into three bands belonging to $n_x = 0, 1, 2$. The difference in confinement energies for $n_x = 0$ and $n_x = 1$ at $n_z = 0$ is 19 meV, decreasing at higher n_z. The initial difference between states with $n_x = 1$ and $n_x = 2$, is higher at approximately 25 meV, indicating super-linear scaling of eigenenergies with mode volume. While three bands are observed for electrons, only two appear for holes given the larger effective mass. The resulting dispersion with n_z is also flatter for the same reason. Otherwise the hole and electronic states have very similar shapes, leading to large overlap

integrals.
The relative position of the confined levels within the potential of the dash is shown in Fig. 5.6c. Given the 40/60 band offset split between conduction and valence band between InAs and InP, the confinement is much deeper for holes than for electrons. The barrier height for the lowest energy electronic state is approximately 50 meV, compared to nearly 250 meV for the lowest energy hole state. As a result, electrons should be able to traverse the QDL stack much more easily than holes. Laser device performance should be affected by this change in two ways. First, hole starvation should result in radiative efficiency losses within the QDLs, as electrons accumulate, leading to spill out into adjacent layers. Additionally, electron leakage across the QDL stack and subsequent injection into the p-side cladding as minority carriers results in increased non-radiative recombination losses compared to a device with greater carrier confinement. This is addressed by adding a electron blocking layer at the top of the SCH, a design change which is discussed in Chapter 6.

For both electrons and holes, we only consider a subset of the states for the full device simulation. The five lowest-lying energy states are used for both electrons and holes, as these have the largest impact of the narrow band of wavelengths around 1550 nm this work is interested in. Due to the low barrier heights of higher lying states, they should also experience an increasing degree of carrier escape into the nearby bulk band edge states in the 1.15Q barrier. The effect of the higher lying levels should therefore be well captured by the smaller subset of states. This also has the benefit of decreasing the computation time by a factor of up to six compared to using the full ensemble of states.
The densities of states (DOS) shown in Fig. 5.6d. are calculated based on the reduced ensemble of states. The basis of these densities is are based on the simplified parabolic models we found in Ch. 2, assuming a dot/dash density of 10^{10} cm^{-2} and a broadening of 40 meV. The former is based on estimates from AFM studies presented in [83], while the latter is based on fitting of room-temperature photoluminescence spectra (see Fig. 5.3). The DOS due to the dashes is dwarfed by the bulk states, which are orders of magnitude higher. The high energy tail of the electronic DOS even shows some overlap with the 1.15Q barrier DOS, indicating a high degree of coupling between the two. Note the lack of a similar overlap for the hole states. In the next chapter we will discuss the shortcomings of treating the dashes as three-dimensionally confined entities, but the shape of the carrier density between a broadened one- and zero-dimensional system is actually very similar near the peak of the distribution. The main difference are the existence of the tail of higher energy states for one-dimensional dashes, and the resulting coupling between non-degenerate transitions in these gain media, and the magnitude of the DOS. Since spatial or spectral hole burning is not included within the model, foregoing the tail states has no meaningful impact on the predictions. With respect to the magnitude, a

simple multiplication of the DOS is easily implementable into PICS3D, which was used to achieve matching between simulation and experiment in terms of threshold current and slope efficiency.

5.4.2 Inclusion of advanced gain model

PICS3D only supports gain models for quantum wells and quantum dots natively, but other gain models can be implemented by providing a tabulated set of gain curves as a function carrier concentrations, electron-hole ratios, temperatures, and electric fields. In order to capture the quantum dash-like gain spectrum, a secondary gain model was therefore sought out. The model chosen was based on Gioannini's work on InAs/InAlGaAs dashes [192]. The dashes studied in the publication resemble the dashes studied in this work, and the inclusion of an optional wetting layer contribution is useful given the uncertainty in terms of the wetting layer presence in this work. The details of the model are examined in 4.7.7. Since we did not have access to the original calculation code, we attempted to recreate the results from the publication. After building a Python implementation of the model, we compared it with results from the model for InAs/InP QDashes in with InAlGaAs barriers. A comparison between the calculations based on parameters either taken directly or inferred from the paper and supporting works and the results presented in the paper is shown in Fig. 5.7. We are comparing two scenarios: we assume there is no wetting

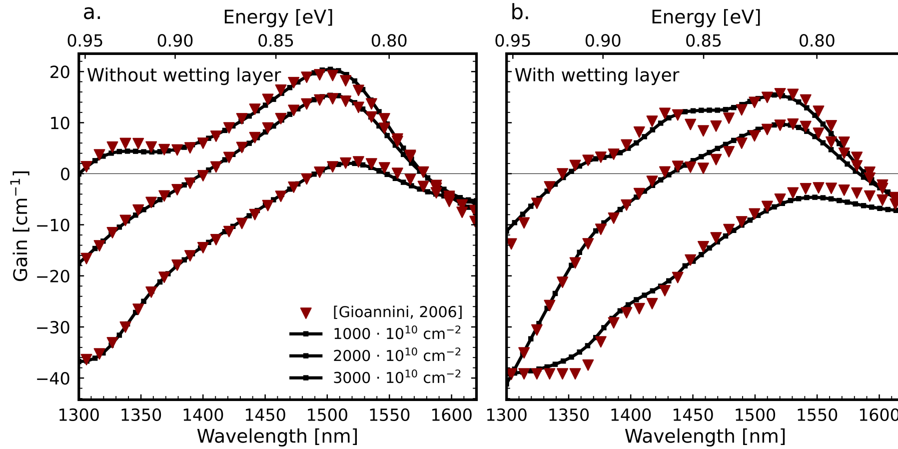

Figure 5.7: Performance of the recreated QDash model from [192] for **a.** with and **b.** without a wetting layer.

layer for Fig. 5.7a., meaning the only contribution to the gain is due to g_{conf}. The results match the results presented in the paper quite well, with only a small discrepancy towards higher energies. The mismatch gets much larger when a wetting layer is considered in Fig. 5.7b. The shape of the gain curves does not agree in several places, indicating that

there is disagreement between the contributions from the various transitions considered in this work. The source of the disagreement is most likely a result of the implementation of the dispersion relations for the hybrid wetting layer-dash states coupled with the error introduced when extracting the states from the scanned publication.

Having implemented the model to a degree of acceptable accuracy, the next issue was applying it to the InAs-InP material system. While material parameters e.g. band gaps and offsets, dipole moments, effective masses, could be transferred from PICS3D, two crucial sets of input parameters were harder to obtain: accurate quantum mechanical states and quasi-Fermi levels. As discussed in 4.6, PICS3D uses a three-dimensionally confined particle-in-a-box approach to calculate states. For cylindrical, lens-shaped, or pyramidal dots with low lateral aspect ratios, this delivers a set of states separated by 10s of meVs. For the dashes in this work, the extent along z is $\geq \lambda_{\text{de Broglie}}$ (see Eq. 2.63). Confinement along z is therefore weak, leading to the tightly spaced band of states shown in Fig. 5.6a and b, with states separated by less than 1 meV. The result is therefore a band of observed states, rather than discrete states. The treatment of dashes that are confined in the xy-plane and propagate as plane waves along z is not supported in PICS3D. To circumvent this limitation and avoid setting up an external quantum mechanical solver, we attempted to use refined versions of the three-dimensionally confined states. let us assume that the main difference between the quasi-one dimensional dash states we are seeking and the zero-dimensional states predicted by the PICS3D solver is an energy correction that reflects the different mode shape along z. From each QD band $(n, m)_x$ the energy for the $(n, m)_z = 0$ state (see Fig. 5.6a,b) is taken as the starting point for the expected energy level of the QDash state. These states were then used as input parameters to the dash gain model described above, and compared with experimental gain data. Each state was then allowed to vary freely within a 30 meV range of its starting value. The objective was matching of experimental gain data gathered via Hakki-Paoli decomposition of bias-dependent lasing spectra. Carrier densities from previous, QD-based simulations were used to estimate electron and hole quasi-Fermi levels.

Despite different optimization algorithms and parameter bound relaxation, we could not achieve a satisfactory match between experimental data and the output of the gain model. Fitting both quasi-Fermi levels and confined energies led to no fit that worked well across the whole spectrum and was consistent across different injected carrier densities. The optimization would also get stuck in local extrema consistently. We therefore concluded that, for this study, the full implementation of the quantum dash gain model will require implementing an additional quantum mechanical solver to obtain coupled quantum dash and wetting layer states. We are hoping to revisit this model in the future to compare it with results obtained using the QD-like model.

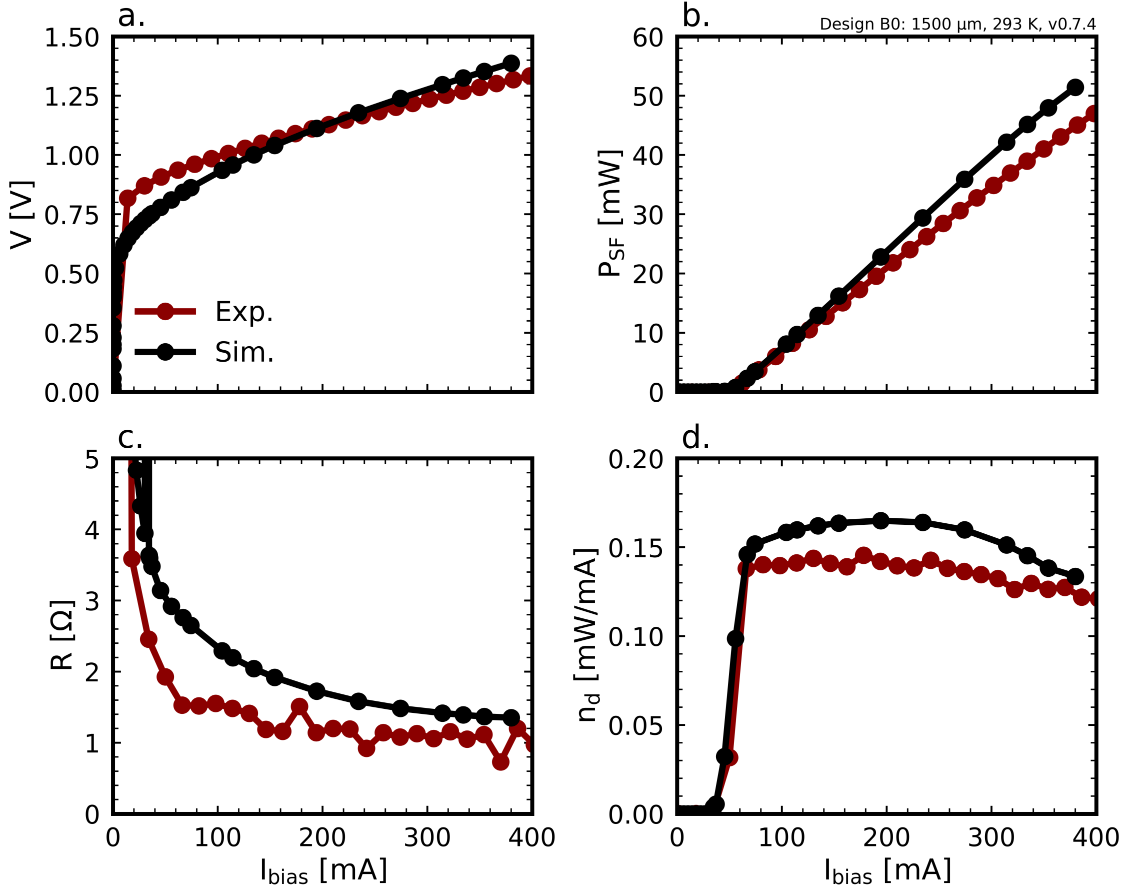

Figure 5.8: Comparison between simulated and experimental data measured on the semi-automatic LIV setup for a 1500 µm baseline device at 293 K. **a.** IV-characteristic, and **b.** LI-characteristic, their derivatives in **c.** and **d.**. Experimental data was collected by Ping Zhao.

5.4.3 Voltage-current and current-power characteristics

Fig. 5.8 shows a comparison between numerical and experimental LI and IV curves and their derivatives for a 1500 µm cavity of the baseline design described previously. Both measurement and simulation was conducted at a temperature of 293 K. The experimental results were measured on the semi-automatic measurement setup, which underestimates the emitted power from the device. We therefore expect the experimental LI characteristic to be yield slightly lower power overall. Experiment and simulation show significant overlap, but there are some subtle differences. The transition of the diode from current blocking to conducting occurs at a lower bias voltage for the simulated device. It also occurs over a more protracted range of biases, while the switch is near instantaneous for the real device. This points to a discrepancy in the band structure between model and the real physical system. Since the band structure is built on a variety of assumptions,

especially in the proximity of the quantum dash layers, this is to be expected. As discussed in 5.2, the model includes grading layers at some interfaces to avoid an overestimation of the resistance due to the limitations of the numerical solver in highly depleted regions of the device. The turn-on over an extended bias range indicates that the band structure in other regions may also require further investigation.
When comparing the LI characteristics in Fig. 5.8b., we see a slight overestimation of the slope efficiency of the model, while the threshold appears accurate. The model also exhibits a distinct super-linearity at currents below 200 mA. Instead of an efficiency decrease with increasing bias, as expected and observed for the experimental device, the simulated device first increases in efficiency before rolling off towards higher bias. The cause is a loss mechanism that decreases with current density, rather than increases. This is incommensurate with loss in semiconductors, indicating an artifact of the simulation. We observe this super-linearity decreasing when electron transport across the QDLs is artificially scaled to mimic significant hot carrier currents. However, increasing the hot carrier transport leads to an overestimation of slope efficiencies at elevated temperatures. The inclusion of a temperature dependent electron hot carrier model is therefore considered for the future. This could also potentially address the mismatch in high injection roll-off, which is stronger for simulation than experiment. To examine the accuracy of representing cavity length dependent mechanisms, we plot the diode voltage V_d , resistance R , threshold current I_{th} , and differential efficiency n_d as a function of cavity length in Fig. 5.9. The match between experiment and simulation is generally quite good, even though there are some notable features. As discussed previously, the barriers to transport across the quantum dash layers may not be represented accurately, leading to the slow diode switching. This means we do not expect the diode voltage extracted via linear fitting of Fig. 5.8a. to be entirely accurate. For similar reasons, the mismatch in R is expected, but as we capture the overall trend well it should not affect the accuracy of model predictions in a meaningful manner.
For the threshold current, the model overestimates I_{th} for short cavities, while underestimating it for longer cavities. This indicates that optical losses are too low, which would benefit longer cavities more than their shorter counterparts, leading to the switch from over to underestimation. Additionally, recombination appears to play a more significant role in the model representation than it should. Since Auger recombination is the largest contributor to overall recombination, it is the most likely source of this discrepancy. However, decreasing the coefficient leads to an underestimation of the threshold current at higher temperatures. We remind ourselves that the Auger recombination mechanisms dominating in QDs and QDashes are different from their counterparts in QWs and bulk devices. The formalism described in 4.5.6 may therefore not be entirely accurate given the different and much reduced density of states for QDashes compared to QWs. Alter-

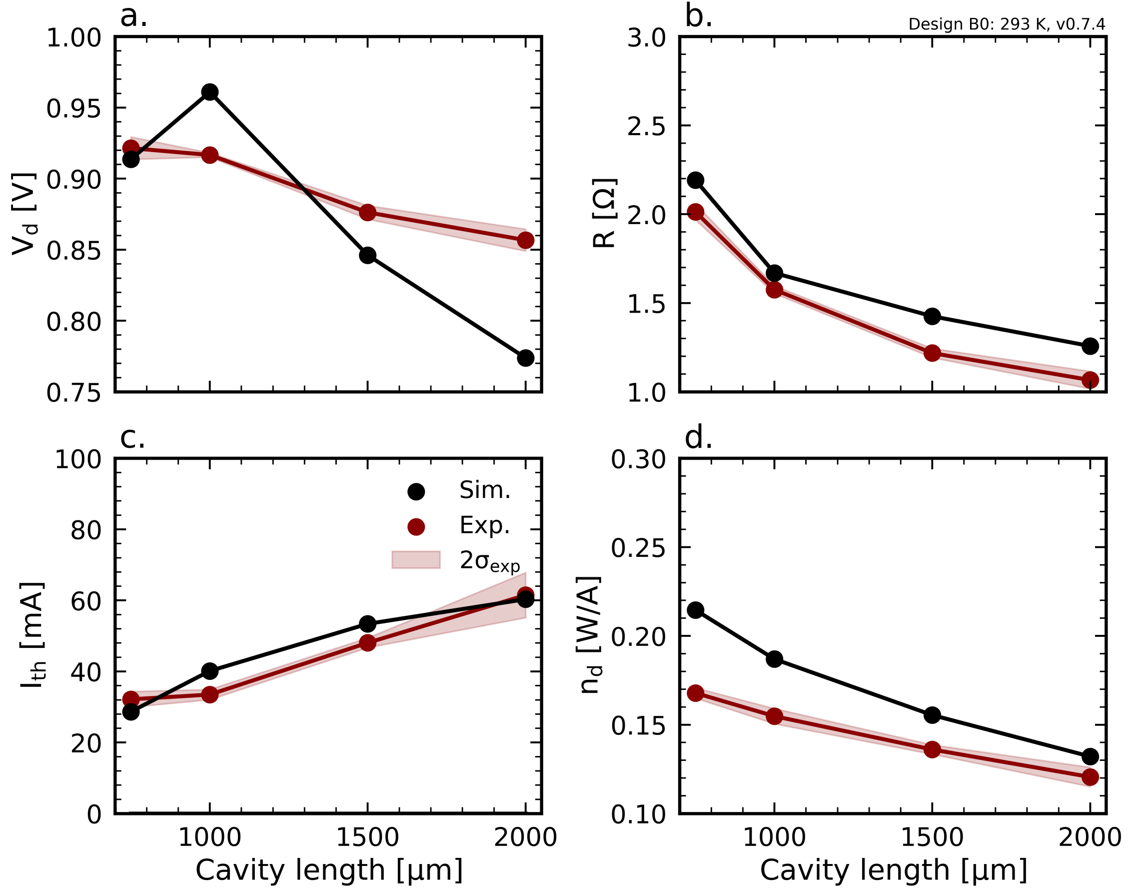

Figure 5.9: Comparison between simulated and measured LIV parameters. **a.** diode turn-on voltage V_d , **b.** resistance R , **c.** threshold current I_{th} , and **d.** differential efficiency n_d as a function of cavity length at 293 K. The shaded area indicates twice the the standard deviation around the mean value for the experimental data measured on the semi-automatic LIV setup. Experimental data was collected by Ping Zhao.

native models can be found in literature and could potentially offer better matching of experimental results [198, 214, 215]. However, they are difficult to integrate into PICS3D without also simultaneously including a custom gain model. This is therefore something to consider for future expansion of the model.

The slope or differential efficiency for the device is pictured in Fig. 5.9d. While the model slightly over-estimates the efficiency, its cavity length dependence is captured quite well. As we recall from 4.2.3, the data measured using the semi-automatic underestimates the light output from the device by approximately 7 %. The difference between experiment and simulation, however, is closer to 25 %. As for the threshold current, the general over-estimation indicates that the background loss may be underestimated and requires some further attention. The super-linearity due to electron blocking in the QDLs also affects

the accuracy of this fit. Lastly, the time-independent model experiences significantly less gain non-linearity, as photon densities in are lower than they are within the mode-locked device. All these factors play into the discrepancy between experiment and simulation and are difficult to separate out.

5.4.4 Characteristic temperatures

As we are interested in the temperature stability of our device performance, we now turn to examining the temperature dependence of the threshold current and the external quantum efficiency, as these will have the largest bearing on the light output of the device. The external quantum efficiency is defined as:

$$\eta_d = \frac{q}{\hbar\omega_c} n_d \tag{5.2}$$

Where ω_c is the angular frequency of the central longitudinal mode in a comb.
The temperature dependence of parameters is conventionally quoted using a parameter's characteristic temperature. The characteristic temperature T_c is related to the parameter value p at a given temperature T as follows:

$$ln(p) = ln(p_0) + \frac{1}{T_c} T \tag{5.3}$$

Plotting the natural logarithm of a parameter as a function of temperature, T_c can be extracted from the slope of the linear regression. T_0 and T_1 are the characteristic temperatures extracted in this manner for the threshold current and external quantum efficiency, respectively. Fig. 5.10 shows the results for the baseline design at 1500 µm cavity length.
The model overestimates the temperature stability of the device both in terms of threshold current and external quantum efficiency, with relative errors for T_0 and T_1 of 21% and 11%, respectively. As temperature increases, the distribution of carriers broadens as the average ensemble energy rises, as shown in Fig. 3.11. The shape of the DOS modulates the strength of the broadening, and thereby the change in gain shape and magnitude with temperature. A broader density of states will experience a stronger reduction in gain. The DOS based on the quantum dot-like approach used in this thesis is much smaller and narrower than the DOS one would obtain if the QDashes had more wire-like character. A comparison can be found in Fig. 5.6d., where we see a significant high energy tail for the one-dimensional system, which is lacking for QDs. The degree of gain broadening is therefore reduced, resulting in a device with a higher temperature stability.
The stronger discrepancy for the threshold current than the efficiency points towards another source of the problem: recombination. As mentioned previously, Auger mechanisms are the largest contributor to recombination near threshold. Due to higher scattering

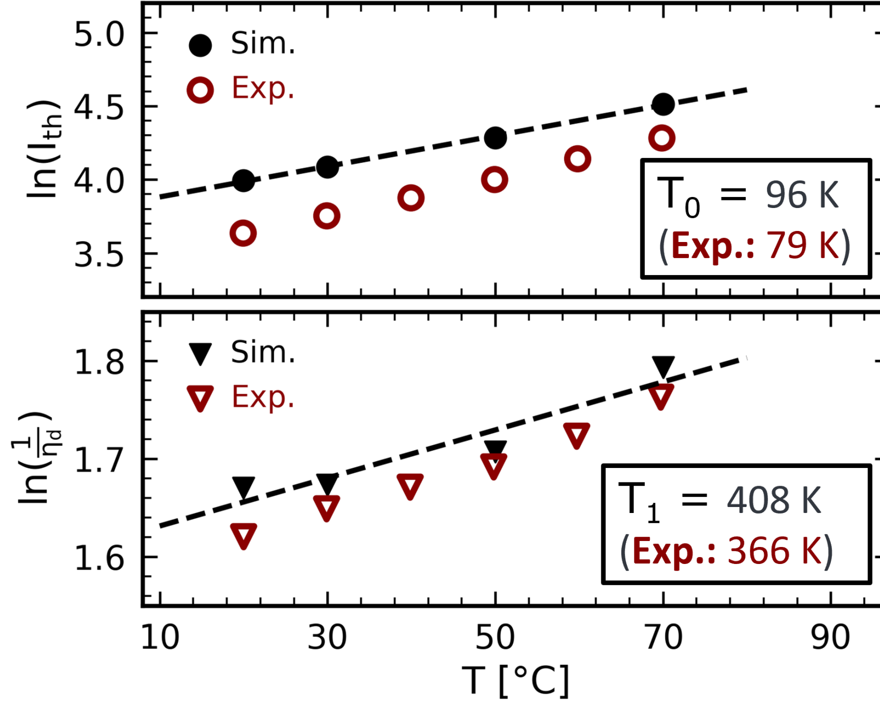

Figure 5.10: Comparison of simulated and measured temperature dependence of **a.** I_{th} and **b.** η_d for a 1500 μm cavity between the simulated and experimental baseline design device. Experimental data was collected by Ping Zhao.

efficiencies as carrier velocities increase, Auger mechanisms become more effective as temperature increases, in addition to the natural increase due to higher carrier densities. This is reflected in the empirical formula in Eq. 4.44, which features an "activation energy" for the scattering process that scales the Auger coefficient with temperature. This energy is essentially a fitting parameter, but the many interactions between this coefficient and the overall device behaviour require different values as a function of cavity length. The inclusion of a microscopic Auger model should be able to rectify this difference and allow a less empirical approach to the exact magnitude of Auger recombination within the device.

5.4.5 Internal efficiency and loss

To differentiate between length dependent effects due to parasitic recombination and absorption by the active region, and the internal dynamics of the laser, we can use the internal differential quantum efficiency [244, 245]:

$$\eta_i = \frac{J_{stim}}{J - J_{th}} = \frac{1}{\eta_{ext}(L) - \alpha_m L} \tag{5.4}$$

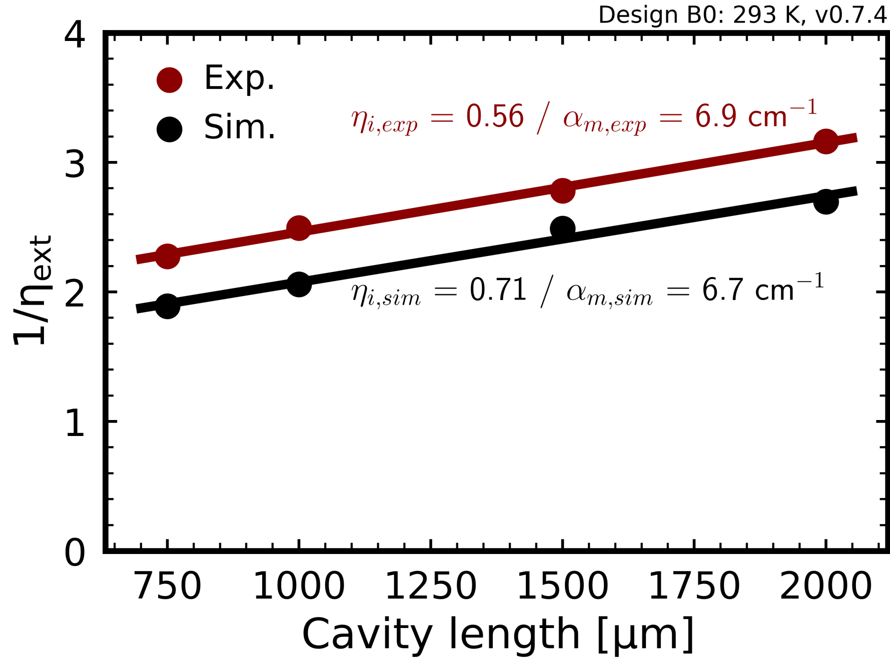

Figure 5.11: Comparison between external efficiencies for experimental and simulated results. The experimental value is multiplied by 1.07 to account for the usage of data from the semi-automatic measurement setup. Experimental data was collected by Ping Zhao.

With the stimulated current density J_{stim}, the total carrier density J, and the threshold current density J_{th}. η_i is then the fraction of the injection current that is converted into stimulated emission. As the right hand side of Eq. 5.4 indicates, this can be done using a linear regression to the cavity length L dependent external differential quantum efficiency $\eta_{ext}(L)$, which yields both η_i and the internal loss α_m.

A comparison between experimental and simulated efficiency is shown in Fig. 5.11. The simulated differential internal efficiency is much higher than the experimental value, which was to be expected given the higher overall slope efficiency. At the same time, the internal optical loss α_i is nearly identical between experiment and simulation, indicating that the discrepancy is not due to the scaling of the background scattering alone as we first assumed. A possible source of this discrepancy is the degree of lateral current spreading below the ridge, which may be underrepresented in the simulation. If we extrapolate the efficiency for a four layer device from Fig. 6.3c., we obtain a value of around 0.58. For a four layer baseline device grown later, the distance between the separate confinement heterostructure and the bottom ridge was shrunk by approximately 20 nm due to a miscalibration during the growth. Its differential internal efficiency is shown in Fig. 8.2a. and lies at approximately 0.62. This increase in efficiency is expected if the driving factor for the discrepancy is lateral current spreading, as the lateral current confinement

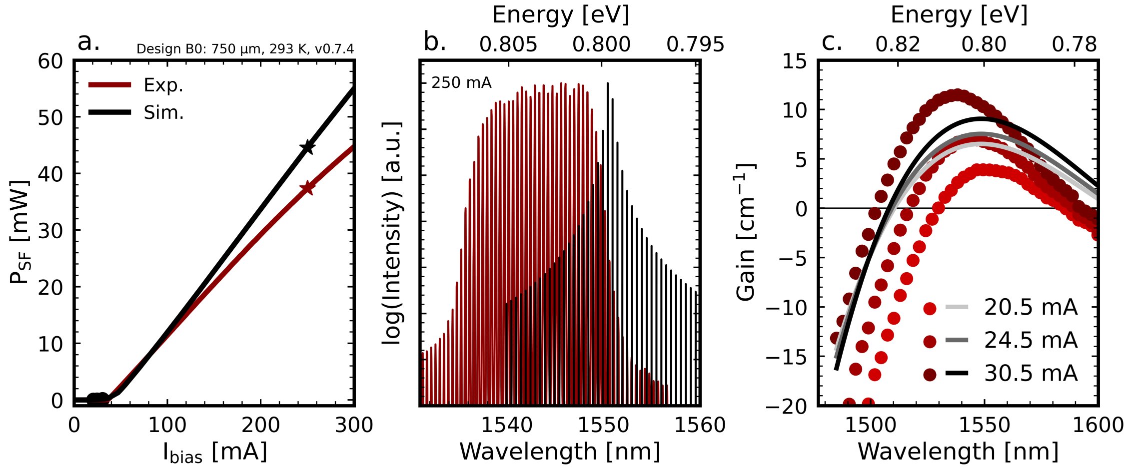

Figure 5.12: Comparison between experimental and simulated lasing spectra and gain curves for 750 µm baseline device at 293 K. **a.** LI-characteristic, **b.** lasing spectrum at $I_{bias} = 250$ mA and **c.** sub-threshold gain curves. Red dots indicate results derived from experimental data, while solid grey lines are interpolated simulation results.

from the ridge remains stronger and coerces the current into the region right below the ridge. More work is needed however, and as additional devices with wider ridges were also fabricated, an additional experimental study can assess the overall impact of current spreading. If it lies at the root of the difference in differential internal efficiency, the discrepancy between simulation and experiment should increase further as ridges get wider and the overestimation of the lateral current spreading efficiency gets worse.

5.4.6 Spectral properties

We will now turn our attention towards the output spectrum and the gain curves from these devices. The output spectrum is where we expect the greatest divergence between model and simulation. Due to the much stronger spatial hole burning for the mode-locked device, the relative intensity between modes should be significantly more even than for the time-independent model.

Fig. 5.12b. confirms this reality, as the model predicts continuous wave operation on a single mode while the actual device produces the frequency comb that we expect. We can also see that the centre of the comb is blue-shifted by almost 10 nm for the real device. This is due to the difference in gain shape between experiment and simulation, shown in Fig. 5.12c. The experimental gain was calculated from sub-threshold emission spectra using the Hakki-Paoli-derived Cassidy method, using a script developed at the NRC [246, 247].

There is a significant discrepancy between the gain profile from the model and the profile derived from experimental data. Note that this is the material gain, rather than the sometimes quoted net gain. Apart from the blue-shift of the position of the gain peak, its magnitude is also more responsive to the changing bias than the simulated gain. The last thing to note is the gain bandwidth, which changes more dramatically than the width of the simulated result.
The more dramatic change in gain with injected current for the experimental results indicates a smaller overall DOS than what is included in the model. Since the dash density is an estimate based on experimental results, the difference must stem from the calculated dash states [120]. It implies that the overall number of states participating in the amplification is lower than anticipated. This contrasts with the underestimation of the slope efficiency and temperature dependence, and indicates that the gain model requires some further attention to discern the root cause of the discrepancy.
A comparison between the experimental and simulated dispersion is shown in Fig. 5.14.

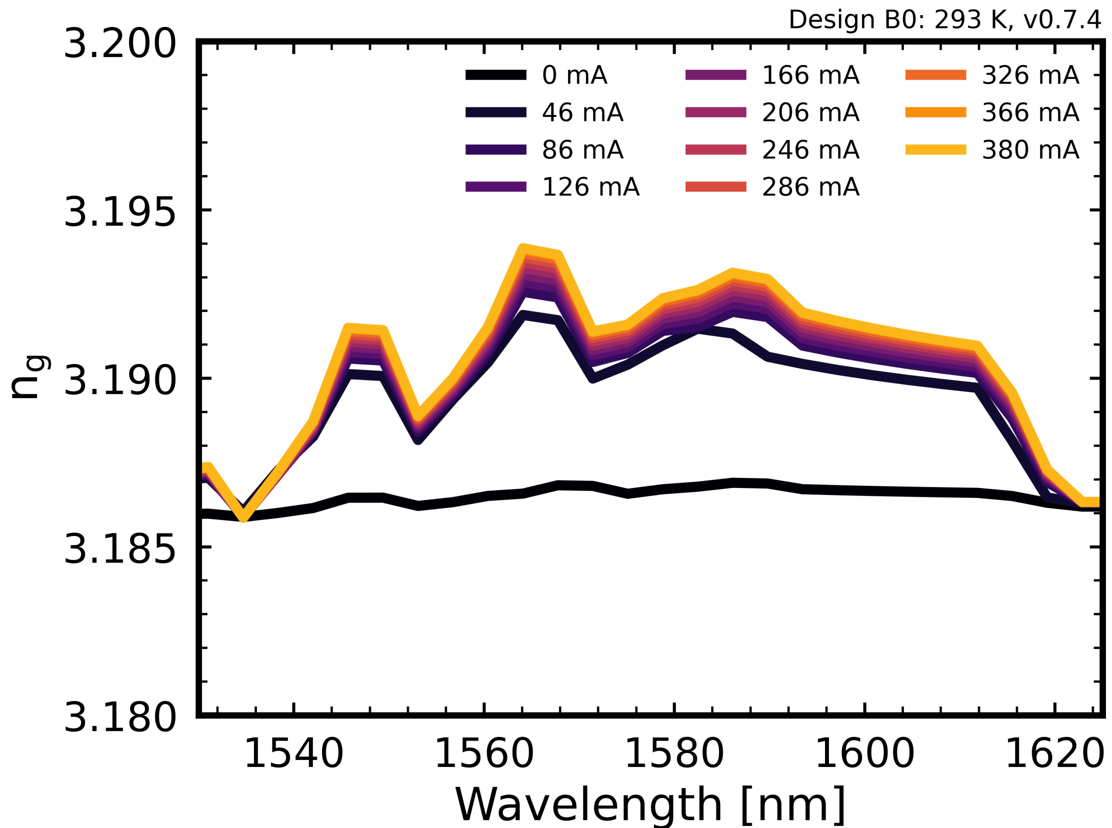

Figure 5.13: Group refractive index for a simulated 2000 µm cavity for different injection levels.

Note that while a 4000 µm cavity was measured, a 2000 µm cavity was simulated. This

was due to the availability of fully mounted devices. Fig. 5.13 shows the simulated group refractive index as a function of injection current. The group refractive index stabilizes after the threshold current density is reached, indicating that it is a predominantly gain driven phenomenon. The different injection current densities between the experimental and simulated device should therefore result in a quantitative but not qualitative difference between the two devices. The expectation would be a less pronounced change in the experimental device as carrier densities are lower.

The normal dispersion of the experimental device was compensated using varying lengths

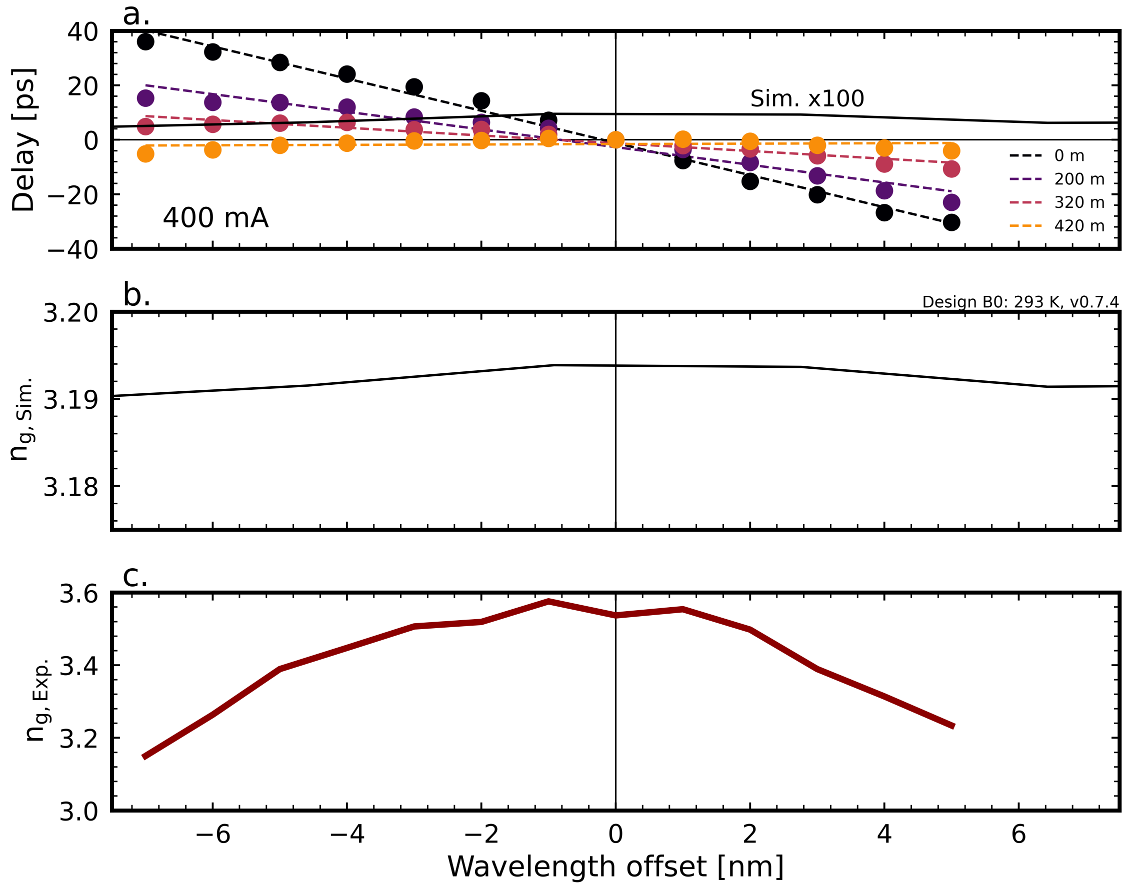

Figure 5.14: **a.** Comparison between experimental group delay with varying levels of fiber compensation and simulated results extrapolated from group index calculations. The wavelength offset assumes a centre lasing wavelength of 1537 nm (experimental) and 1555 nm (simulated). **b.** Simulated and **c.** experimental group refractive index. The experimental index is based on the mostly compensated configuration with 420 m of fibre in-line of both measurement arms. All measurements were conducted at 400 mA injection current. A 4000 µm cavity was measured experimentally while a 2000 µm cavity was simulated.

of silica single mode fibre with an anomalous dispersion of 14.3 ps/nm/km. This allows

near full compensation of the linear contribution to the group delay, leaving a quadratic dependence. From the free spectral range we can extract a group refractive index near the centre of the lasing emission, and combined with the delay measured in Fig. 5.14a. for the linearly compensated case, we can estimate the experimental group refractive index shown in Fig. 5.14c. The model predicts a much weaker group refractive index dispersion than is observed experimentally. The sources of this discrepancy are predominantly due to two factors: the overestimated density of states in the model results in a weaker response of the refractive index to injected carriers, leading to this underestimation of the refractive index change. Additionally, there are the non-linear contributions to the index change in the model are orders of magnitude below their real-life counterparts due to the absence of pulse formation in the model. A comparison between the experimental and simulated results is therefore mostly pointless.

5.5 Understanding carrier distributions

A model which captures the underlying physics at play within the real-life device correctly needs to reproduce behaviours for different geometries and test conditions without the need for calibration factors. However, certain material parameters are difficult to access or even estimate from experimental data. These need to be treated as free "fitting" parameters of the simulation. Ideally, their number should be kept small to avoid excessive assumptions from casting additional doubt on simulated outcomes. Fitted parameters should therefore be independent of device length or test temperature, or their geometry or temperature-dependence needs to be captured in a separate sub-model.

In order to understand how the model and its assumptions may misrepresent the physical reality of the device, it is important to understand the impact of each region within the device on its overall behaviour. Since most semiconductor recombination processes scale at least linearly with carrier density, understanding where carriers accumulate in the device can help pinpoint which models and mechanism are not represented accurately. Additionally, determining where carriers are accumulating within the device can be helpful in determining points to address with potential design changes. For this purpose, Fig. 5.15 shows the carrier concentration for a 750 and 1500 µm device at 293 and 343 K. We will discuss the ratio between the two carrier types in different regions of the device in the next section. For now, the discussion will be focussed on where carriers accumulate in absolute terms. We can see that carrier densities are very similar for the majority carrier type, as the electron density on the n-side (left side) and hole density on the p-side (right side) are largely unaffected by device length (L), temperature (T), and bias (I_{bias}). Outside of majority carrier type areas, carrier concentrations for both types are high within the active region (labelled *Active* in Fig. 5.15b.), etch stop (labelled *Etch* in Fig. 5.15b.)

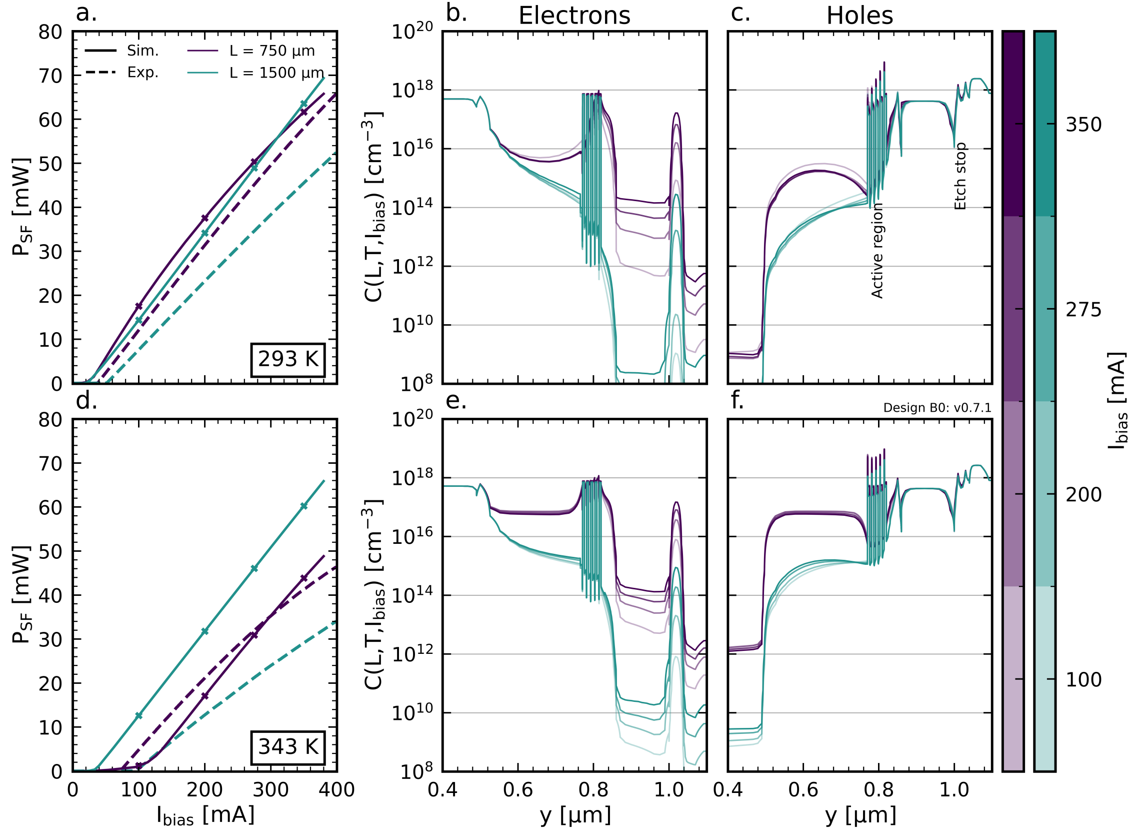

Figure 5.15: LI curve and carrier concentration profiles $C(L, T, I_{bias})$ at the symmetry line for the active region. Devices of cavity lengths of 750 and 1500 µm were simulated at **a.** - **c.** 293 K and **d.** - **f.** 343 K. The dashed lines in a. and d. are measured experimental LI curves. The bias points at which the carrier densities are sampled are marked in **a.** and **d.**

and to a lesser degree within the separate confinement heterostructure (SCH). These are regions where altering material parameters is more likely to affect carrier transport and recombination dynamics and thereby device behaviour, and additional care must be taken to choose parameters that result in a reasonable physical state of the device. The comparison for different lengths and temperatures will follow in the context of comparison with a baseline device, which will highlight the change of each parameter more clearly than can be extracted from the absolute density plot with its large range of densities.

5.5.1 Hole-electron ratio

In order to assess how altering a material parameter, such as an Auger coefficient, will affect the length and temperature dependence of the simulation accuracy, it is useful to compare how carrier densities vary as we increase device length and temperature. While

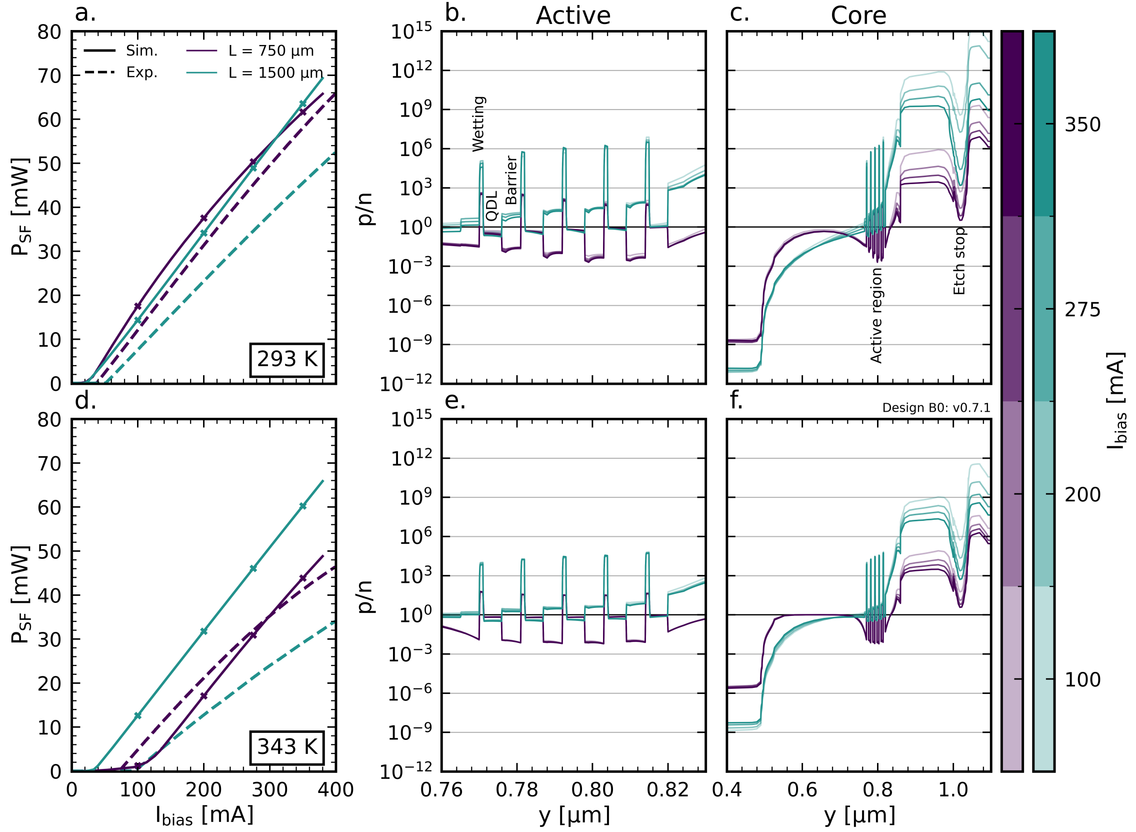

Figure 5.16: LI curve and hole-electron (or pn) ratio, $\frac{p}{n}$, at the symmetry line for the active region. Devices of cavity lengths of 750 and 1500 µm were simulated at 293 K (**a.** - **c.**) and 343 K (**d.** - **f.**). The bias points at which the ratios are sampled are marked in **a.** and **d.**

they will vary everywhere in the device, their variation is most relevant in parts of the device where the electron-hole ratio approaches unity. For example, most recombination mechanisms scale linearly or higher with the carrier density product. Examining the hole-electron ratio, or *pn*-ratio , can show which areas of a device have equal densities of electrons and holes, resulting in high levels of recombination. The *pn*-ratio for a 750 and 1500 µm device are shown in Fig. 5.16 for the active region (Fig. 5.16b. and e.) and the entire core region (Fig. 5.16c. and f.). The top row is at 293 K, while the bottom row represents the same devices but at a uniform device temperature of 343 K.

The first thing to note is the nearly completely unaffected *pn*-ratio in the active region as bias is increased, with most change instead occurring on the (right) p-side of the device. Higher bias currents lead to a significant increase in minority electron carrier densities, leading to a depression of the *pn*-ratio . This effect is equally strong in short and long cavities, both decreasing by approximately 10^3 as current is increased from 100 mA to 350 mA, even though shorter cavities have a higher minority carrier density (and thereby

lower *pn*-ratio) overall. This is the second notable detail, the higher *pn*-ratio for the greater cavity length outside of the n-side core region. The shorter devices have a uniform *pn*-ratio closer to 1, higher than the longer devices ratio of 10^{-2} near the n-InP/core interface, only reaching 1 near the quantum dash layer (QDL) layer stack. The larger difference between short and long device *pn*-ratio on the p-side, rather than the n-side, indicate that electrons are more easily traversing the device for the shorter cavity lengths. This seems to be related to the active region in the centre, as hole accumulation in the QDLs and especially wetting layers is more pronounced for the longer devices. Overall, the *pn*-ratio in the wetting layers is far above one for longer devices, while for shorter devices, the ratio is much closer to one, indicating that any recombination within the wetting layers is going to affect their behaviour much stronger. In the barriers between layers, longer devices show an excess of holes, while shorter devices accumulate electrons here.

Within the QDLs themselves, holes and electrons are very evenly matched. There is a small interlayer asymmetry, with QDLs near the n-side showing *pn*-ratio slightly below 1. This is observed for both short and long devices at 293 K, but only persists for the longer device at 343 K. For the shorter cavity, the *pn*-ratio in the QDLs near the n-side approaches unity as device temperature increases, indicating improved carrier transport across the QDL-stack with temperature. Either electrons are more effectively transported across the stack, away from the n-side, to recombine further into the stack or become minority carriers on the p-side, or holes are transported more efficiently, and thereby balance the carrier density in the first stack.

A possible explanation lies within the wetting layer working as a carrier blockade: if we presume hole transport is hindered by positively charged wetting layers due to repulsion, the much lowered hole carrier density in the shorter device's wetting layers explains why interlayer asymmetry improves as devices get hotter.

Whatever the specific mechanism blocking electron transport might be, it is inversely proportional to carrier density. Temperature and injection current density both reduce the *pn*-ratio across the device. For example, as the uniform device temperature is increased to 343 K, the *pn*-ratio decreases by roughly two orders of magnitude in the active region, and nearly three orders of magnitude near the etch stop. The *pn*-ratio within the etch stop itself appears to approach a cavity length dependent limit, that is closer to unity than anywhere else in the n- or p-side cladding.

The significant accumulation of holes in the wetting layers goes against previous findings in literature for QD systems, which observe the opposite effect [248]. It should be noted that there are two significant differences between the results presented here and the work by [248]. Firstly, the QDs examined in [248] are grown in DWELL structures. Firstly, the carrier-confining DWELLs are 11.5 nm wide, compared to the < 1 nm wetting layer

thickness in the devices studied in our work. The narrower wetting layer results in a much larger confinement energy for the two-dimensional states, moving them further from the bottom of the potential well and into closer proximity to the barrier. Secondly, [248] examines QDs in the InAs/GaAs system, while we examine InAs/InP QDashes. The slightly larger band gap of GaAs compared to InP ($E_{g,GaAs}^{(300K)} - E_{g,InP}^{(300K)} \approxeq 0.1eV$) provides additional confinement. As a result of both of these differences, electronic well states are significantly closer to the barrier edge than hole ones. Electron escape from well states is therefore much faster than the equivalent hole mechanism, leading to the severely asymmetrical occupation in favour of holes within the wetting layer. In [248] both electron and hole DWELL states experience similar confinement energies, with the hole confinement energy even being slightly smaller. The difference in effective masses therefore dominates transport, leading to electron rather than hole accumulation in contrast to the trend observed for the devices in this work.
To summarize, we can note the following observations from examining the *pn*-ratio :

- Since *pn*-ratio is approximately unity within the QDLs, transport across the active region of neither carrier type seems to be hindered to the point of causing a significant intralayer electron-hole occupation asymmetry.

- For short devices, the barrier layers between QDLs are hole-starved, while for long devices there are too few electrons.

- The areas where we expect recombination to be strongest are the n-side core, the QDLs, and the etch stop. Everywhere else the *pn*-ratio is far from unity, indicating that a lack of one carrier type is going to starve recombination.

- The wetting layer trap holes more efficiently than electrons, and has a larger impact for shorter than longer devices.

5.5.2 Comparison with a baseline device

To illustrate the difference between short and long devices at low and high temperatures, Fig. 5.17 shows the normalized electron and hole concentrations for a slice along the y-axis in the centre of one of the device facets. The normalization is done with respect to the carrier concentration of an 1500 µm device at 293 K and an applied bias current of 100 mA, which functions as a baseline device for the rest of this work. The parameters for this simulation can be found in 8.1.
The first thing to note is that the electron density is more affected by device length, temperature, and injected current density than holes are. Concentration ratios are far

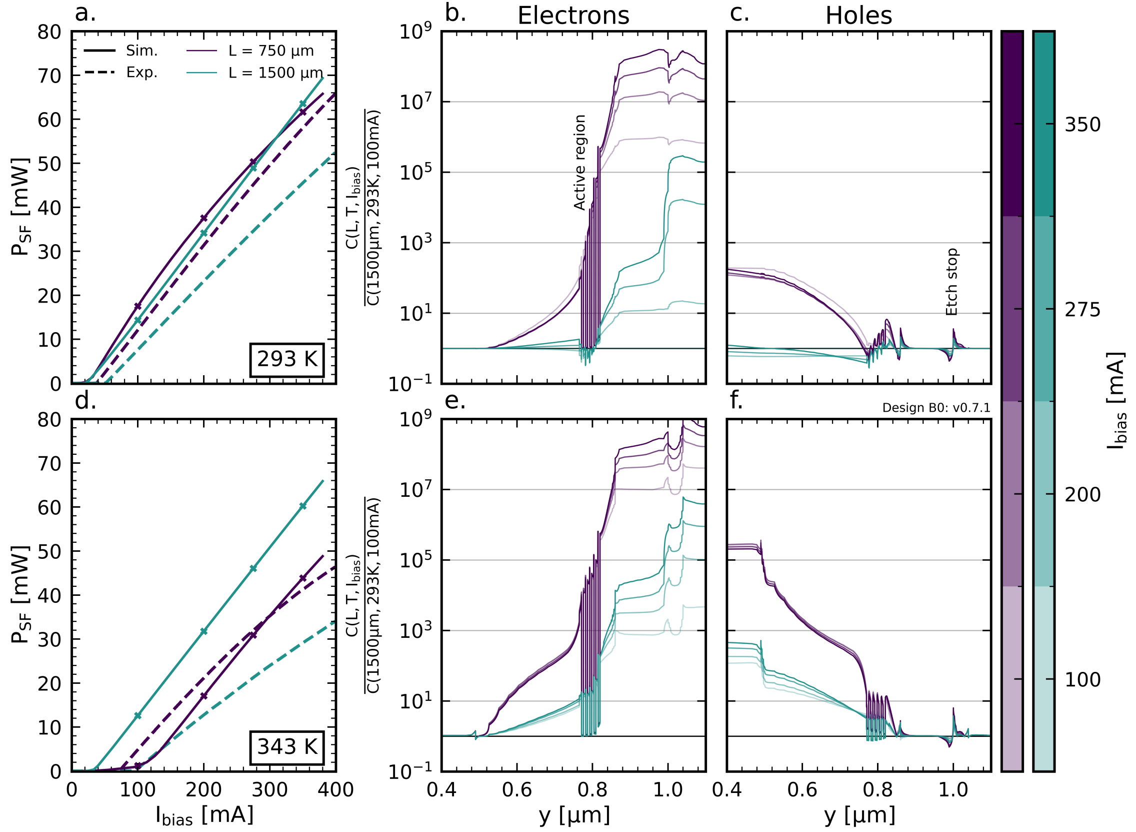

Figure 5.17: LI curve and normalized carrier concentration profiles $C(L, T, I_{bias})$ at the symmetry line for the full device. Devices of cavity lengths of 750 and 1500 µm were simulated at 293 K (**a. - c.**) and 343 K (**d. - f.**). The normalization was done using the electron and hole carrier densities of the 1500 µm cavity at 293 K for $I_{bias} = 100$ mA. The bias points at which the carrier densities are sampled are marked in **a.** and **d.**

larger on the p-side (right side of the graph) than on the n-side (left side of the graph), indicating that the minority carrier injection increases more strongly for electrons than holes. It also scales super-linearly with injection current density: while the 750 µm devices have twice the current density, the minority carrier density increases by five orders of magnitude. This effect is weaker when device temperatures are increased, with the ratio in electron density between long and short cavities at 343 K being only three orders of magnitude apart. Due to the overall higher carrier density in shorter devices, the impact of thermally activated carriers is smaller as they represent a smaller fraction of the overall carrier population. For similar reasons, the increase in electron density with bias is smaller for devices at higher temperatures.

The cavity length dependent increase in electron density is not spatially uniform, with several noteworthy details: as mentioned previously, the increase is more significant on

the p-side, so above the active region, where shorter devices have approximately 10^5 more carriers than their longer counterparts. For longer devices, transport across the etch stop is also much improved with bias given that there are now more carriers reaching the depletion zones around the etch stop. For shorter devices, where depletion zones are much thinner, there is a much smaller increase in the minority carrier density above the etch stop compared to below it. Therefore, carrier movement across it does not change significantly with bias.

Regarding holes, the concentration on the p-side remains unchanged as bias, temperature, and device length increase, excluding the etch stop near 1 µm. Above the etch stop, the carrier density increases, and decreases below it. The accumulation above the etch stop is stronger at higher temperatures, and the difference between the shorter and longer device decreases.

Regarding the n-side, there is very limited change for both devices with bias. Interestingly, for the longer device the hole concentration near the active region decreases with increasing bias, with a cross-over point roughly 50 nm below the active region. Above this point, there is a monotonous decrease in normalized hole density with increasing bias, while below it, there is a decrease below 200 mA, followed by an increase above that bias current. There is no such cross-over for the devices at higher temperature and shorter cavity lengths. The hole concentration on the n-side is significantly higher for the shorter device, approximately two orders of magnitude, pointing to easier hole transport across the QDL stack, which agrees with the observations for the pn-ratio -plots.

6

Impact of structural design variations on device performance

6.1 Defining a design goal

A design optimization stands and falls with its objective function. There is a large list of performance characteristics that can be employed to assess the performance of a given laser device [249]:

- **Threshold current:** a lower threshold current is an indicator of higher efficiency as non-radiative (and thereby parasitic) recombination effects in semiconductors become more pronounced at higher carrier densities.

- **Slope efficiency** refers to the relationship between injection current and laser power above threshold. A higher slope indicates a higher efficiency as carriers are converted into photons rather than lost to non-radiative processes.

- **Wall plug efficiency:** optical power output normalized by electrical power input. Similar to slope efficiency, but taking the efficiency of the supporting electrical system into account, which may include active cooling solutions, rectifiers, and other components required to operate the lasing device from an AC power source.

- **Spectral linewidth:** in the context of lasers for communication networks, linewidth limits the data channel density and thereby overall transmission rates in wavelength multiplexing as well as frequency and phase-shift keying [250]. For quantum communication schemes, it also limits the coherence length and thereby the distance over which data can be transferred at high fidelity.

- **Output noise:** the discrete nature of the optical transitions responsible for laser emission results in a Poissonian noise component (shot noise) that can not be avoided. However, other processes, such as cavity jitter, can further raise this noise level [250]. Low noise figures are desirable for low power operation as well as long haul networks with extended repeater spacings.

- **Temperature stability:** the insensitivity of key laser characteristics to a change in temperature is crucial in maintaining signal strength and fidelity, and raises the economic viability of a laser design by reducing the active cooling requirement.

- **Physical size:** many applications for lasers require arrays of lasers or devices that fit within a small physical package. Lateral dimension of the laser can therefore be a factor when matching laser and application. The monolithic integration of many diode lasers allows for extremely tight packaging and is one of the drivers behind their ubiquity.

This is a non-exhaustive list, and there are other characteristics that are relevant for mode-locked devices especially, such as pulse width, pulse shape, and repetition rate.
For this work, we decided to focus on the temperature stability of the threshold current and slope efficiency, as these were both parameters that should be less affected by the limitations of PICS3D when trying to represent a mode-locked device. The numerical predictions should therefore afford the necessary quantitative accuracy to provide meaningful feedback for an more informed laser fabrication run. The goal is to develop a device with the lowest possible threshold current and highest possible slope efficiency at elevated temperatures, aiming to achieve the highest possible light output at a given bias current without introducing excessive noise.
There were also two boundary conditions to the optimization process: the final device would ideally operate at a repetition rate of approximately 11 GHz, which meant a cavity length of 1500 µm (see Eq.3.71). Additionally, the device was to remain growable within a single step, which meant that certain design changes were out of the question. This was motivated by considerations for the potential economics of these devices, as the hope is that these will become part of utility scale network projects were unit prices play a significant role. Armed with the knowledge about the inner dynamics of the baseline device, as well as the design goal, in an addition to the understanding of the limits to the optimization space, we therefore set out to examine potential pathways towards a higher performing device.

Design change	Section	Primary author	Simulated	Fabricated
Tunneling injection	6.2.1	C. E. Valdivia	-	-
Tunnel diode contacts	6.2.2	G. M. Hasan	-	-
Buried heterojunction	6.2.4	S. W. Schaefer	-	-
Heat spreaders	6.2.3	S. W. Schaefer	-	-
Number of quantum dash layers	6.2.5	S. W. Schaefer	Yes	Yes
Quantum dash layer spacing	6.2.6	S. W. Schaefer	Yes	Yes
SCH-ridge separation	6.2.7	S. W. Schaefer	Yes	-
Unipolar barrier layers	6.2.8	S. W. Schaefer	Yes	Yes

Table 6.1: Topics investigated during the literature review.

6.2 Design variations

Semiconductor lasers have been the subject of intense research for the better part of 7 decades, resulting in a wealth of knowledge about different laser designs in various material systems. The first step in design optimization was therefore a survey of existing work, and seeing if design changes that were successful in other material systems or slightly different laser designs could be applied to the device designed by researchers at the NRC. The original literature review was conducted by Christopher E. Valdivia, Gazi M. Hasan, and the author. The topics covered and the primary author for each topic within the original review document is indicated in Tab. 6.1 to allow delineation between work done by the author and others. Not all the potentially beneficial design changes could be investigated given the finite resources and time frame of the project. The design changes that were either modeled and/or fabricated are indicated in Tab. 6.1 and shown schematically in Fig. 6.1. Due to the timeline of the project, the growths were separated into two design

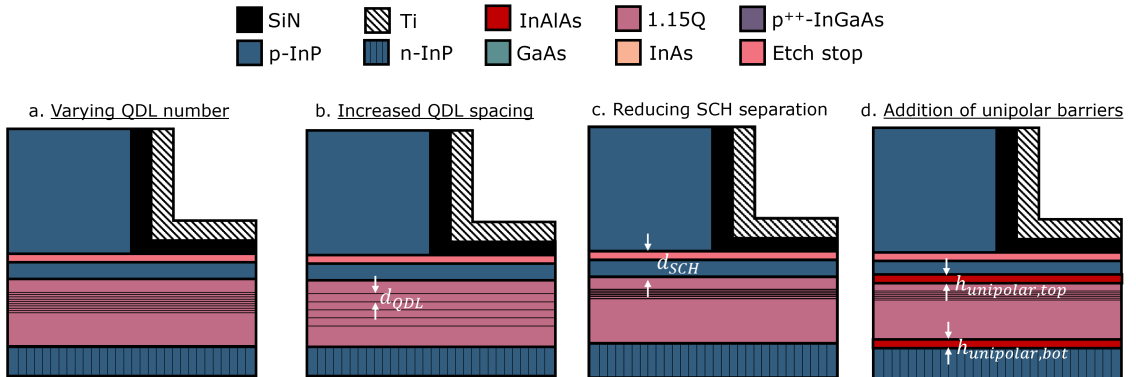

Figure 6.1: Overview over design changes that were investigated using numerical simulation. Underlined designs were fabricated and tested.

and growth cycles, with knowledge gained from the first cycle of devices grown informing potential designs for the second cycle. The first cycle was concerned with determining the

optimal number of QDLs to match the design considerations. As outlined in 6.2.5, the results indicated that four QDLs provided the best high temperature performance, so the second cycle was based on devices featuring four QDLs.
The following sections will examine the literature for each design change, discuss results from the model and experiment where available, and then conclude with a direct comparison between the experimental results for the various designs grown in the second cycle.

6.2.1 Tunneling injection

This section is a summary of literature research done by Gazi M. Hasan which was edited by C. E. Valdivia.
The many advantages of QD and QDash lasers over bulk and QW-based devices, such as lower threshold current, increased temperature stability, broader gain and reduced dispersion, only partially manifested. For example, while characteristic temperatures are higher for QD and QDash devices, they are significantly lower than the theoretical limit would suggest [158]. This is due to a variety of reasons, with one of the greatest contributors being the large relative size of the density of states in the vicinity of the dash due to wetting layer and barrier states compared to the states within the QDs and QDashes. These states siphon carriers from injection into the dots and dashes, limiting the degree of population inversion achievable [251]. This limits the gain, with in addition to parasitic recombination in the optically inactive barrier and wetting layers, leads to an increase in threshold currents and higher characteristics temperatures [252].
A potential solution to avoid this accumulation in the vicinity of the QDL is the addition of quantum well (QW) in close physical proximity to the QDL which facilitates transport into the QD via tunneling between the QW and QD states [253]. The two-dimensional density of states is large enough to provide a reservoir of thermalized carriers, which reduces the carrier leakage and thereby parasitic recombination from active region. Additional advantages include linewidth enhancement factors, higher differential gain, and reduced gain compression and chirp. Lastly, it also has been shown to increase the characteristic temperature [254–256]. There are several successful demonstrations employing injection QWs for InAs/InP QDs, predominantly using InGaAs wells tuned to the lowest electronic state in the QD [257–260]. Holes generally thermalize faster, so adding an injection well targeting confined hole states offers a smaller performance improvement [260, 261]. However, there are studies that include both which indicate that even higher temperature stabilities can be obtained this way [252, 262]. In order to optimize the current transferred between the injection well and the confined state, resonance between the two is ideal, even though an energetic mismatch between the states can be accomodated if it is a multiple of phonon energies in the layer structure. This enables carrier transfer via resonant and

phonon-assisted tunneling, leading to overall higher injection efficiencies [259, 263].
The effective introduction of tunneling injection wells requires close knowledge of the structure and available confined states within the QDs and QDashes. At the time of assessing which design changes to consider, there was some doubt regarding the accuracy of the dash states calculated via PICS3D. Furthermore, the addition of the injection wells would have required extensive fabrication and characterization work to obtain structures with sufficiently high quality to obtain a positive effect on the overall device behaviour. The growth of the injection wells also alters the growth conditions for the QDL stack in the active region. This could lead to a chirping of the layers, where QDashes grown in different layers vary as a result of a globally changing strain or composition profile. Considering these factors, we decided to forego an investigation of tunneling injection at this point, and may revisit at a later date in the context of a more extensive study using a more mature version of the model.

6.2.2 Tunnel diode contacts

In general, for equivalently doped material, p-type semiconductors will have higher resistivity, and greater absorption and scattering coefficients, the latter due to intervalence band absorption, than n-type material [29]. The uniformity of the carrier injection into the active region is highly relevant to the maximum attainable gain, leading to better performing devices [264, 265]. Uniform injection requires lower resistivity, which requires an increase in the dopant density for p-type material, which further reduces the optical properties and introduces additional defect sites for parasitic recombination.
A potential solution that has been explored is switching the p-type cladding to n-type and adding a tunneling junction above the active region that allows conversion of injected electrons into holes within the active region. For InGaAsP lattice matched to InP a tunneling junctions consisting of p^+-AlAs/n^+-InP have shown low resistivity and to be comparatively easy to fabricate [264, 266].
While these junctions are highly relevant in vertical cavity surface emitting lasers (VCSELs), where the mode has a large overlap with the p-type cladding, the overlap in the devices tested here is much smaller, as shown in Fig. 3.4a. The effort of developing a high quality tunnel junction stands in stark contrast to the potential benefits of slightly reduced resistive and absorption losses. We therefore decided to forego a thorough investigation of this design change for the time being.

6.2.3 Heat spreaders

A higher core temperature reduces the performance if through various mechanisms, which we discussed in Ch. 3.4.5. The key points are related to the change in band structure, and carrier density and distribution. The narrowing of band gaps reduces the effectiveness of current blocking structure, such as the barrier layers discussed in 6.2.8. As more thermal energy becomes available to carriers, the occupation of higher lying states increases. For barriers, this means the effective barrier height, which may already be reduced due to band gap narrowing, decreases further. In confined systems, such as QDs and QDashes, the higher lying states will be closer to the barrier band edge, enabling carrier escape into the barriers. The broadening of the carrier distribution also results in fewer carriers at a given energy, reducing the gain while broadening the gain bandwidth. Depending on the structure of the energy levels, this can also mean a dramatic change in the emission wavelength as lasing occurs on a different set of states [267]. An increase in temperature will also lead to additional minority carriers becoming available due to thermal promotion, leading to increased parasitic recombination in the cladding. As the refractive index varies with temperature as well, a high core temperature can reduce the optical mode confinement by reducing the refractive index contrast between the core and cladding layers, in addition to causing an overall shift of the longitudinal mode structure.
Most of the heat is generated near the peak of the mode due to optical absorption, and in the active region due to resistive heating and recombination heat, as we discussed in 4.8. For most devices, these two regions are identical. Removing heat from the active region is an easy way to improve almost all laser performance parameters. There are multiple ways to increase the amount of heat removed, all focused on decreasing the thermal resistance between the active region and an external heat sink. One simple approach is reducing the distance between heat sink and active region by mounting the device upside down, as to avoid the high thermal resistance of the substrate [268, 269]. The reduction in thermal resistance can be significant, reducing it by a quarter for InGaAsP devices on InP wafers and halving for GaAs and Si devices when combined with a heat spreading superstructure [270, 271]. Since the thermal resistivity of most semiconductors, especially when grown as heterostructures, is rather low, the addition of a highly thermally conductive material in the vicinity of the active region can cut down on the thermal resistance. Au and diamond heat spreaders fashioned by enclosing the active region have shown to increase the characteristic temperatures for VCSELs significantly [271, 272]. A similar integration for edge-emitting ridge waveguide lasers would be significantly more involved, akin to burying the heterojunction.
For this reason and the lack of accurate thermal transport modeling in the current version of the model, we decided to not investigate the addition of heat spreaders further. Once the model is capable of more reliable quantitative prediction of the device temperature,

the integration of heat spreaders will be re-examined. We will discuss this further in the outlook.

6.2.4 Buried heterojunction

As outlined in 3.4.1, buried heterojunction waveguides offer several advantages over broad area and ridge waveguides. The added material facilitates more efficient removal of heat, increasing the heat removed from the active region by approximately one third, and increases the mode confinement, leading to increased intensity near the active region and thereby to higher gain [273–275]. This leads to improved temperature stability, and overall lower threshold currents and was shown to allow the operation of InAs/InP QD lasers at up to 90°C [276–278]. The general approach to fabrication of buried heterojunctions is the re-deposition of a semi-insulating variant of the cladding layer material unto an exposed ridge waveguide. The ridge waveguide etch followed by a regrowth in addition to the requirement for high quality current blocking layers renders buried heterojunctions to be both more complex to fabricate and reduces the overall production yield [273,278,279]. These factors make buried heterojunction costlier to produce than ridge waveguides [275]. There are alternative approaches that can be grown in a single step, however these face issues with current leakage that requires further expensive processing to resolve [280]. The strong confinement due to the buried heterojunction can result in an asymmetrical far field lateral mode shape, which, depending on the application, might require further packaging optics to obtain a suitable mode shape [272].
Due to the constraint for the design optimization to not cause a significant increase in the fabrication complexity of the devices, we opted to not investigate this approach further. While it has clear benefits, these are not necessarily outweighed by the economic drawbacks.

6.2.5 Number of quantum dash layers

One of the issues that arises as a result of quantum-confined gain sections in lasers is the limited overlap between the optical mode and the gain region. Quantum wells (QWs) usually feature thicknesses of a few nanometers, while the extent of the mode is several microns, as shown in Fig. 3.4. Quantum dots (QDs) and quantum dashes (QDashes) have even less overlap, which can limit the absolute device gain despite high material gain. The solution is adding additional layers, thereby increasing the total gain area.
However, as we recall from Eq. 3.53, lasing is dependent on the degree of population inversion. The greater the number of states, the larger the injected carrier density has to be to achieve sufficient inversion for lasing. This means higher threshold currents, resulting

in greater recombination losses and reduced overall power efficiency [281]. Greater overlap between the active region and the mode also results in a larger fraction of spontaneously emitted photons coupling into the lasing modes, increasing the phase noise and cavity jitter and broadening the spectral linewidth [117, 282]. Determining the optimal number of QDLs is therefore crucial to optimizing the device performance. This is therefore the first parameter we decided to investigate.

The results of preliminary simulation and subsequent device fabrication are shown in Fig.

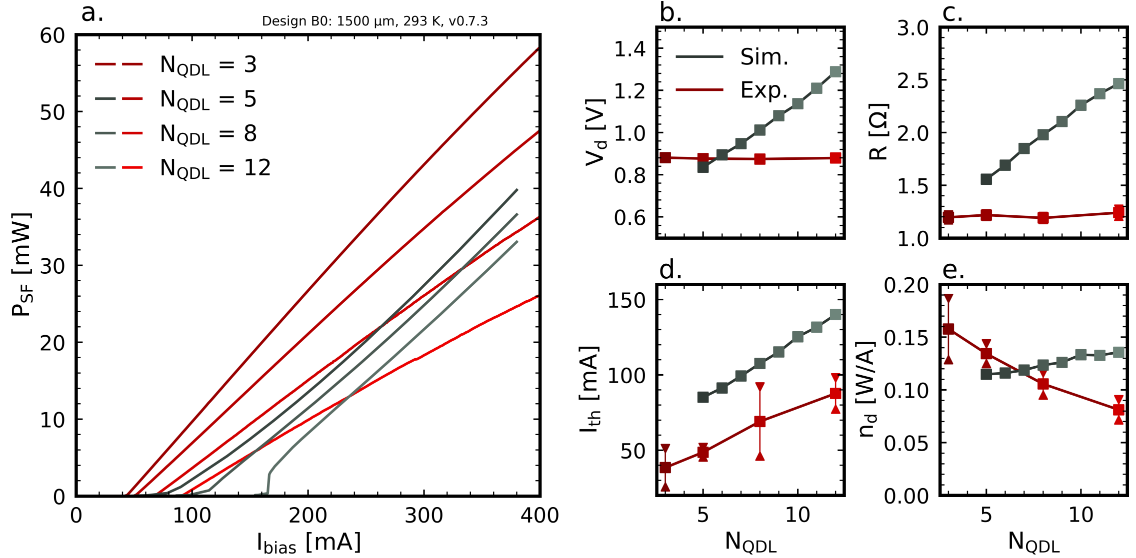

Figure 6.2: **a.** LI characteristic and **b. - e.** LIV parameters for baseline design devices with varying numbers of quantum dash layers (QDLs). Devices with four or less QDLs did not lase consistently, so were not included in these plots. The bars on the experimental data indicate the standard deviation for the experimental parameters. Experimental data was collected by Ping Zhao.

6.2. Devices with 5 to 12 QDLs were simulated, and devices with 3, 5, 8, and 12 QDLs were fabricated and characterized using the semi-automatic setup.

The simulated devices do not capture the physical reality in several important ways, especially for higher QDL numbers. The series resistance R and diode voltage V_d both increase with layer number, while they only show a small change in the fabricated devices. This indicates that the simulation of transport across the QDL stack within the model requires further calibration. The approach in this work was to scale the hot carrier currents to achieve reasonable resistances for five layer devices. Comparison with experimental results for higher layer numbers clearly show that these currents are either not sufficiently enhanced yet, or there is another strong mechanism transporting carriers across the QDL stack. It is possible that higher lying dash states near the barrier edge play an important role, even though simulations that included states lying near the barrier for this purpose

showed no significant difference in resistance. It is also worth noting that the band structure in PICS3D uses abrupt junctions at each interface, as the scaling approach used elsewhere in the device was not possible due to the limited layer thicknesses. While this did not necessarily result in the formation of depletion layers, the band discontinuity at the interfaces is potentially too great and requires a slight decrease.
For the threshold current I_{th} , the simulation results agree qualitatively, while quantitatively they predict a threshold current that is off by a factor of two. The obvious implication is that the magnitude of the density of states is too large, or recombination mechanism coefficients require rescaling, as discussed in 4.5.6. As indicated previously, an update to the gain and Auger models is one of the next steps for this work to narrow the gap between experiment and numerical prediction, improving the accuracy.
Lastly, when comparing differential efficiency n_d between fabricated and simulated devices, a trend opposite to what was observed for I_{th} appears: while the simulation predictions are quantitatively not far from the experimental data, qualitative agreement is poor. The model predicts an improvement in slope efficiency as layers get added, while the opposite is true experimentally. This contrast in results can have a variety of root causes: if transport across the QDL stack is highly inefficient, parasitic absorption from QDLs with incomplete inversion would put a limit on the number of QDLs that is desirable. Additionally, gain suppression and broadening as a result of pulsed operation are mechanisms that are not captured by the model, but are potentially significant mechanisms that reduce the gain and can help to explain the gap between prediction and observation. Implementation of a more sophisticated gain model and occupation functions, combined with shifting to a time-domain model should help address these issues.
Overall, the insight gained for device design is that more layers result in a higher threshold current as well as reduced slope efficiency due to the additional absorption from unoccupied states. It is therefore prudent to use the smallest possible number of QDLs that fulfill the lasing condition for the given cavity when examining I_{th} and n_d alone. However, there is an additional consideration to be made: as further QDLs are added, the temperature-dependence of the device is expected to decrease, reflected in higher characteristic temperatures. The suspected cause is a decrease in the electron escape from the active region. The small energetic difference between confined dash states and the barrier in the conduction band, as shown in Fig. 5.6c., result in electron escape acting as a significant loss mechanism for these devices [283]. If the occupation of each dash is lowered, the occupation of higher lying states is less likely.

Fig. 6.3a. and b. therefore show the characteristic temperatures T_0 and T_1 for the threshold current and slope efficiency as a function of QDL number. The stability of the threshold current peaks around 8 layers, while the slope efficiency is most stable for the three layer device. The highest power output should therefore be achieved by a device

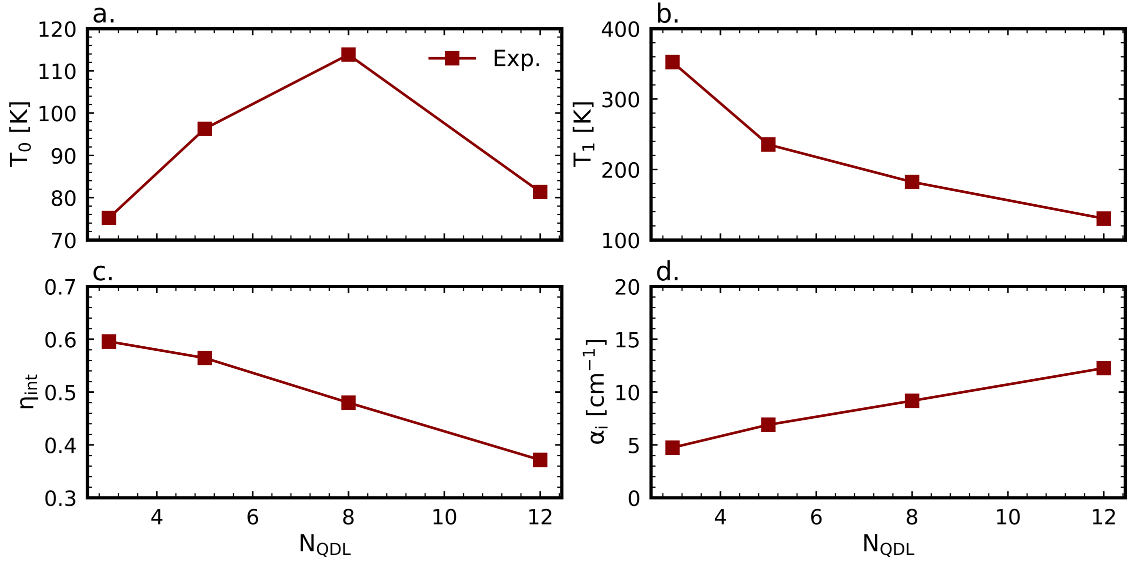

Figure 6.3: **a.** T_0 and **b.** T_1 for a 1500 µm cavity, as well as **c.** internal efficiency η_{int} and **d.** modal loss α_{modal} as a function of quantum dash layer number N_{QDL}. The devices were measured at temperatures between 293 to 323 K and cavities ranging from 500 to 2000 µm were used to extract the internal efficiency and modal loss. Experimental data was collected by Ping Zhao.

with a number of layers between these two. Linear extrapolation indicates that four QDLs is the most sensible trade-off. The second stage of design changes was therefore based on a four layer device.

6.2.6 Quantum dash layer spacing

While there is a plethora of work assessing the impact of barrier widths when adding tunnelling injection wells, there is no clear investigation into the effect the spacing has beyond the impact on QDash morphology due to strain [84, 284]. There appear to be different philosophies regarding optimal layer separation, with some designs favouring barriers thicker than the baseline design explored in this work. In the InAlGaAs system, Schwertberger et al. grow 25 nm barriers [237,285], while even thicker 30 to 40 nm barriers are used in InGaAsP devices [286,287]. We therefore decided to investigate the impact the spacing has on the performance of our lasing device. The simulated and experimental results are shown in Fig. 6.4. They values are normalized by the four quantum dash baseline value for $d_{QDL} = 11$ nm. Over 30 devices were sampled for each value of d_{QDL}, with the values presented in Fig. 6.4 manual measurements from two representative devices with average performance. As we will discuss in 6.3.2, most devices exhibit lasing on multiple

lateral modes beyond a certain bias point. The fitting underlying the plot was done in the regime between threshold current and the onset of lateral multimode lasing. The devices sampled for this section are the baseline, design 1, and design 2. This change is depicted in Fig. 6.1b.

The simulation predicted a significant improvement of properties as the distance be-

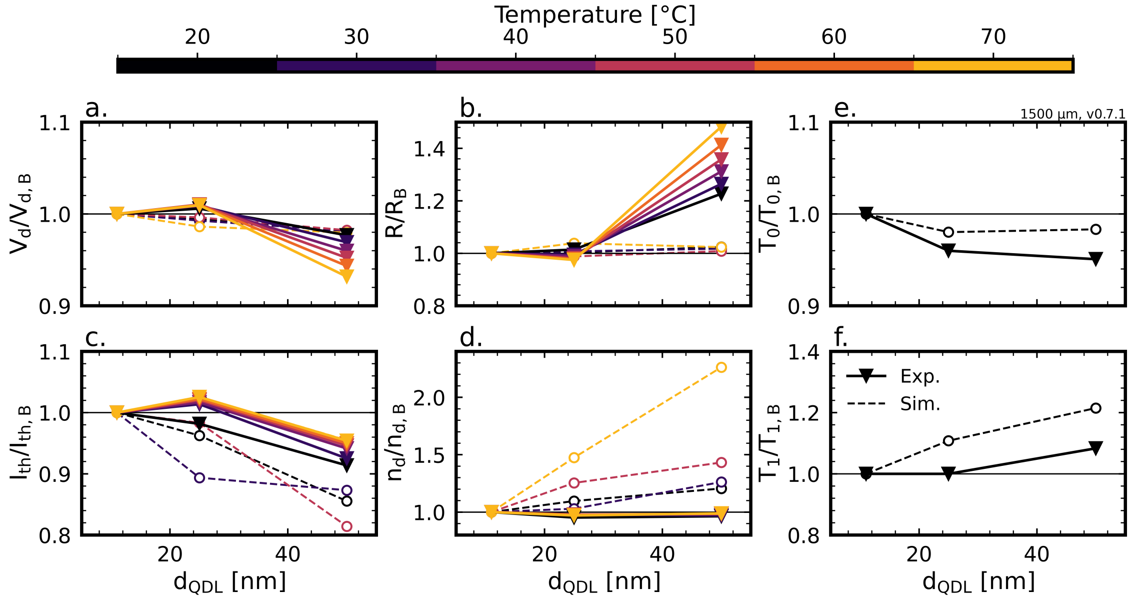

Figure 6.4: Normalized LIV parameters **a.** diode voltage, **b.** series resistance, **c.** threshold current, **d.** slope efficiency, as well as characteristic temperatures **e.** T_0 and **f.** T_1 for a 1500 µm device from growth cycle 2. The numbers are normalized by the baseline value for the second growth cycle. Absolute experimental values are presented in 6.3. The data is for cw measurements.

tween adjacent QDLs increases, most notably a significant decrease in threshold current coupled with an increase in slope efficiency, especially at elevated temperatures. This should lead to an overall improvement of T_0 and T_1 . Comparing against experimental results, the improvement in threshold current only appears for the thicker barrier, while it actually increases for 25 nm QDL spacing, contrary to the simulated prediction. The slope efficiency does not see the predicted doubling, and there is further research in assessing why this prediction was made by the model. The efficiency remains mostly unchanged, with a small decrease for the middle layer spacing. The severe overestimation of the improvement could be due to the lack of core heating in the model. As carriers attain higher thermal energies, the leakage suppressing effect of the thicker barriers becomes increasingly irrelevant. The absence of the necessary hot carriers to drive this degradation mechanisms in the model lead it to vastly overestimate the improvement that can be garnered from separating the layers further.

In terms of temperature stability, a decrease of T_0 with d_{QDL} indicates that increased layer spacing deteriorates the threshold current slightly. However, since I_{th} is smaller for the larger QDL spacing, the end result is a performance increase at elevated temperatures. This is also partially due to the increase of T_1 with QDL period, improving by roughly 10% compared to the baseline design for the thickest barrier. The trends match the simulated predictions, albeit the predicted changes are more severe for both T_0 and T_1 . The discrepancy is most likely a result of incorrect band offsets at the unipolar barrier interfaces, resulting in more efficient carrier escape prevention numerically than is observed in the physical device.
The end result is of increasing the QDL period is higher emission at elevated temperatures, which means making this relatively easy design change is a worthwhile exercise to reduce high temperature threshold currents by about 5% with no significant performance penalty in any other regard.

6.2.7 Separate confinement heterostructure-ridge separation

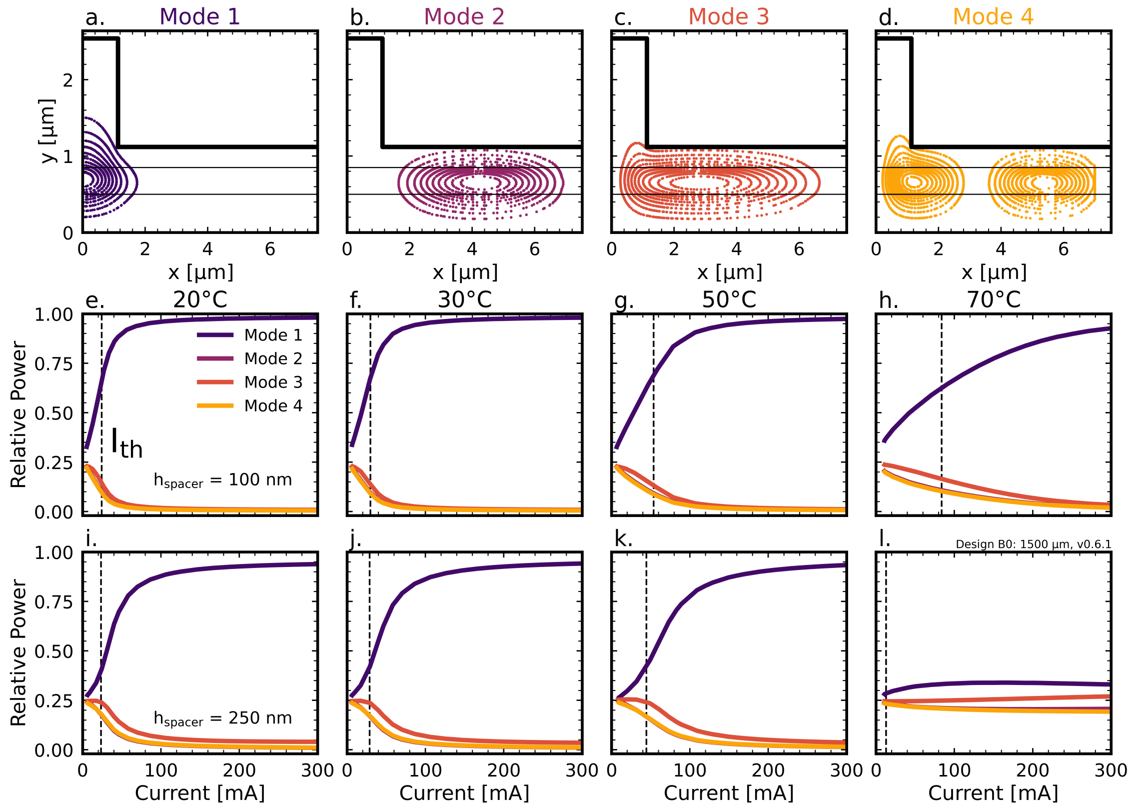

Figure 6.5: Mode shape and relative power distribution between **a. - d.** the first four lateral modes for **e. - h.** h_{spacer} = 100 nm and **i. - l.** h_{spacer} = 250 nm.

As we discussed in the section on tunnel diode contacts (6.2.2), the overlap of the optical

mode with the p-cladding is generally detrimental to device performance due to higher optical scattering coefficients. As discussed previously, this is predominantly due to intervalence band absorption and the surface roughness of the ridge sides as a result of the etch process. Reducing the overlap between the optical mode and the ridge can therefore be beneficial. Increasing the distance between the separate confinement heterostructure (SCH), which defines the vertical mode centre, and the ridge is the simplest way to reduce the overlap.

However, increasing this distance has two drawbacks: the fraction of injected carriers lost to lateral current spreading will also increase, leading to additional parasitic recombination outside of the mode volume. More importantly, since the refractive index profile of the ridge also acts as the horizontal wave guide, reducing the overlap reduces its efficacy. If the overlap is reduced too far, this can lead to higher order lateral modes achieving sufficient gain to start lasing as the device becomes effectively gain guided. This is generally undesirable, as most applications require a single optical mode as close to TE_{10} in shape (Fig. 6.5a.) as possible.

Incidentally, if the SCH is moved too close to the bottom of the ridge, lasing on multiple lateral modes can occur as well. Due to the aforementioned increase in losses as the overlap between optical mode and ridge increases, a large overlap can increase the gain threshold of the fundamental mode to the point where it matches the threshold of other modes. Determining the correct separation between the bottom of the ridge and SCH is therefore essential to achieve the highest possible performance.

Fig. 6.5 shows the predicted lateral optical modes and relative distribution of optical power between those modes for devices simulated with two different separation distances between the ridge bottom and SCH. The model includes up to 5 simultaneously active lateral modes, of which we show the first four. The value for h_{spacer} in the baseline design is 160 nm, and the figure depicts the expected relative contribution from each mode. We can see that thinning the spacer by 60 nm to 100 nm still results in the fundamental mode dominating the emission spectrum, with negligible contributions from other modes. Only at higher device temperatures a contribution from the other modes can be observed, and even then the emission is still predominantly into the first mode.

The picture is different when the SCH is moved further away from the bottom of the ridge. Here the contribution from other modes starts to play a major role at much lower temperatures, culminating in a completely even distribution of energy between the different lateral modes modes at 70°C. The large separation results in a loss of horizontal mode guiding, and as lateral current leakage increases the higher order modes see sufficient gain to also start lasing.

Based on further discussion with the researchers at the NRC, work done in the context of other projects on similar laser designs has shown that the model predictions for the

thinning of the spacer layer are inaccurate. Results presented in 6.3.2 confirm this picture: due to an issue during the growth process, all devices have a spacer thickness of approximately 140 nm, 20 nm thinner than targeted. And as we will explore, this has a profound effect on the lasing behaviour above a certain threshold. A secondary, slightly tilted lateral mode appears for almost all devices, disrupting the mode-locking mechanism. The model does not predict this mode.
What it does predict, however, is a decrease of all lasing parameters. Threshold current and slope efficiency for the thinner spacer are higher and lower than baseline, by roughly 4% and 8 %. Combined with the uncertainty regarding the accuracy of simulated lateral mode shapes, we decided to forego exploring this design variation further without additional work on the model, especially with respect to gain and lateral current transport.

6.2.8 Unipolar barrier layers

Stimulated recombination within the active region is the only contribution to laser output power within the device. Every other form of recombination represents a loss mechanism that decreases the device performance. Guiding injected carriers into regions of the device where it contributes to stimulated emission and preventing it from leaking elsewhere is a governing design principle within laser design. It is one of the factors driving the higher performance of ridge waveguide lasers over gain-guided devices, as the ridge acts as a guide for both the optical mode and the carriers injected from the top. This reduces the lateral leakage into regions that have little to no overlap with the optical mode. The separate confinement heterostructure (SCH) fulfills a similar role, preventing carrier leakage across the active region into the cladding region of opposite polarity. The effectiveness of the SCH in achieving this change is linked to the height of the barrier for holes at the n-cladding/SCH and electrons at the SCH/p-cladding interfaces.
The height of this barrier is primarily related to the semiconductor compositions and relative dopant concentrations, which are subject to external design considerations such as resistivity and band gap. If the barriers are too small to inhibit carrier leakage, a layer can be interposed at the interface with more suitable barriers. This is a common strategy in organic semiconductors, which often integrate both electron and hole blocking layers to prevent carriers from escaping [288,289]. For semiconductor devices, the selective carrier blocking layers have seen application in infrared detectors, where a reduction in dark current and collection efficiency are seen after blocking layer introduction [290]. The short radiative lifetimes in semiconductors combined with the efficient current blocking in heterostructures reduce the impact of carrier leakage to overall loss compared to organic semiconductors [291]. Since adding further layers adds fabrication complexity and generally results in a penalty to majority carrier transport and additional parasitic recom-

bination. This is a worthwhile trade-off in material systems with longer radiative lifetimes, such as InGaN/GaN diodes, but generally unfavourable for InGaAsP/InP [292]. While unfavourable for ridge waveguide devices, current blocking structures are an essential part of buried heterojunction lasers. For these devices, parasitic currents through the cladding are a significant contribution to overall loss, which can be mitigated using blocking structures [279, 293].

In order to determine whether or not unipolar barriers are a worthwhile design change

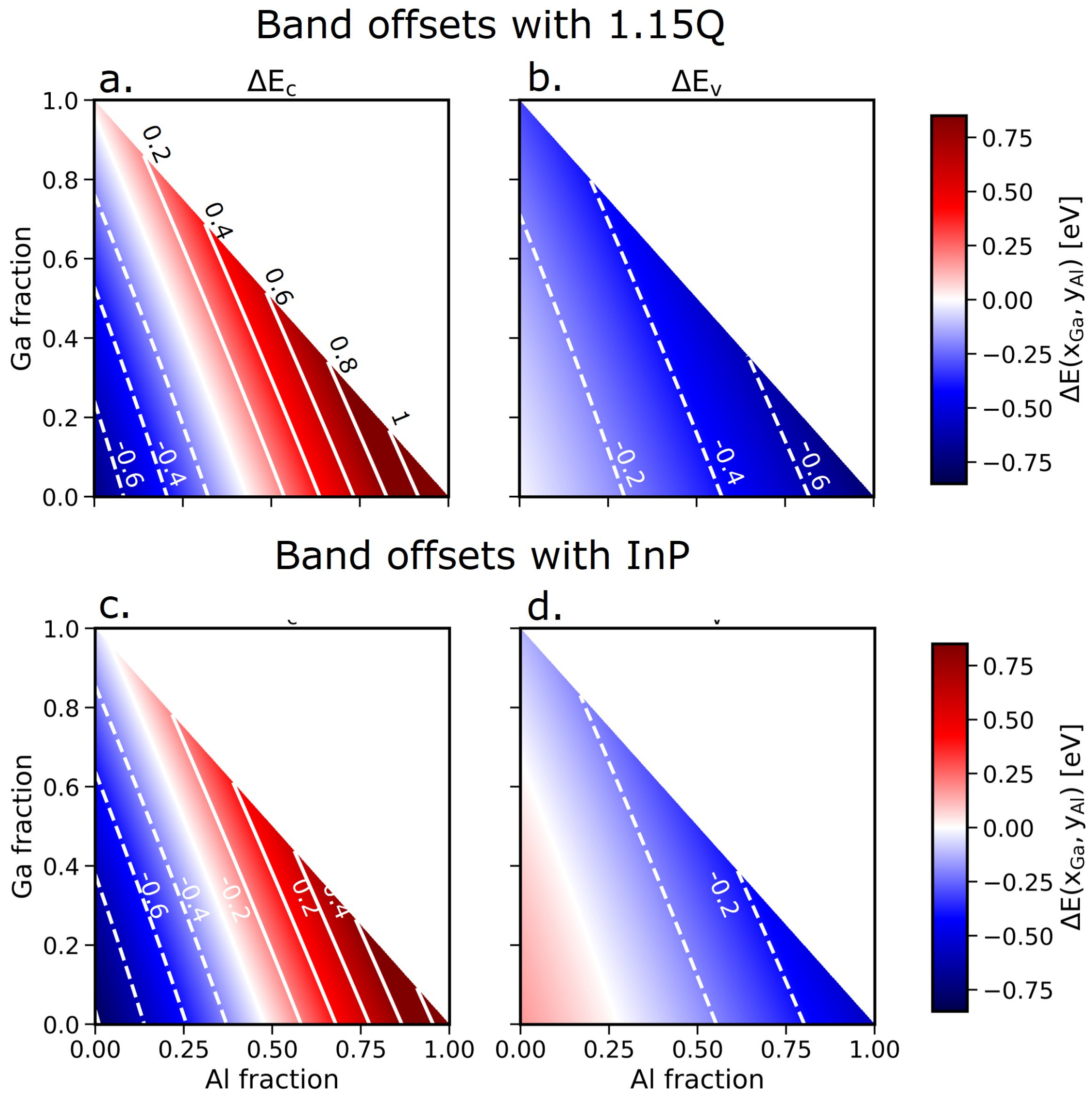

Figure 6.6: Band offsets for undoped InAlAs with **a. - b.** 1.15QInP and **c. - d.** InP for the conduction and valence band. All semiconductors are assumed to be undoped.

to investigate, we conducted simulations adding carrier blocking layers to the device at

both the top and the bottom of the SCH. This is depicted in Fig. 6.1d. We experimented with different compositions, selecting InAlAs as a blocking material. It had been grown successfully at high quality on InP-lattice matched InGaAsP by our collaborators at the NRC. It has sufficiently large band offsets with both cladding and SCH materials as shown in Fig. 6.6 to act as an effective carrier blocking structure and can be doped to select for either carrier type by altering the band alignment. The layer was integrated by replacing sub-ridge p-cladding with InAlAs, maintaining a total thickness of h_{spacer} of 160 nm. Preliminary simulations indicated that blocking structures at the bottom of the SCH had an overall negative impact on performance, while adding them at the SCH/p-cladding interface resulted in a meaningful improvement of overall performance. The devices were grown accordingly, and the experimental results for the 1500 µm devices are shown in Fig. 6.7. Here we compare three different designs: the baseline design for the second growth cycle, which does not include an InAlAs barrier, and design 3 and design 4, which include a 30 nm and 100 nm InAlAs barrier at the SCH/p-cladding interface. All other parameters remain unchanged.

The addition of the additional barrier material results in a small decrease in the diode

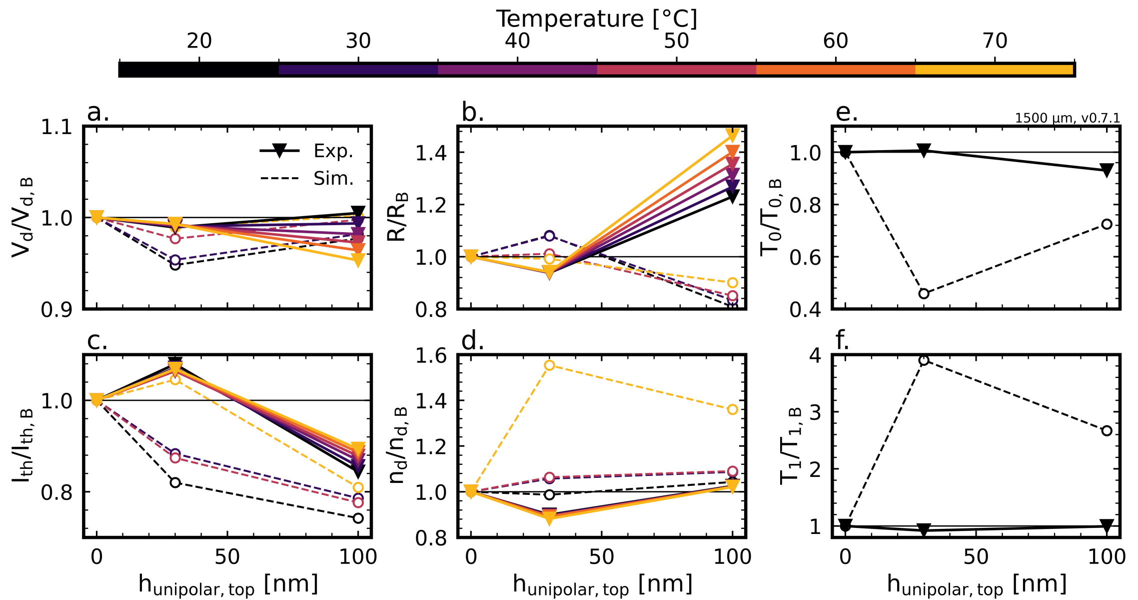

Figure 6.7: Normalized LIV parameters **a.** diode voltage, **b.** series resistance, **c.** threshold current, **d**. slope efficiency, as well as characteristic temperatures **e.** T_0 and **f.** T_1 for a 1500 µm device from growth cycle 2. The numbers are normalized by the baseline value for the second growth cycle. Absolute experimental values are presented in 6.3. The data is for cw measurements.

voltage at higher temperatures. The resistance decreases for the thinner barrier and then rises by approximately 50% at 70°C for the $h_{unipolar,top}$ = 100 nm device compared to the baseline. This should be reflected in an overall increase in power draw from the device at

a given current. This is counteracted by a noticeable reduction in threshold current. The improvement due to the addition of the blocking layer is larger at lower temperatures. This is reflected in a slight drop in T_0 , indicating that the blocking efficiency for electrons decreases with temperature. This is due to reduced barrier offsets and higher energy electrons observing thinner tunnelling barriers with temperature.
Interestingly, the trend for both threshold current and slope efficiency is not monotone for increasing $h_{unipolar,top}$. For the thinner barrier, the resistance actually decreases compared to the barrier-less baseline design. This points towards an enhancement of current flow across the SCH/p-cladding interface, leading to better hole injection but also enhancing electron leakage reflected in higher threshold currents and lower slope efficiencies. The exact nature of this enhancement is unclear, and the subject of future research into the mechanism that drives this behaviour.
When we compare the predictions made by the simulation with the final device results, there is agreement in some parts and discrepancy in others. The prediction of the threshold current improvement is overestimated by the simulation, but the trend towards lower improvement with elevated temperature holds. For most other parameters, the predictions are quite far from the experimental reference. The predicted trend for resistance as a function of $h_{unipolar,top}$ is inverted compared to the experimental results. For the diode voltage, the temperature dependent trend for $h_{unipolar,top} = 100$ nm is also inverted compared to the experimental observation. This culminates in a large underestimation of the threshold current temperature dependence coupled with a large overestimation of the slope efficiency stability. These results point towards a likely issue with the transport modelled at the unipolar barrier being vastly different from the physical reality. This is a starting point for future work on further improving the model.

6.3 Comparison of experimental results for second growth cycle

Identifier	Design	QDL period d_{QDL} [nm]	Unipolar barrier thickness $h_{unipolar,top}$ [nm]
B	Baseline	11	-
1	Design 1	25	-
2	Design 2	50	-
3	Design 3	11	30
4	Design 4	11	100
5	Design 5	25	100
6	Design 6	50	100

Table 6.2: Designs chosen for fabrication in the second growth cycle.

After examining the results of the different design variations in isolation, we will now

examine them in direct comparison to see if any further trends emerge. Of the proposed designs for the second growth cycle, six were chosen for fabrication, with designs selected to allow for evaluation of three different aspects important to future laser designs: first, the role of quantum dash layer separation (baseline with design 1 and 2), discussed in 6.2.6, second, the impact of increased carrier confinement on overall device behaviour (baseline with design 3 and 4) in 6.2.8, and third, the interplay between both design changes (design 4, 5, and 6). The selected designs and their designations can be found in Tab. 6.2. They can be separated into three runs, each targeting a different device parameter. Here we will now present an overarching comparison between the experimental results for the different designs and compare them relative to one another. Note that the baseline for the second cycle differs from the baseline design discussed in 5 by having one quantum dash layers less.

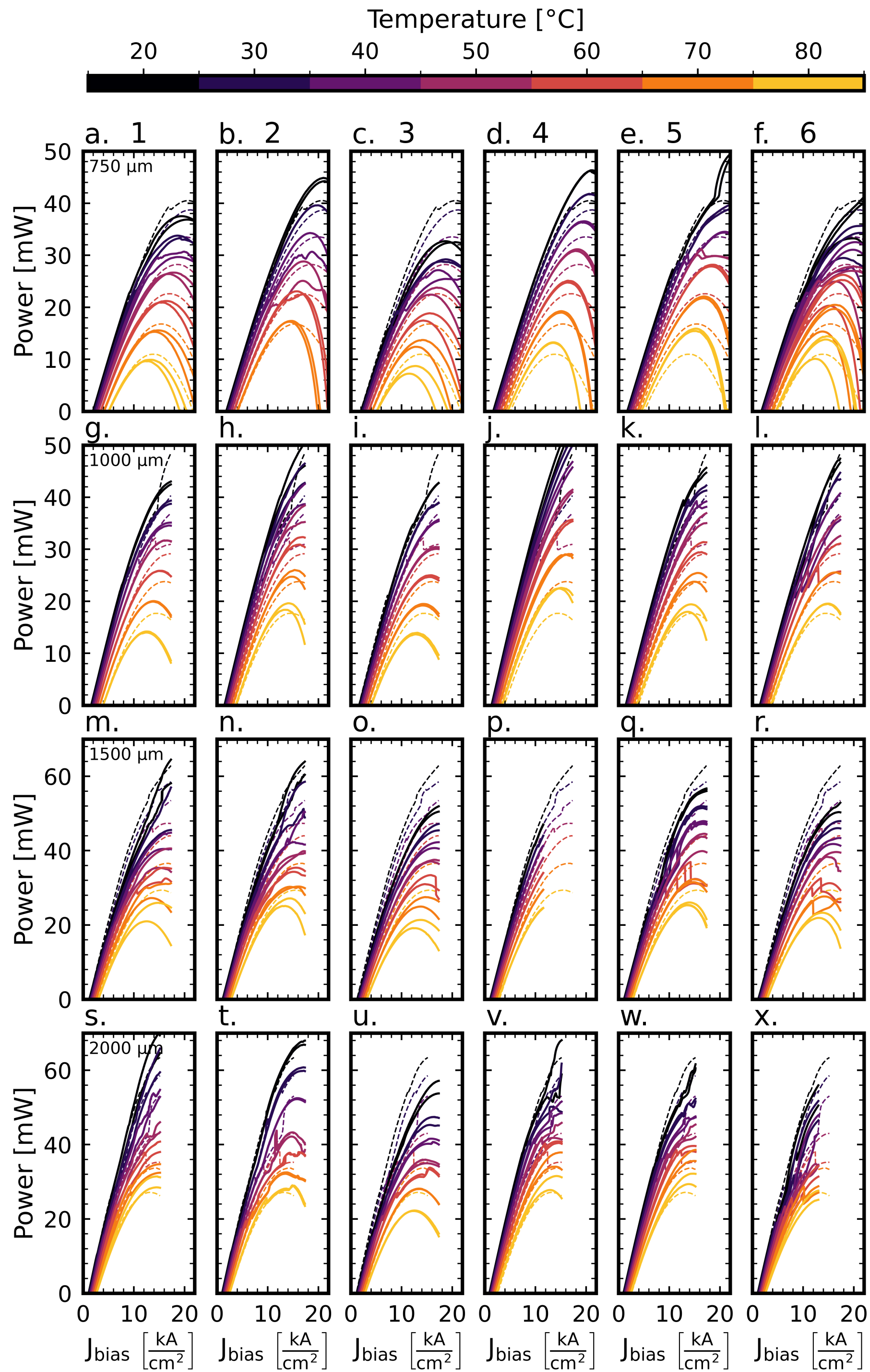

Figure 6.8: Experimental single facet laser power as a function of cw bias current density J_{bias} for the different designs at increasing temperature. Column indices indicate the six different design alterations, while rows are related to the four cavity lengths (**a.-f.** 750 µm, **g.-l.** 1000 µm, **m.-r.** 1500 µm, and **s.-x.** 2000 µm) fabricated and tested. The dashed line indicates the reference baseline design.

6.3.1 Experimental LIV curves

Fig. 6.8 shows the resultant single facet laser power curves as a function of bias current density for all six design alterations at the four cavity lengths examined in this work, with the batch 2 baseline for each cavity length and temperature as a dashed line. A minimum of two devices were measured at each cavity length, chosen based on preliminary semi-automated but less accurate measurement of the entire bar. This allowed selecting the devices with the most average characteristics to represent each design. All devices were measured consecutively at seven temperatures, ranging from 20°C to 80°C, with a two minute hold time prior to measurement at each temperature. The temperature refers to the temperature of the heated stage, rather than the internal temperature of the device, which expected to be higher by 40 - 60 K [155]. All devices were measured with both pulsed (3 μs pulse width, 1% duty cycle) and continuous (cw) bias. Unless stated explicitly, bias in this section will refer to cw bias. The maximum bias current was increased linearly from 400 to 700 mA as cavity lengths increased. The resulting reduced maximum current density for larger cavity lengths was chosen to avoid damage at the uncoated facets as a result of their higher optical power density.

6.3.2 Lateral multi-mode lasing

The first thing to note is the discontinuities that all device designs experience, especially at longer cavity lengths. This is most likely a result of insufficient distance between the separate confinement heterostructure (SCH) and the bottom of the ridge. As discussed in Ch. 6.2.7, this has two main effects: higher current densities below the ridge as current spreading is reduced and increased optical losses for even symmetry modes. Modes with even symmetry, such as TE_{10}, are centred below the ridge and therefore show larger overlap with the sides of the ridge. The first higher order lateral mode has odd symmetry, and is therefore less affected by these losses due to its central position being further away from the ridge. A more thorough explanation of the lateral mode structure can be found in Ch. 6.2.7. In addition, the reduced current spreading leads to higher carrier densities in the active region, which can further exacerbate this problem. As the available gain increases, mode-selective mechanisms such as spatial hole burning can be overwhelmed, allowing for similar gain conditions for more than one lasing state. These two effects combined lead to metastable behaviour, where multiple stable lasing states are accessible with only minimal perturbation. A comparatively small change in bias seems to be sufficient to move the system from one metastable state to another. The different lasing states can have different efficiencies and losses, which seems to be the case in the case of the batch 2 lasing devices. As the laser moves from one lasing regime to the next, it appears to oscillate

between different lasing states. The difference in efficiencies leads to sharp changes in the LI characteristic, which we observe as the discontinuous jumps in power. These jumps are more prevalent for longer cavities at higher biases, and are reproducible between separate measurements and devices. For example, Fig. 6.9 shows the cw-LI characteristic and its second derivative for the baseline design at 20°C before and after the temperature sweep. Since the first derivative is the instantaneous slope efficiency, its second derivative can be useful in identifying abrupt changes of slope efficiencies, indicative of a switch in the lasing state. The two curves and their curves coincide significantly, showing discontinuities at very similar bias values. This indicates that the source of the bias switching is based on competing internal states of the laser rather than spurious external noise. The curves for two separate devices, D1 and D2, also show a high degree of similarity. The bias conditions at which a switch occurs do vary slightly for the different devices of the same cavity length, but are generally in close proximity to one another. It is therefore unlikely that the metastable lasing is the result of localized fabrication inhomogeneities and rather the product of the overall design.

While Fig. 6.9 shows the behaviour for the baseline design at 20°C, how do the other

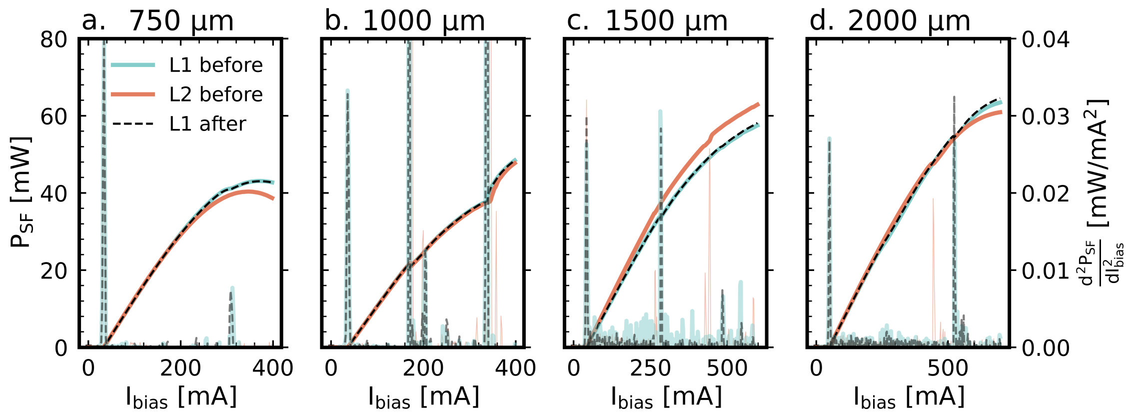

Figure 6.9: Experimental single facet laser power as a function of cw bias current I_{bias} for the baseline design at 20°C. The right axes shows the second derivative of the laser power to aid with the identification of lasing state switching. The measurements were conducted before and after the temperature sweep. L1 and L2 refer to the measurement taken from two separate devices on the same bar. For cavity lengths of **a.** 750 µm, **b.** 1000 µm, **c.** 1500 µm, and **d.** 2000 µm.

design changes affect the stability of the lasing state? For this purpose, the normalized second derivative for the devices in Fig. 6.8 is plotted in Fig. 6.10. The first peak is related to the lasing turn-on at the threshold current density. Similarly for 750 µm cavities, which experience roll-off severe enough to completely subdue lasing emission, the final peak at elevated temperatures (>50°C) is the lasing turn-off. All other peaks are related to rapid changes in the lasing state which are accompanied by discontinuities in the slope

efficiency, or noise in the measurement setup. To reduce the impact of the latter, all data was subjected to a 10 mA wide boxcar filter. The boxcar width of 10 mA represents 6 data points.

The expectation for a device operating in a stable lasing state would be a single peak at turn-on and an optional second peak at very high current densities for turn-off for sufficiently short cavities. Looking at all the devices tested in Fig. 6.10, the behaviour for devices seems to relatively uniform across the bars cleaved at different cavity lengths. Examples of this are the baseline and design 4 devices with 750 µm cavity lengths (Fig. 6.10a. and e.). These devices also seem more impervious to relative device position: devices closer to the edge of the bar, where factors such as strain and facet damage from the cleaving process are more pronounced, can have significantly reduced device performance. This can be seen most strongly for the short cavity devices with designs 1, 2, and 3 (Fig. 6.10b., c., and d.). The second derivative is dominated by noise towards the upper edge as the devices fail to maintain even a metastable lasing state.

If we compare the overall lasing behaviour uniformity, we observe that most bars show relatively similar onsets of lasing across all their devices, and, when present, similar bias values at which an additional lasing state starts to interfere, e.g. Fig. 6.10o. For these 1500 µm long cavities of the baseline design, there seems to be an interfering lasing state that experiences sufficient gain at around 10 kA/cm^2, which is very similar for all devices in the bar. However, there is a secondary transition that occurs near 14 to 18 kA/cm^2, which varies slightly in onset bias current density for the different devices. We can therefore conclude that gain for the secondary, competing lasing state is significantly affected by the small device to device fabrication inhomogeneities for devices on the same bar. This is also exemplified by bars such as the 1000 µm cavities for baseline and design 4 (Fig. 6.10h. and l.): the devices near the centre of the bar behave much differently to the ones in closer proximity to the edges. For the baseline design, this results in very stable lasing for central devices and a significant amount of instability near the edges. For design 4, the effect is the opposite, with devices near the centre showing instability at lower bias current densities and the outer devices remaining stable until nearly double the bias is reached. This further emphasizes the fickle balance between the two lasing state, and the relative ease with which the interfering state or states are suppressed.

Observing larger trends across all devices and designs, we see that longer cavities worsen the instability, an expected result of the lower relative gain threshold of other lasing states given the higher absolute gain in longer cavities. Additionally, at room temperature, most design changes seem to favour the perturbing state over the initial lasing state. The baseline (leftmost column in Fig. 6.10) generally represents the least perturbed LI-curve. Design 4 performs similarly for the 750 µm cavities, but then shows marginally greater instability as cavity lengths increase, especially at very high current densities. There are

no clear trends with QDL spacing or unipolar barrier thickness, apart from small changes in the onset of the instability. The impact of temperature on the lasing instability can be examined using the temperature-dependent second derivative curves in Fig. 6.11. We can see that temperature seems to suppress the instability, starting as early as 30°C and upwards in the case of the baseline design cleaved to 750 µm cavity length (Fig. 6.11a.). There is a disturbance in the lasing state at lower temperatures, indicated by the peak near 18 kA/cm^2, which then disappears as device temperature decreases. This indicates that there is a minimum gain condition that enables the second state to become viable which is easily suppressed, as even the small increase in device temperature by 10 K entirely prohibits the cavity shifting into the alternate lasing state. If we compare the performance of the 750 µm baseline design with the other designs, we notice that most other designs seem to decrease the stability of the initial lasing state. Only design 4, which adds a 100 nm thick InAlAs barrier at the top of the SCH to the baseline design, appears to improve the stability. Design 4 also has the lowest threshold current density and highest slope efficiency of all devices, which we will discuss in more detail in the next section. The addition of only 30 nm of InAlAs in design 3 seems to move the onset of the metastability to lower current densities and stabilize it there, as it can be observed at up to 40°C. There seems to be a highly non-linear change in behaviour between the thinner and thicker barrier layer. This may be due to mode pulling as a result of the refractive index change.
Increasing the QDL layer period seems to increase the instability. Designs 1 and 2, with QDL periods of 25 and 50 nm, respectively, show instabilities at up to 50°C, much higher than the baseline design with its 11 nm QDL period. It is noteworthy that the behaviour for design 2 was very different between the two devices tested, with one device exhibiting no instability whatsoever. This is also apparent in the first derivative plots in Fig. 8.4. However, using the LIV data from the semi-automatic setup, where each device on the laser bar was tested at room temperature (see Fig. 6.10), extending the QDL spacing seems to increase the instability. In this setup, devices are contacted automatically and measured using a wide-area sensor, therefore the light collection efficiency of the setup changes with the device position on the bar. This and the larger distance between device and sensor leads result from this setup to generally underestimate the device efficiency, while they should be qualitatively very similar to the manual measurement. The small difference in contacting the devices between the manual and the automatic setup, with contact points chosen to coincide for both setups, seems to be sufficient to avoid meaningful state instability.

It is difficult to distinguish between a shift in lateral and longitudinal mode structure laying at the root of the meta-stability from a lasing state's power output alone. We therefore conducted two measurements: one was observing the mode-locked signal using

the setup described in 4.2.4 and a measurement of the far-field mode shape. The latter measurement was conducted by Mohamed Rahim. It shows that there is a second lateral mode that sets in and competes with the fundamental mode, resulting in the discontinuities in the LI shape. The higher order mode is however not the mode the model predicts, shown in Fig. 5.2b. Instead, it has a similar shape to the fundamental mode, but with its wavevector slightly tilted with respect to the cavity axis along x.
The instability has a distinct signature in the spectral output of the laser as well, as can be seen in Fig. 6.12a. For a 1500 µm long cavity, applied biases below 300 mA result in a single stable lasing mode. As bias is increased further, the second lasing state is reached, with two stable co-existing modes. Its spectroscopic signature can first be spotted around 325 mA, with several short wavelength longitudinal modes starting to show emission intensities that are within an order of magnitude of the longitudinal modes belonging to the fundamental lateral mode. As bias is increased further, these shorter modes increase in intensity until they are within a few dBm of the original modes, eventually forming a distinct lobe in the gain at around 360 mA bias. This lobe trends towards shorter wavelengths as bias increases, decreasing in relative intensity as it becomes energetically further separated from the initial lobe. The result is a distinct Y-shape.
The mechanism driving the continued red-shift is unclear, but combined with the asymmetric far-field mode shape observed, there appears to be some fundamental asymmetry to the cavity. The origin of this asymmetry is the subject of current research, as it has potential for multiple combs coexisting within the same cavity.

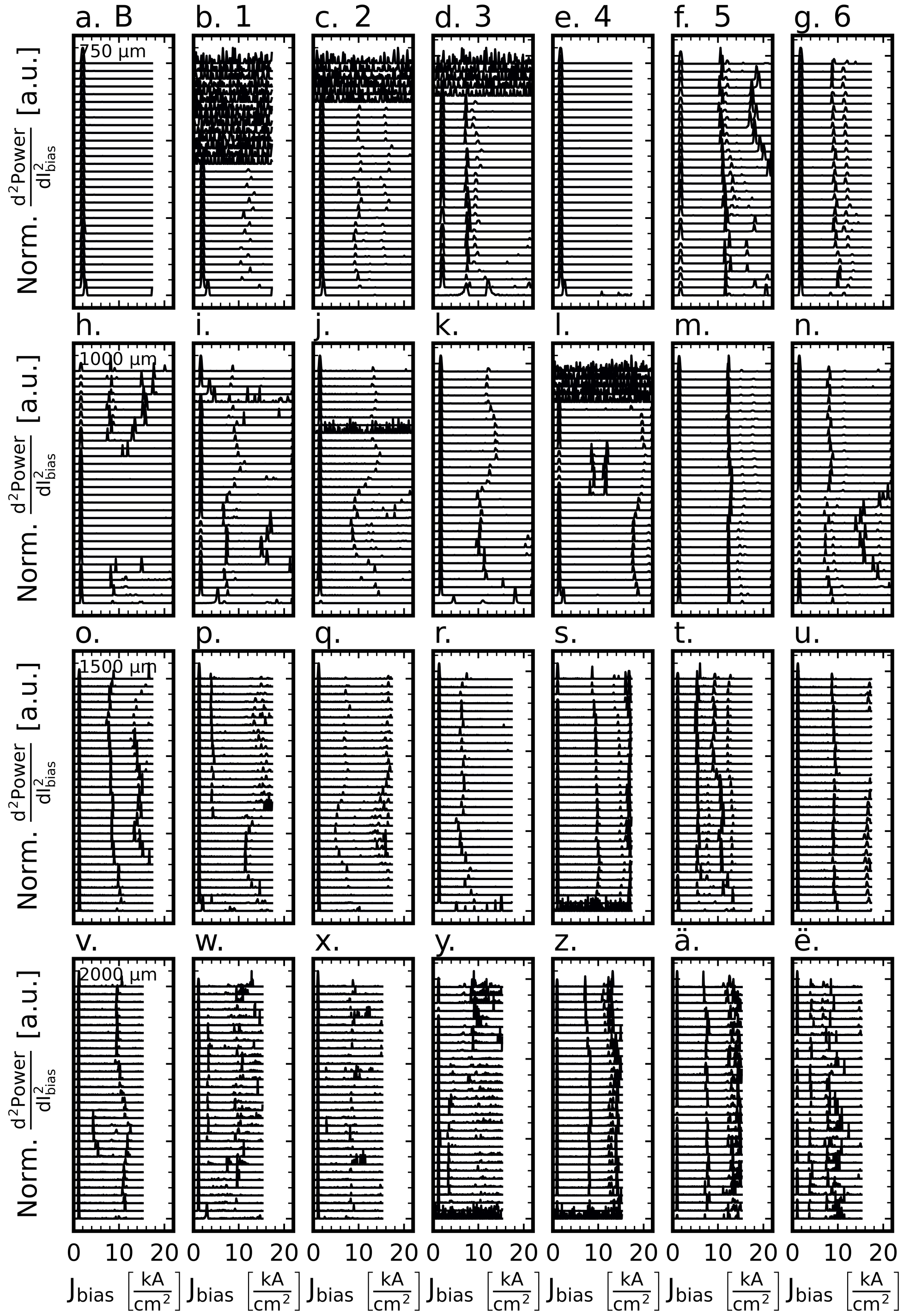

Figure 6.10: Normalized and offset second derivative of single facet laser power as a function of cw bias current density J_{bias} for the different designs at room temperature, measured using the semi-automatic bar testing setup. The power data has been averaged prior to gradient calculation using a 10 mA wide kernel. Column indices indicate the baseline and six different design alterations, while rows correspond to the four cavity lengths (**a.-g.** 750 µm, **h.-n.** 1000 µm, **o.-u.** 1500 µm, and **v.-ë.** 2000 µm) fabricated and tested.

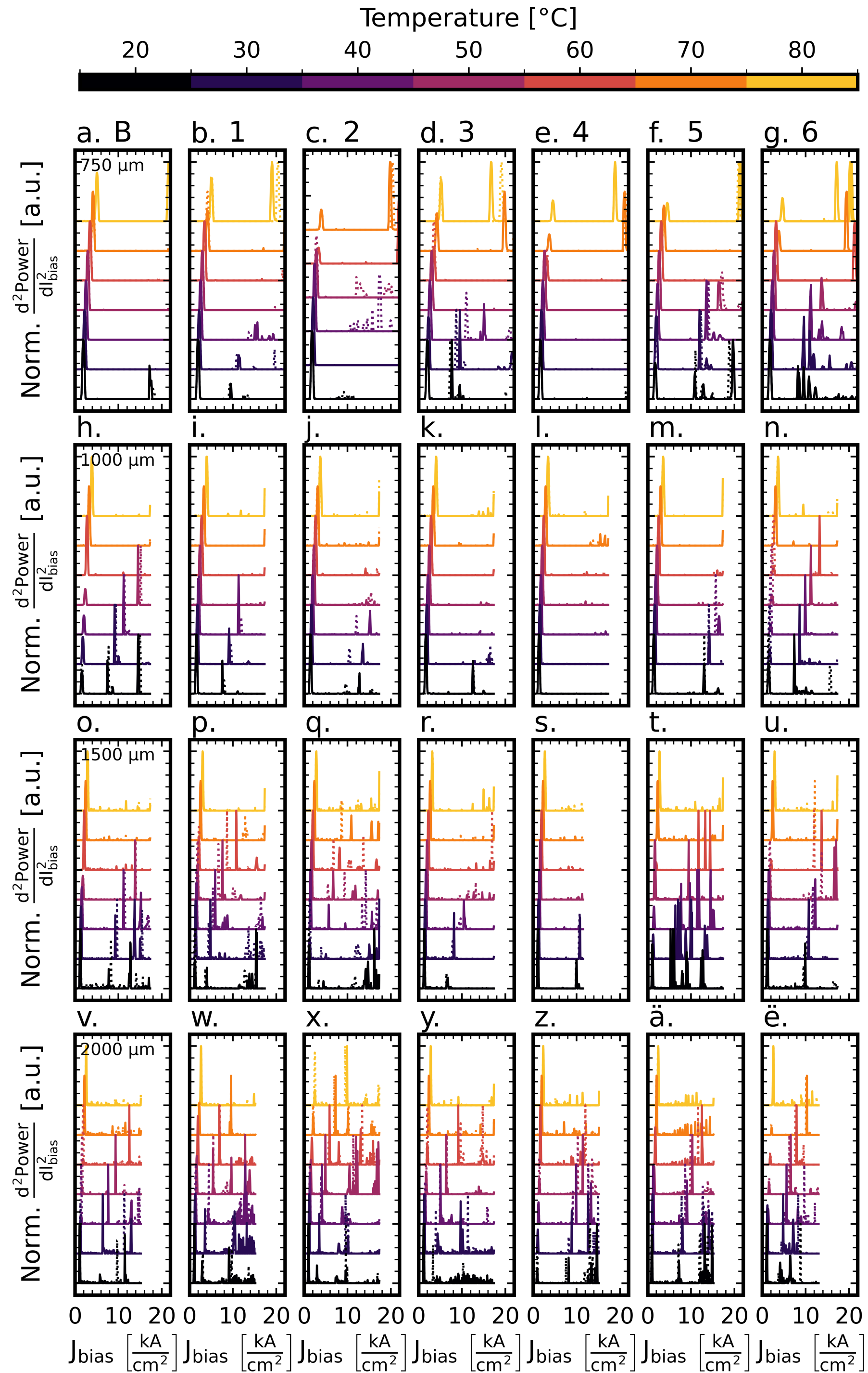

Figure 6.11: Normalized and offset second derivative of manually measured single facet laser power as a function of cw bias current density J_{bias} for the different designs at increasing temperature. Dashed lines are the results from the second device on the same bar. The power data has been averaged prior to gradient calculation using a 10 mA wide kernel. Column indices indicate the baseline and six different design alterations, while rows correspond to the four cavity lengths (**a.-g.** 750 µm, **h.-n.** 1000 µm, **o.-u.** 1500 µm, and **v.-ë.** 2000 µm) fabricated and tested.

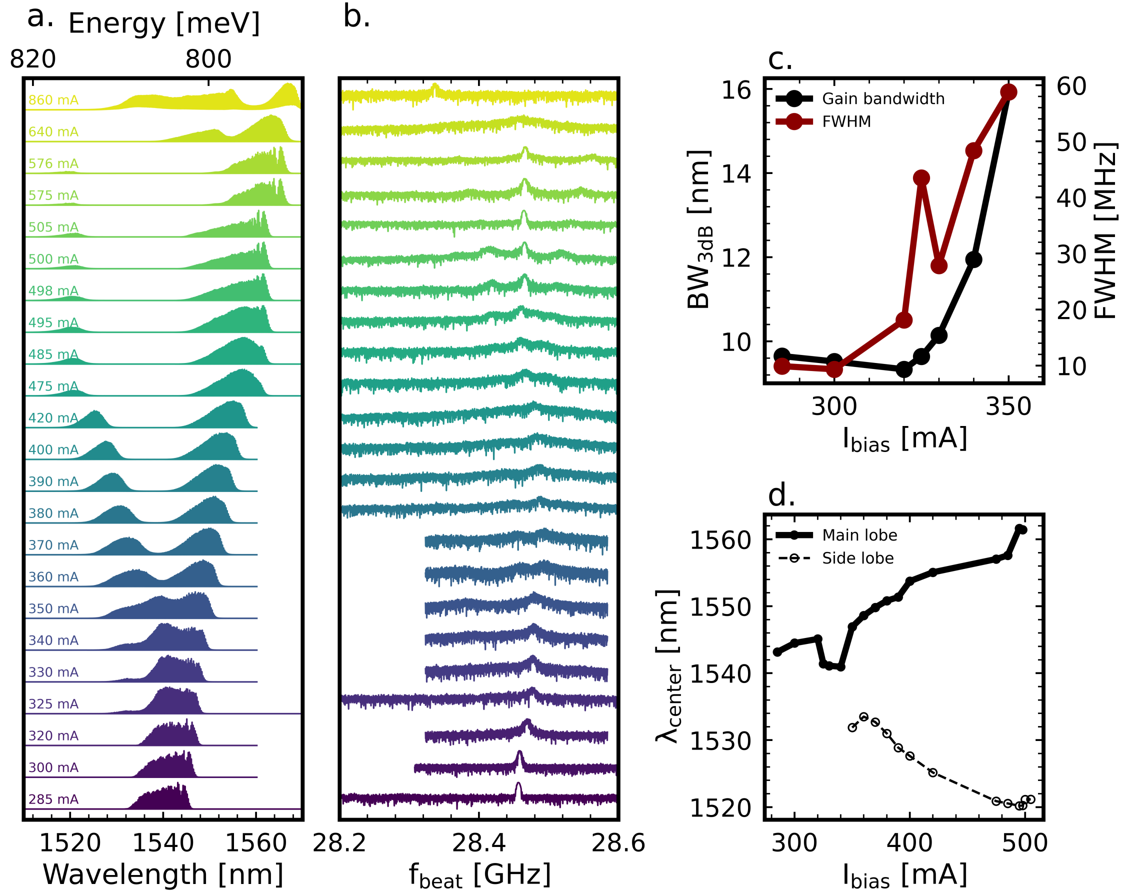

Figure 6.12: The evolution of the **a.** output lasing spectrum, b. resulting photo-diode signal, and **c.** gain bandwidth of the lasing spectrum BW_{3dB} and full-width half-maximum (FWHM) of the peak in the diode signal. **d.** shows the centre position of the two lobes that form the gain spectrum as a function of applied bias.

6.3.3 Comparison of LIV parameters

The lasing instability caused by the appearance of the second mode, a result of the accidental thinning of h_{spacer} for the second growth cycle, only affects devices above a 100 to 200 mA. Using a fitting window for fitting the LI and IV characteristics below the onset of lateral multimode lasing, we can therefore extract parameter values that should reflect the performance of a device without the thinned spacer. Note that each value is based on a minimum of two separate devices. The devices were selected using a preliminary testing of a full laser bar containing 30 devices, from which two representative device were selected and remeasured using the manual measurement setup. The temperature dependent measurements were conducted successively, with a two minute hold time to allow the device to settle into the new temperature. While no error bars are provided, given the relatively small sample size, Fig. 8.3 in the appendix provides an overview of the spread of values observed for different devices for the same design.

Fig. 6.13 shows the trends for the diode voltage for all the designs studied in the second

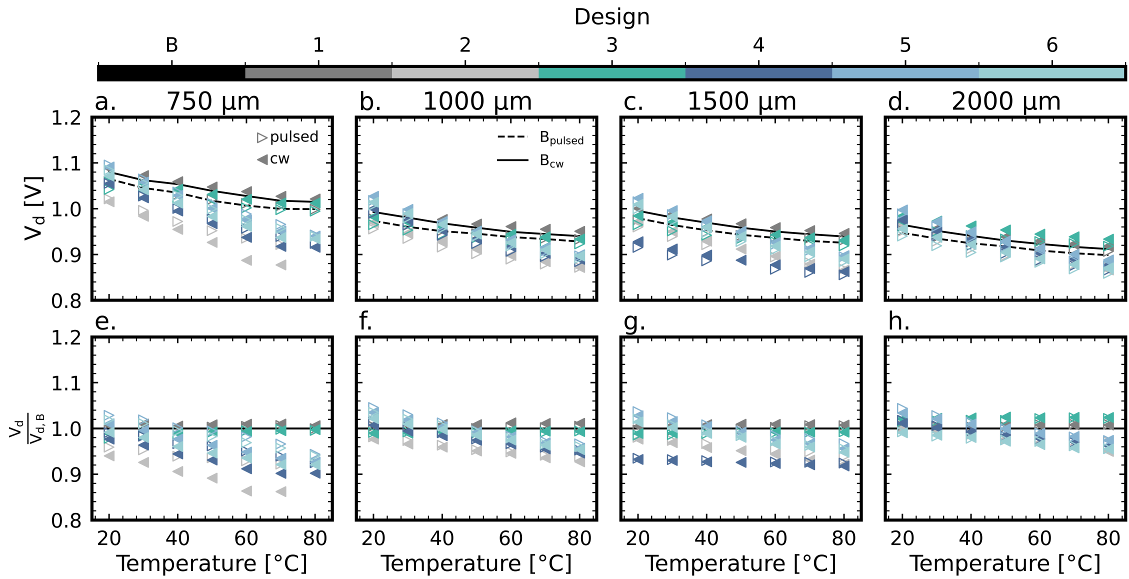

Figure 6.13: V_d extracted from experimental data for the six chosen design changes and the baseline comparison as a function of temperature for the four cavity lengths manufactured, **a.** 750, **b.** 1000, **c.** 1500 and **d.** 2000 µmȦbsolute values in **a. - d.**, with normalized values in **e. - h.**.

growth cycle, both for pulsed and cw bias. We observe a general decrease in diode voltage, most notable for devices with increased QDL spacing. Overall the diode voltage for the shortest devices with the highest overall carrier densities is affected the most, while the changes for the longer cavities are smaller. A curious trend is the decrease in diode voltage for design 4, which is more significant for the 750 and 1500 µm devices than for 1000 and

2000 µm ones. However, absolute changes are below 100 meV at 20°C and below 150 meV at 80°C, so overall small compared to the changes we observe for the resistance.

For the resistance, the differences are more dramatic. Almost all design variants tested

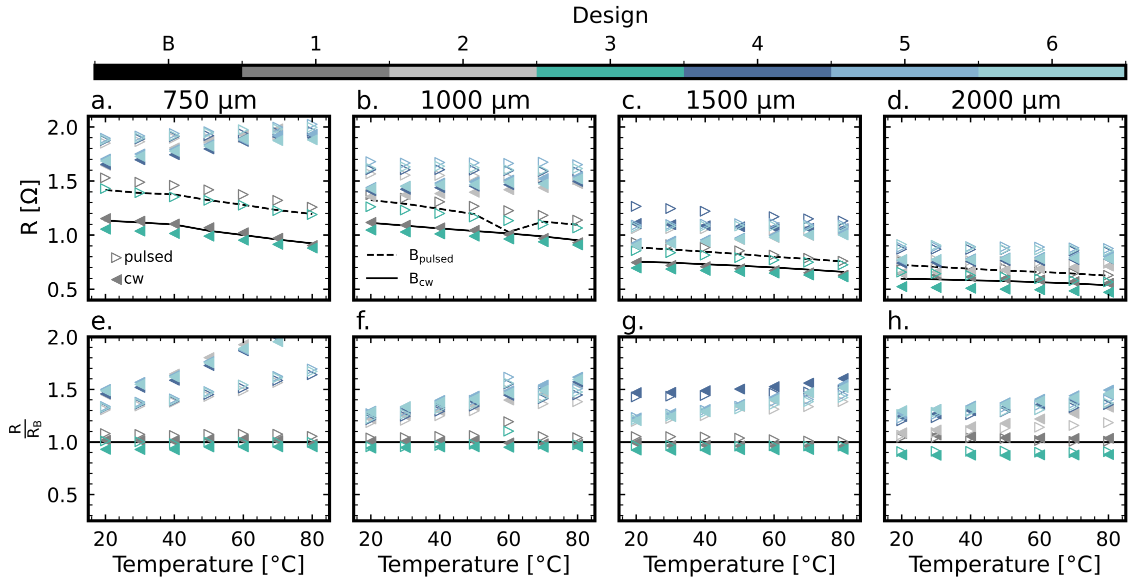

Figure 6.14: R extracted from experimental data for the six chosen design changes and the baseline comparison as a function of temperature for the four cavity lengths manufactured, **a.** 750, **b.** 1000, **c.** 1500 and **d.** 2000 µmȦbsolute values in **a. - d.**, with normalized values in **e. - h.**.

result in an increase of device resistance, with the changes generally being more dramatic towards higher temperatures. Only design 1 and 3 show resistivities similar to the baseline. This is curious, as design 3 introduces a 30 nm InAlAs barrier layer at the SCH/p-cladding interface, which is expected to inhibit hole injection into the separate confinement heterostructure. No significant reduction of the hole transport is observed. A greater resistivity is observed for designs 4-6, which all feature much thicker 100 nm barrier layers. Design 2, which has no such layer but features an increased QDL spacing of 50 nm shows an equivalently large change in the resistance. The increase for these designs is more pronounced for cw than pulsed bias, higher temperatures, and shorter cavities, pointing to a heating related effect that is more relevant for these designs. Whatever the mechanism, the outcome is a significant resistance penalty for these design, with a doubling of the resistance for 750 µm devices and a 50% increase around the target device length of 1500 µm. Since this will reduce the absolute power efficiency, identifying the cause of this resistance increase is a worthwhile goal for future research.

Fig. 6.15 shows a comparison between the threshold currents for the different designs, and we see some encouraging trends. While design 1 and 3 cause an increase in the threshold current, especially as devices get longer, all other designs improve upon the baseline

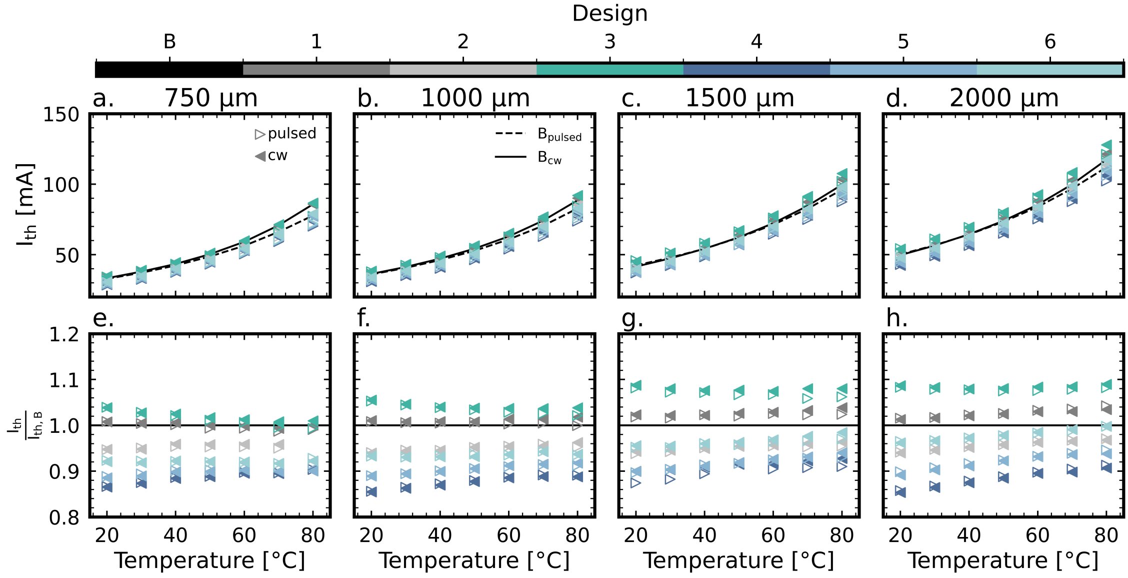

Figure 6.15: I_{th} extracted from experimental data for the six chosen design changes and the baseline comparison as a function of temperature for the four cavity lengths manufactured, **a.** 750, **b.** 1000, **c.** 1500 and **d.** 2000 µmÅbsolute values in **a. - d.**, with normalized values in **e. - h.**.

design. The largest improvement is seen for the 100 nm InAlAs devices from design 4, which show a 10 to 15 % reduction in threshold depending on cavity length and temperature. The reduction is greater at lower temperatures, but still amounts to roughly 10% at 80°C. What is interesting to observe is that while both design 2 and design 4 cause a reduction of the threshold current, their combination in design 6, which combines the 50 nm QDL period with a 100 nm thick InAlAs blocking layer, performs worse than the 100 nm InAlAs device with the baseline QDL period of 11 nm. If they were both addressing the same issue and thereby improve the device performance through the same mechanism, the expectation would be coincidence of design 4 and 6. The fact that design 6 performs worse indicates that the two improvement mechanisms are counteracting one another. The ordering of design 4, 5 and 6 strengthen this line of reasoning further: the threshold current for 6 is greater than the current for 5, which is greater than the current for 4. All three feature the barrier layer, but have increasing QDL periods of 11, 25, and 50 nm. So as the period increases, the benefit gleaned from the addition of the unipolar barrier decreases. This behaviour is more pronounced for longer cavities, where the overlap between the optical mode and the active region plays a larger role in the overall device behaviour. Examination of the simulation results for these devices did not reveal an obvious culprit for this behaviour, but further simulation with an updated model may provide the necessary insight to determine what is driving this curious behaviour.

In terms of slope efficiency, shown in Fig. 6.16, almost all designs perform worse than

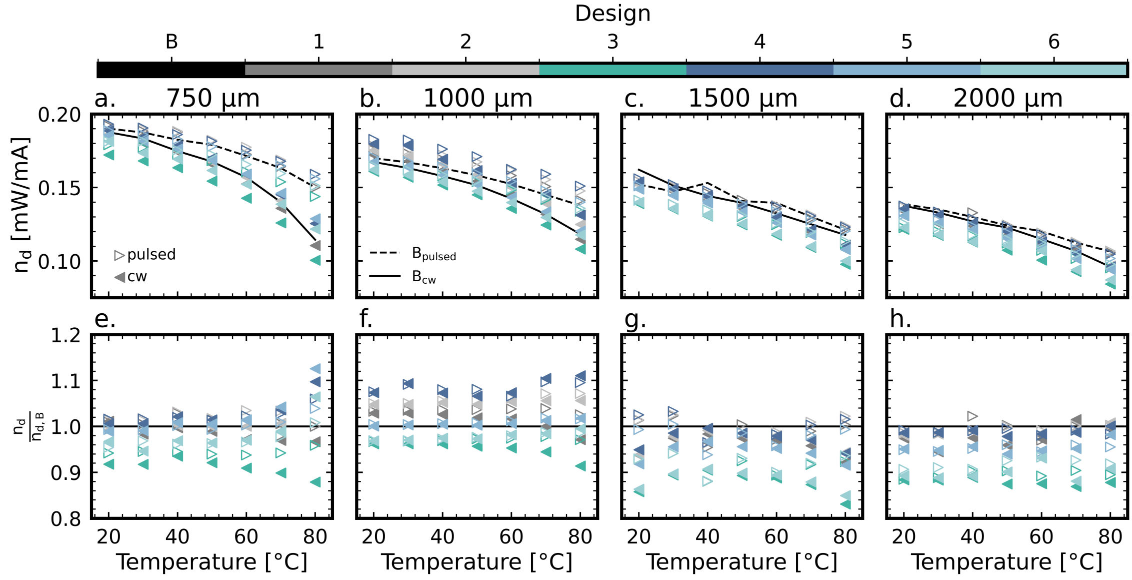

Figure 6.16: n_d extracted from experimental data for the six chosen design changes and the baseline comparison as a function of temperature for the four cavity lengths manufactured, **a.** 750, **b.** 1000, **c.** 1500 and **d.** 2000 µmȦbsolute values in **a.** - **d.**, with normalized values in **e.** - **h.**.

the baseline design, even though the changes are comparatively small apart from design 3 and 6. We would like to note that we see a similar pattern as we did for the threshold current in terms of the performance of design 4 and 2 being greater than their combination in design 6. The same trends discussed previously hold here as well, with performance increasing from design 6, to 5 to 4. For the threshold current, this behaviour was more pronounced for the longer cavities at higher temperatures, which holds true within the slope efficiency as well.

The outlying behaviour of the 1000 µm cavity is notable, as it is the only cavity length for which any design change exhibits an improved efficiency. Design 4 is the best performing design variation here as well, offering a 12% efficiency increase over the baseline design. This could be the result of a crossover point between two different loss mechanisms, one increasing with carrier density and another with cavity length. The lack of instability for both 750 and 1000 µm cavities as seen in Fig. 6.8e. and l. indicate that this is not the result of a fitting issue, as both maintain lasing in the fundamental mode for nearly the entire bias range probed. Simulation with the most recent version of the model and further analysis of the experimental results is required to determine what the origin of this bump in efficiency could be.

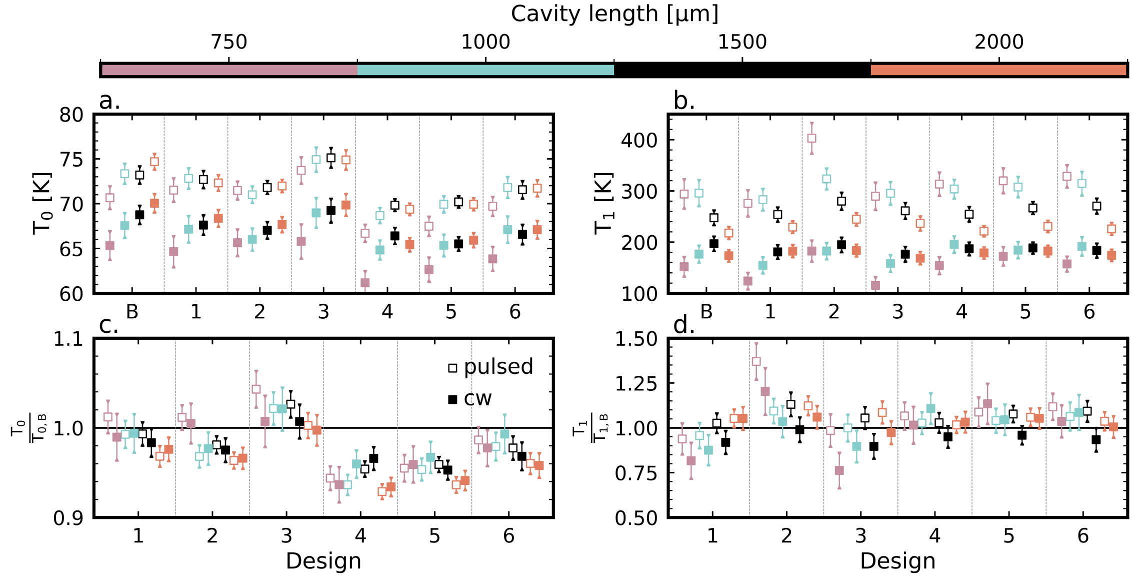

Figure 6.17: Absolute characteristic temperatures **a.** T_0 and **b.** T_1 , and relative to the baseline (**c.** and **d.**).

6.3.4 Characteristic temperatures

Fig. 6.17 shows the characteristic temperatures for the different designs. The bars are based on the diagonal of the covariance matrix of the linear regression to the LIV parameters and indicate confidence intervals for each characteristic temperature.

For T_0 , we observe a general decrease in the temperature stability, except for design 3 which sees a small bump for short cavities. However, this mostly illustrates the shortcomings of T_0 as a metric, as it artificially inflates the temperature stability of devices with large threshold currents. The discussion will mostly focus on values for continuous bias measurements, as these translate into final device operation most easily. Almost all designs exhibit the highest relative characteristic temperature of their threshold current compared to baseline between 1000 and 1500 µm, with both shorter and longer devices generally performing worse. The only design that refutes this trend is design 2, which peaks at 750 µm.

The difference in T_0 between pulsed (empty boxes) and direct current (filled boxes) measurements also shows the significant role that heating plays in these devices. The difference is between 5 and 6 K for most devices, indicating that some representation within the model is necessary to achieve a closer approximation of the physical device.

For T_1 , trends are relatively uniform again. The biggest improvement in terms of temperature stability stems from design 2, which sees a nearly 20% increase for its 750 µmcavity. As it had a slope efficiency nearly identical to the baseline device, this indicates a quite useful improvement of overall device behaviour. Further work investigating whether or not

this design change increases susceptibility to roll-off, which we could not examine due to the lasing instability, is necessary, but it appears as a promising pathway towards higher performing short cavity lasers.

Even more promising is design 4, which has shown lower threshold current densities and comparable slope efficiencies with values for T_1 that are just slightly below baseline. While its T_0 is lower by roughly 5 K, the significant difference in threshold current results in higher emission for all device lengths, and at all temperatures. Especially at higher temperatures near 80°C, the design 4 devices provide several milliwatts more than other designs.

6.3.5 Comparison with original design

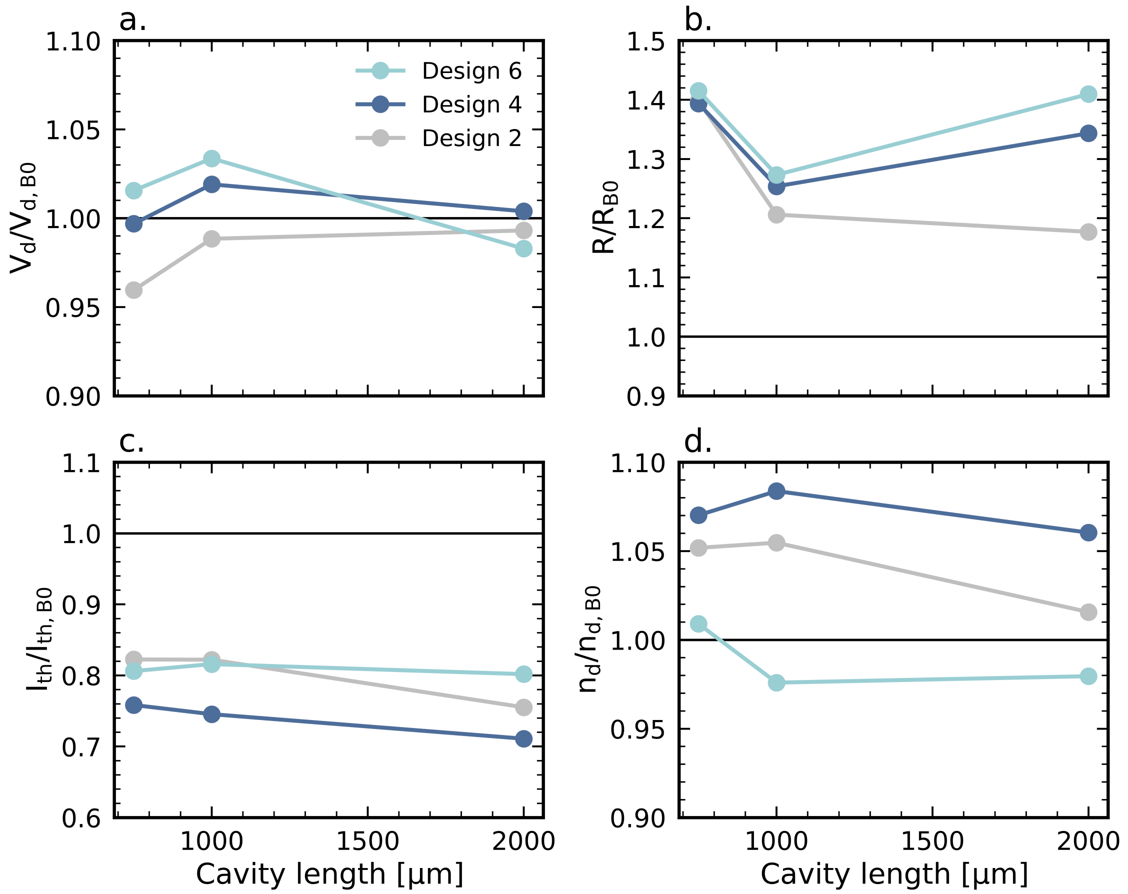

Figure 6.18: Experimental device performance parameters at 293 K normalized by the values for baseline design (B0) at varying cavity lengths, **a.** diode voltage V_d , **b.** series resistance R , **c.** threshold current I_{th} , and **d.** differential efficiency n_d .

The ultimate purpose of this work was to take improve the baseline design B0 in terms of

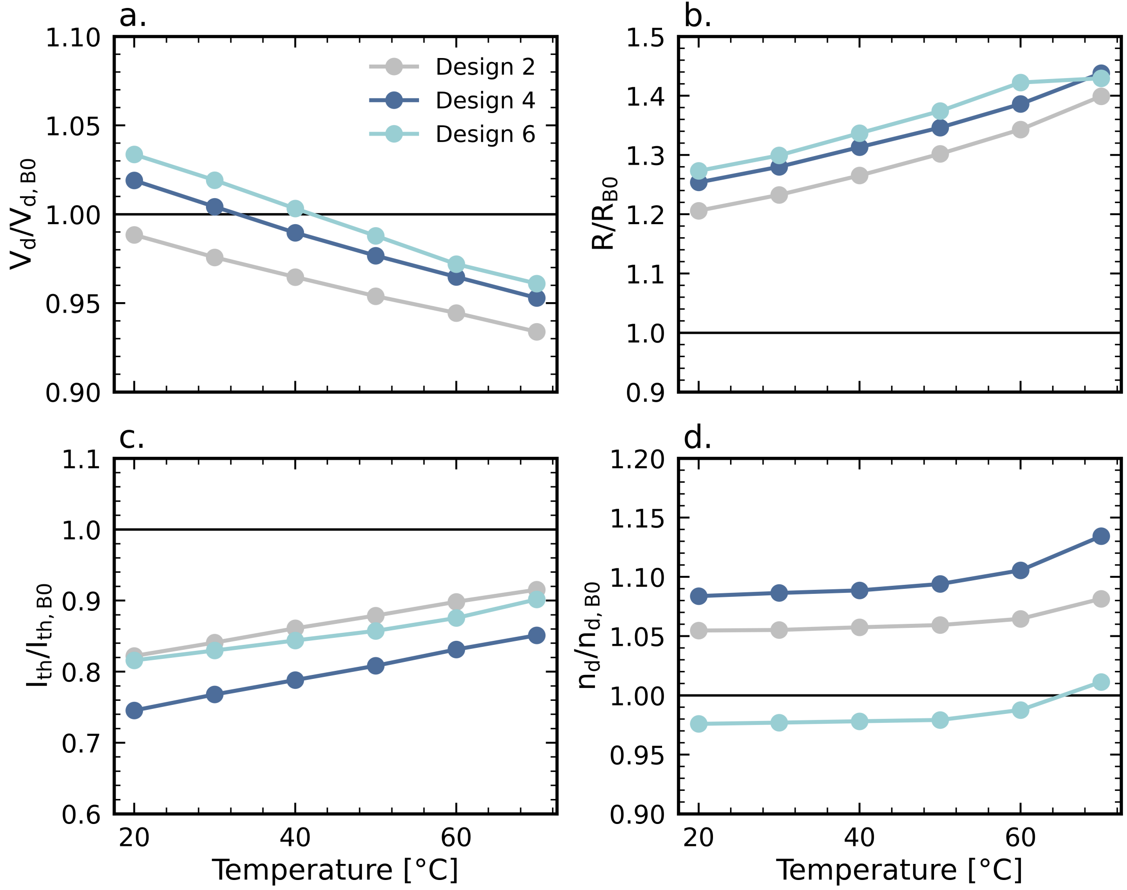

Figure 6.19: Experimental device performance parameters for 1000 µm devices normalized by the values for baseline design (B0) at varying cavity temperatures, **a.** diode voltage V_d , **b.** series resistance R , **c.** threshold current I_{th} , and **d.** differential efficiency n_d .

its sensitivity to elevated temperatures and gain bandwidth. As discussed in the previous sections, there were two designs that were the most promising in terms of performance improvement over the second growth cycle baseline. These designs were design 2, which featured a QDL spacing increased to 50 nm, and design 4, which added a 100 nm InAlAs barrier at SCH:p-InP interface. For comparison purposes, we will also consider design 6, which combines the two aforementioned design changes, in this section. Examining the device performance at room temperature in Fig. 6.18, we can see a significant improvement over the initial baseline design that was used at the outset of this thesis. While diode voltages are slightly higher and there is a significant penalty to the series resistance, all designs offer a significantly reduction of the threshold current density, which is coupled with an increase of the slope efficiency for designs 2 and 4. This is predominantly due to the reduction of QDLs from 5 to 4 in the updated design. The improvement trend holds as the device temperatures are increased: Fig. 6.19 shows the temperature trends for 1000

µm devices. Series resistance creeps further upwards compared to the baseline design, and the improvement in threshold current is smaller at higher temperatures than near room temperature. However, the differential efficiency of the optimized designs further improves on the baseline devices at higher temperatures. The addition of a 100 nm InAlAs electron blocking layer therefore represents a meaningful improvement of the overall device performance at higher temperatures.

To obtain a quantitative measure for the degree of improvement, we examine the wall

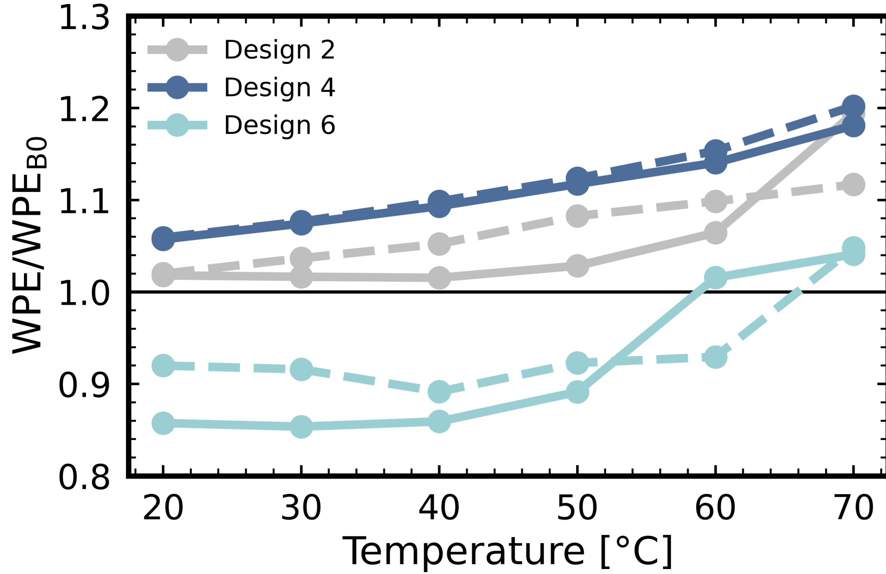

Figure 6.20: Experimental wall plug efficiency at I_{bias} = 300 mA for 1000 µm (dashed lines) and 2000 µm (solid lines) devices normalized by the values for baseline design (B0) at varying device temperatures.

plug efficiency (WPE) of the lasers. This quantity is defined as follows:

$$WPE = \frac{2 * P_{SF}}{I_{bias} V_{bias}} \tag{6.1}$$

with the single facet optical power output P_{SF} and the bias current I_{bias} and voltage V_{bias}. This measure quantifies the ability of a device to turn injected electrical power into output optical power. The definition given here uses a definition commonly used for lasers and other optoelectronic devices, even though it is not the true wall plug efficiency, as it omits losses due to supporting systems such as power supplies and cooling equipment.

The comparison in terms of wall plug efficiencies for the improved and baseline designs are shown in Fig. 6.20. The efficiency improvement lies anywhere between 8 to 20% for shorter cavities. The efficiency gain increases with temperature for all designs, with designs 2 and 4 showing a marked deviation from the baseline device behaviour near 70°C. This indicates that the barrier preventing electron overspill into the p-side is working as

intended.

Another objective of this work was attempting to broaden the lasing spectrum to increase

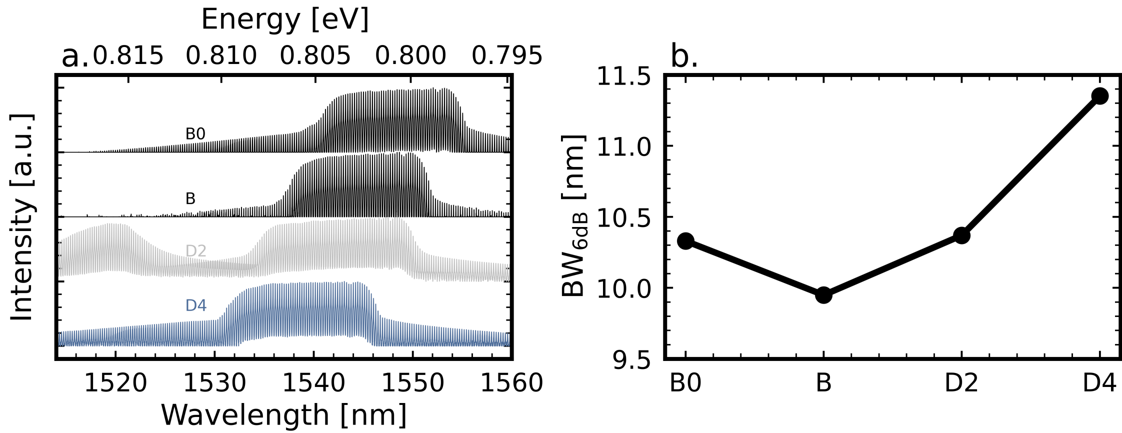

Figure 6.21:]
a. Normalized experimental lasing spectra current for different device designs. The spectra were captured at room temperature under 300 mA of injection using 1500 µm devices. B0: Batch 1 baseline, B: Batch 2 baseline, D2: Design 2, D4: Design 4. **b.** lasing spectrum bandwidth at 3 dB offset.

the number of available data transmission channels per device. Due to the limitations of the simulation software used, the predictions of the numerical model were unlikely to provide meaningful quantitative insight into the spectral characteristics of the final device. As Fig. 6.21 shows, the design changes did not alter the width of the lasing spectrum significantly, apart from the appearance of a secondary comb due to the higher order lateral mode we discussed earlier, which can be seen near shorter wavelengths for design 2 in Fig. 6.21a. The shape of the spectra does not change significantly between the different designs, even though design 4 produces a slightly flatter lasing spectrum. The result is a 3 dB spectral width that is comparatively uniform for all designs, with a small broadening of approximately 1 nm for the best performing design. If this device is to be used for data transmission, the suppression of the higher order mode requires further investigation, as it may interfere with mode-locking. However, as temperature increases and the higher order lateral mode is suppressed by increasing loss, the device mode-locks reliably.

As shown here, the end result of this work is an new device design that offers improved performance at higher temperatures without sacrificing spectral bandwidth. While the appearance of the additional lateral mode is a significant issue that requires further investigation, devices using design 4 already outperform the initial device design over a wide window of operating conditions, especially in the context of elevated temperatures.

7

Conclusion and outlook

Mode-locked quantum dash lasers are a promising light source for expanding the ever-increasing capacity requirements of optical networks. Due to the high number of modes and short pulse widths, they can provide light sources for large numbers of channels via wavelength and time-domain multiplexing schemes. Since one mode-locked laser can replace a whole array of single frequency lasers, this has the potential to be both more economical to deploy and increase the energy efficiency of the entire system.

The main contribution of this work is the development of a quantum dash laser model in Crosslight PICS3D, a commercial simulation platform. With respect to future scientific research, this allows interrogating a much larger variety of potential design changes than would have been possible by experiment alone. It also allows a level of insight into the device that is challenging to achieve experimentally. For example, obtaining a quantitative and spatially resolved picture of the different contributions to loss can not be obtained from experiment, but is accessible via simulation.
In a technological context, for quantum dash lasers to become commercially viable and therefore see widespread application, their development cost needs to decrease. The potential benefits obtained by employing mode-locked QD and QDash lasers rather than established QW devices currently do not outweigh the significant research and development cost required to turn these devices into products. The telecommunications industry is generally conservative when it comes to the adaptation of new technologies, as component reliability is paramount for their eventual operation in networks. The barrier to commercialization therefore needs to be as low as possible. The model developed in this work is built on a commercial laser simulation platform, Crosslight PICS3D, which means there is a lower barrier for integration into existing commercial research processes.

Another contribution of this thesis is the investigation of the impact of different design parameters outlined in Ch. 6. With the aim of optimizing the device performance at ele-

vated temperatures and guided by model results, lasers incorporating three different design changes were fabricated and characterized. The changes investigated were an altered number of quantum dash layers, increased spacing between dash layers, and introduction of a carrier blocking layer at the top of the separate confinement heterostructure.
Increasing the number of layers results in an overall reduction of light output, while lowering it to less than four layers results in an unfavourable increase in threshold current with temperature. A reduction in quantum dash layer number from five to four is found to provide an overall benefit to high temperature operation. A significant reduction of threshold current is observed when increasing the spacing of quantum dash layers, accompanied by a minor decrease in slope efficiency. The change also causes a minor reduction in the temperature stability of the threshold current, while simultaneously improving the stability of the slope efficiency.
The addition of an electron leakage blocking barrier at the interface between the separate confinement heterostructure and the p-side cladding also shows potential for incorporation into future designs. A 100 nm thick InAlAs barrier results in a significant decrease in threshold current and a small increase of the slope efficiency. Especially at high temperatures, this change results in a meaningful improvement of the overall device performance. The end result is an increase in the wall plug efficiency of these devices of up to 20%, without a change in the gain bandwidth.
Interestingly, combining the two design changes by widening the distance between adjacent quantum dash layers while adding an unipolar barrier cancels the benefits obtained from either variation. Overall, the device combining a thick InAlAs barrier with the layer spacing of the baseline design was found to be the highest performing. However, there is more research to be done on the simulation side, as the mechanism driving this behaviour is currently unclear.

The last significant contribution of this work is the creation of a Python interface to allow advanced scripts to interact with the Crosslight PICS3D layer of the model. This has multiple potential applications for future research. It allowed this work to conduct vast parameter sweeps with relative ease. Executing simulations based on Python scripts made it possible to access a much larger parameter space than would have been possible otherwise. It also allowed for feedback-driven design optimization, which was implemented but is not shown in this thesis. Even larger parameter spaces can be explored using an optimization algorithm. The Python interface allows the algorithm to analyze simulation results to obtain an input to its objective function and then use this feedback to inform the parameters of the next optimization step can allow future design studies to explore even larger parameter spaces.
Data created by the wide parameter sweeps also allows exploration of the design space by other means. The model and scripting interface can create large data sets which enable

machine-learning based design optimization methods. As proven by the recent acceleration of large language model development, these methods scale very efficiently with their data set size [294]. Generation of this data is prohibitively time- and resource-intensive when done experimentally. For meaningful analysis via machine learning, this model and others like it are therefore a necessity to allow accelerated device development, further reducing the barrier to commercialization for this technology.

Looking forward, there are several steps in the future with the model established. While the model delivers reliable predictions for some structural parameters, its results deviate from experiment for others. For example, the data discussed in Ch. 6 has not been compared to the model beyond the discussion presented there. It holds information on aspects of the model that do not capture the physical system. One important aspect is the viability of the quantum dot-like model. As described in section 4.7.7, there are gain models that may be more suitable to the representation of quantum dashes than the quantum dot-like model used in this work. The implementation of one such model was started, but there is further work necessary in order to integrate it fully with the existing model.
Another improvement to the model would be capturing mode-locking behavior. Due to the limitations of the formalism used in PICS3D, which we explained in section 4.7, an extension to the model is required. There is a body of work on time-domain models describing the mode-locking dynamics in quantum dot and dash lasers [148, 240, 241, 295]. As discussed in Ch. 5, these will often feature phenomenological parameters that capture some aspects of the material response, carrier dynamics or geometry that are computationally expensive to integrate self-consistently. Examples would be the lateral mode shape or the carrier injection efficiency. Both are parameters that vary as a function of injection current, either directly due to gain shaping or indirectly due to heating effects. Integration of parameters calculated using the time-independent PICS3D model can provide a closer approximation of the real cavity conditions, improving the precision of the whole model.

As a final point, out of the long list of potential design changes, only two were examined in the context of this thesis. Several variations were not explored due to the current limitations of the model. The added fabrication complexity of design changes such as heat spreaders and tunneling carrier injection wells requires numerical support to justify the significant amount of engineering work required for their integration. For example, injection wells require near resonance between the dash levels and the sub-bands within the injection well, which requires quantitatively accurate models to guide the fabrication process. Once the accuracy of the model has been improved, this list of changes provides an obvious starting point for future investigations in the process of bringing mode-locked quantum dash laser technology to the optical networks of the future.

8

Appendix

8.1 Simulation variables

Standard simulation parameters used in v0.7.4. This is identical to the file *base_params.csv* in *ridge_laser*.

```
# base_params.csv
# Parameters that can be specified dynamically using the Python wrapper
    ↪ for CrosslightSim
# Comments can be inserted with '#'
# Empty lines will be ignored
#
# Version refers to the version the functionality of a parameter was last
    ↪ altered, '-' indicates that it is unclear
# Past version 0.5.0, this refers to when a parameter was first introduced
    ↪ .
#
# CHANGE LOG
# [0.6.1] 2022-10-14 Moved from .xls to .csv file to enable easier version
    ↪  control via git
#       Added ability to read .csv base_param files in seb_pkg/crosslight/
    ↪ sim_create/read_baseparams
# [0.7.0] 2022-10-31 Added INCLUDE_UNIPOLAR_BARRIER
#   2022-11-01 Added INCLUDE_BALLAST
# [0.7.1] 2022-11-06 Added ability to dynamically define new C-Preparser (
    ↪ CPP) keywords by adding the keyword (CPP_KEYWORD) to the notes of a
    ↪  parameter
#       sim_create.py will then add these parameters to a list of
```

```
    ↪ parameters to apply to each file

PARAMETER      UNIT     VALUE      VERSION DESCRIPTION
#
    ↪ -------------------------|-------------------|-----------------------|-------|--
    ↪

# OPTICAL MATERIAL PARAMETERS
    ↪ ==========================================================================
    ↪

BACKLOSS_QD      m$^{-1}$   450       -  Background loss for QD-type
    ↪ structures
BACKLOSS_QW      m$^{-1}$   100       -  Background loss for QW-type
    ↪ structures
GAIN_CROSS_SATURATION  -     no       0.7.2 {yes,no} switches between the
    ↪ general suppression ('no') or cross-saturation model ('yes')
GAIN_SATURATION_COEFF  m$^3$    0      0.7.2 Gain saturation coefficient
    ↪ epsilon, see p.772 in the manual. NOTE: VALUE > 0 while enable gain
    ↪  suppression, even if GAIN_CROSS_SATURATION=no
INGAASP_ELEC_CARR_LOSS  m$^2$    5e-23     0.4.13 Free-carrier absorption
    ↪ coefficient for electrons in InGaAsP
INGAASP_HOLE_CARR_LOSS  m$^2$    5e-23     0.4.13 Free-carrier absorption
    ↪ coefficient for holes in InGaAsP
INP_ELEC_CARR_LOSS   m$^2$    5e-23     0.4.13 Free-carrier absorption
    ↪ coefficient for electrons in InP
INP_HOLE_CARR_LOSS   m$^2$    5e-23     0.4.13 Free-carrier absorption
    ↪ coefficient for holes in InP
ACT_NCARR_LOSS     m$^2$    5e-23     0.4.13 Free-carrier absorption
    ↪ coefficient for electrons in cx-InGaAsP/InP
ACT_PCARR_LOSS     m$^2$    3e-22     0.4.13 Free-carrier absorption
    ↪ coefficient for holes in cx-InGaAsP/InP
TAR_WAVEL      nm      1550      -  Target wavelength for the center of the
    ↪ mode-searching algorithm
R_RIGHT_FACET     -      0.32      -  Reflectivity of right laser facet
R_LEFT_FACET     -      0.32      -  Reflectivity of left laser facet
DIPOLE_SCALING_QW   -      1       -  Scaling of dipole transition element
    ↪ in the active region for QW devices
```

```
DIPOLE_SCALING_QD    -      1       -  Scaling the dipole transition element
    ↪ in the active region for QD devices
LONG_IGNORE_RTG_PHASE  -      no      0.7.3 Ignores the longitudinal phase
    ↪ in the mode search -> enable in conjunction with gain saturation

# DEVICE
    ↪ ==========================================================================
    ↪
# [0.7.1] 2022-12-02 Added dynamic definition of thickness of p-side and n
    ↪ -side SCH layers
#       Changed offset between sub-ridge p-cladding and active region to 50
    ↪  nm (previous 30 nm)
#       OCL_PSIDE1_THICK 0.020 -> 0.040
#     2023-01-22 Changed standard ridge height to 1.5 um to match
    ↪ experimental growth (1.38 um previously)



basis_model     -      qd       0.4.8 {qd,qw} Tells the model whether or not
    ↪  to run a QDash or QW simulation
ZLENGTH      um      1500      0.4.8 Length of the ridge waveguide
LAY_THICK     um      0.290      0.4.8 Thickness of lower SCH (minus 30 nm)
    ↪ to ensure OCL is always TAR_OCL um thick
TAR_OCL      um      0.350      -  Target thickness of OCL
NUM_WELLS     -      5       -  Number of wells/QDLs in active region
SUBSTR_THICK    um      0.500      -  Thickness of substrate; if auto_device
    ↪  is active, will be thinned so device is always TAR_DEV um thick.
ES_THICK     um      0.010      -  Thickness of the etch stop center
TAR_DEVICE     um      2.350      -  Target device thickness
RIDGE_SCWID     um      1.13      -  Width of the semiconductor in the ridge
    ↪
RIDGE_DEWID     um      0.22      -  Width of the dielectric in the ridge
RIDGE_METWID    um      0.17      -  Width of the side-metallization
BASE_WID      um      6       -  Extent of the device simulation beyond the
    ↪ base
QW_TOP_OCL_THICK   um      0.025      -  Thickness of upper OCL layer for QW
    ↪  device
QD_TOP_OCL_THICK   um      0.030      -  Thickness of upper OCL layer for QD
    ↪  device; relevant for LAY_THICK calculation even if not in qd_core
```

```
CAP_THICK      um      0.005      -  Thickness of capping layer; WL, BAR, and
    ↪  CAP should add to 0.010 um
STRAIN_THICK     um      0.001      -  [DEPRECATED] Thickness of straining
    ↪ layer
BAR_THICK      um      0.006      -  [QDash only]: Barrier thickness (will
    ↪ have 1 nm substracted for matching layer and WL_THICK for wetting
    ↪ layer)
UPPER_CLAD_THICK    um      0.160      -  Target thickness of the p-InP
    ↪ cladding between active region and etch stop. Will get thinned by
    ↪ grading of THJ and ES
GRADE_LENGTH_ES     um      0.010      -  Length over which etch stop is
    ↪ graded on either end
GRADE_LENGTH_BHJ    um      0.010      -  Length over which n-InP:1.15Q
    ↪ junction is graded.
GRADE_LENGTH_THJ    um      0.010      0.4.13 Length over which 1.15Q:p-InP
    ↪ junction is graded. Overwritten if INCLUDE_UNIPOLAR_BARRIER is 'yes
    ↪ '.
ES_INP_TOP_THICK    um      0.040      0.4.13 Thickness of InP layer on top
    ↪ of etch stop that gets thinner as grading layer thickness rises
OCL_PSIDE0_THICK    um      0.010      0.7.1 Thickness of the first layer
    ↪ above the active region on the p-side of the SCH
OCL_PSIDE1_THICK    um      0.020      0.7.1 Thickness of the second layer
    ↪ above the active region on the p-side of the SCH
OCL_NSIDE0_THICK    um      0.020      0.7.1 Thickness of the first layer
    ↪ above the bulk of the SCH on the n-side of the SCH
OCL_NSIDE1_THICK    um      0.010      0.7.1 Thickness of the second layer
    ↪ above the bulk of the SCH on the n-side of the SCH
DIELECTRIC_RIDGE_THICK   um      0.200      0.7.1 Thickness of the dielectric
    ↪  layer at the base of the ridge
MAIN_RIDGE_THICK    um      1.060      0.7.1 Thickness/height of main ridge
    ↪ body
METAL_RIDGE_THICK    um      0.200      0.7.1 Thickness of metallization
    ↪ layer at the base of the ridge
TOP_OHMIC_THICK     um      0.100      0.7.1 Thickness of the heavily-doped
    ↪ InGaAs contact layer at the top of the device

# DASH
    ↪ ==============================================================================
```

```
   ↪
# [0.7.0] 2022-11-02 Added automatic calculation of QD_HOST_MATER_NUM in
   ↪ seb_pkg/crosslight/sim_create.py
# [0.7.1] 2023-01-19 Added dynamic change of level position using
   ↪ ALTER_ENERGY_LEVEL. Note: Level truncation happens first.

QD_HOST_MATER_NUM   -     5      0.4.13 Material number associated with QD
   ↪  host material. Automatically calculated by seb_pkg\crosslight\
   ↪ sim_create.py
LOAD_SPECIFIC_QD    -     no      0.5.0 {yes,no} Instruct CrosslightSim to
   ↪ replace the box.qdd file with one taken from ridge_laser\qd_lib
QD_LIBRARY      -     qdot_v0.4.0    0.5.0 Name of directory to take box.
   ↪ qdd from; must be located in ridge_laser\qd_lib
TRUNCATE_QDD     -     no      0.6.0 {yes,no} whether or not to truncate
   ↪ the .qdd file
NUM_STATES_ELEC     -     3      0.6.0 Number of electronic states to
   ↪ truncate the .qdd file to
NUM_STATES_HOLE     -     3      0.6.0 Number of hole states to truncate
   ↪ the .qdd file to
ALTER_ENERGY_LEVELS    -     no      0.7.1 {yes,no} whether or not to alter
   ↪  the .qdd file energy levels
BAND_TO_ALTER     -     HH      0.7.1 {LH, HH, BOTH} Decides which valence
   ↪ band levels are altered (LH: Light-Hole, HH: Heavy-Hole, BOTH: LH
   ↪ and HH)
DASH_ELEC0_OFFSET   eV     0.000     0.7.1 Modification of first electron
   ↪ level. Higher levels can be modified by changing the number
   ↪ following ELEC (e.g. DASH_ELEC3_OFFSET to change the 4th level
   ↪ position)
DASH_HOLE0_OFFSET   eV     0.000     0.7.1 Modification of first hole
   ↪ level. Higher levels can be modified by changing the number
   ↪ following HOLE (e.g. DASH_HOLE3_OFFSET to change the 4th level
   ↪ position)
ALTER_LEVEL_SPACING    -     no      0.7.1 {yes,no} Whether or not to alter
   ↪  the level spacing between adjacent QDash levels
DASH_ELEC_SPACING   -     1      0.7.1 Factor by which to squeeze the
   ↪ electron levels
DASH_HOLE_SPACING   -     1      0.7.1 Factor by which to squeeze the hole
   ↪  level spacing
```

```
QD_DENS      m$^{-3}$   1e14     -  QD surface density
WET_RATIO     -      0.1      -  Wetting area ratio of QDs vs. wetting
    ↪ layer (no appreciable impact)
DOS_RED_FAC     -      1.4      -  QD density of states reduction factor (
    ↪ artificial)
QD_TAU_BROADEN    s      1e-13     -  Broadening of QD energy levels. Sum
    ↪ of inhomogneous broadening due to size/composition fluctuation and
    ↪ intraband scattering
QDASH_GA_FRACTION   -      0.0001     0.5.1 Gallium fraction in QD material
    ↪ ; Indium content is defined as 1-f(Ga)
QDASH_AS_FRACTION   -      0.9999     0.5.1 Arsenide fraction in QD
    ↪ material; Phosphorous content is defined as 1-f(Ga)
QDASH_HEIGHT    um      0.003     0.5.1 Height of the QD to be used for
    ↪ height in qdot_layer_mater
AVERAGE_COUPLED_DOTS  -      1      0.5.1 Number of dots coupled on average
MODE_SEARCH_NUM    -      40      0.6.0 Number of longitudinal modes
    ↪ explored
ENERGY_BROADENING   s      0.3e-13     0.6.0 Broadening energy of each dash
    ↪ -transition

# WETTING LAYER
    ↪ ==========================================================================
    ↪
# [0.6.1] 2022-10-14 This was an alternative approach to including the
    ↪ wetting layer by modelling it as a incredibly dense set of trap
    ↪ states. No longer in use.

INCLUDE_WETTING_LAYER  -      no      0.5.0 (CPP_KEYWORD) Turn the usage of
    ↪  the wetting layer on selectively
WL_THICK      um      0.0003      -  Thickness of wetting layer; WL and BAR
    ↪ should add to 0.005 um
WL_DONLEVEL     eV      0.335     0.4.8 [DEPRECATED] Offset of WL donor
    ↪ trap level from conduction band of 1.15Q
WL_ACCLEVEL     eV      0.613     0.4.8 [DEPRECATED] Offset of WL acceptor
    ↪ trap level from conduction band of 1.15Q
WL_2LDOS      m2      1e15     0.4.11 [DEPRECATED] Trap density representing
    ↪  local density of states of the WL
WL_nTAU      s      1e-9     0.4.8 [DEPRECATED] Trapping/detrapping time
```

```
    ↪ constant for WL
WL_pTAU       s      1e-9     0.4.8 [DEPRECATED] Trapping/detrapping time
    ↪ constant for WL
WL_nRECVEL     m/s      1e6      0.4.10 [DEPRECATED] Recombination velocity
    ↪  representing recombination in the WL
WL_pRECVEL     m/s      1e6      0.4.7 [DEPRECATED] Recombination velocity
    ↪ representing recombination in the WL

# BALLAST LAYER
    ↪ ==============================================================================
    ↪
# [0.7.0] 2022-11-01 Added ballast layer within the substrate layer
#   2022-11-02 Moved material definition from PICS3D into seb_pkg/
    ↪ crosslight/sim_create.py

INCLUDE_BALLAST    -     no      0.7.0 (CPP_KEYWORD) {yes,no} Include a
    ↪ pure ballast layer within the substrate that pulls the mode away
    ↪ from the ridge
SUBBALL_GA_FRACTION   -     0.500     0.7.0 Gallium fraction in hybrid
    ↪ ballast layer material; Indium content is defined as 1-f(Ga)
SUBBALL_AS_FRACTION   -     0.500     0.7.0 Arsenide fraction in hybrid
    ↪ ballast layer material; Phosphide content is defined as 1-f(As)
SUBBALL_BOT_THICK   um     0.400     0.7.0 Thickness of the substrate
    ↪ below the ballast layer
SUBBALL_BAL_THICK   um     0.050     0.7.0 Thickness of the ballast layer
SUBBALL_TOP_THICK   um     0.010     0.7.0 Distance between the SCH and
    ↪ the substrate
SUBBALL_GRADE_THICK   um     0.003     0.7.0 Thickness of the grading
    ↪ layer between the substrate and ballast layer material

# HYBRID BALLAST LAYER
    ↪ ==============================================================================
    ↪
# [0.6.1] 2022-10-14 Added the hybrid ballast layer below the active
    ↪ region

INCLUDE_HYBRID_BALLAST  -     no      0.6.1 (CPP_KEYWORD) {yes, no}
    ↪ Include a hybrid ballast/hole-blocking layer below the active
```

```
↪ region
HYBBALL_X_FRACTION   -     0.185     0.6.1 Gallium fraction in hybrid
   ↪ ballast layer material; Indium content is defined as 1-f(Ga) / 1-f(
   ↪ Ga)-f(Al) (latter for INGAALAS_HYBBALL=yes)
HYBBALL_Y_FRACTION   -     0.405     0.6.1 Arsenide/Aluminum (no/yes for
   ↪ INGAALAS_HYBBALL) fraction in hybrid ballast layer material; Indium
   ↪ /Phosphide content is defined as 1-f(Ga)-f(Al) / 1 - f(As)
HYBBALL_BOT_THICK   um     0.100     0.6.1 Thickness of the n-side facing
   ↪ 1.15Q. Will be auto-thinned to ensure OCL meets target thickness.
HYBBALL_BAL_THICK   um     0.005     0.6.1 Thickness of the hybrid ballast
   ↪  layer
HYBBALL_TOP_THICK   um     0.030     0.6.1 Distance between the active
   ↪ region and ballast layer (not incl. HYBBAL_GRADE_THICK)
HYBBALL_GRADE_THICK   um     0.003     0.6.1 Thickness of the grading
   ↪ layer between ballast and 1.15Q
INGAALAS_HYBBALL   -     no      0.7.0 (CPP_KEYWORD) {yes, no} Use
   ↪ InGaAlAs macros instead of InGaAsP for hybrid ballast
HYBBALL_MATERIAL   -     ingaasp_xyt    0.7.0 Material of the hybrid
   ↪ ballast layer
HYBBALL_GRADE_MATERIAL  -     ingaasp_grading_off  0.7.0 Material to grade
   ↪  in and out of the hybrid ballast layer

# UNIPOLAR BARRIER LAYER
   ↪ ==============================================================================
   ↪
# [0.7.0] 2022-10-28 Added a unipolar barrier layer at the OCL-p-cladding
   ↪ interface; requries further material libary definitions (grading
   ↪ layers, etc.)
#      Will override GRADE_LENGTH_THJ
#   2022-11-01 Changed definitions to make it clear that this layer is to
   ↪ block predominantly electrons

INCLUDE_ELEC_BARRIER  -     no      0.7.0 (CPP_KEYWORD) {yes, no} whether
   ↪ or not to include a unipolar barrier layer between OCL and p-
   ↪ cladding
UNIPOLAR_ELEC_GA_FRACTION -     0.0001     0.7.0 Gallium fraction in
   ↪ unipolar electron barrier layer material; Indium content is defined
   ↪  as 1-f(Ga)-f(Al)
```

```
UNIPOLAR_ELEC_AL_FRACTION -      0.5000      0.7.0 Aluminum fraction in unipolar electron barrier layer material; Indium content is defined as 1-f(Ga)-f(Al)
UNIPOLAR_ELEC_THICK    um      0.005      0.7.0 Thickness of the unipolar electron barrier layer
UNIPOLAR_ELEC_GRADE_THICK um      0.003      0.7.0 Thickness of the grading layer on each side of the unipolar electron barrier

# ETCH STOP ==================================================================================
# [0.7.1] 2023-05-04 Added commands to programmatically alter the etch stop composition
#       Moved commands from BAND PARAMETERS pertaining to the etch stop here

ES_AFFINITY_MOD    eV      -0.025      0.4.13 Value by which to shift the bulk affinity of the etch stop and associated grading layers
ES_BANDGAP_MOD     eV      0       0.4.13 Value by which to change the band gap (and thereby position of the valence band) of the etch stop and associated grading layers
ES_GA_FRACTION     -      0.214      0.7.1 Gallium fraction inside the etch stop
ES_AS_FRACTION     -      0.468      0.7.1 Arsenide fraction inside the etch stop

# DOPING ==================================================================================


DOP_LEVEL_NCORE    m$^{-3}$    1E+20      -  n-doping on the n-side of the OCL
DOP_LEVEL_PCORE    m$^{-3}$    1E+20      -  p-doping on the p-side of the OCL
DOP_LEVEL_BAR    m$^{-3}$    1E+20      -  p-doping of the barrier between QDs/QWs
DOP_LEVEL_ACT    m$^{-3}$    1E+20      -  p-doping in the active layer (QW or QDL): also doping level of WL
```

```
DOP_LEVEL_SUBRIDGE   m$^{-3}$   5E+23     0.6.0 p-doping the sub-ridge p-
    ↪ cladding
DOP_LEVEL_INP_TOP   m$^{-3}$   5E+24     0.6.0 p-doping in the layer on
    ↪ top of the etch stop
DOP_LEVEL_RIDGE    m$^{-3}$   1E+24     0.6.0 p-doping in the ridge
DOP_LEVEL_SUBSTRATE   m$^{-3}$   1E+24     0.7.0 n-doping in the substrate
DOP_LEVEL_ES     m$^{-3}$   1E+20     0.7.0 p-doping in the etch stop
DON_LEVEL_nINP     eV     0.0262     0.4.13 Activation energy of donor
    ↪ species n-InP
ACC_LEVEL_nINP     eV     0.0262     0.4.10 Activation energy of acceptor-
    ↪ like trap species n-InP
ACC_DENS_nINP    m$^{-3}$   1e21      -  Density of acceptor-like trap
    ↪ species in n-InP
DON_LEVEL_pINP     eV     0.0262      -  Activation energy of acceptor
    ↪ species p-InP
ACC_LEVEL_pINP     eV     0.0262      -  Activation energy of donor-like
    ↪ trap species p-InP
DON_DENS_pINP    m$^{-3}$   1e21      -  Density of donor-like trap species
    ↪  in p-InP
QDL_TRAP_DENS    m$^{-3}$   1e21      -  Density of QDL defect state
QDL_TRAP_LEVEL     eV     0.540      -  Energy level of 1.15Q defect state w
    ↪ .r.t. to conduction band
QDL_TRAP_NCAPCROSS    m$^2$     1.5e-19      -  Electron capture cross
    ↪ section for QDL layer trap state (based on Fe-center, Bimberg,
    ↪ 1997)
QDL_TRAP_PCAPCROSS    m$^2$     4e-20      -  Hole capture cross section for
    ↪ QDL layer trap state (based on Fe-center, Bimberg, 1997)
OCL_TRAP_DENS    m$^{-3}$   1e21      -  Density of 1.15Q defect state
OCL_TRAP_LEVEL     eV     0.675      -  Energy level of QDL defect state w.r
    ↪ .t. to conduction band
OCL_TRAP_NCAPCROSS    m$^2$     1.5e-19      -  Electron capture cross
    ↪ section for 1.15Q midgap defect (based on Fe-center, Bimberg, 1997)
    ↪
OCL_TRAP_PCAPCROSS    m$^2$     4e-20      -  Hole capture cross section for
    ↪ 1.15Q midgap defect (based on Fe-center, Bimberg, 1997)
WL_TRAP_DENS     m$^{-3}$   1e21      -  Density of WL defect state
WL_TRAP_LEVEL     eV     0.175      -  Energy level of WL defect state w.r.t
    ↪ . to conduction band
```

```
WL_TRAP_NCAPCROSS   m$^2$    1.5e-19     -  Electron capture cross section
    ↪  for WL defect (based on Fe-center, Bimberg, 1997)
WL_TRAP_PCAPCROSS   m$^2$    4e-20      -  Hole capture cross section for
    ↪ WL defect (based on Fe-center, Bimberg, 1997)

# THERMAL AND HEATING
    ↪ ==================================================================================
    ↪

TEMP      K     293       -  Temperature at which the mesh nodes will be
    ↪ initialized
HEAT_ON      -      no       -  (CPP_KEYWORD) {yes,no} enable the heat
    ↪ generation and flow simulation in the device
HEAT_SIMPLE      -      no       0.7.4 (CPP_KEYWORD) {yes,no} enable the
    ↪ simplified heat generation and flow simulation in the device
HEAT_OPTABS      -      yes       -  {yes,no} whether or not to consider
    ↪ optical absorption for the heating calculation
THERMAL_COND_SUBSTR   W/m/K    0.8      0.5.1 2D thermal conductivity of
    ↪ the InP substrate, assuming 625 um thick InP
HEAT_TRANSIENT     -      yes      0.7.2 {yes,no} Whether or not to use a
    ↪ heat transient for the model

# PYTHON CONTROL
    ↪ ==================================================================================
    ↪

auto_wavel      -      no       0.4.10 Enables the algorithm to automatically
    ↪  guess the center lasing wavelength
auto_device      -      no       -  Enables the algorithm to thin the
    ↪ substrate to obtain an overall device thickness of TAR_DEVICE
auto_OCL      -      yes       -  Enables the algorithm to thin the SCH to
    ↪ obtain an OCL thickness equal to TAR_OCL
auto_memory      -      yes       -  Enables the algorithm to dynamically
    ↪ calculate the amount of RAM to allocate additionally for large
    ↪ matrices
GAIN_CALC_ONLY     -      yes      0.5.1 (CPP_KEYWORD) Only do the (much
    ↪ shorter) gain calculation
```

```
# TUNNELING TRANSPORT
    ↪ ===========================================================================
    ↪
# [0.7.1] 2023-03-22 Added QTRANS_TAU_TDEP and QTRANS_TAU_REFT for
    ↪ temperature-dep. carrier capture rates in the MQW region

TUN_ON       -     no      -  (CPP_KEYWORD) {yes,no} Enables/disables
    ↪ tunneling in the device
AUTO_TUN_RANGE    um     2e-2     0.4.7 Range for the tunneling junctions
    ↪ added to the model via auto_tunneling
AUTO_TUN_BARHEIGHT   eV     0.1      0.4.7 Minimum barrier height (in eV)
    ↪ to trigger an automatically set up tunneling region via
    ↪ auto_tunneling
BOT_HJ_TYPE      -     propagation_matrix  -  barrier model for electron
    ↪ tunneling model at n-InP:1.15Q interface
BOT_HJ_SCALEFAC    -     1      -  Tunneling scaling factor for n-InP:1.15
    ↪ Q interface
TOP_HJ_TYPE      -     propagation_matrix  0.4.12 barrier model for
    ↪ electron tunneling model at 1.15Q:p-InP interface
TOP_HJ_SCALEFAC    -     1      0.4.8 Tunneling scaling factor for 1.15Q:p
    ↪ -InP interface
QTRANS_SEQTRANS    -     yes      -  Sequential [yes] or collective [no]
    ↪ quantum transport
QTRANS_SEQCAP    -     yes      -  Sequential carrier capture
QTRANS_COLCAP    -     no      -  Collective carrier capture
QTRANS_WBT     -     hot_auger_indirect  -  Transport model for
    ↪ q_transport command
QTRANS_NEIGHBOUR   -     1      -  Furthest neighbour the carrier can
    ↪ travel to (1 = nearest neighbours)
QTRANS_ELEC_FLYOVERFAC  -     1      -  Scaling factor for electron
    ↪ flyover over MQW region
QTRANS_ELEC_CAPFAC   -     1      -  Scaling factor for non-local electron
    ↪  capture by MQW region
QTRANS_HOLE_FLYOVERFAC  -     1      -  Scaling factor for hole flyover
    ↪ over MQW region
QTRANS_HOLE_CAPFAC   -     1      -  Scaling factor for non-local hole
    ↪ capture by MQW region
QTRANS_ELEC_MFP    um     0.01     -  Electron mean free path for quantum
```

```
    ↪ transport model
QTRANS_HOLE_MFP     um     0.01     -  Hole mean free path for quantum
    ↪ transport model
QTRANS_TAU_TDEP     -      no       0.7.1 For trap_detrap_tau: whether or not
    ↪  to scale the capture rate with temperature (assuming time
    ↪ constants are provided at QTRANS_TAU_REFT)
QTRANS_TAU_REFT     K      20       0.7.1 For trap_detrap_tau: reference
    ↪ temperature if QTRANS_TAU_TDEP = yes
QTRANS_ELEC_TAU     s      1e-12    -  For trap_detrap_tau: trapping time
    ↪ for electrons in QW trapping/detrapping model
QTRANS_HOLE_TAU     s      1e-12    -  For trap_detrap_tau: trapping time
    ↪ for holes in QW trapping/detrapping model
QTRANS_DYNAMIC_TAU  -      no       0.7.2 For trap_detrap_tau: enable
    ↪ cavity length-dependent hole trap time calculation
QTRANS_DTAU_SCALING   -    1        0.7.2 For trap_detrap_tau: scaling
    ↪ factor for length-dep. hole trap-time scaling
QTRANS_DTAU_EXPONENT  -    1        0.7.2 For trap_detrap_tau: exponent for
    ↪  length-dep. hole trap-time scaling
QTRANS_DTAU_SLOPE   s/um   3.2e-14  0.7.2 For trap_detrap_tau: linear
    ↪ slope for linear hole trap time interpolation
QTRANS_DTAU_OFFSET  s      -1.14e-11  0.7.2 For trap_detrap_tau: time
    ↪ offset for linear hole trap time interpolation
QTRANS_ES_MFP     um     0.100    -  [DEPRECATED] Mean-free path of
    ↪ carriers at etch stop
QTRANS_ES_CARMOB  m$^{2}$/(Vs)  0.100    -  [DEPRECATED] Carrier
    ↪ mobility for etch stop non-local transport
QTRANS_ES_CARTYPE   -    hole     -  {electron, hole} Carrier type for
    ↪ which tunneling through the etch stop is to be considered
QTRANS_ES_TAU     s     1e-12     -  [DEPRECATED] Characteristic trapping
    ↪ time for carriers in etch stop
QTRANS_ES_SCALEFAC  -     1        -  Tunneling scaling factor for
    ↪ tunneling across etch stop
QTRANS_ES_BROADWID  kT     1        -  Broadening of energy width in units
    ↪ of kT
QTRANS_HOTAUGER_THRESH  m$^{-3}$  8e23     -  Carrier density within MQW
    ↪ region at which hot Auger carrier escape from QWs is considered
QTRANS_HOTAUGER_CN  m$^6$/s    0       -  Electron coefficient for Auger
    ↪ assisted carrier escape from active region
```

```
QTRANS_HOTAUGER_CP    m$^6$/s     2e-39      -  Hole coefficient for Auger
    ↪ assisted carrier escape from active region

# MOBILITIES
    ↪ ================================================================================
    ↪

HMOB_INP_PASS     m$^2$/Vs    0.0037      -  [DEPRECATED] Hole mobility of
    ↪ InP in passive regions
HMOB_INP_ACT     m$^2$/Vs    0.0037      -  [DEPRECATED] Hole mobility of InP
    ↪  in active regions
HMOB_INGAASP_PASS    m$^2$/Vs    0.0037      -  [DEPRECATED] Hole mobility in
    ↪  InGaAsP

# AUGER RECOMBINATION
    ↪ ================================================================================
    ↪

AUGER_ACT_ENERGY_QW    eV      0.060      0.4.7 Activation energy of
    ↪ dominating Auger recombination process for QW; based on J. Piprek,
    ↪ 2000
AUGER_COEFF_QW     m$^{6}$s$^{-1}$  1.7169e-39     0.4.7 Reference
    ↪ coefficient of Auger process for QW; based on J. Piprek, 2000
AUGERN_ACT_ENERGY_QD   eV      0.060      0.7.1 Activation energy of
    ↪ dominating Auger recombination process for electrons in QD
AUGERN_COEFF_QD     m$^6$/s     2.9e-38      0.4.11 Reference electron
    ↪ coefficient of Auger process for QD
AUGERP_ACT_ENERGY_QD   eV      0.060      0.7.1 Activation energy of
    ↪ dominating Auger recombination process for holes in QD
AUGERP_COEFF_QD     m$^6$/s     2.9e-38      0.4.11 Reference hole
    ↪ coefficient of Auger process for QD
AUGERN_COEFF_INGAASP_XYT m$^6$/s     8e-41      0.4.13 Electron Auger
    ↪ recombination coefficient for InGaAsP
AUGERP_COEFF_INGAASP_XYT m$^6$/s     8e-41      0.4.13 Hole Auger
    ↪ recombination coefficient for InGaAsP
AUGERN_WL      m$^{6}$s$^{-1}$  8E-39      0.4.13 Electron Auger
    ↪ recombination coefficient in wetting layer
AUGERP_WL      m$^{6}$s$^{-1}$  8E-39      0.4.13 Hole Auger recombination
```

```
    ↪ coefficient in wetting layer
AUGERN_ES      m$^{6}$s$^{-1}$  8E-39     0.5.0 Electron Auger
    ↪ recombination coefficient in etch stop
AUGERP_ES      m$^{6}$s$^{-1}$  8E-39     0.5.0 Hole Auger recombination
    ↪ coefficient in etch stop
AUGERN_CORE      m$^{6}$s$^{-1}$  8E-39     0.5.0 [DEPRECATED] Electron
    ↪ Auger recombination coefficient in 1.15Q
AUGERP_CORE      m$^{6}$s$^{-1}$  8E-39     0.5.0 [DEPRECATED] Hole Auger
    ↪ recombination coefficient in 1.15Q
AUGERN_ACTIVE     m$^{6}$s$^{-1}$  4e-39     0.4.13 [DEPRECATED] Electron
    ↪ Auger recombination coefficient in QD/QW
AUGERP_ACTIVE     m$^{6}$s$^{-1}$  4E-39     0.4.13 [DEPRECATED] Hole Auger
    ↪  recombination coefficient in QD/QW

# BAND PARAMETERS
    ↪ ===========================================================================
    ↪

THJ_AFFINITY_MOD    eV     0.050     0.4.13 Value by which to shift the
    ↪ bulk affinity of the top heterojunction
THJ_BANDGAP_MOD     eV     0      0.4.13 Value by which to change the band
    ↪ gap (and thereby position of the valence band) of the top
    ↪ heterojunction
BHJ_AFFINITY_MOD    eV     0      0.4.13 Value by which to shift the bulk
    ↪ affinity of the bottom heterojunction
BHJ_BANDGAP_MOD     eV     0      0.4.13 Value by which to change the band
    ↪ gap (and thereby position of the valence band) of the bottom
    ↪ heterojunction
QW_BAND_OFFSET     -     0.6      0.4.13 Ratio of total band offset that is
    ↪  due to the conduction band discontinuity in the QW (Note:
    ↪ symmetric for both sides)
QD_HOST_BAND_OFFSET    -     0.36     0.4.13 Ratio of total band offset
    ↪ that is due to the conduction band discontinuity in the QD host
    ↪ material
QD_DOT_BAND_OFFSET    -     0.36     0.4.15 Ratio of total band offset that
    ↪  is due to the conduction band discontinuity in the QD dot material

# NEWTON SOLVER PARAMETERS
```

```
    ↪ ==========================================================================
    ↪
# [0.7.1] 2023-04-20 Added USE_SELF_CONSISTENT to allow ability to conduct
    ↪  simulations self-consistently

MAINMB      MB     1024     -  Memory added to numerical solver to
    ↪ accommodate more complex meshes
SPARSEMB     MB     1024     -  Memory added to sparse filler to support
    ↪ terms far off the diagonal
SCAN1_VALUETO     V     0.4      -  Value at which to stop the scan and
    ↪ proceed to the next step
SCAN1_STEPPRINT     V     0.2      0.4.10 Interval at which to save a cross
    ↪ -section of simulation parameters
SCAN1_STEPINIT     V     1e-4     0.4.10 Initial step size for solver
SCAN1_STEPMAX     V     0.1      -  Maximum step size for solver
SCAN2_VALUETO     V     1      -  Value at which to stop the scan and
    ↪ proceed to the next step
SCAN2_STEPPRINT     V     0.2      -  Interval at which to save a cross-
    ↪ section of simulation parameters
SCAN2_STEPINIT     V     1e-4     -  Initial step size for solver
SCAN2_STEPMAX     V     0.1      -  Maximum step size for solver
CURR_AUTOVAL     A     1e-4     -  Current value for which to switch from
    ↪ voltage-driven to current driven simulation
SCAN3_VALUETO     A     0.15     -  Value at which to stop the scan and
    ↪ proceed to the next scan
SCAN3_STEPPRINT     A     0.2      -  Interval at which to save a cross-
    ↪ section of simulation parameters
SCAN3_STEPINIT     A     2e-4     -  Initial step size for solver
SCAN3_STEPMAX     A     2e-3     -  Maximum step size for solver
SCAN3_STEPMIN     A     1e-7     -  Minimum step size for solver
RTGAIN_AUTOVAL     -     0.5      -  Round-trip gain value at which to
    ↪ proceed to the next scan
RTGAIN_AUTOWITHIN    -     0.05     -  Round-trip gain range at which it is
    ↪  considered in sufficient proximity to RTGAIN_AUTOVAL
SCAN4_VALUETO     A     0.15     -  Value at which to stop the scan and
    ↪ proceed to the next step
SCAN4_STEPPRINT     A     0.02     -  Interval at which to save a cross-
    ↪ section of simulation parameters
```

```
SCAN4_STEPINIT    A     1e-6     -  Initial step size for solver
SCAN4_STEPMAX    A     0.01     -  Maximum step size for solver
SCAN4_STEPMIN    A     1e-10     -  Minimum step size for solver
NEWT_DAMP_EQ    -     5      -  Damping factor between steps of the Newton
    ↪  solver for equilibrium calculation
NEWT_VARTOL_EQ    -     1e-9     -  Relative tolerance for variable
    ↪ solution for equilibrium calculation
NEWT_RESTOL_EQ    -     1e-9     -  Relative tolerance for residual for
    ↪ equilibrium calculation
NEWT_MAX_ITER_EQ    -     100      -  Maximum number of iterations for
    ↪ equilibrium calculation
NEWT_OPT_ITER_EQ    -     15      -  Optimum number of iterations for
    ↪ equilibrium calculation
NEWT_STOP_ITER_EQ    -     50      -  Number of iterations after which to
    ↪ evaluate solution trend for equilibrium calculation
NEWT_DAMP_BIAS    -     2.5      -  Damping factor between steps of the
    ↪ Newton solver for bias calculation
NEWT_VARTOL_BIAS    -     1e-4     -  Relative tolerance for variable
    ↪ solution for bias calculation
NEWT_RESTOL_BIAS    -     1e-4     -  Relative tolerance for residual for
    ↪ bias calculation
NEWT_MAX_ITER_BIAS    -     20      -  Maximum number of iterations for
    ↪ bias calculation
NEWT_OPT_ITER_BIAS    -     12      -  Optimum number of iterations for
    ↪ bias calculation
NEWT_STOP_ITER_BIAS    -     15      -  Number of iterations after which to
    ↪  evaluate solution trend for bias calculation
NEWT_DAMP_NTH    -     2.5      -  Damping factor between steps of the
    ↪ Newton solver for bias calculation
NEWT_VARTOL_NTH    -     1e-4     -  Relative tolerance for variable
    ↪ solution for near threshold calculation
NEWT_RESTOL_NTH    -     1e-4     -  Relative tolerance for residual for
    ↪ near threshold calculation
NEWT_MAX_ITER_NTH    -     20      -  Maximum number of iterations for near
    ↪  threshold calculation
NEWT_OPT_ITER_NTH    -     12      -  Optimum number of iterations for near
    ↪  threshold calculation
NEWT_STOP_ITER_NTH    -     15      -  Number of iterations after which to
```

```
    ↪ evaluate solution trend for near calculation
RTG_PHASEDENS    -     1.25e25     0.4.8 Phase density used for round-trip
    ↪  gain calculation
ZPLANES       -      11      0.4.8 Number of planes modelled between the two
    ↪  facets of the waveguide
MQW_CALC      -      yes      -  {yes,no} whether or not to update the MQW
    ↪ energy level calculation for calculations near threshold and above
TRANSIENT_ON     -      yes      0.4.7 (CPP_KEYWORD) {yes,no} whether or not
    ↪  to use a transient to solve the last scan step of the model.
    ↪ Improves stability.
TRANSIENT_TIME     s      10       -  Time scale for the solver to ramp from
    ↪ the initial to final value
USE_SELF_CONSISTENT    -      no      0.7.1 (CPP_KEYWORD) {yes,no} whether
    ↪ or not to use the self-consistent Schrodinger solver

# MULTIPLE LATERAL MODES
    ↪ ================================================================================
    ↪
# [0.7.1] 2022-11-03 Added search for multiple lateral modes

EXPLORE_MULTIPLE_MODES  -      no      0.7.1 (CPP_KEYWORD) {yes,no} Allows
    ↪ the solver to look for multiple lateral modes
MM_NUM_LATMODES     -      2      0.7.1 Number of lateral modes to search
    ↪ for

# IMPORTED GAIN
    ↪ ================================================================================
    ↪
# [0.7.1] 2022-11-04 Added ability to import gain dynamically
#    2022-11-25 Added dynamic gain table offsets as well as dynamic
    ↪ extrapolation commands
#    2023-01-24 Added gain calculation and re-adjustment before full
    ↪ calculation

IMPORTED_GAIN     -      no      0.7.1 (CPP_KEYWORD) {yes,no} whether or not
    ↪  to read the gain from a file rather than allowing Crosslight to
    ↪ calculate it at each step
GAIN_TABLE     -     experimental   0.7.1 Name of the gain table to be
```

```
    ↪ imported into the main simulation (minus the .txt)
EXPORTED_GAIN    -      no      0.7.1 (CPP_KEYWORD) {yes,no} whether or not
    ↪  to export the gain table from the gain-calculation
GT_CONC_OFFSET_UPPER  1/m$^{-3}$   0      0.7.1 Offset (positive or
    ↪ negative) for upper concentration limit
GT_CONC_OFFSET_LOWER  1/m$^{-3}$   0      0.7.1 Offset (positive or
    ↪ negative) for lower concentration limit
GT_EXTRAP_ENERGY   -      yes      0.7.1 {yes,no} Whether or not to
    ↪ extrapolate the gain for energies outside of the range provided by
    ↪ the gain table
GT_EXTRAP_CONC    -      yes      0.7.1 {yes,no} Whether or not to
    ↪ extrapolate the gain for concentrations outside of the range
    ↪ provided by the gain table
GT_EXTRAP_PNR    -      no      0.7.1 {yes,no} Whether or not to
    ↪ extrapolate the gain for pn-ratios outside of the range provided by
    ↪  the gain table
GT_EXTRAP_T     -      yes      0.7.1 {yes,no} Whether or not to
    ↪ extrapolate the gain for temperatures outside of the range provided
    ↪  by the gain table
GT_EXTRAP_FIELD    -      no      0.7.1 {yes,no} Whether or not to
    ↪ extrapolate the gain for bias fields outside of the range provided
    ↪ by the gain table
REIMPORT_GAIN    -      no      0.7.1 {yes,no} Export and re-import gain to
    ↪  speed up calculation
ALTER_GAIN      -      no      0.7.1 {yes,no} Modify the gain table
GT_IMPORT_INDEX    -      no      0.7.1 {yes,no} whether or not to import
    ↪ the index from the gain table
GT_IMPORT_SPON    -      no      0.7.1 {yes,no} whether or not to import
    ↪ the spontaneous emission from the gain table
GT_NRG_OFFSET    eV      0      0.7.1 Offset by which to shift the
    ↪ calculated gain profile
GT_GAIN_FAC     -      1      0.7.1 Factor by which gain taken from .gain
    ↪ calculation is multiplied: gain = gain_calc * GT_GAIN_FAC +
    ↪ GT_GAIN_OFFSET
GT_GAIN_OFFSET    1/m     0      0.7.1 Offset to add to the gain profile:
    ↪ gain = gain_calc * GT_GAIN_FAC + GT_GAIN_OFFSET
GT_INDEX_FAC     -      1      0.7.1 Factor by which index taken from .gain
    ↪ calculation is multiplied: index = index * GT_INDEX_FAC +
```

```
    ↪ GT_INDEX_OFFSET
GT_INDEX_OFFSET    -     0      0.7.1 Offset to add to the index profile:
    ↪ index = index * GT_INDEX_FAC + GT_INDEX_OFFSET
GT_CONC_MIN     1/m3    1e22     0.7.1 Lower electron concentration limit
    ↪ of QD gain calculation
GT_CONC_MAX     1/m3    1e24     0.7.1 Upper electron concentration limit
    ↪ of QD gain calculation

# MESHING
    ↪ ================================================================
    ↪
# [0.7.1] 2023-04-07 Added dynamic wetting layer mesh line adjustment,
    ↪ depending on thickness [WIP]

BAR_HMESH_LINES    -     6      -  Horizontal mesh lines for the barrier
    ↪ layer
WL_HMESCH_DYNAMIC   -     no      0.7.1 {yes,no} Whether or not to adjust
    ↪ the number of horizontal wetting layer mesh lines dynamically based
    ↪  on WL_HMESH_SPACING
WL_HMESH_SPACING   nm     0.2      0.7.1 Target distance between adjacent
    ↪ horizontal mesh lines in the wetting layer
WL_HMESH_LINES    -     2      -  Horizontal mesh lines for the wetting
    ↪ layer
CAP_HMESH_LINES    -     5      -  Horizontal mesh lines for the capping
    ↪ layer
```

8.2 Distribution of LIV parameters for baseline design

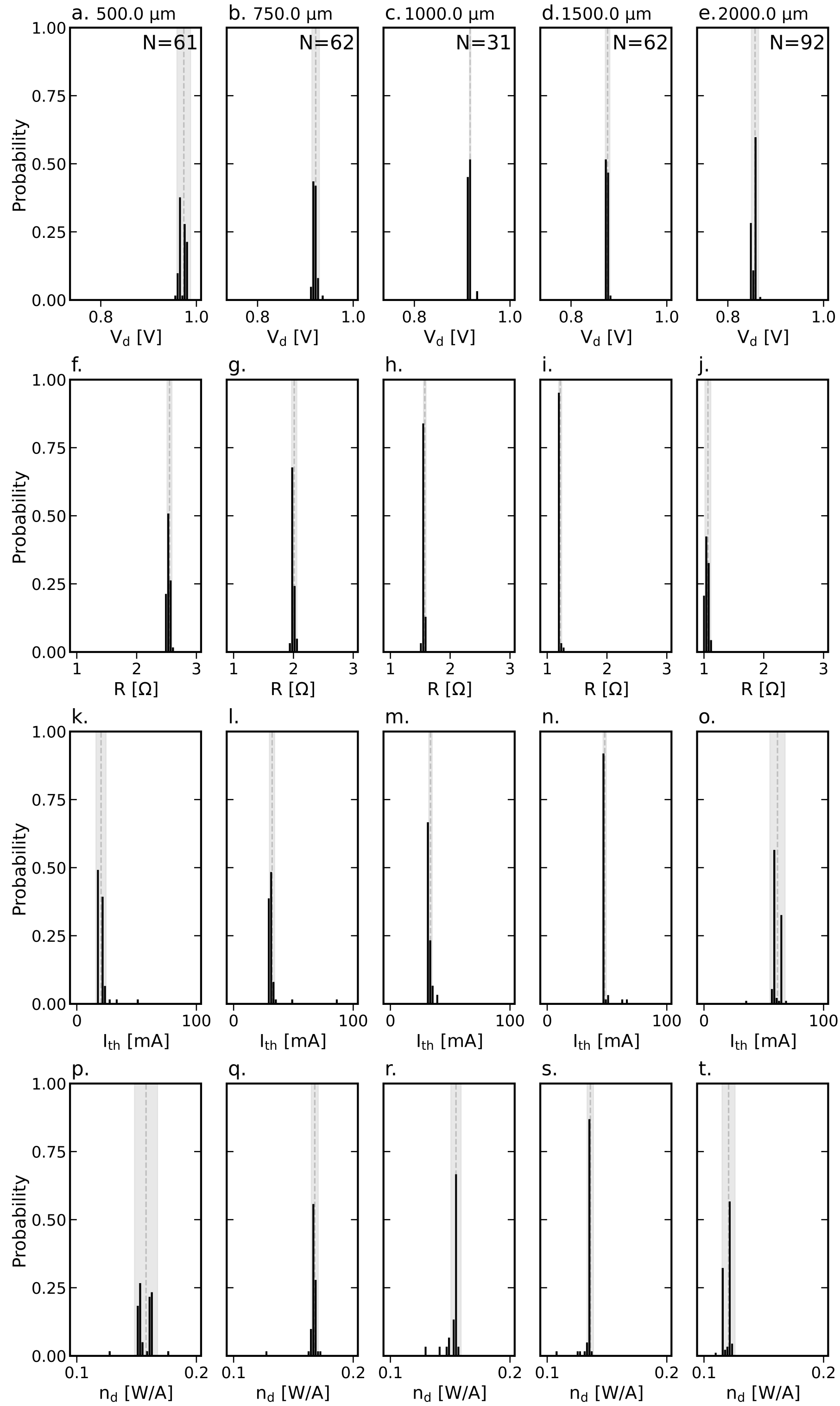

Figure 8.1: Distribution of extracted parameters at room temperature of all measured experimental curves for devices with 5 QDLs. The shaded grey area indicates twice the standard deviation for each parameter, with the dashed curve representing the mean value.

8.3 Second growth cycle

8.3.1 Internal efficiency and modal loss

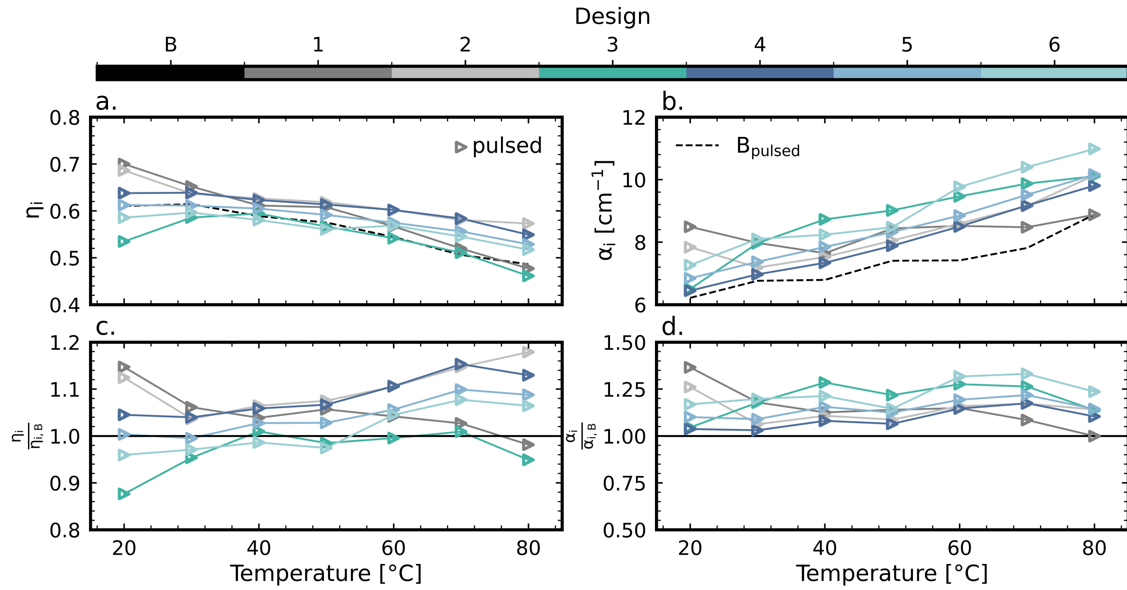

Figure 8.2: **a.** Internal efficiency η_i and **b.** modal loss α_i, and relative to the baseline (**c.** and **d.**).

8.3.2 All LIV parameters

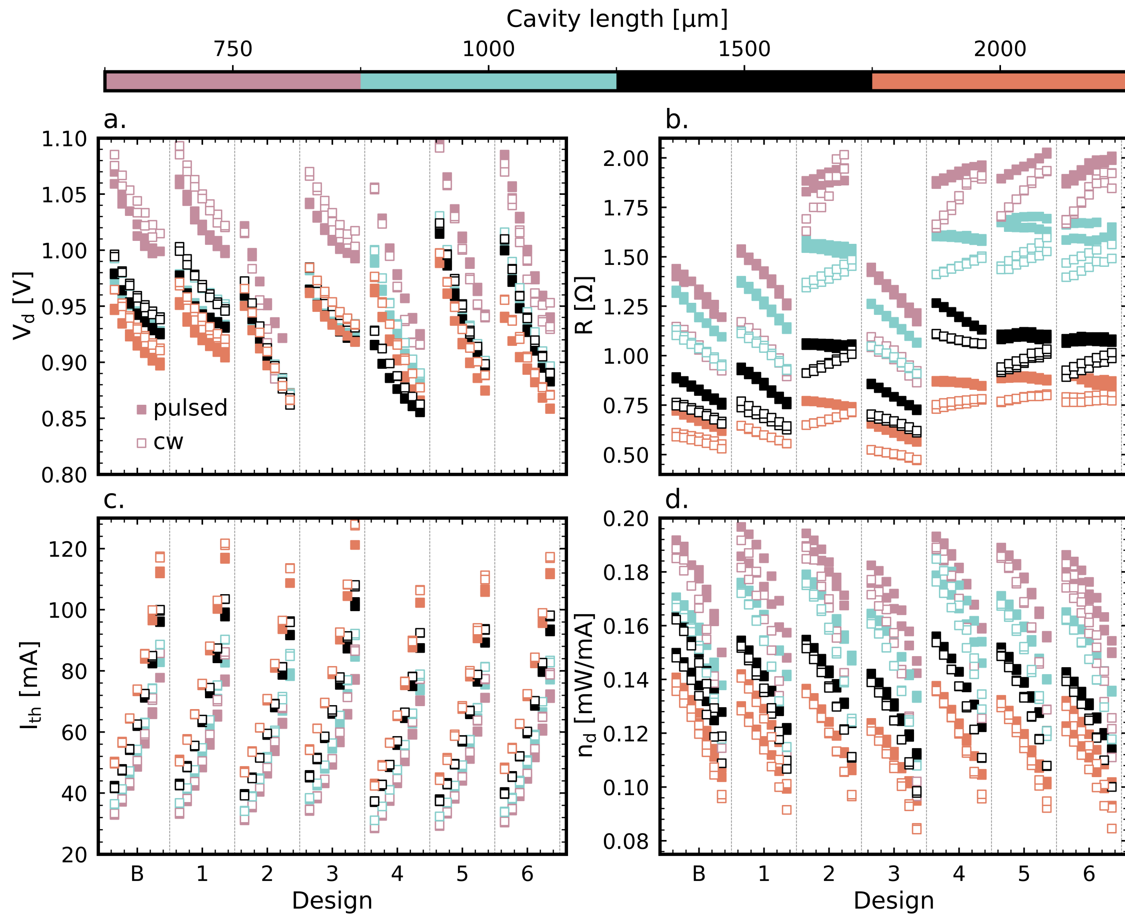

Figure 8.3: All LIV parameters measured for devices from the second growth cycle. Within each column, device temperature increases from left to right.

8.3.3 LI curves: first derivative

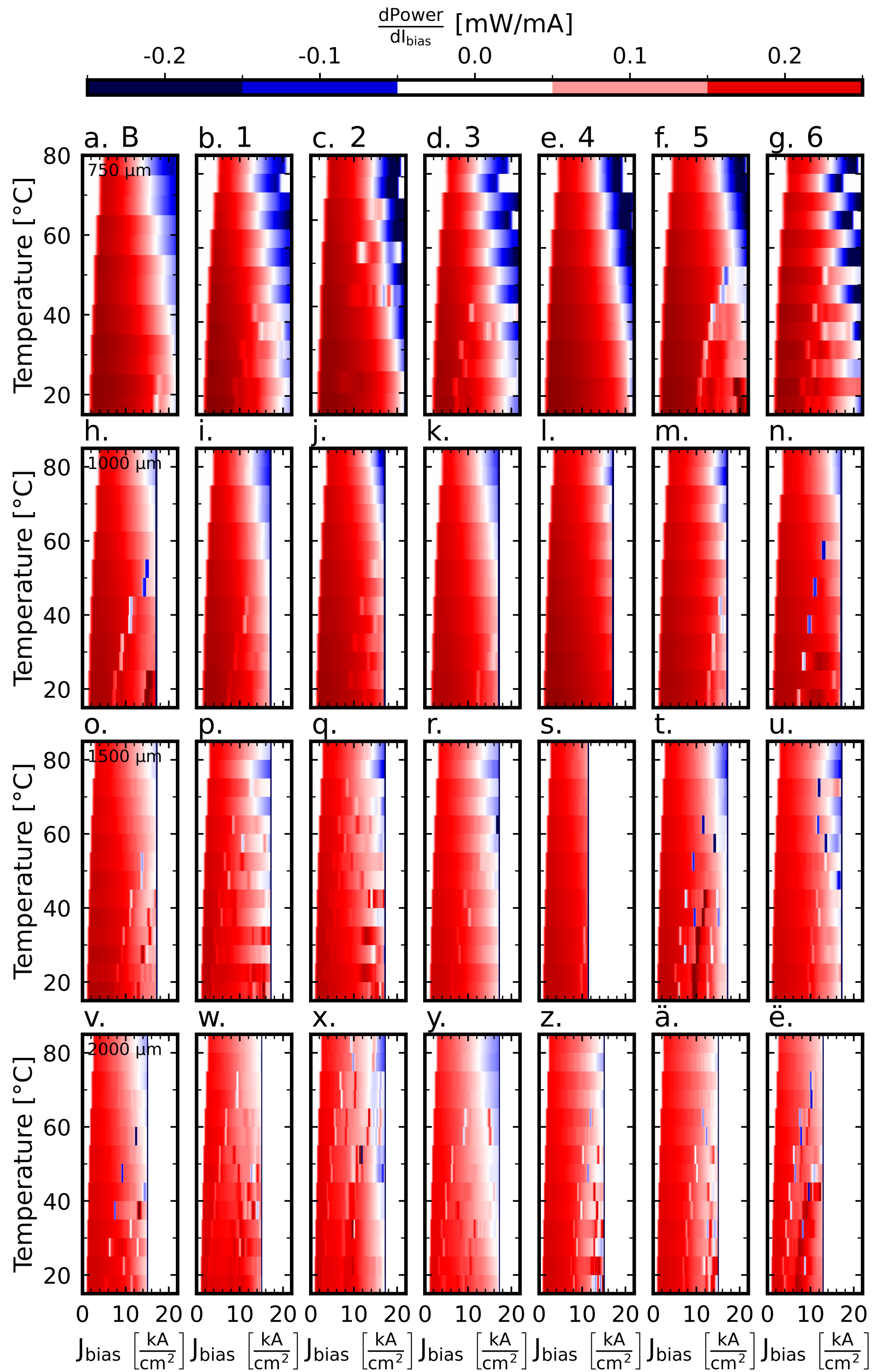

Figure 8.4: First derivative for devices at various cavity lengths in batch 2.

8.3.4 Characteristic temperature fitting

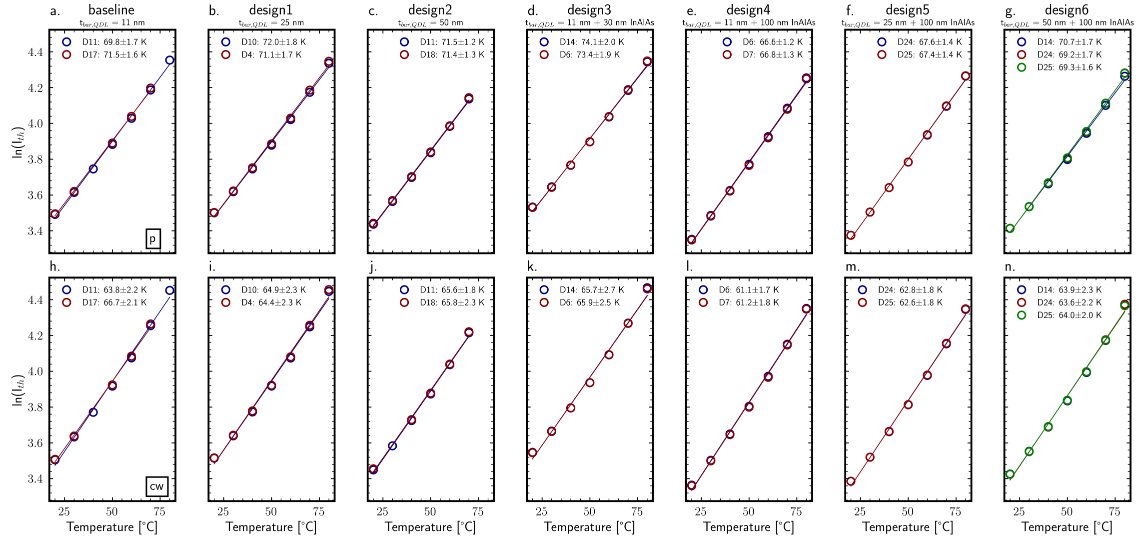

Figure 8.5: Fitting of characteristic temperature T_0 of the threshold current I_{th} for experimental data in batch 2 for pulsed (**a. - g.**) and continuous bias (**h. - n.**) for 750 µm cavity length.

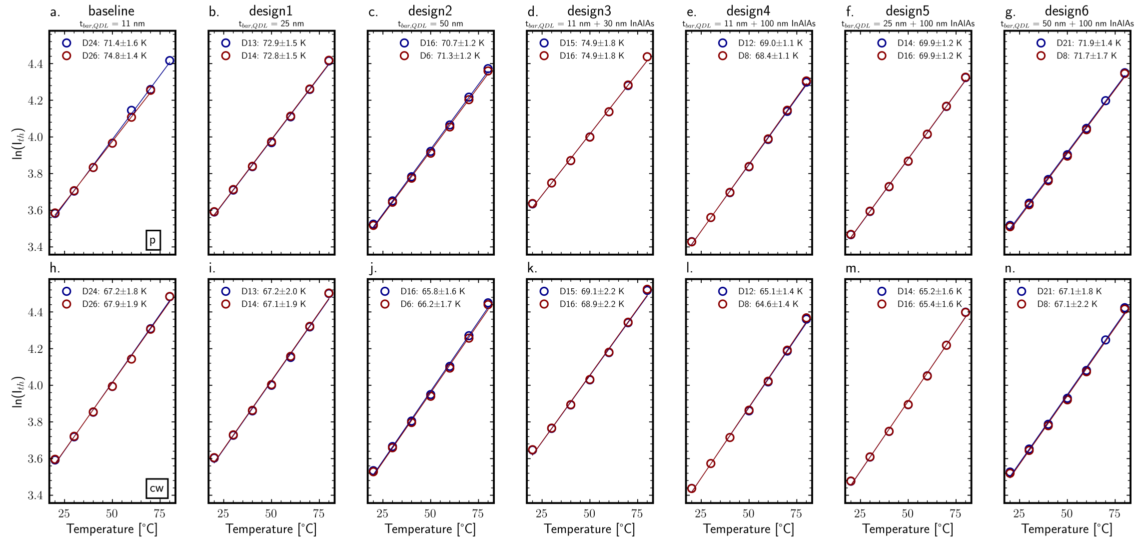

Figure 8.6: Fitting of characteristic temperature T_0 of the threshold current I_{th} for experimental data in batch 2 for pulsed (**a. - g.**) and continuous bias (**h. - n.**) for 1000 µm cavity length.

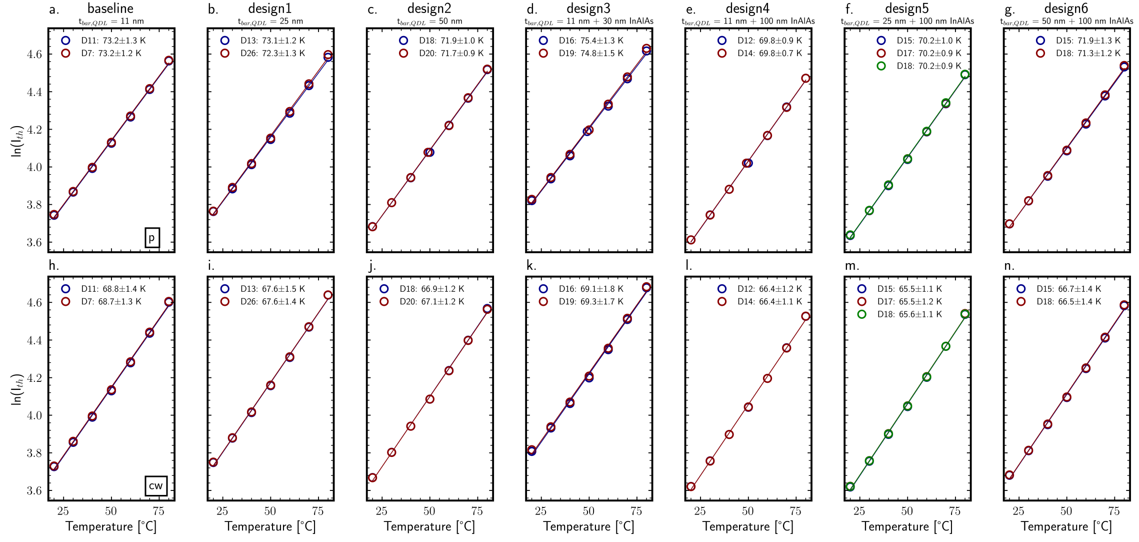

Figure 8.7: Fitting of characteristic temperature T_0 of the threshold current I_{th} for experimental data in batch 2 for pulsed (**a. - g.**) and continuous bias (**h. - n.**) for 1500 µm cavity length.

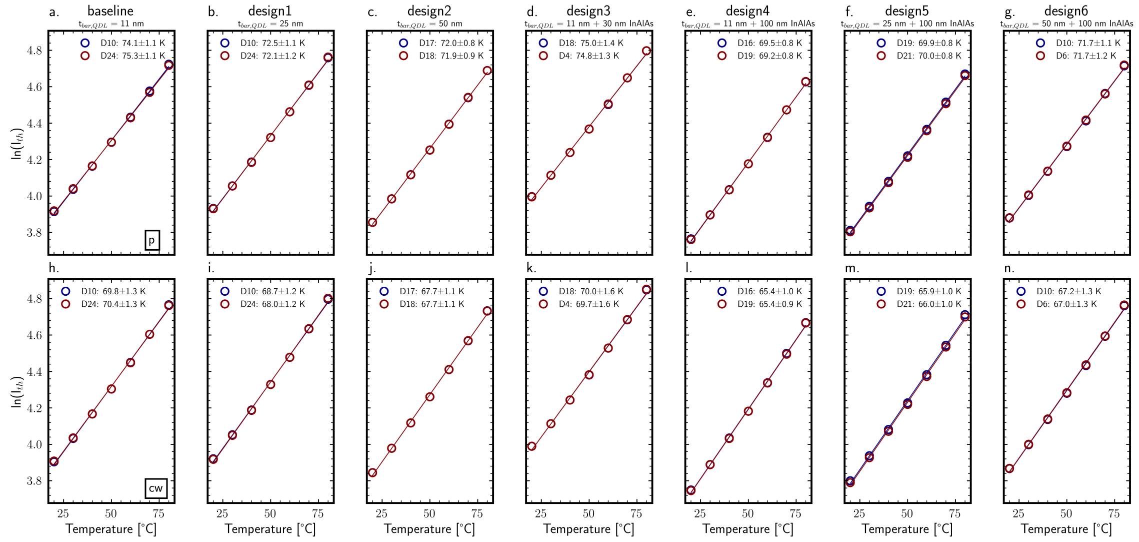

Figure 8.8: Fitting of characteristic temperature T_0 of the threshold current I_{th} for experimental data in batch 2 for pulsed (**a. - g.**) and continuous bias (**h. - n.**) for 2000 µm cavity length.

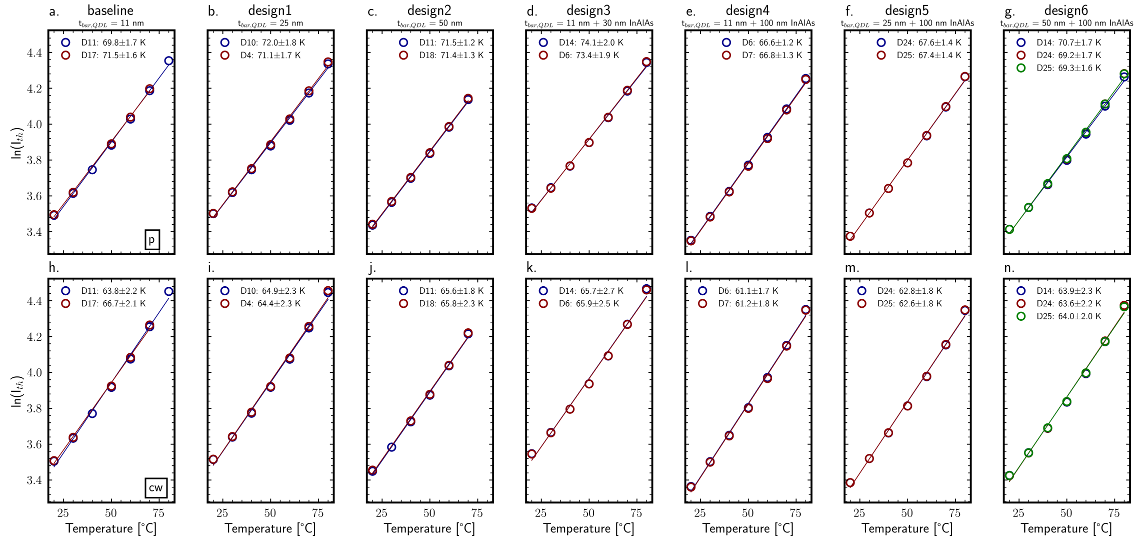

Figure 8.9: Fitting of characteristic temperature T_1 of the slope efficiency for experimental data in batch 2 for pulsed (**a. - g.**) and continuous bias (**h. - n.**) for 750 µm cavity length.

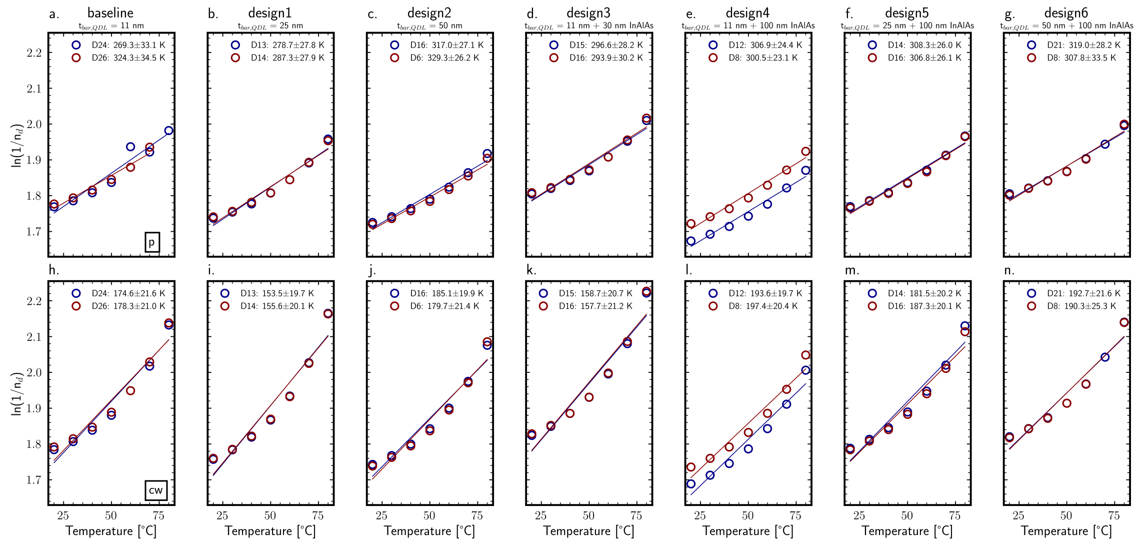

Figure 8.10: Fitting of characteristic temperature T_1 of the slope efficiency for experimental data in batch 2 for pulsed (**a. - g.**) and continuous bias (**h. - n.**) for 1000 µm cavity length.

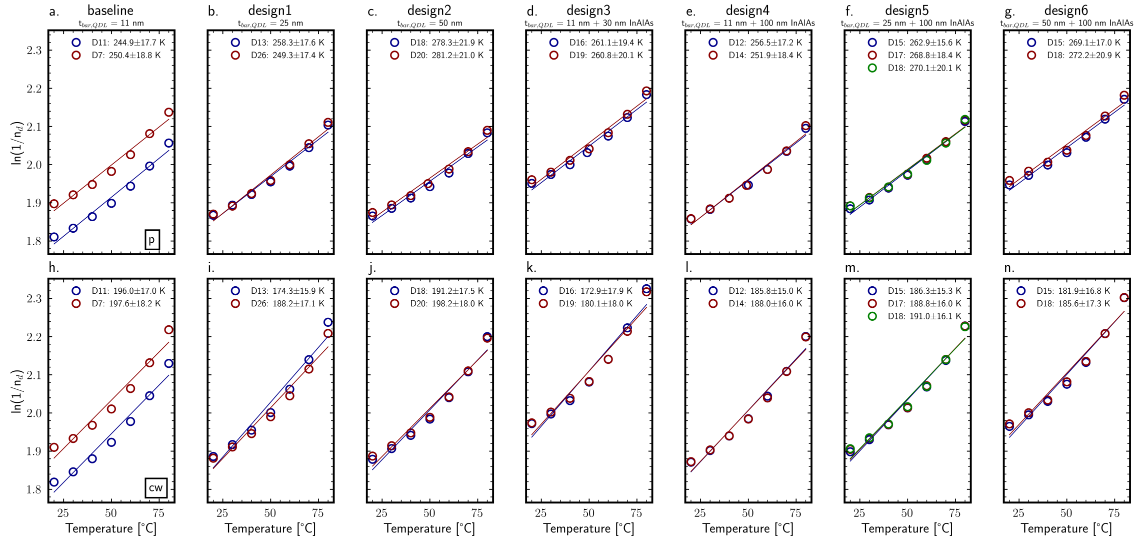

Figure 8.11: Fitting of characteristic temperature T_1 of the slope efficiency for experimental data in batch 2 for pulsed (**a. - g.**) and continuous bias (**h. - n.**) for 1500 µm cavity length.

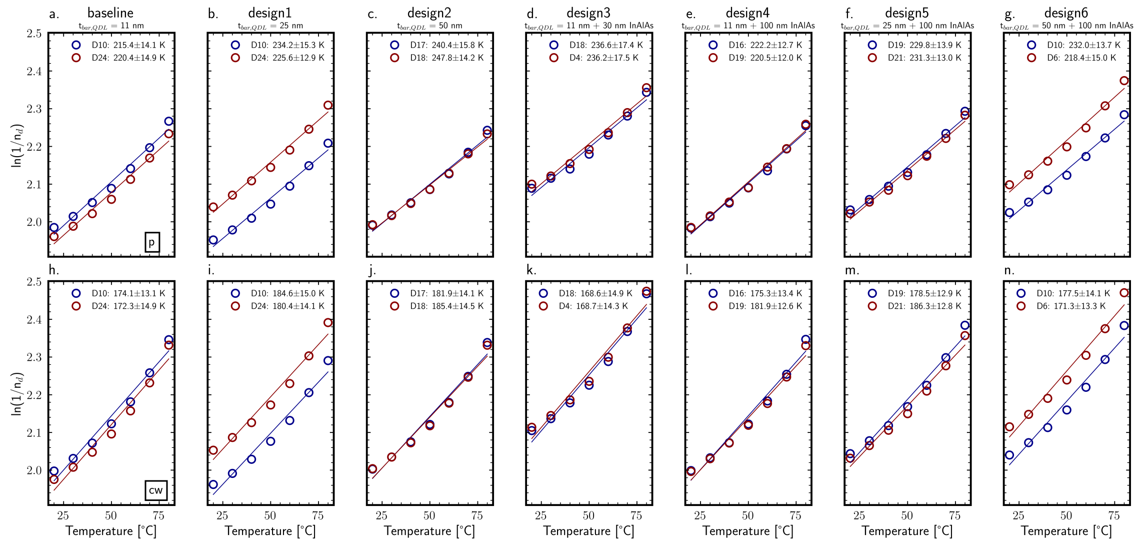

Figure 8.12: Fitting of characteristic temperature T_1 of the slope efficiency for experimental data in batch 2 for pulsed (**a. - g.**) and continuous bias (**h. - n.**) for 2000 µm cavity length.

8.4 Code snippets

This section provides sample code that was useful in the analysis of various experimental laser characteristics, as well as scripts that may find use by future users of Crosslight PICS3D. This includes the beginnings of an interface to create PICS3D simulation files using Python rather than the built in software ($sim_c reate.py$). There are additional scripts which allow runing simulations on a separate server without the need to remote to it $sim_h andler.py$. Most of these scripts will require access to the $seb_p kg$-module which was created during this project. The module is available in the SUNLAB repository or upon request from the author.

8.4.1 Data analysis functions

These are functions used to read, format, and graph data from both experiment and simulation.

Fitting LIV curves

This function will return the threshold current and slope efficiency for an LI curve. **data** should be a two-column vector, with the first column representing bias current and the second laser power.

```
def fit_LI(data, rel_thresh=0.05, upper_thresh=0.8, output_lims=False,
    ↪ verbose=False,
method='legacy', covariance=False, ith_range=75, ith_offset=20,
min_ith=5, max_ith=200, smooth_offset=5, avoid_fit=False):
"""
Return a line fit (eta, y-intercept, threshold) to the lasing portion of
    ↪ an L-I curve.
fitted curve L = p[0]*I + p[1]
slope efficiency = p[0]
threshold current = -p[1]/p[0]
"""


#-----------------------------------------------------------------------
# LEGACY METHOD
if method == 'legacy':
       tdat = data[(data[:, 1] > rel_thresh * data[:, 1].max()), :]
```

```
        tdat = tdat[tdat[:, 0] <= upper_thresh * tdat[np.argmax(tdat[:, 1])
            ↪ , 0], :]

elif method == 'dynamic_upper_thresh':
        tdat = data[(data[:, 1] > rel_thresh * data[:, 1].max()), :]

        grad = np.gradient(tdat[:, 1], tdat[:, 0])

        if np.mean(grad[-5:]) <= np.mean(grad[:5]):
        # Significant roll-off detected
                roll_off_idx = np.max(np.argwhere(grad >= upper_thresh*np.
                    ↪ mean(grad[:5])))
                if roll_off_idx <= tdat.shape[0]:
                        roll_off_idx = 1
        else:
                roll_off_idx = np.min(np.argwhere(tdat[:, 1] <=
                    ↪ upper_thresh * np.max(tdat[:, 1])))

        if verbose:
                print(f'dynamic_upper_thresh:␣roll-off␣at␣{tdat[
                    ↪ roll_off_idx,␣0]}␣mA.')

        tdat = tdat[:roll_off_idx, :]

#-------------------------------------------------------------
# FILTER POTENTIAL ROLL-OFF AND BREAKDOWN SECTIONS OF THE LI-CURVE
elif method == 'filter_rolloff_breakdown':
        # Temporary threshhold current
        rel_thresh_idx = np.min(np.argwhere(data[:, 1] >= rel_thresh * data
            ↪ [:, 1].max())) - 1
        ith = data[rel_thresh_idx, 0]
        if verbose:
                print(f'Ith:␣{ith:.2f}␣mA')
        # Determine roll-off and break down current bias
        iro, _, ibd, _ = find_rolloff_and_breakdown(ith, data[:, 0], data
            ↪ [:, 1])

        if iro is None:
```

```
        # No roll-off detected
        iro = data[:, 0].max()
    else:
        if verbose:
            print(f'LI: roll-off detected at {iro:.1f} mA.')
    if ibd is None:
        # No breakdown detected
        ibd = data[:, 0].max()
    else:
        if verbose:
            print(f'LI: negative differential efficiency detected at {ibd:.1f} mA.')

    hard_limit = data[np.max(np.argwhere(data[:,1] <= 0.9 * data[:, 1].max())), 0]
    ulim = np.min([hard_limit, iro, ibd])

    if verbose:
        print(f'Lower limit: {data[rel_thresh_idx,0]:.2f} mA')
        print(f'Upper limit: {ulim:.2f} mA')

    upper_lim_idx = np.argmin(np.abs(data[:, 0] - ulim)) + 1
    if verbose:
        print(f'{upper_lim_idx - rel_thresh_idx} steps used for fitting.')
    if upper_lim_idx - rel_thresh_idx <= 2:
        tdat = np.array([[0, 0]])
    else:
        tdat = data[rel_thresh_idx:upper_lim_idx, :]
elif method == 'ith_range':

    bias = data[:, 0]
    power = data[:, 1]

    # Calculate the first derivative
    first_gradient = np.gradient(power, bias)
    # Filter the first derivative for potentially highly discontinuous
    # Disabled by smooth_offset = 0
```

```
if smooth_offset > 0:
        disc_idxs = np.argwhere(np.abs(first_gradient) > 0.5)
        if disc_idxs.__len__() > 0:
                disc_idxs = disc_idxs[0]
                disc_idxs = np.append(disc_idxs, [int(np.min(
                    ↪ disc_idxs) - (idx + 1)) for idx in range(
                    ↪ smooth_offset)])
                disc_idxs = np.append(disc_idxs, [int(np.max(
                    ↪ disc_idxs) + (idx + 1)) for idx in range(
                    ↪ smooth_offset)])

                disc_idxs = np.clip(disc_idxs, 0, len(first_gradient
                    ↪ ) - 1)
                first_gradient[disc_idxs] = 0
# Calculate the second derivative
second_gradient = np.gradient(first_gradient, bias)

xvals = bias[bias < max_ith]
yvals = second_gradient[bias < max_ith]
yvals = yvals[xvals > min_ith]
xvals = xvals[xvals > min_ith]

# Temporary threshold current
peaks = signal.find_peaks(yvals, prominence=8e-3)
if peaks[0].__len__() == 0:
        max_dx = np.argmax(yvals)
if verbose:
        print(f'Fell␣back␣to␣using␣maximum␣value␣to␣determine␣peak␣
            ↪ at␣{xvals[max_dx]:.2f}␣mA')
else:
        max_dx = int(np.min(peaks[0]))

ith_p = xvals[max_dx]

if verbose:
        print(f'Start␣|␣End␣of␣fit␣range:␣{ith_p:.1f}␣|␣{ith_p+
            ↪ ith_range:.1f}␣mA')
```

```
        idxs = np.intersect1d(np.argwhere(bias > ith_p + ith_offset), np.
            ↪ argwhere(bias < ith_p + ith_offset + ith_range))
        tdat = data[idxs, :]

#------------------------------------------------------------
# Fit the remainder of the LI-curve (if available)
if tdat[:, 1].sum() == 0:
        print('plot_Li:␣Filtering␣of␣linear␣section␣impossible.␣Using␣full␣
            ↪ range.')
        tdat = data
        p = np.polyfit(tdat[:, 0], tdat[:, 1], 1, cov=covariance)
if covariance:
        dnd, dith = np.diag(p[1])
        p = p[0]
        dith = dith/p[0]

lower_lim, upper_lim = tdat[0, 0], tdat[-1, 0]

nd, b, ith = p[0], p[1], -p[1] / p[0]

# Overwrite linear fit values with ones derived using 'ith_range'
if method == 'ith_range' and avoid_fit:
        ith = ith_p
        nd = np.interp(ith_p + 5, tdat[:, 0], np.gradient(tdat[:, 1], tdat
            ↪ [:, 0]))
        b = -ith*nd
        if covariance:
                dnd, dith = 0, 0

return_tuple = [nd, b, ith]
if output_lims:
        return_tuple.append([lower_lim, upper_lim])
if covariance:
        return_tuple.extend([dnd, dith])

return return_tuple
```

sim_data.py

```
# sim_data
# Class struct designed to handle the output from Crosslight's Pics3D
    ↪ software suite

# Directory structure expected by SimData:
# <sim_dir>
# |- <sim>.zp_000x (number of .zp files = number of simulation steps)
# |- <sim>.sol
# |- <sim>.msh (mesh and simulation output files are expected to have the
    ↪ same name)
# |- data {This dir and subdirs are created by .unpack}
# |- raw
# |- <sim>_step000x
# |-'absorption_xy' etc.
# |- plots
# |- vtk_files
# |- movies


# Gets the version of the device from the absolute device path
# 'directory' method assumes it is saved in the path structure in GDrive)
# 'file' method assumes it contains a .txt file with the version number as
    ↪  its name
def get_version(sim_dir, method='file'):
return clp.get_version(sim_dir, method)
class SimData:
       def __init__(self, sim_dir, save_dir='default', load_data=True,
           ↪ overwrite=False):
```

8.4.2 Creating PICS3D files

These functions require a C++ pre-compiler *cpp* (or *gpp*) and a version of *make*, accessible by the system. These come pre-loaded with most Linux distributions but may require external tools such as *MinGW32* on Windows.

sim_create.py

```
class CrosslightSim:
        def __init__(self, sim_vars, base_var_file, input_dir, calc_dir,
            ↪ SimSheep=None, overwrite=False, **kwargs):
```

Bibliography

[1] "Data Never Sleeps 10.0 | Domo." https://www.domo.com/data-never-sleeps.

[2] "Beyond 20/20 WDS - Table view - World seaborne trade by types of cargo and by group of economies, annual." https://unctadstat.unctad.org/wds/TableViewer/tableView.aspx?ReportId=32363.

[3] S and P Global, "Global Trade Outlook 2022." https://www.spglobal.com/marketintelligence/en/mi/research-analysis/global-trade-outlook-2022.html, Jan. 2022.

[4] W. Klaus, P. J. Winzer, and K. Nakajima, "The Role of Parallelism in the Evolution of Optical Fiber Communication Systems," *Proceedings of the IEEE*, vol. 110, pp. 1619–1654, Nov. 2022.

[5] E. Masanet, A. Shehabi, N. Lei, S. Smith, and J. Koomey, "Recalibrating global data center energy-use estimates," *Science*, vol. 367, pp. 984–986, Feb. 2020.

[6] C. Freitag, M. Berners-Lee, K. Widdicks, B. Knowles, G. S. Blair, and A. Friday, "The real climate and transformative impact of ICT: A critique of estimates, trends, and regulations," *Patterns*, vol. 2, p. 100340, Sept. 2021.

[7] A. S. G. Andrae and T. Edler, "On Global Electricity Usage of Communication Technology: Trends to 2030," *Challenges*, vol. 6, pp. 117–157, June 2015.

[8] S. Karlilar, M. Balcilar, and F. Emir, "Environmental sustainability in the OECD: The power of digitalization, green innovation, renewable energy and financial development," *Telecommunications Policy*, vol. 47, p. 102568, July 2023.

[9] V. C. Coroama, L. M. Hilty, and M. Birtel, "Effects of Internet-based multiple-site conferences on greenhouse gas emissions," *Telematics and Informatics*, vol. 29, pp. 362–374, Nov. 2012.

[10] J. Malmodin and D. Lundén, "The energy and carbon footprint of the global ICT and E & M sectors 2010-2015," *Sustainability (Switzerland)*, vol. 10, no. 9, 2018.

[11] J. Cho and Y. Kim, "Improving energy efficiency of dedicated cooling system and its contribution towards meeting an energy-optimized data center," *Applied Energy*, vol. 165, pp. 967–982, Mar. 2016.

[12] M. K. Patterson, "The effect of data center temperature on energy efficiency," in *2008 11th Intersociety Conference on Thermal and Thermomechanical Phenomena in Electronic Systems*, pp. 1167–1174, May 2008.

[13] I. V. Kulkova, *Material Engineering for Monolithic Semiconductor Mode-Locked Lasers*. PhD thesis, Technical University of Denmark, 2014.

[14] J. N. Kemal, P. Marin-Palomo, V. Panapakkam, P. Trocha, S. Wolf, K. Merghem, F. Lelarge, A. Ramdane, S. Randel, W. Freude, and C. Koos, "Coherent WDM transmission using quantum-dash mode-locked laser diodes as multi-wavelength source and local oscillator," *Optics Express*, vol. 27, pp. 31164–31175, Oct. 2019.

[15] M. Johnson-Groh, "Beyond telecommunications." https://spie.org/news/photonics-focus/septoct-2021/fiber-optic-cables-enable-deep-ocean-science, Jan. 2021.

[16] R. Tucker, G. Eisenstein, and S. Korotky, "Optical time-division multiplexing for very high bit-rate transmission," *Journal of Lightwave Technology*, vol. 6, pp. 1737–1749, Nov. 1988.

[17] S. Kawanishi, H. Takara, K. Uchiyama, I. Shake, and K. Mori, "3 Tbit/s (160 Gbit/s×19 ch) OTDM/WDM Transmission Experiment," in *Optical Fiber Communication Conference*, p. PD1, Optica Publishing Group, Feb. 1999.

[18] C. Brackett, "Dense wavelength division multiplexing networks: Principles and applications," *IEEE Journal on Selected Areas in Communications*, vol. 8, pp. 948–964, Aug. 1990.

[19] J. Armstrong, "OFDM for Optical Communications," *Journal of Lightwave Technology*, vol. 27, pp. 189–204, Feb. 2009.

[20] N. Deng, C.-K. Chan, and L.-K. Chen, "A Hybrid OTDM Scheme With Enhanced Demultiplexing Performance," *IEEE Photonics Technology Letters*, vol. 19, pp. 1454–1456, Oct. 2007.

[21] L. Chang, S. Liu, and J. E. Bowers, “Integrated optical frequency comb technologies,” *Nature Photonics*, vol. 16, pp. 95–108, Feb. 2022.

[22] H. Sanjoh, H. Yasaka, Y. Sakai, K. Sato, H. Ishii, and Y. Yoshikuni, “Multiwavelength light source with precise frequency spacing using a mode-locked semiconductor laser and an arrayed waveguide grating filter,” *IEEE Photonics Technology Letters*, vol. 9, pp. 818–820, June 1997.

[23] G. E. Keiser, “A Review of WDM Technology and Applications,” *Optical Fiber Technology*, vol. 5, pp. 3–39, Jan. 1999.

[24] A. Ellis and F. Gunning, “Spectral density enhancement using coherent WDM,” *IEEE Photonics Technology Letters*, vol. 17, pp. 504–506, Feb. 2005.

[25] Z. Lu, J. Liu, P. J. Poole, Y. Mao, J. Weber, G. Liu, and P. Barrios, “InAs/InP Quantum Dash Semiconductor Coherent Comb Lasers and their Applications in Optical Networks,” *Journal of Lightwave Technology*, vol. 39, pp. 3751–3760, June 2021.

[26] A. A. Aboketaf, L. Cao, D. Adams, A. W. Elshaari, S. F. Preble, M. T. Crowley, L. F. Lester, and P. Ampadu, “Hybrid OTDM and WDM for multicore optical communication,” in *2012 International Green Computing Conference (IGCC)*, pp. 1–5, June 2012.

[27] Mohanp06, “Bravais lattice,” *Wikipedia*, May 2023.

[28] H. Foell, “Lecture scipt: Semiconductor Technology,” 2015.

[29] M. Cardona and Y. Y. Peter, *Fundamentals of Semiconductors*, vol. 619 of *Graduate Texts in Physics*. Springer, 4 ed., 2010.

[30] N. W. Ashcroft and N. D. Mermin, *Solid State Physics*. Harcourt College Publishers, 1976.

[31] T. E. o. E. Britannica, “Quasi-particle,” *Encyclopaedia Britannica*, May 2018.

[32] J. H. Davies, *The Physics of Low-Dimensional Semiconductors: An Introduction*. Cambridge university press, 1998.

[33] C. Kane and J. Moore, “Topological insulators,” *Physics World*, vol. 24, p. 32, Feb.

2011.

[34] C. Kittel, *Introduction to Solid State Physics*. Hoboken, NJ: Wiley, 8th ed ed., 2005.

[35] "Band structure and carrier concentration of Gallium Arsenide (GaAs)." https://www.ioffe.ru/SVA/NSM/Semicond/GaAs/bandstr.html.

[36] Y. Zhang, G. Conibeer, S. Liu, J. Zhang, and J.-F. Guillemoles, "Review of the mechanisms for the phonon bottleneck effect in III–V semiconductors and their application for efficient hot carrier solar cells," *Progress in Photovoltaics: Research and Applications*, vol. 30, no. 6, pp. 581–596, 2022.

[37] E. Burstein, "Anomalous Optical Absorption Limit in InSb," *Physical Review*, vol. 93, pp. 632–633, Feb. 1954.

[38] T. S. Moss, G. J. Burrell, and B. Ellis, *Semiconductor Opto-Electronics*. Butterworth-Heinemann, Oct. 2013.

[39] B. Bennett, R. Soref, and J. Del Alamo, "Carrier-induced change in refractive index of InP, GaAs and InGaAsP," *IEEE Journal of Quantum Electronics*, vol. 26, pp. 113–122, Jan. 1990.

[40] W. Shockley and W. T. Read, "Statistics of the Recombinations of Holes and Electrons," *Physical Review*, vol. 87, pp. 835–842, Sept. 1952.

[41] R. N. Hall, "Electron-Hole Recombination in Germanium," *Physical Review*, vol. 87, pp. 387–387, July 1952.

[42] M. Chu, Y. Sun, U. Aghoram, and S. E. Thompson, "Strain: A Solution for Higher Carrier Mobility in Nanoscale MOSFETs," *Annual Review of Materials Research*, vol. 39, no. 1, pp. 203–229, 2009.

[43] F. Guffarth, R. Heitz, A. Schliwa, O. Stier, N. N. Ledentsov, A. R. Kovsh, V. M. Ustinov, and D. Bimberg, "Strain engineering of self-organized InAs quantum dots," *Physical Review B*, vol. 64, p. 085305, Aug. 2001.

[44] S. Adachi, "Optical dispersion relations for GaP, GaAs, GaSb, InP, InAs, InSb, AlxGa1-xAs, and In1-xGaxAsyP1-y," *Journal of Applied Physics*, vol. 66, pp. 6030–6040, Dec. 1989.

[45] M. A. Green, “Self-consistent optical parameters of intrinsic silicon at 300K including temperature coefficients,” *Solar Energy Materials and Solar Cells*, vol. 92, pp. 1305–1310, Nov. 2008.

[46] J. Piprek, ed., *Handbook of Optoelectronic Device Modeling and Simulation.* Series in Optics and Optoelectronics, Boca Raton: CRC Press, Taylor & Francis Group, 2018.

[47] Y. Lacroix, C. A. Tran, S. P. Watkins, and M. L. W. Thewalt, “Low-temperature photoluminescence of epitaxial InAs,” *Journal of Applied Physics*, vol. 80, pp. 6416–6424, Dec. 1996.

[48] A. P. Roth, R. G. Goodchild, S. Charbonneau, and D. F. Williams, “New photoluminescence lines in GaAs layers grown by metalorganic vapor phase epitaxy,” *Journal of Applied Physics*, vol. 54, pp. 3427–3430, June 1983.

[49] W. Demtröder, *Laser Spectroscopy: Basic Concepts and Instrumentation.* Advanced Texts in Physics, Berlin, Heidelberg: Springer, 2003.

[50] M. Yamada, *Theory of Semiconductor Lasers: From Basis of Quantum Electronics to Analyses of the Mode Competition Phenomena and Noise*, vol. 185 of *Springer Series in Optical Sciences.* Tokyo: Springer Japan, 2014.

[51] M. Faugeron, F. Lelarge, M. Tran, Y. Robert, E. Vinet, A. Enard, J. Jacquet, and F. Van Dijk, “High Peak Power, Narrow RF Linewidth Asymmetrical Cladding Quantum-Dash Mode-Locked Lasers,” *IEEE Journal of Selected Topics in Quantum Electronics*, vol. 19, pp. 1101008–1101008, July 2013.

[52] T. Birks, D. Mogilevtsev, J. Knight, and P. St. J. Russell, “Dispersion compensation using single-material fibers,” *IEEE Photonics Technology Letters*, vol. 11, pp. 674–676, June 1999.

[53] M. J. Weber, D. Milam, and W. L. Smith, “Nonlinear Refractive Index Of Glasses And Crystals,” *Optical Engineering*, vol. 17, pp. 463–469, Oct. 1978.

[54] H. Haken, *Laser Theory.* Berlin, Heidelberg: Springer, 1984.

[55] T. Sadeev, H. Huang, D. Arsenijević, K. Schires, F. Grillot, and D. Bimberg, “Highly efficient non-degenerate four-wave mixing under dual-mode injection in In-

P/InAs quantum-dash and quantum-dot lasers at 1.55 Mm," *Applied Physics Letters*, vol. 107, p. 191111, Nov. 2015.

[56] J. Schwinger, "On Gauge Invariance and Vacuum Polarization," *Physical Review*, vol. 82, pp. 664–679, June 1951.

[57] E. Garmire, "Nonlinear optics in daily life," *Optics Express*, vol. 21, pp. 30532–30544, Dec. 2013.

[58] C. H. Henry, R. A. Logan, and K. A. Bertness, "Spectral dependence of the change in refractive index due to carrier injection in GaAs lasers," *Journal of Applied Physics*, vol. 52, pp. 4457–4461, July 1981.

[59] M. Yamada and H. Ishiguro, "Gain Calculation of Undoped GaAs Injection Laser Taking Account of Electronic Intra-Band Relaxation," *Japanese Journal of Applied Physics*, vol. 20, p. 1279, July 1981.

[60] B. W. Hakki and T. L. Paoli, "Cw degradation at 300 K of GaAs double-heterostructure junction lasers. II. Electronic gain," *Journal of Applied Physics*, vol. 44, pp. 4113–4119, Sept. 1973.

[61] A. A. Ukhanov, A. Stintz, P. G. Eliseev, and K. J. Malloy, "Comparison of the carrier induced refractive index, gain, and linewidth enhancement factor in quantum dot and quantum well lasers," *Applied Physics Letters*, vol. 84, pp. 1058–1060, Feb. 2004.

[62] M. Lorke, F. Jahnke, and W. W. Chow, "Excitation dependences of gain and carrier-induced refractive index change in quantum-dot lasers," *Applied Physics Letters*, vol. 90, p. 051112, Feb. 2007.

[63] R. N. Hall, G. E. Fenner, J. D. Kingsley, T. J. Soltys, and R. O. Carlson, "Coherent Light Emission From GaAs Junctions," *Physical Review Letters*, vol. 9, pp. 366–368, Nov. 1962.

[64] M. I. Nathan, W. P. Dumke, G. Burns, F. H. Dill, and G. Lasher, "STIMULATED EMISSION OF RADIATION FROM GaAs *p-n* JUNCTIONS," *Applied Physics Letters*, vol. 1, pp. 62–64, Nov. 1962.

[65] N. Holonyak and S. F. Bevacqua, "Coherent (visible) light emission from GaAsP junctions," *Applied Physics Letters*, vol. 1, pp. 82–83, Dec. 1962.

[66] V. K. Arora, “Quantum well wires: Electrical and optical properties,” *Journal of Physics C: Solid State Physics*, vol. 18, pp. 3011–3016, May 1985.

[67] J. Boddison-Chouinard, A. Bogan, N. Fong, K. Watanabe, T. Taniguchi, S. Studenikin, A. Sachrajda, M. Korkusinski, A. Altintas, M. Bieniek, P. Hawrylak, A. Luican-Mayer, and L. Gaudreau, “Gate-controlled quantum dots in monolayer WSe2,” *Applied Physics Letters*, vol. 119, p. 133104, Sept. 2021.

[68] Y. Fu, M. Willander, and T. H. Wang, “Etching trenches to effectively create electron quantum wires for single-electron-transistor applications,” *Applied Physics Letters*, vol. 78, pp. 3705–3707, June 2001.

[69] J. P. Cuypers and W. van Haeringen, “On the theory of envelope functions in lattice-matched heterostructures,” *Physica B: Condensed Matter*, vol. 168, pp. 58–66, Jan. 1991.

[70] N. Usami, “Types of silicon–germanium (SiGe) bulk crystal growth methods and their applications,” in *Silicon–Germanium (SiGe) Nanostructures* (Y. Shiraki and N. Usami, eds.), Woodhead Publishing Series in Electronic and Optical Materials, pp. 72–82, Woodhead Publishing, Jan. 2011.

[71] M. Lappa, “Thermal convective instabilities in cylindrical enclosures and floating liquid columns under normal and microgravity conditions,” in *Surface Tension-Driven Flows and Applications*, pp. 103–120, Jan. 2005.

[72] M. B. Panish and H. Temkin, “Gas-Source Molecular Beam Epitaxy: GaInAsP/InP MBE with Non-elemental Sources. Heterostructures and Device Properties,” in *Molecular Beam Epitaxy* (R. F. C. Farrow, ed.), pp. 275–343, Park Ridge, NJ: William Andrew Publishing, Jan. 1995.

[73] M. B. Panish and S. Sumski, “Gas source molecular beam epitaxy of GaxIn1-xPyAs1-y,” *Journal of Applied Physics*, vol. 55, pp. 3571–3576, May 1984.

[74] W. T. Tsang, “Chemical beam epitaxy of InP and GaAs,” *Applied Physics Letters*, vol. 45, pp. 1234–1236, Dec. 1984.

[75] M. B. Panish, “Molecular Beam Epitaxy of GaAs and InP with Gas Sources for As and P,” *Journal of The Electrochemical Society*, vol. 127, p. 2729, Dec. 1980.

[76] I. Vurgaftman, J. R. Meyer, and L. R. Ram-Mohan, “Band parameters for III–V

compound semiconductors and their alloys," *Journal of Applied Physics*, vol. 89, pp. 5815–5875, June 2001.

[77] C. Incorporated, "Corning SMF-28 Optical Fiber," product Information, Corning Incorporated, New Jersey, United States, 2002.

[78] "ITU." https://www.itu.int:443/en/pages/default.aspx.

[79] P. J. Poole, J. McCaffrey, R. L. Williams, J. Lefebvre, and D. Chithrani, "Chemical beam epitaxy growth of self-assembled InAs/InP quantum dots," *Journal of Vacuum Science & Technology B: Microelectronics and Nanometer Structures Processing, Measurement, and Phenomena*, vol. 19, pp. 1467–1470, July 2001.

[80] P. Miska, C. Paranthoen, J. Even, O. Dehaese, H. Folliot, N. Bertru, S. Loualiche, M. Senes, and X. Marie, "Optical spectroscopy and modelling of double-cap grown InAs/InP quantum dots with long wavelength emission," *Semiconductor Science and Technology*, vol. 17, p. L63, Sept. 2002.

[81] G.-H. Duan, A. Shen, A. Akrout, F. V. Dijk, F. Lelarge, F. Pommereau, O. LeGouezigou, J.-G. Provost, H. Gariah, F. Blache, F. Mallecot, K. Merghem, A. Martinez, and A. Ramdane, "High performance InP-based quantum dash semiconductor mode-locked lasers for optical communications," *Bell Labs Technical Journal*, vol. 14, no. 3, pp. 63–84, 2009.

[82] R. Rosales, K. Merghem, A. Martinez, A. Akrout, J.-P. Tourrenc, A. Accard, F. Lelarge, and A. Ramdane, "InAs/InP Quantum-Dot Passively Mode-Locked Lasers for 1.55-μ m Applications," *IEEE Journal of Selected Topics in Quantum Electronics*, vol. 17, pp. 1292–1301, Sept. 2011.

[83] R.-J. K. Obhi, S. W. Schaefer, C. E. Valdivia, J. R. Liu, Z. G. Lu, P. J. Poole, and K. Hinzer, "Indium arsenide single quantum dash morphology and composition for wavelength tuning in quantum dash lasers," *Applied Physics Letters*, vol. 122, p. 051104, Jan. 2023.

[84] P. Poole, K. Kaminska, P. Barrios, Z. Lu, and J. Liu, "Growth of InAs/InP-based quantum dots for 1.55 Mm laser applications," *Journal of Crystal Growth*, vol. 311, pp. 1482–1486, Mar. 2009.

[85] R. Wang, A. Stintz, T. Rotter, K. Malloy, L. Lester, A. Gray, T. Newell, and P. Varangis, "Low threshold oxide-confined InAs quantum dash ridge waveguide

lasers on InP substrates," in *LEOS 2001. 14th Annual Meeting of the IEEE Lasers and Electro-Optics Society (Cat. No.01CH37242)*, vol. 2, pp. 405–406 vol.2, Nov. 2001.

[86] C. Paranthoen, N. Bertru, O. Dehaese, A. Le Corre, S. Loualiche, B. Lambert, and G. Patriarche, "Height dispersion control of InAs/InP quantum dots emitting at 1.55 Mm," *Applied Physics Letters*, vol. 78, pp. 1751–1753, Mar. 2001.

[87] W. G. Jeong, P. D. Dapkus, U. H. Lee, J. S. Yim, D. Lee, and B. T. Lee, "Epitaxial growth and optical characterization of InAs/InGaAsP/InP self-assembled quantum dots," *Applied Physics Letters*, vol. 78, pp. 1171–1173, Feb. 2001.

[88] P. Poole, R. Williams, J. Lefebvre, and S. Moisa, "Using As/P exchange processes to modify InAs/InP quantum dots," *Journal of Crystal Growth*, vol. 257, pp. 89–96, Sept. 2003.

[89] H. R. Gutiérrez, M. A. Cotta, J. R. R. Bortoleto, and M. M. G. De Carvalho, "Role of group V exchange on the shape and size of InAs/InP self-assembled nanostructures," *Journal of Applied Physics*, vol. 92, pp. 7523–7526, Dec. 2002.

[90] L. V. Asryan and R. A. Suris, "Inhomogeneous line broadening and the threshold current density of a semiconductor quantum dot laser," *Semiconductor Science and Technology*, vol. 11, pp. 554–567, Apr. 1996.

[91] P. Poole, R. Williams, J. Lefebvre, J. McCaffrey, and N. Rowell, "Trimming the size of InAs/InP quantum dots grown by CBE," in *Conference Proceedings. 2000 International Conference on Indium Phosphide and Related Materials (Cat. No.00CH37107)*, pp. 396–399, May 2000.

[92] M. Gioannini, "Numerical Modeling of the Emission Characteristics of Semiconductor Quantum Dash Materials for Lasers and Optical Amplifiers," *IEEE Journal of Quantum Electronics*, vol. 40, pp. 364–373, Apr. 2004.

[93] S. Fafard, J. P. McCaffrey, Y. Feng, C. N. Allen, H. Marchand, L. Isnard, P. Desjardins, S. Guillon, and R. A. Masut, "Towards quantum dot laser diodes emitting at 1.5 microns," in *1998 International Conference on Applications of Photonic Technology III: Closing the Gap between Theory, Development, and Applications*, vol. 3491, pp. 271–276, SPIE, Dec. 1998.

[94] M. Z. M. Khan, T. K. Ng, and B. S. Ooi, "Self-assembled InAs/InP quantum dots

and quantum dashes: Material structures and devices," *Progress in Quantum Electronics*, vol. 38, pp. 237–313, Nov. 2014.

[95] T. H. Maiman, "Optical and Microwave-Optical Experiments in Ruby," *Physical Review Letters*, vol. 4, pp. 564–566, June 1960.

[96] A. L. Schawlow and C. H. Townes, "Infrared and Optical Masers," *Physical Review*, vol. 112, pp. 1940–1949, Dec. 1958.

[97] D. H. Sliney and S. L. Trokel, *Medical Lasers and Their Safe Use.* Springer Science & Business Media, Dec. 2012.

[98] R. E. Russo, X. L. Mao, J. Yoo, and J. J. Gonzalez, "Chapter 3 - Laser ablation," in *Laser-Induced Breakdown Spectroscopy (Second Edition)* (J. P. Singh and S. N. Thakur, eds.), pp. 41–70, Amsterdam: Elsevier, Jan. 2007.

[99] B. P. Abbott, R. Abbott, R. Adhikari, P. Ajith, B. Allen, G. Allen, R. S. Amin, S. B. Anderson, W. G. Anderson, M. A. Arain, M. Araya, H. Armandula, P. Armor, Y. Aso, S. Aston, P. Aufmuth, C. Aulbert, S. Babak, P. Baker, S. Ballmer, C. Barker, D. Barker, B. Barr, P. Barriga, L. Barsotti, M. A. Barton, I. Bartos, R. Bassiri, M. Bastarrika, B. Behnke, M. Benacquista, J. Betzwieser, P. T. Beyersdorf, I. A. Bilenko, G. Billingsley, R. Biswas, E. Black, J. K. Blackburn, L. Blackburn, D. Blair, B. Bland, T. P. Bodiya, L. Bogue, R. Bork, V. Boschi, S. Bose, P. R. Brady, V. B. Braginsky, J. E. Brau, D. O. Bridges, M. Brinkmann, A. F. Brooks, D. A. Brown, A. Brummit, G. Brunet, A. Bullington, A. Buonanno, O. Burmeister, R. L. Byer, L. Cadonati, J. B. Camp, J. Cannizzo, K. C. Cannon, J. Cao, L. Cardenas, S. Caride, G. Castaldi, S. Caudill, M. Cavaglià, C. Cepeda, T. Chalermsongsak, E. Chalkley, P. Charlton, S. Chatterji, S. Chelkowski, Y. Chen, N. Christensen, C. T. Y. Chung, D. Clark, J. Clark, J. H. Clayton, T. Cokelaer, C. N. Colacino, R. Conte, D. Cook, T. R. C. Corbitt, N. Cornish, D. Coward, D. C. Coyne, J. D. E. Creighton, T. D. Creighton, A. M. Cruise, R. M. Culter, A. Cumming, L. Cunningham, S. L. Danilishin, K. Danzmann, B. Daudert, G. Davies, E. J. Daw, D. DeBra, J. Degallaix, V. Dergachev, S. Desai, R. DeSalvo, S. Dhurandhar, M. Díaz, A. Dietz, F. Donovan, K. L. Dooley, E. E. Doomes, R. W. P. Drever, J. Dueck, I. Duke, J.-C. Dumas, J. G. Dwyer, C. Echols, M. Edgar, A. Effler, P. Ehrens, E. Espinoza, T. Etzel, M. Evans, T. Evans, S. Fairhurst, Y. Faltas, Y. Fan, D. Fazi, H. Fehrmenn, L. S. Finn, K. Flasch, S. Foley, C. Forrest, N. Fotopoulos, A. Franzen, M. Frede, M. Frei, Z. Frei, A. Freise, R. Frey, T. Fricke, P. Fritschel, V. V. Frolov, M. Fyffe, V. Galdi, J. A. Garofoli, I. Gholami, J. A. Giaime, S. Gi-

ampanis, K. D. Giardina, K. Goda, E. Goetz, L. M. Goggin, G. González, M. L. Gorodetsky, S. Goßler, R. Gouaty, A. Grant, S. Gras, C. Gray, M. Gray, R. J. S. Greenhalgh, A. M. Gretarsson, F. Grimaldi, R. Grosso, H. Grote, S. Grunewald, M. Guenther, E. K. Gustafson, R. Gustafson, B. Hage, J. M. Hallam, D. Hammer, G. D. Hammond, C. Hanna, J. Hanson, J. Harms, G. M. Harry, I. W. Harry, E. D. Harstad, K. Haughian, K. Hayama, J. Heefner, I. S. Heng, A. Heptonstall, M. Hewitson, S. Hild, E. Hirose, D. Hoak, K. A. Hodge, K. Holt, D. J. Hosken, J. Hough, D. Hoyland, B. Hughey, S. H. Huttner, D. R. Ingram, T. Isogai, M. Ito, A. Ivanov, B. Johnson, W. W. Johnson, D. I. Jones, G. Jones, R. Jones, L. Ju, P. Kalmus, V. Kalogera, S. Kandhasamy, J. Kanner, D. Kasprzyk, E. Katsavounidis, K. Kawabe, S. Kawamura, F. Kawazoe, W. Kells, D. G. Keppel, A. Khalaidovski, F. Y. Khalili, R. Khan, E. Khazanov, P. King, J. S. Kissel, S. Klimenko, K. Kokeyama, V. Kondrashov, R. Kopparapu, S. Koranda, D. Kozak, B. Krishnan, R. Kumar, P. Kwee, P. K. Lam, M. Landry, B. Lantz, A. Lazzarini, H. Lei, M. Lei, N. Leindecker, I. Leonor, C. Li, H. Lin, P. E. Lindquist, T. B. Littenberg, N. A. Lockerbie, D. Lodhia, M. Longo, M. Lormand, P. Lu, M. Lubinski, A. Lucianetti, H. Lück, B. Machenschalk, M. MacInnis, M. Mageswaran, K. Mailand, I. Mandel, V. Mandic, S. Márka, Z. Márka, A. Markosyan, J. Markowitz, E. Maros, I. W. Martin, R. M. Martin, J. N. Marx, K. Mason, F. Matichard, L. Matone, R. A. Matzner, N. Mavalvala, R. McCarthy, D. E. McClelland, S. C. McGuire, M. McHugh, G. McIntyre, D. J. A. McKechan, K. McKenzie, M. Mehmet, A. Melatos, A. C. Melissinos, D. F. Menéndez, G. Mendell, R. A. Mercer, S. Meshkov, C. Messenger, M. S. Meyer, J. Miller, J. Minelli, Y. Mino, V. P. Mitrofanov, G. Mitselmakher, R. Mittleman, O. Miyakawa, B. Moe, S. D. Mohanty, S. R. P. Mohapatra, G. Moreno, T. Morioka, K. Mors, K. Mossavi, C. MowLowry, G. Mueller, H. Müller-Ebhardt, D. Muhammad, S. Mukherjee, H. Mukhopadhyay, A. Mullavey, J. Munch, P. G. Murray, E. Myers, J. Myers, T. Nash, J. Nelson, G. Newton, A. Nishizawa, K. Numata, J. O'Dell, B. O'Reilly, R. O'Shaughnessy, E. Ochsner, G. H. Ogin, D. J. Ottaway, R. S. Ottens, H. Overmier, B. J. Owen, Y. Pan, C. Pankow, M. A. Papa, V. Parameshwaraiah, P. Patel, M. Pedraza, S. Penn, A. Perraca, V. Pierro, I. M. Pinto, M. Pitkin, H. J. Pletsch, M. V. Plissi, F. Postiglione, M. Principe, R. Prix, L. Prokhorov, O. Punken, V. Quetschke, F. J. Raab, D. S. Rabeling, H. Radkins, P. Raffai, Z. Raics, N. Rainer, M. Rakhmanov, V. Raymond, C. M. Reed, T. Reed, H. Rehbein, S. Reid, D. H. Reitze, R. Riesen, K. Riles, B. Rivera, P. Roberts, N. A. Robertson, C. Robinson, E. L. Robinson, S. Roddy, C. Röver, J. Rollins, J. D. Romano, J. H. Romie, S. Rowan, A. Rüdiger, P. Russell, K. Ryan, S. Sakata, L. S. De La Jordana, V. Sandberg, V. Sannibale, L. Santamaría, S. Saraf, P. Sarin, B. S. Sathyaprakash, S. Sato, M. Satterthwaite, P. R. Saulson, R. Savage, P. Savov, M. Scanlan, R. Schilling, R. Schn-

abel, R. Schofield, B. Schulz, B. F. Schutz, P. Schwinberg, J. Scott, S. M. Scott, A. C. Searle, B. Sears, F. Seifert, D. Sellers, A. S. Sengupta, A. Sergeev, B. Shapiro, P. Shawhan, D. H. Shoemaker, A. Sibley, X. Siemens, D. Sigg, S. Sinha, A. M. Sintes, B. J. J. Slagmolen, J. Slutsky, J. R. Smith, M. R. Smith, N. D. Smith, K. Somiya, B. Sorazu, A. Stein, L. C. Stein, S. Steplewski, A. Stochino, R. Stone, K. A. Strain, S. Strigin, A. Stroeer, A. L. Stuver, T. Z. Summerscales, K.-X. Sun, M. Sung, P. J. Sutton, G. P. Szokoly, D. Talukder, L. Tang, D. B. Tanner, S. P. Tarabrin, J. R. Taylor, R. Taylor, J. Thacker, K. A. Thorne, A. Thüring, K. V. Tokmakov, C. Torres, C. Torrie, G. Traylor, M. Trias, D. Ugolini, J. Ulmen, K. Urbanek, H. Vahlbruch, M. Vallisneri, C. V. D. Broeck, M. V. Van Der Sluys, A. A. Van Veggel, S. Vass, R. Vaulin, A. Vecchio, J. Veitch, P. Veitch, C. Veltkamp, A. Villar, C. Vorvick, S. P. Vyachanin, S. J. Waldman, L. Wallace, R. L. Ward, A. Weidner, M. Weinert, A. J. Weinstein, R. Weiss, L. Wen, S. Wen, K. Wette, J. T. Whelan, S. E. Whitcomb, B. F. Whiting, C. Wilkinson, P. A. Willems, H. R. Williams, L. Williams, B. Willke, I. Wilmut, L. Winkelmann, W. Winkler, C. C. Wipf, A. G. Wiseman, G. Woan, R. Wooley, J. Worden, W. Wu, I. Yakushin, H. Yamamoto, Z. Yan, S. Yoshida, M. Zanolin, J. Zhang, L. Zhang, C. Zhao, N. Zotov, M. E. Zucker, H. Z. Mühlen, and J. Zweizig, "LIGO: The Laser Interferometer Gravitational-Wave Observatory," *Reports on Progress in Physics*, vol. 72, p. 076901, July 2009.

[100] P. Rohwetter, J. Kasparian, K. Stelmaszczyk, Z. Hao, S. Henin, N. Lascoux, W. M. Nakaema, Y. Petit, M. Queißer, R. Salamé, E. Salmon, L. Wöste, and J.-P. Wolf, "Laser-induced water condensation in air," *Nature Photonics*, vol. 4, pp. 451–456, July 2010.

[101] F. T. Arecchi, A. Berné, and P. Bulamacchi, "High-Order Fluctuations in a Single-Mode Laser Field," *Physical Review Letters*, vol. 16, pp. 32–35, Jan. 1966.

[102] A. B. Zylstra, A. L. Kritcher, O. A. Hurricane, D. A. Callahan, J. E. Ralph, D. T. Casey, A. Pak, O. L. Landen, B. Bachmann, K. L. Baker, L. Berzak Hopkins, S. D. Bhandarkar, J. Biener, R. M. Bionta, N. W. Birge, T. Braun, T. M. Briggs, P. M. Celliers, H. Chen, C. Choate, D. S. Clark, L. Divol, T. Döppner, D. Fittinghoff, M. J. Edwards, M. Gatu Johnson, N. Gharibyan, S. Haan, K. D. Hahn, E. Hartouni, D. E. Hinkel, D. D. Ho, M. Hohenberger, J. P. Holder, H. Huang, N. Izumi, J. Jeet, O. Jones, S. M. Kerr, S. F. Khan, H. Geppert Kleinrath, V. Geppert Kleinrath, C. Kong, K. M. Lamb, S. Le Pape, N. C. Lemos, J. D. Lindl, B. J. MacGowan, A. J. Mackinnon, A. G. MacPhee, E. V. Marley, K. Meaney, M. Millot, A. S. Moore, K. Newman, J.-M. G. Di Nicola, A. Nikroo, R. Nora, P. K. Patel, N. G. Rice, M. S. Rubery, J. Sater, D. J. Schlossberg, S. M. Sepke, K. Sequoia, S. J. Shin, M. Sta-

dermann, S. Stoupin, D. J. Strozzi, C. A. Thomas, R. Tommasini, C. Trosseille, E. R. Tubman, P. L. Volegov, C. R. Weber, C. Wild, D. T. Woods, S. T. Yang, and C. V. Young, "Experimental achievement and signatures of ignition at the National Ignition Facility," *Physical Review E*, vol. 106, p. 025202, Aug. 2022.

[103] Y. Takahashi, H. Hagino, Y. Tanaka, B.-S. Song, T. Asano, and S. Noda, "High-Q nanocavity with a 2-ns photon lifetime," *Optics Express*, vol. 15, no. 25, p. 17206, 2007.

[104] M. Abramowitz and I. A. Stegun, *Handbook of Mathematical Functions with Formulas, Graphs, and Mathematical Tables. National Bureau of Standards Applied Mathematics Series 55. Tenth Printing.* Dec. 1972.

[105] M. Suter and P. Dietiker, "Calculation of the finesse of an ideal Fabry–Perot resonator," *Applied Optics*, vol. 53, pp. 7004–7010, Oct. 2014.

[106] M. Henzler, "The roughness of cleaved semiconductor surfaces," *Surface Science*, vol. 36, pp. 109–122, Apr. 1973.

[107] P. Quadbeck, Ph. Ebert, K. Urban, J. Gebauer, and R. Krause-Rehberg, "Effect of dopant atoms on the roughness of III–V semiconductor cleavage surfaces," *Applied Physics Letters*, vol. 76, pp. 300–302, Jan. 2000.

[108] A. G. Fox and T. Li, "Resonant modes in a maser interferometer," *The Bell System Technical Journal*, vol. 40, pp. 453–488, Mar. 1961.

[109] J. Huang and L. W. Casperson, "Gain and saturation in semiconductor lasers," *Optical and Quantum Electronics*, vol. 25, pp. 369–390, June 1993.

[110] R. Paschotta, "Laser crystals." https://www.rp-photonics.com/laser_crystals.html, Sept. 2023.

[111] R. Paschotta, "Laser gain media." https://www.rp-photonics.com/laser_gain_media.html, Sept. 2023.

[112] W. S. Hopkins, V. Verzilov, G. Sciaini, I. Burgess, and M. Boland, "Establishing a Canadian free-electron laser research program," *Canadian Journal of Physics*, vol. 97, pp. vii–x, Dec. 2019.

[113] S. Melnikov, A. Sinyanskii, A. Sizov, and G. Miley, *Lasers with Nuclear Pumping.*

Cham: Springer International Publishing, 1 ed., 2014.

[114] F. Kurtner, J. der Au, and U. Keller, "Mode-locking with slow and fast saturable absorbers-what's the difference?," *IEEE Journal of Selected Topics in Quantum Electronics*, vol. 4, pp. 159–168, Mar. 1998.

[115] R. Paschotta and U. Keller, "Passive mode locking with slow saturable absorbers," *Applied Physics B*, vol. 73, pp. 653–662, Nov. 2001.

[116] H. A. Haus, "Theory of mode locking with a fast saturable absorber," *Journal of Applied Physics*, vol. 46, pp. 3049–3058, Sept. 2008.

[117] C. Henry, "Theory of the linewidth of semiconductor lasers," *IEEE Journal of Quantum Electronics*, vol. 18, pp. 259–264, Feb. 1982.

[118] S. Ding, B. Dong, H. Huang, J. Bowers, and F. Grillot, "Spectral dispersion of the linewidth enhancement factor and four wave mixing conversion efficiency of an InAs/GaAs multimode quantum dot laser," *Applied Physics Letters*, vol. 120, p. 081105, Feb. 2022.

[119] H. Dery and G. Eisenstein, "The impact of energy band diagram and inhomogeneous broadening on the optical differential gain in nanostructure lasers," *IEEE Journal of Quantum Electronics*, vol. 41, pp. 26–35, Jan. 2005.

[120] R.-J. K. Obhi, "Characterizing and Modelling Quantum Dashes for InP-Based Semiconductor Lasers," Master's thesis, University of Ottawa, Ottawa, May 2022.

[121] J. D. Joannopoulos, ed., *Photonic Crystals: Molding the Flow of Light.* Princeton: Princeton University Press, 2nd ed ed., 2008.

[122] K. Saito and R. Ito, "Buried-heterostructure AlGaAs lasers," *IEEE Journal of Quantum Electronics*, vol. 16, pp. 205–215, Feb. 1980.

[123] I. Kaminow, L. Stulz, J. Ko, A. Dentai, R. Nahory, J. DeWinter, and R. Hartman, "Low-threshold InGaAsP ridge waveguide lasers at 1.3 Mm," *IEEE Journal of Quantum Electronics*, vol. 19, pp. 1312–1319, Aug. 1983.

[124] I. P. Kaminow, R. E. Nahory, M. A. Pollack, L. W. Stulz, and J. C. DeWinter, "Single-Mode CW Ridge-Waveguide Laser Emitting at 1.55μm," in *Integrated and Guided Wave Optics*, p. MD5, Optica Publishing Group, Jan. 1980.

[125] I. P. Kaminow, L. W. Stulz, J. S. Ko, B. I. Miller, R. D. Feldman, J. C. Dewinter, and M. A. Pollack, "Low threshold ridge waveguide laser at 1.55 micron," *Electronics Letters*, vol. 19, pp. 877–879, Oct. 1983.

[126] R. Tucker and I. Kaminow, "High-frequency characteristics of directly modulated InGaAsP ridge waveguide and buried heterostructure lasers," *Journal of Lightwave Technology*, vol. 2, pp. 385–393, Aug. 1984.

[127] J. S. Yu and Y. T. Lee, "Reactive ion etching of InP for optoelectronic device applications: Comparison in CH4, CH4/H2, and CH4/Ar gas," *Journal of the Korean Physical Society*, vol. 37, pp. 241–246, Sept. 2000.

[128] K. P. Yap, A. Delâge, J. Lapointe, B. Lamontagne, J. H. Schmid, P. Waldron, B. A. Syrett, and S. Janz, "Correlation of Scattering Loss, Sidewall Roughness and Waveguide Width in Silicon-on-Insulator (SOI) Ridge Waveguides," *Journal of Lightwave Technology*, vol. 27, pp. 3999–4008, Sept. 2009.

[129] Y. Wang and C.-Q. Xu, "Actively Q-switched fiber lasers: Switching dynamics and nonlinear processes," *Progress in Quantum Electronics*, vol. 31, pp. 131–216, Jan. 2007.

[130] E. U. Rafailov, M. A. Cataluna, and W. Sibbett, "Mode-locked quantum-dot lasers," *Nature Photonics*, vol. 1, pp. 395–401, July 2007.

[131] R. A. Fisher, P. L. Kelley, and T. K. Gustafson, "SUBPICOSECOND PULSE GENERATION USING THE OPTICAL KERR EFFECT," *Applied Physics Letters*, vol. 14, pp. 140–143, Feb. 1969.

[132] T. Brabec, C. Spielmann, P. F. Curley, and F. Krausz, "Kerr lens mode locking," *Optics Letters*, vol. 17, pp. 1292–1294, Sept. 1992.

[133] G. Agrawal, "Effect of gain dispersion on ultrashort pulse amplification in semiconductor laser amplifiers," *IEEE Journal of Quantum Electronics*, vol. 27, pp. 1843–1849, June 1991.

[134] G. Agrawal and N. Olsson, "Self-phase modulation and spectral broadening of optical pulses in semiconductor laser amplifiers," *IEEE Journal of Quantum Electronics*, vol. 25, pp. 2297–2306, Nov. 1989.

[135] X. Huang, A. Stintz, H. Li, L. F. Lester, J. Cheng, and K. J. Malloy, "Passive mode-

locking in 1.3 Mm two-section InAs quantum dot lasers," *Applied Physics Letters*, vol. 78, pp. 2825–2827, May 2001.

[136] C. Gosset, K. Merghem, A. Martinez, G. Moreau, G. Patriarche, G. Aubin, A. Ramdane, J. Landreau, and F. Lelarge, "Subpicosecond pulse generation at 134GHz using a quantum-dash-based Fabry-Perot laser emitting at 1.56μm," *Applied Physics Letters*, vol. 88, p. 241105, June 2006.

[137] K. Merghem, R. Rosales, S. Azouigui, A. Akrout, A. Martinez, F. Lelarge, G.-H. Duan, G. Aubin, and A. Ramdane, "Low noise performance of passively mode locked quantum-dash-based lasers under external optical feedback," *Applied Physics Letters*, vol. 95, p. 131111, Sept. 2009.

[138] M. Dontabactouny, C. Rosenberg, E. Semenova, D. Larsson, K. Yvind, R. Piron, F. Grillot, O. Dehaese, N. Chevalier, and S. Loualiche, "10-GHz 1.59-Mm quantum dash passively mode-locked two-section lasers," in *Semiconductor Lasers and Laser Dynamics IV*, vol. 7720, pp. 281–290, SPIE, Apr. 2010.

[139] J. Renaudier, R. Brenot, B. Dagens, F. Lelarge, B. Rousseau, F. Poingt, O. Legouezigou, F. Pommereau, A. Accard, P. Gallion, and G.-H. Duan, "45 GHz self-pulsation with narrow linewidth in quantum dot Fabry-Perot semiconductor lasers at 1.5 Mm," *Electronics Letters*, vol. 41, pp. 1007–1008, Sept. 2005.

[140] J. Renaudier, G.-H. Duan, J.-G. Provost, H. Debregeas-Sillard, and P. Gallion, "Phase correlation between longitudinal modes in semiconductor self-pulsating DBR lasers," *IEEE Photonics Technology Letters*, vol. 17, pp. 741–743, Apr. 2005.

[141] C. W. Thiel, "Four-Wave Mixing and its Applications," technical, Montana State University, Sept. 2000.

[142] R. L. Abrams and R. C. Lind, "Degenerate four-wave mixing in absorbing media," *Optics Letters*, vol. 2, pp. 94–96, Apr. 1978.

[143] G. P. Agrawal, "Four-wave mixing and phase conjugation in semiconductor laser media," *Optics Letters*, vol. 12, p. 260, Apr. 1987.

[144] O. Aso, M. Tadakuma, and S. Namiki, "Four-Wave Mixing in Optical Fibers and Its Applications," *Furukawa Review*, no. 19, 2000.

[145] A. Martinez, G. Aubin, F. Lelarge, R. Brenot, J. Landreau, and A. Ramdane, "Vari-

able optical delays at 1.55 Mm using fast light in an InAs/InP quantum dash based semiconductor optical amplifier," *Applied Physics Letters*, vol. 93, p. 091116, Sept. 2008.

[146] T. Mukai and T. Saitoh, "Detuning characteristics and conversion efficiency of nearly degenerate four-wave mixing in a 1.5- mu m traveling-wave semiconductor laser amplifier," *IEEE Journal of Quantum Electronics*, vol. 26, pp. 865–875, May 1990.

[147] H. Nakajima and R. Frey, "Collinear nearly degenerate four-wave mixing in intracavity amplifying media," *IEEE Journal of Quantum Electronics*, vol. 22, pp. 1349–1354, Aug. 1986.

[148] P. Bardella, L. L. Columbo, and M. Gioannini, "Self-generation of optical frequency comb in single section quantum dot Fabry-Perot lasers: A theoretical study," *Optics Express*, vol. 25, pp. 26234–26252, Oct. 2017.

[149] G. P. Agrawal, "Highly nondegenerate four-wave mixing in semiconductor lasers due to spectral hole burning," *Applied Physics Letters*, vol. 51, pp. 302–304, Aug. 1987.

[150] G. P. Agrawal, "Population pulsations and nondegenerate four-wave mixing in semiconductor lasers and amplifiers," *JOSA B*, vol. 5, pp. 147–159, Jan. 1988.

[151] M. Yousefi and D. Lenstra, "Rate-equation description of multi-mode semiconductor lasers," in *SPIE OPTO* (B. Witzigmann, M. Osinski, F. Henneberger, and Y. Arakawa, eds.), (San Francisco, California, United States), p. 89800B, Mar. 2014.

[152] D. Lenstra and M. Yousefi, "Rate-equation model for multi-mode semiconductor lasers with spatial hole burning," *Optics Express*, vol. 22, p. 8143, Apr. 2014.

[153] X.-Q. Li, H. Nakayama, and Y. Arakawa, "Phonon bottleneck in quantum dots: Role of lifetime of the confined optical phonons," *Physical Review B*, vol. 59, pp. 5069–5073, Feb. 1999.

[154] J. Piprek, J. White, and A. SpringThorpe, "What limits the maximum output power of long-wavelength AlGaInAs/InP laser diodes?," *IEEE Journal of Quantum Electronics*, vol. 38, pp. 1253–1259, Sept. 2002.

[155] J. Piprek, P. Abraham, and J. Bowers, "Self-consistent analysis of high-temperature effects on strained-layer multiquantum-well InGaAsP-InP lasers," *IEEE Journal of Quantum Electronics*, vol. 36, pp. 366–374, Mar. 2000.

[156] M. Z. M. Khan, "Towards InAs/InP Quantum-Dash Laser-Based Ultra-High Capacity Heterogeneous Optical Networks: A Review," *IEEE Access*, vol. 10, pp. 9960–9988, 2022.

[157] J. P. Reithmaier, A. Somers, S. Deubert, R. Schwertberger, W. Kaiser, A. Forchel, M. Calligaro, P. Resneau, O. Parillaud, S. Bansropun, M. Krakowski, R. Alizon, D. Hadass, A. Bilenca, H. Dery, V. Mikhelashvili, G. Eisenstein, M. Gioannini, I. Montrosset, T. W. Berg, M. V. D. Poel, J. Mørk, and B. Tromborg, "InP based lasers and optical amplifiers with wire-/dot-like active regions," *Journal of Physics D: Applied Physics*, vol. 38, pp. 2088–2102, July 2005.

[158] Y. Arakawa and H. Sakaki, "Multidimensional quantum well laser and temperature dependence of its threshold current," *Applied Physics Letters*, vol. 40, pp. 939–941, June 1982.

[159] G. Liu, A. Stintz, H. Li, K. Malloy, and L. Lester, "Extremely low room-temperature threshold current density diode lasers using InAs dots in In0.15Ga0.85As quantum well," *Electronics Letters*, vol. 35, no. 14, p. 1163, 1999.

[160] A. Stintz, G. Liu, H. Li, L. Lester, and K. Malloy, "Low-threshold current density 1.3-Mm InAs quantum-dot lasers with the dots-in-a-well (DWELL) structure," *IEEE Photonics Technology Letters*, vol. 12, pp. 591–593, June 2000.

[161] H. Saito, K. Nishi, A. Kamei, and S. Sugou, "Low chirp observed in directly modulated quantum dot lasers," *IEEE Photonics Technology Letters*, vol. 12, pp. 1298–1300, Oct. 2000.

[162] T. Newell, D. Bossert, A. Stintz, B. Fuchs, K. Malloy, and L. Lester, "Gain and linewidth enhancement factor in InAs quantum-dot laser diodes," *IEEE Photonics Technology Letters*, vol. 11, pp. 1527–1529, Dec. 1999.

[163] G. Park, O. Shchekin, D. Huffaker, and D. Deppe, "Low-threshold oxide-confined 1.3-Mm quantum-dot laser," *IEEE Photonics Technology Letters*, vol. 12, pp. 230–232, Mar. 2000.

[164] X. Huang, A. Stintz, C. P. Hains, G. T. Liu, J. Cheng, and K. J. Malloy, "Efficient high-temperature CW lasing operation of oxide-confined long-wavelength InAs quantum dot lasers," *Electronics Letters*, vol. 36, pp. 41–42, Jan. 2000.

[165] P. Varangis, H. Li, G. Liu, T. Newell, A. Stintz, B. Fuchs, K. Malloy, and L. Lester,

"Low-threshold quantum dot lasers with 201 nm tuning range," *Electronics Letters*, vol. 36, no. 18, p. 1544, 2000.

[166] G. Huyet, D. O'Brien, S. P. Hegarty, J. G. McInerney, D. Bimberg, C. Ribbat, V. M. Ustinov, S. S. Mikhrin, A. R. Kovsh, and A. V. Uskov, "Reduced sensitivity to external feedback in quantum dot lasers," in *Quantum Dots, Nanoparticles, and Nanoclusters*, vol. 5361, pp. 21–28, SPIE, June 2004.

[167] S. Melnik, G. Huyet, and A. Uskov, "The linewidth enhancement factor α of quantum dot semiconductor lasers," *Optics Express*, vol. 14, no. 7, p. 2950, 2006.

[168] D. O'Brien, S. P. Hegarty, G. Huyet, and A. V. Uskov, "Sensitivity of quantum-dot semiconductor lasers to optical feedback," *Optics Letters*, vol. 29, pp. 1072–1074, May 2004.

[169] K. Mukai, Y. Nakata, K. Otsubo, M. Sugawara, N. Yokoyama, and H. Ishikawa, "1.3-um CW lasing characteristics of self-assembled InGaAs-GaAs quantum dots," *IEEE Journal of Quantum Electronics*, vol. 36, pp. 472–478, Apr. 2000.

[170] O. Shchekin, G. Park, D. Huffaker, Q. Mo, and D. Deppe, "Low-threshold continuous-wave two-stack quantum-dot laser with reduced temperature sensitivity," *IEEE Photonics Technology Letters*, vol. 12, pp. 1120–1122, Sept. 2000.

[171] F. Klopf, S. Deubert, J. P. Reithmaier, and A. Forchel, "Correlation between the gain profile and the temperature-induced shift in wavelength of quantum-dot lasers," *Applied Physics Letters*, vol. 81, pp. 217–219, June 2002.

[172] M. G. Thompson, A. R. Rae, M. Xia, R. V. Penty, and I. H. White, "InGaAs Quantum-Dot Mode-Locked Laser Diodes," *IEEE Journal of Selected Topics in Quantum Electronics*, vol. 15, pp. 661–672, May 2009.

[173] D. Ouyang, N. N. Ledentsov, D. Bimberg, A. R. Kovsh, A. E. Zhukov, S. S. Mikhrin, and V. M. Ustinov, "High performance narrow stripe quantum-dot lasers with etched waveguide," *Semiconductor Science and Technology*, vol. 18, pp. L53–L54, Dec. 2003.

[174] L. Y. Karachinsky, T. Kettler, I. I. Novikov, Y. M. Shernyakov, N. Y. Gordeev, M. V. Maximov, N. V. Kryzhanovskaya, A. E. Zhukov, E. S. Semenova, A. P. Vasil'ev, V. M. Ustinov, G. Fiol, M. Kuntz, A. Lochmann, O. Schulz, L. Reissmann, K. Posilovic, A. R. Kovsh, S. S. Mikhrin, V. A. Shchukin, N. N. Ledentsov,

and D. Bimberg, "Metamorphic 1.5 Mm-range quantum dot lasers on a GaAs substrate," *Semiconductor Science and Technology*, vol. 21, p. 691, Apr. 2006.

[175] H. Saito, K. Nishi, and S. Sugou, "Ground-state lasing at room temperature in long-wavelength InAs quantum-dot lasers on InP(311)B substrates," *Applied Physics Letters*, vol. 78, pp. 267–269, Jan. 2001.

[176] C. Cornet, A. Schliwa, J. Even, F. Doré, C. Celebi, A. Létoublon, E. Macé, C. Paranthoën, A. Simon, P. M. Koenraad, N. Bertru, D. Bimberg, and S. Loualiche, "Electronic and optical properties of InAs-InP quantum dots on InP(100) and InP(311)B substrates: Theory and experiment," *Physical Review B*, vol. 74, p. 035312, July 2006.

[177] J. Brault, M. Gendry, G. Grenet, G. Hollinger, Y. Desières, and T. Benyattou, "Role of buffer surface morphology and alloying effects on the properties of InAs nanostructures grown on InP(001)," *Applied Physics Letters*, vol. 73, pp. 2932–2934, Nov. 1998.

[178] H. Weman, E. Martinet, M.-A. Dupertuis, A. Rudra, K. Leifer, and E. Kapon, "Two-dimensional quantum-confined Stark effect in V-groove quantum wires: Excited state spectroscopy and theory," *Applied Physics Letters*, vol. 74, pp. 2334–2336, Apr. 1999.

[179] G. Liu, Z. Lu, J. Liu, Y. Mao, M. Vachon, C. Song, P. Barrios, and P. J. Poole, "Passively mode-locked quantum dash laser with an aggregate 5.376 Tbit/s PAM-4 transmission capacity," *Optics Express*, vol. 28, pp. 4587–4593, Feb. 2020.

[180] T. W. Hänsch, "Nobel Lecture: Passion for precision," *Reviews of Modern Physics*, vol. 78, pp. 1297–1309, Nov. 2006.

[181] P. Marin-Palomo, J. N. Kemal, P. Trocha, S. Wolf, K. Merghem, F. Lelarge, A. Ramdane, W. Freude, S. Randel, and C. Koos, "Comb-based WDM transmission at 10 Tbit/s using a DC-driven quantum-dash mode-locked laser diode," *Optics Express*, vol. 27, pp. 31110–31129, Oct. 2019.

[182] Z. Lu, "Quantum-dot coherent comb lasers for terabit optical networking systems," in *Integrated Optics: Devices, Materials, and Technologies XXIII*, vol. 10921, pp. 65–74, SPIE, Mar. 2019.

[183] Z. Lu, J. Liu, L. Mao, C.-Y. Song, J. Weber, and P. Poole, "12.032 Tbit/s coher-

ent transmission using an ultra-narrow linewidth qantum dot 34.46-GHz C-Band coherent comb laser," in *Next-Generation Optical Communication: Components, Sub-Systems, and Systems VIII*, vol. 10947, pp. 116–122, SPIE, Feb. 2019.

[184] V. Ataie, E. Temprana, L. Liu, E. Myslivets, B. P.-P. Kuo, N. Alic, and S. Radic, "Flex-grid compatible ultra wide frequency comb source for 31.8 Tb/s coherent transmission of 1520 UDWDM channels," in *OFC 2014*, pp. 1–3, Mar. 2014.

[185] S. Liu, X. Wu, D. Jung, J. C. Norman, M. J. Kennedy, H. K. Tsang, A. C. Gossard, and J. E. Bowers, "High-channel-count 20 GHz passively mode-locked quantum dot laser directly grown on Si with 41 Tbit/s transmission capacity," *Optica*, vol. 6, p. 128, Feb. 2019.

[186] B. Corcoran, M. Tan, X. Xu, A. Boes, J. Wu, T. G. Nguyen, S. T. Chu, B. E. Little, R. Morandotti, A. Mitchell, and D. J. Moss, "Ultra-dense optical data transmission over standard fibre with a single chip source," *Nature Communications*, vol. 11, p. 2568, May 2020.

[187] Z. Lu, J. Liu, Y. Mao, K. Zeb, G. Liu, P. J. Poole, J. Weber, M. Rahim, G. Pakulski, C. Song, M. Vachon, P. Barrios, D. Poitras, S. Wang, and W. Jiang, "Quantum dash multi-wavelength lasers for Tbit/s coherent communications and 5G wireless networks," *Journal of the European Optical Society-Rapid Publications*, vol. 17, p. 9, Dec. 2021.

[188] P. J. Poole, Z. Lu, J. Liu, P. Barrios, Y. Mao, and G. Liu, "A Performance Comparison Between Quantum Dash and Quantum Well Fabry-Pérot Lasers," *IEEE Journal of Quantum Electronics*, vol. 57, pp. 1–7, Dec. 2021.

[189] S. Z. Li, "Photonic Integrated Circuit Simulator 3D (PICS3D)." Crosslight Software, Aug. 2023.

[190] Z. M. Fang, K. Y. Ma, D. H. Jaw, R. M. Cohen, and G. B. Stringfellow, "Photoluminescence of InSb, InAs, and InAsSb grown by organometallic vapor phase epitaxy," *Journal of Applied Physics*, vol. 67, pp. 7034–7039, June 1990.

[191] D. K. Gaskill, N. Bottka, L. Aina, and M. Mattingly, "Band-gap determination by photoreflectance of InGaAs and InAlAs lattice matched to InP," *Applied Physics Letters*, vol. 56, pp. 1269–1271, Mar. 1990.

[192] M. Gioannini, "Analysis of the Optical Gain Characteristics of Semiconductor

Quantum-Dash Materials Including the Band Structure Modifications Due to the Wetting Layer," *IEEE Journal of Quantum Electronics*, vol. 42, pp. 331–340, Mar. 2006.

[193] F. P. Kesamanly, I. U. V. Maltsev, D. N. Nasledov, L. A. Nikolaeva, M. N. Pivovarov, V. A. Skripkin, and I. U. I. Ukhanov, "Structure of the conduction band in indium arsenide(Indium arsenide crystals conduction band structure with various electron concentrations, determining electron mass dependence on concentration and temperature)," *Fizika i Tekhnika Poluprovodnikov*, vol. 3, pp. 1182–1187, 1969.

[194] Y.-S. Kim, K. Hummer, and G. Kresse, "Accurate band structures and effective masses for InP, InAs, and InSb using hybrid functionals," *Physical Review B*, vol. 80, p. 035203, July 2009.

[195] L.-c. Kuang, *Deep-Level Transient Spectroscopy for the Determination of Trap Parameters in Semiconductor Devices.* PhD thesis, Winnipeg, Manitoba, 1997.

[196] D.-S. Han and L. V. Asryan, "Effect of the Wetting Layer on the Output Power of a Double Tunneling-Injection Quantum-Dot Laser," *Journal of Lightwave Technology*, vol. 27, pp. 5775–5782, Dec. 2009.

[197] J.-F. Hayau, P. Besnard, O. Dehaese, F. Grillot, R. Piron, S. Loualiche, A. Martinez, K. Merghem, and A. Ramdane, "Effect of the wetting layer on intensity noise in quantum dot laser," in *2009 35th European Conference on Optical Communication*, pp. 1–2, Sept. 2009.

[198] P. Blood, "Gain and Recombination in Quantum Dot Lasers," *IEEE Journal of Selected Topics in Quantum Electronics*, vol. 15, no. 3, pp. 808–818, 2009.

[199] E. Azoff, "Closed-form method for solving the steady-state generalised energy-momentum conservation equations," *COMPEL - The international journal for computation and mathematics in electrical and electronic engineering*, vol. 6, pp. 25–30, Jan. 1987.

[200] E. Azoff, "Energy transport numerical simulation of graded AlGaAs/GaAs heterojunction bipolar transistors," *IEEE Transactions on Electron Devices*, vol. 36, pp. 609–616, Apr. 1989.

[201] M. Benzaquen, B. Belache, C. Blaauw, and R. A. Bruce, "Electrical characteristics of

zinc-doped indium phosphide," *Journal of Applied Physics*, vol. 68, pp. 1694–1701, Aug. 1990.

[202] NIST, "DLMF: §25.12 Polylogarithms - Chapter 25 Zeta and Related Functions." https://dlmf.nist.gov/25.12#ii.

[203] D. Bednarczyk and J. Bednarczyk, "The approximation of the Fermi-Dirac integral F12 (η)," *Physics Letters A*, vol. 64, pp. 409–410, Jan. 1978.

[204] A. R. Beattie and P. T. Landsberg, "Auger Effect in Semiconductors," *Proceedings of the Royal Society of London. Series A, Mathematical and Physical Sciences*, vol. 249, no. 1256, pp. 16–29, 1959.

[205] A. Hangleiter and R. Häcker, "Enhancement of band-to-band Auger recombination by electron-hole correlations," *Physical Review Letters*, vol. 65, pp. 215–218, July 1990.

[206] A. Haug, "Band-to-band Auger recombination in semiconductors," *Journal of Physics and Chemistry of Solids*, vol. 49, pp. 599–605, Jan. 1988.

[207] M. J. Kerr and A. Cuevas, "General parameterization of Auger recombination in crystalline silicon," *Journal of Applied Physics*, vol. 91, pp. 2473–2480, Feb. 2002.

[208] A. Haug, "Auger recombination in direct-gap semiconductors: Band-structure effects," *Journal of Physics C: Solid State Physics*, vol. 16, pp. 4159–4172, July 1983.

[209] A. R. Beattie, "Auger transitions in semiconductors and their computation," *Journal of Physics C: Solid State Physics*, vol. 18, pp. 6501–6515, Dec. 1985.

[210] G. Fuchs, J. Hörer, A. Hangleiter, V. Härle, F. Scholz, R. W. Glew, and L. Goldstein, "Intervalence band absorption in strained and unstrained InGaAs multiple quantum well structures," *Applied Physics Letters*, vol. 60, pp. 231–233, Jan. 1992.

[211] P. Lochner, A. Kurzmann, J. Kerski, P. Stegmann, J. König, A. D. Wieck, A. Ludwig, A. Lorke, and M. Geller, "Real-Time Detection of Single Auger Recombination Events in a Self-Assembled Quantum Dot," *Nano Letters*, vol. 20, pp. 1631–1636, Mar. 2020.

[212] A. V. Uskov, Y. Boucher, J. Le Bihan, and J. McInerney, "Theory of a self-assembled

quantum-dot semiconductor laser with Auger carrier capture: Quantum efficiency and nonlinear gain," *Applied Physics Letters*, vol. 73, pp. 1499–1501, Sept. 1998.

[213] S. C. Heck, S. Osborne, S. B. Healy, E. P. O'Reilly, F. Lelarge, F. Poingt, O. Le Gouezigou, and A. Accard, "Experimental and Theoretical Study of InAs/InGaAsP/InP Quantum Dash Lasers," *IEEE Journal of Quantum Electronics*, vol. 45, pp. 1508–1516, Dec. 2009.

[214] P. Blood, H. Pask, I. Sandall, and H. Summers, "Recombination in quantum dot ensembles," in *Novel In-Plane Semiconductor Lasers VI*, vol. 6485, pp. 137–146, SPIE, Feb. 2007.

[215] E. B. Dogonkin, G. G. Zegrya, and A. S. Polkovnikov, "Microscopic theory of Auger recombination in quantum wires," *Journal of Experimental and Theoretical Physics*, vol. 90, pp. 378–388, Feb. 2000.

[216] M. Asada, Y. Miyamoto, and Y. Suematsu, "Gain and the threshold of three-dimensional quantum-box lasers," *IEEE Journal of Quantum Electronics*, vol. 22, pp. 1915–1921, Sept. 1986.

[217] B. Romero, J. Arias, I. Esquivias, and M. Cada, "Simple model for calculating the ratio of the carrier capture and escape times in quantum-well lasers," *Applied Physics Letters*, vol. 76, pp. 1504–1506, Mar. 2000.

[218] G. W. Ford, J. T. Lewis, and R. F. O'Connell, "Quantum Langevin equation," *Physical Review A*, vol. 37, pp. 4419–4428, June 1988.

[219] F. Hartmann, *Green's Functions and Finite Elements.* Springer Science & Business Media, Aug. 2012.

[220] G. B. Arfken, G. B. Arfken, H. J. Weber, and F. E. Harris, *Mathematical Methods for Physicists: A Comprehensive Guide.* Academic Press, 2013.

[221] Y. Saad, *Numerical Methods for Large Eigenvalue Problems: Revised Edition.* SIAM, 2011.

[222] B. Tromborg, H. Olesen, and X. Pan, "Theory of linewidth for multielectrode laser diodes with spatially distributed noise sources," *IEEE Journal of Quantum Electronics*, vol. 27, pp. 178–192, Feb. 1991.

[223] W. Rudno-Rudziński, G. Sek, K. Ryczko, R. Kudrawiec, J. Misiewicz, A. Somers, R. Schwertberger, J. P. Reithmaier, and A. Forchel, “Optically probed wetting layer in InAs/InGaAlAs/InP quantum-dash structures,” *Applied Physics Letters*, vol. 86, p. 101904, Mar. 2005.

[224] W. Y. Liang and A. R. Beal, “A study of the optical joint density-of-states function,” *Journal of Physics C: Solid State Physics*, vol. 9, p. 2823, July 1976.

[225] M. Yamada, S. Ogita, M. Yamagishi, and K. Tabata, “Anistropy and broadening of optical gain in a GaAs/AlGaAs multiquantum-well laser,” *IEEE Journal of Quantum Electronics*, vol. 21, pp. 640–645, June 1985.

[226] A. Dikshit and J. Pikal, “Carrier Distribution, Gain, and Lasing in 1.3->tex<$mu hboxm$>/tex<InAs–InGaAs Quantum-Dot Lasers,” *IEEE Journal of Quantum Electronics*, vol. 40, pp. 105–112, Feb. 2004.

[227] D. Zhou, R. Piron, M. Dontabactouny, E. Homeyer, O. Dehaese, T. Batte, M. Gicquel, F. Grillot, K. Tavernier, J. Even, and S. Loualiche, “Effect of stack number on the threshold current density and emission wavelength in quantum dash/dot lasers,” *physica status solidi c*, vol. 6, pp. 2217–2221, Oct. 2009.

[228] H. Fangohr, D. S. Chernyshenko, M. Franchin, T. Fischbacher, and G. Meier, “Joule heating in nanowires,” *Physical Review B*, vol. 84, p. 054437, Aug. 2011.

[229] R. Stratton, “Semiconductor current-flow equations (diffusion and degeneracy),” *IEEE Transactions on Electron Devices*, vol. 19, pp. 1288–1292, Dec. 1972.

[230] G. Wachutka, “Rigorous thermodynamic treatment of heat generation and conduction in semiconductor device modeling,” *IEEE Transactions on Computer-Aided Design of Integrated Circuits and Systems*, vol. 9, pp. 1141–1149, Nov. 1990.

[231] D. Bimberg and J. Mycielski, “Recombination-induced heating of free carriers in a semiconductor,” *Physical Review B*, vol. 31, pp. 5490–5493, Apr. 1985.

[232] Z. Sobiesierski, D. I. Westwood, P. J. Parbrook, K. B. Ozanyan, M. Hopkinson, and C. R. Whitehouse, “As/P exchange on InP(001) studied by reflectance anisotropy spectroscopy,” *Applied Physics Letters*, vol. 70, pp. 1423–1425, Mar. 1997.

[233] M. Gonzalez, J. Garcia, L. Gonzalez, J. Silveira, Y. Gonzalez, J. Gomez, and

F. Briones, "In situ measurements of As-P exchange during InAs-InP(0 0 1) quantum wires growth," *Applied Surface Science*, vol. 188, pp. 188–192, Mar. 2002.

[234] S. Yoon, Y. Moon, T.-W. Lee, E. Yoon, and Y. D. Kim, "Effects of As-P exchange reaction on the formation of InAs-InP quantum dots," *Applied Physics Letters*, vol. 74, pp. 2029–2031, Apr. 1999.

[235] D. Fuster, M. U. González, L. González, Y. González, T. Ben, A. Ponce, S. I. Molina, and J. Martínez-Pastor, "Size control of InAs-InP(001) quantum wires by tailoring P-As exchange," *Applied Physics Letters*, vol. 85, pp. 1424–1426, Aug. 2004.

[236] G. Agnello, V. Tokranov, M. Yakimov, M. Lamberti, Y. Zheng, and S. Oktyabrsky, "Structural and Optical Effects of Capping Layer Material and Growth Rate on the Properties of Self-Assembled InAs Quantum Dot Structures," *MRS Proceedings*, vol. 829, p. B2.1, 2004.

[237] R. Schwertberger, D. Gold, J. Reithmaier, and A. Forchel, "Long-wavelength InP-based quantum-dash lasers," *IEEE Photonics Technology Letters*, vol. 14, pp. 735–737, June 2002.

[238] S. Healy and E. O'Reilly, "Theoretical Investigation of Anisotropic Gain Mechanisms in InGaAsP-Based 1.5-Mm Quantum Dash Lasers," *IEEE Journal of Quantum Electronics*, vol. 46, pp. 742–753, May 2010.

[239] S. C. Heck, S. B. Healy, S. Osborne, E. P. O'Reilly, F. Lelarge, F. Poingt, A. Accard, F. Pommereau, O. Le Gouezigou, and B. Dagens, "An analysis of 1.55 Mm InAs/InP quantum dash lasers," *Applied Physics Letters*, vol. 92, p. 251105, June 2008.

[240] M. Gioannini, P. Bardella, and I. Montrosset, "Time-Domain Traveling-Wave Analysis of the Multimode Dynamics of Quantum Dot Fabry–Perot Lasers," *IEEE Journal of Selected Topics in Quantum Electronics*, vol. 21, pp. 698–708, Nov. 2015.

[241] S. Meinecke, *Spatio-Temporal Modeling and Device Optimization of Passively Mode-Locked Semiconductor Lasers*. Springer Theses, Cham: Springer International Publishing, 2022.

[242] J. Yu, S. Kim, and T. Kim, "PtTiPtAu and PdTiPtAu ohmic contacts to p-InGaAs," in *Compound Semiconductors 1997. Proceedings of the IEEE Twenty-Fourth International Symposium on Compound Semiconductors*, (San Diego, CA, USA), pp. 175–178, IEEE, 1997.

[243] J. C. Lin, S. Y. Yu, and S. E. Mohney, "Characterization of low-resistance ohmic contacts to n- and p-type InGaAs," *Journal of Applied Physics*, vol. 114, p. 044504, July 2013.

[244] JR. Biard, WN. Carr, and BS. Reed, "Analysis of a GaAs laser," *Trans. AIME*, vol. 230, pp. 286–290, 1964.

[245] L. Asryan, S. Luryi, and R. Suris, "Internal efficiency of semiconductor lasers with a quantum-confined active region," *IEEE Journal of Quantum Electronics*, vol. 39, pp. 404–418, Mar. 2003.

[246] B. W. Hakki and T. L. Paoli, "Gain spectra in GaAs double-heterostructure injection lasers," *Journal of Applied Physics*, vol. 46, pp. 1299–1306, Mar. 1975.

[247] D. T. Cassidy, "Technique for measurement of the gain spectra of semiconductor diode lasers," *Journal of Applied Physics*, vol. 56, pp. 3096–3099, Dec. 1984.

[248] M. Saldutti, A. Tibaldi, F. Cappelluti, and M. Gioannini, "Impact of carrier transport on the performance of qd lasers on silicon: a drift-diffusion approach," *Photonics Research*, vol. 8, p. 1388, Aug. 2020.

[249] H. Radamson and L. Thylen, *Monolithic Nanoscale Photonics-Electronics Integration in Silicon and Other Group IV Elements.* Academic Press, Sept. 2014.

[250] C. Henry, "Theory of spontaneous emission noise in open resonators and its application to lasers and optical amplifiers," *Journal of Lightwave Technology*, vol. 4, pp. 288–297, Mar. 1986.

[251] D. R. Matthews, H. D. Summers, P. M. Smowton, and M. Hopkinson, "Experimental investigation of the effect of wetting-layer states on the gain–current characteristic of quantum-dot lasers," *Applied Physics Letters*, vol. 81, pp. 4904–4906, Dec. 2002.

[252] L. Asryan and S. Luryi, "Tunneling-injection quantum-dot laser: Ultrahigh temperature stability," *IEEE Journal of Quantum Electronics*, vol. 37, pp. 905–910, July 2001.

[253] H. Sun, L. Davis, S. Sethi, J. Singh, and P. Bhattacharya, "Properties of a tunneling injection quantum-well laser: Recipe for 'cold' device with a large modulation bandwidth," *IEEE Photonics Technology Letters*, vol. 5, pp. 870–872, Aug. 1993.

[254] P. K. Kondratko, S.-L. Chuang, G. Walter, T. Chung, and N. Holonyak, Jr., “Observations of near-zero linewidth enhancement factor in a quantum-well coupled quantum-dot laser,” *Applied Physics Letters*, vol. 83, pp. 4818–4820, Dec. 2003.

[255] S. Fathpour, Z. Mi, and P. Bhattacharya, “High-speed quantum dot lasers,” *Journal of Physics D: Applied Physics*, vol. 38, p. 2103, June 2005.

[256] Z. Mi, P. Bhattacharya, and S. Fathpour, “High-speed 1.3μm tunnel injection quantum-dot lasers,” *Applied Physics Letters*, vol. 86, p. 153109, Apr. 2005.

[257] W. Rudno-Rudziński, M. Syperek, A. Maryński, J. Andrzejewski, J. Misiewicz, S. Bauer, V. I. Sichkovskyi, J. P. Reithmaier, M. Schowalter, B. Gerken, A. Rosenauer, and G. Sek, “Control of Dynamic Properties of InAs/InAlGaAs/InP Hybrid Quantum Well-Quantum Dot Structures Designed as Active Parts of 1.55 Mm Emitting Lasers,” *physica status solidi (a)*, vol. 215, no. 4, p. 1700455, 2018.

[258] S. Bhowmick, M. Z. Baten, T. Frost, B. S. Ooi, and P. Bhattacharya, “High Performance InAs/InGaAlAs/InP Quantum Dot 1.55 Mm Tunnel Injection Laser,” *IEEE Journal of Quantum Electronics*, vol. 50, pp. 7–14, Jan. 2014.

[259] W. Rudno-Rudziński, M. Syperek, J. Andrzejewski, E. Rogowicz, G. Eisenstein, S. Bauer, V. I. Sichkovskyi, J. P. Reithmaier, and G. Sek, “Carrier transfer efficiency and its influence on emission properties of telecom wavelength InP-based quantum dot – quantum well structures,” *Scientific Reports*, vol. 8, p. 12317, Aug. 2018.

[260] T. S. Sosnowski, T. B. Norris, H. Jiang, J. Singh, K. Kamath, and P. Bhattacharya, “Rapid carrier relaxation in InGaAs/GaAs quantum dots characterized by differential transmission spectroscopy,” *Physical Review B*, vol. 57, pp. R9423–R9426, Apr. 1998.

[261] A. A. George, P. M. Smowton, Z. Mi, and P. Bhattacharya, “Long wavelength quantum-dot lasers selectively populated using tunnel injection,” *Semiconductor Science and Technology*, vol. 22, p. 557, Apr. 2007.

[262] D.-S. Han and L. V. Asryan, “Output power of a double tunneling-injection quantum dot laser,” *Nanotechnology*, vol. 21, p. 015201, Nov. 2009.

[263] S. Bauer, V. Sichkovskyi, and J. P. Reithmaier, “Growth and optical characteristics of InAs quantum dot structures with tunnel injection quantum wells for 1.55 μm high-speed lasers,” *Journal of Crystal Growth*, vol. 491, pp. 20–25, June 2018.

[264] S. Sekiguchi, T. Miyamoto, T. Kimura, G. Okazaki, F. Koyama, and K. Iga, "Improvement of Current Injection Uniformity and Device Resistance in Long-Wavelength Vertical-Cavity Surface-Emitting Laser Using a Tunnel Junction," *Japanese Journal of Applied Physics*, vol. 39, p. 3997, July 2000.

[265] T. Miyamoto, K. Mori, H. Maekawa, Y. Inaba, F. K. F. Koyama, and K. I. K. Iga, "Carrier Transport in p-Type GaInAsP/InP Distributed Bragg Reflectors," *Japanese Journal of Applied Physics*, vol. 33, p. 4614, Aug. 1994.

[266] S. Sekiguchi, T. Kimura, T. Miyamoto, F. Koyama, and K. Iga, "Long Wavelength GaInAsP/InP Laser with n-n Contacts Using AlAs/InP Hole Injecting Tunnel Junction," *Japanese Journal of Applied Physics*, vol. 38, p. L443, Apr. 1999.

[267] I. C. Sandall, P. M. Smowton, J. D. Thomson, T. Badcock, D. J. Mowbray, H.-Y. Liu, and M. Hopkinson, "Temperature dependence of threshold current in p-doped quantum dot lasers," *Applied Physics Letters*, vol. 89, p. 151118, Oct. 2006.

[268] A. Rantamaki, J. Rautiainen, L. Toikkanen, I. Krestnikov, M. Butkus, E. U. Rafailov, and O. Okhotnikov, "Flip Chip Quantum-Dot Semiconductor Disk Laser at 1200 nm," *IEEE Photonics Technology Letters*, vol. 24, pp. 1292–1294, Aug. 2012.

[269] N. M. Collins, *Heat Spreader Design for Improved Performance and Reliability of II-V Quantum Dot Lasers.* M.S., University of California, Santa Barbara, United States – California, 2020.

[270] M.-C. Amann, "Polarization control in ridge-waveguide-laser diodes," *Applied Physics Letters*, vol. 50, pp. 1038–1040, Apr. 1987.

[271] J. Fu, R. Yang, G. Chen, J. P. Fleurial, and G. J. Snyder, "Integrated electroplated heat spreaders for high power semiconductor lasers," *Journal of Applied Physics*, vol. 104, p. 064907, Sept. 2008.

[272] A. Broda, A. Kuźmicz, G. Rychlik, K. Chmielewski, A. Wójcik-Jedlińska, I. Sankowska, K. Gołaszewska-Malec, K. Michalak, and J. Muszalski, "Highly efficient heat extraction by double diamond heat-spreaders applied to a vertical external cavity surface-emitting laser," *Optical and Quantum Electronics*, vol. 49, p. 287, Aug. 2017.

[273] A. Evans, S. R. Darvish, S. Slivken, J. Nguyen, Y. Bai, and M. Razeghi, "Buried het-

erostructure quantum cascade lasers with high continuous-wave wall plug efficiency," *Applied Physics Letters*, vol. 91, p. 071101, Aug. 2007.

[274] F. J. Duarte, "Tunable Lasers Handbook," in *Tunable Lasers Handbook*, Optics and Photonics, p. iii, San Diego: Academic Press, Jan. 1995.

[275] V. Rustichelli, C. Calò, F. Lemaitre, S. Andreou, N. Michel, F. Pommereau, H. Ambrosius, and K. Williams, "Monolithic Integration of Buried-Heterostructures in a Generic Integrated Photonic Foundry Process," *IEEE Journal of Selected Topics in Quantum Electronics*, vol. 25, pp. 1–8, Sept. 2019.

[276] O. Svelto, S. Longhi, G. Della Valle, G. Huber, S. Kück, M. Pollnau, H. Hillmer, T. Kusserow, R. Engelbrecht, F. Rohlfing (deceased), J. Kaiser, R. Malz, G. Marowsky, K. Mann, P. Simon, C. K. Rhodes, F. J. Duarte, A. Borsutzky, J. A. L'huillier, M. W. Sigrist, H. Wächter, E. Saldin, E. Schneidmiller, M. Yurkov, R. Sauerbrey, J. Hein, M. Gianella, J. Helmcke, K. Midorikawa, F. Riehle, S. Steinberg, and H. Brand, "Lasers and Coherent Light Sources," in *Springer Handbook of Lasers and Optics* (F. Träger, ed.), Springer Handbooks, pp. 641–1046, Berlin, Heidelberg: Springer, 2012.

[277] T. Tsukada and Y. Shima, "Thermal characteristics of buried-heterostructure injection lasers," *IEEE Journal of Quantum Electronics*, vol. 11, pp. 494–498, July 1975.

[278] D. Franke, M. Moehrle, A. Sigmund, H. Kuenzel, U. W. Pohl, and D. Bimberg, "Improved threshold of buried heterostructure InAs/GaInAsP quantum dot lasers," *Journal of Applied Physics*, vol. 109, p. 083104, Apr. 2011.

[279] P. M. Charles, M. Agresti, G. Burns, G. M. Berry, D. Bertone, A. Davies, R. Y. Fang, P. Gotta, C. Kompocholis, G. Magnetti, J. Massa, G. Meneghini, R. Paoletti, G. Rossi, A. Taylor, P. Valenti, and M. Meliga, "Optimization of InGaAsP/InP buried heterostructure DFB lasers for 10-Gbit/s operation up to 100 C," in *Laser Diodes, Optoelectronic Devices, and Heterogenous Integration*, vol. 4947, pp. 154–163, SPIE, Mar. 2003.

[280] S. J. Pearton, "Ion implantation for isolation of III-V semiconductors," *Materials Science Reports*, vol. 4, pp. 313–363, Jan. 1990.

[281] M. Z. M. Khan, T. K. Ng, U. Schwingenschlogl, P. Bhattacharya, and B. S. Ooi,

"Modeling the lasing spectra of InAs/InP Quantum dash lasers," *Applied Physics Letters*, vol. 98, p. 101105, Mar. 2011.

[282] C. Henry, "Phase noise in semiconductor lasers," *Journal of Lightwave Technology*, vol. 4, pp. 298–311, Mar. 1986.

[283] G. Moreau, S. Azouigui, D.-Y. Cong, K. Merghem, A. Martinez, G. Patriarche, A. Ramdane, F. Lelarge, B. Rousseau, B. Dagens, F. Poingt, A. Accard, and F. Pommereau, "Effect of layer stacking and p-type doping on the performance of InAs/InP quantum-dash-in-a-well lasers emitting at 1.55μm," *Applied Physics Letters*, vol. 89, p. 241123, Dec. 2006.

[284] M. Z. M. Khan, T. K. Ng, C.-S. Lee, P. Bhattacharya, and B. S. Ooi, "Chirped InAs/InP quantum-dash laser with enhanced broad spectrum of stimulated emission," *Applied Physics Letters*, vol. 102, p. 091102, Mar. 2013.

[285] R. Alizon, D. Hadass, V. Mikhelashvili, G. Eisenstein, R. Schwertberger, A. Somers, JP. Reithmaier, A. Forchel, M. Calligaro, S. Bansropun, *et al.*, "Multiple wavelength amplification in wide band high power 1550 nm quantum dash optical amplifier," *Electronics Letters*, vol. 40, no. 12, pp. 760–761, 2004.

[286] P. Caroff, C. Paranthoen, C. Platz, O. Dehaese, H. Folliot, N. Bertru, C. Labbé, R. Piron, E. Homeyer, A. Le Corre, and S. Loualiche, "High-gain and low-threshold InAs quantum-dot lasers on InP," *Applied Physics Letters*, vol. 87, p. 243107, Dec. 2005.

[287] F. Lelarge, B. Rousseau, B. Dagens, F. Poingt, F. Pommereau, and A. Accard, "Room temperature continuous-wave operation of buried ridge stripe lasers using InAs-InP (100) quantum dots as active core," *IEEE Photonics Technology Letters*, vol. 17, pp. 1369–1371, July 2005.

[288] J. R. Botha and A. W. R. Leitch, "Thermally activated carrier escape mechanisms from InGaAs/GaAs quantum wells," *Physical Review B*, vol. 50, pp. 18147–18152, Dec. 1994.

[289] M. Gurioli, J. Martinez-Pastor, M. Colocci, C. Deparis, B. Chastaingt, and J. Massies, "Thermal escape of carriers out of GaAs/AlGaAs quantum-well structures," *Physical Review B*, vol. 46, pp. 6922–6927, Sept. 1992.

[290] S. Y. Wang, S. D. Lin, H. W. Wu, and C. P. Lee, "High performance InAs/GaAs

quantum dot infrared photodetectors with AlGaAs current blocking layer," *Infrared Physics & Technology*, vol. 42, pp. 473–477, June 2001.

[291] K. Toprasertpong, S. M. Goodnick, Y. Nakano, and M. Sugiyama, "Effective mobility for sequential carrier transport in multiple quantum well structures," *Physical Review B*, vol. 96, p. 075441, Aug. 2017.

[292] S. Mokkapati and C. Jagadish, "III-V compound SC for optoelectronic devices," *Materials Today*, vol. 12, pp. 22–32, Apr. 2009.

[293] T. Ohtoshi, K. Yamaguchi, and N. Chinone, "Analysis of current leakage in InGaAsP/InP buried heterostructure lasers," *IEEE Journal of Quantum Electronics*, vol. 25, pp. 1369–1375, June 1989.

[294] B. Zoph, C. Raffel, D. Schuurmans, D. Yogatama, D. Zhou, D. Metzler, E. H. Chi, J. Wei, J. Dean, L. B. Fedus, M. P. Bosma, O. Vinyals, P. Liang, S. Borgeaud, T. B. Hashimoto, and Y. Tay, "Emergent abilities of large language models," *TMLR*, 2022.

[295] M. Rossetti, P. Bardella, and I. Montrosset, "Time-Domain Travelling-Wave Model for Quantum Dot Passively Mode-Locked Lasers," *IEEE Journal of Quantum Electronics*, vol. 47, pp. 139–150, Feb. 2011.